Inclusive Jet Cross Sections in Proton-Proton Collisions at 7.0 TeV Center-of-Mass Energy with the ATLAS Detector at the Large Hadron Collider

Thesis by

Kerstin M. Perez

In Partial Fulfillment of the Requirements
for the Degree of
Doctor of Philosophy

California Institute of Technology
Pasadena, California

2011
(Submitted June 7, 2011)

Abstract

Inclusive jet cross sections are measured using the full 2010 ATLAS data set, corresponding to approximately 37 pb^{-1} of proton-proton collisions at a center-of-mass energy of 7 TeV provided by the Large Hadron Collider. The cross sections are defined using the anti-k_t algorithm with two jet size parameters, $R = 0.6$ and $R = 0.4$, and shown as a function of jet transverse momentum and rapidity. The measurements extend to a maximum transverse momentum of 1.5 TeV and a maximum absolute rapidity of 4.4, far surpassing previous inclusive jet analyses. The cross sections are corrected for detector effects and compared to predictions from next-to-leading order perturbative quantum chromodynamics that are corrected for the non-perturbative effects of hadronization and underlying event. Comparisons are made to predictions obtained from a variety of modern parton distribution functions. Good agreement is seen across the full measured range, validating the theory in a new kinematic region. Small discrepancies in the high transverse momentum and high rapidity regions indicate the utility of including this data in the derivation of future parton distribution functions.

Contents

List of Figures

List of Tables

Chapter 1 Introduction

The inclusive jet cross section measurement is, above all, a fundamental test of perturbative quantum chromodynamics. Quantum chromodynamics (QCD) is the theory of the interactions of quarks and gluons, the constituent particles of hadrons such as the proton, under the influence of the strong force. Since its formulation in 1973, QCD has been extensively verified, most recently by jet measurements using Tevatron Run I (1992-1996) [1] and Tevatron Run II (2002-2011) [2][3] data and by measurements of deep inelastic scattering of electrons and positions on protons at HERA (1992-2007) [4]. The jet cross section analysis presented in this thesis exploits the unprecedented collision intensity and center-of-mass energy provided by the Large Hadron Collider (LHC) and the large solid-angle coverage of the ATLAS calorimeter system to extend these investigations to previously untested kinematic regions.

Together with assessing the validity of perturbative QCD, inclusive jet cross section measurements probe the structure of proton by testing existing and providing input to improved parton distribution functions (PDFs), which quantify the probability for a quark or gluon to carry a specific fraction of the total hadron momentum. Accurate formulation of these PDFs is essential for precision QCD calculations. Although many parameters of the PDFs are well-constrained by previous experiments, ATLAS jet measurements investigate new regions of jet production. In particular, the high-energy jets produced from proton-proton collisions at the LHC provided insight to the distribution of gluons with high momentum fraction. This distribution influences not only tests of QCD, but also background estimates for a plethora of new physics searches.

Even inside the kinematic range previously measured by other experiments, the inclusive jet cross section analysis provides crucial validation of ATLAS jet reconstruction with initial data. Within the first year of data taking, ATLAS was already producing measurements that rely on accurate knowledge of jet energies and positions. The demands on jet performance will only grow more stringent as the amount of data delivered by the LHC increases. Reliable comparisons of measured jet cross sections with precision QCD predictions gives confidence in both jet reconstruction and detector performance.

The inclusive jet cross sections presented in this thesis are double-differential cross sections, measured in bins of jet transverse momentum, p_T, and rapidity, y. The jet transverse momentum is the component of the jet momentum perpendicular to the direction of the initial colliding particles. The jet rapidity is defined as:

$$y = \frac{1}{2} ln(\frac{E + p_z}{E - p_z}), \tag{1.1}$$

where E is the energy of the jet and p_z is the component of the jet momentum along the direction of the colliding particles. The final jet cross section is then given by:

$$\frac{d^2\sigma}{dp_T dy} = \frac{N_{jets}}{\Delta p_T \Delta y \mathcal{L}} \tag{1.2}$$

Here, N_{jets} is the total number of jets produced in a given bin of Δp_T and Δy, and $\mathcal{L}$ is the total integrated luminosity, which quantifies the amount of data used for the measurement. The simplicity of this equation of course belies the complications of defining a jet, accurately measuring its position and energy, and correcting for all detector efficiencies and resolutions. These issues will be discussed in due course throughout this thesis.

The previous paragons of inclusive jet cross section measurements at a hadron collider are those reported by the CDF and D0 collaborations at the Tevatron. The first Run I measurements [1] were based on proton-antiproton collisions at a center-of mass energy of 1.8 TeV. The initial CDF analysis [5] found an excess of jets with transverse energies greater than 200 GeV in comparison with predictions from QCD, giving tantalizing hints at the existence of additional hard scatterings off of constituent particles inside the quarks. However, the D0 analysis did not see such an excess, instead demonstrating agreement with theoretical predictions up to $p_T < 500$ GeV and a psuedorapidity[1]of $|\eta| < 3.0$. Later CDF analyses confirmed that the previous anomaly could be erased, bringing their results in agreement with those of D0, by increasing the probability for gluons to have large momentum fractions within the PDFs used for theoretical comparisons. This episode, while ultimately confirming the validity of QCD at Tevatron energies, underlines the importance of accurate PDF modeling for searches for new physics in high-p_T jet signatures.

The most recent Run II jet measurements take advantage of collisions at a center-of-mass

---

[1] Pseudorapidity is defined as: $\eta = \frac{1}{2} ln(\frac{|p|+p_z}{|p|-p_z})$. In the approximation of a massless object, pseudorapidity and rapidity are equivalent.

energy of 1.96 TeV and a dramatically increased total luminosity with respect to Run I. The D0 inclusive jet cross section measurements [2] utilize 0.70 fb^{-1} of integrated luminosity, $\sim$ 20 times more data than is analyzed in this thesis. With this data, D0 finds agreement with theoretical predictions up to $p_T < 600$ GeV and $|y| < 2.4$. The CDF analysis [3] extends this agreement up to $p_T < 700$ GeV within $|y| < 2.1$ using 1.11 fb^{-1} of data.

Using the full ATLAS 2010 data set, consisting of approximately 37 pb^{-1} collected in proton-proton collisions at a center-of-mass energy of 7 TeV, the measurements presented in this thesis surpass the D0 and CDF measurements in reach in both p_T and rapidity. Cross sections are measured up to $p_T < 1.5$ TeV and $|y| < 4.4$. Jets are formed using the anti-k$_t$ algorithm with two different jet sizes, $R = 0.4$ and $R = 0.6$, each of which probe different aspects of the non-perturbative QCD effects of underlying event, fragmentation, and hadronization. With these measurements, a variety of existing PDFs, several non-perturbative models, and, in fact, perturbative QCD itself are tested in a previously unexplored kinematic regime.

Chapter 2 Quantum Chromodynamics

2.1 The Standard Model

The Standard Model [6] describes particle interactions at the universe's smallest distances and its highest energies probed today. It is a coherent theory that describes the behavior of all experimentally-observed particles under the influence of the electromagnetic force, the weak force, and the strong force. In this model, each force is transmitted by one or several particles. These force-mediators act on the particles of matter, and, in some cases, each other. The predictions made possible by this theory have withstood the tests of the last 50 years of high-energy physics experiment, requiring only minor modifications to the parameters of the model. There do exist, however, particle interactions that are not described by this theory. The most conspicuous omission is a description of gravity, which is fortunately negligible at the distance and energy scales usually considered in particle physics experiments.

The strength of the Standard Model lies in its combination of elegant mathematical formulation with extensive phenomenological motivation and verification. The quantitative groundwork began in the 1920s and 1930s with the formulation of relativistic quantum mechanics [7]. This theory was able to describe small scales (hence, quantum) and large energies (hence, relativistic) by describing the behavior of interacting particles through the mathematics of interacting fields. The exact formalism follows from imposing Lorentz-invariant symmetries onto these fields. The three theoretical building blocks of the Standard Model, quantum electrodynamics, electroweak theory, and quantum chromodynamics, are all derived from this procedure.

Quantum electrodynamics (QED) describes the interactions of charged particles via the exchange of charge-neutral photons. It is formulated by imposing a U(1), or rotational, symmetry onto the simplest field Lagrangian that obeys the correct equations of motion. In order for this symmetry to apply in all frames of reference, additional fields, called gauge fields, must be introduced. These gauge fields, which must be massless, spin-1 bosons that dictate how the fields describing charged particles communicate with one another, are identified as photons. The full theory of QED, developed throughout the 1940s by Richard Feynman, Julian Schwinger, Sin-Itiro Tomonaga and others [8], immediately allowed the computation of previously unexplained phenomena, such as the Lamb shift observed in the energy levels of hydrogen. Its success has continued into the modern era of high-energy particle accelerators, predicting, for example, the total cross section for electron-positron scattering at LEP energies [9].

The description of the weak force builds from the Lagrangian of QED. This time, an SU(2) symmetry, which corresponds to rotations of 2-dimensional vectors, combines with the U(1) symmetry of QED to produce additional gauge fields. The gauge fields mix with the gauge field of QED to form the W^+, W^-, and Z^0 bosons that transmit the weak force. Unlike the photon, which is massless, the $W^\pm$ and Z^0 bosons have masses close to 80 and 90 GeV, respectively. Due to these large masses, the weak force has a short range and is feeble at low energies. At masses higher than the Z mass, the electromagnetic and weak forces unify into a single force, known as the electroweak force. By 1967, Sheldon Glashow, Abdus Salam, and Steven Weinberg had completed this mathematical portrait of electroweak interactions [10, 11, 12]. This electroweak model was shortly thereafter confirmed by the observation of neutral current interactions mediated by the Z boson in Gargamelle in 1973 [13], the observation of parity violation in deep inelastic electron scattering at SLAC [14], and the discovery of the $W^\pm$ and Z^0 bosons at the UA1 and UA2 experiments at LEP in 1983 [15, 16].

Well before the discovery of these electroweak bosons, however, a proliferation of other seemingly fundamental particles had been observed. This started in 1947, with the discovery of the K-meson [17], but over the ensuing decades grew to include dozens of other massive particles. While the behavior of these particles could be explained by the electroweak theory, they seemed to be purely ad-hoc additions to the particle structure of the universe. In 1964, Murray Gell-Mann and George Zweig proposed the quark model [18, 19, 20], which asserts that these particles, as well as the familiar proton and neutron, are in fact composites of smaller constituents. These constituent particles are called quarks, which have spin-1/2 and electric charge 2/3 or -1/3. Particles made of quark/antiquark pairs are called mesons, and particles made of three quarks are called baryons. Since none of these quarks had ever been observed, it was largely assumed that they were merely convenient pedantic constructs, used to help organize the growing mountain of particle observations.

In 1968, experiments scattering electrons off of protons and neutrons at SLAC confirmed that these are in fact composite objects [21, 22]. Doubts as to the quark model persisted, however, in particular since the data implied that a large fraction of the internal momentum of the proton and neutron was carried by a neutral particle that was not accounted for by quarks. The constituents were instead referred to, by Richard Feynman, as partons [23].

These remaining doubts were resolved in 1973, when the quark model was formalized into the quantum theory of the strong interaction by Harold Fritzsch and Murray Gell-Mann [24, 25]. This theory extended the electroweak Lagrangian to be symmetric under SU(3) variations, or rotations of 3-dimensional vectors, which introduces eight new physical gauge fields. These fields are identified as eight particles called gluons, which are charge-neutral and mediate the strong force between quarks. It is the strong force that binds these real, physical quarks into the observed composite quark structures, called hadrons. Due to Richard Feynman's previous nomenclature, both quarks and gluons are commonly referred to as partons.

In order to identify these quarks as the constituents of the observed particle spectrum and to explain why the strong force is not observed at long distances, the concept of color charge must be introduced. Quarks are spin-1/2 objects and as such must obey Pauli statistics. Without color charge, it would seem that the quarks inside some hadrons exist in identical quantum states, in violation of the Pauli exclusion principle. The existence of an additional quantum number, called color, resolves this problem. By convention, the three colors red, green, and blue correspond to particles; anti-red, anti-green, and anti-blue correspond to anti-particles. The SU(3) symmetry of the strong force can then be thought of as the group of transformations acting on 3-dimensional color charge vectors. In nature, only stable color-neutral states exist, and hence at large distances no strong color force is felt. It is this color feature that gives the theory of the strong interaction its name: quantum chromodynamics (QCD).

The combination of electroweak theory and QCD successfully describes the observed particles and interactions of high-energy particle physics. The fundamental particle content of this Standard Model, along with some common particle notation, is summarized in Tables 2.1 and 2.1. There are five force-mediating bosons: the photon, the W^+, the W^-, the Z^0, and the gluon. The constituents of matter are all fermions and can be further classified as either quarks, which interact via the electroweak and strong force, or leptons, which only interact via the electroweak force. Neutrinos, which are charge-neutral leptons, interact only weakly. Three generations, or families, of fermions have been experimentally observed. For the quarks, these correspond to the up and down, charm and strange, and top and bottom quarks; for the leptons, these correspond to the electron and electron neutrino, muon and muon neutrino, and tau and tau neutrino. The six types of quark are also known as the six quark flavors. The second and third generations of leptons are more massive and unstable than the first, and hence all the familiar, stable matter of the universe is made of up quarks, down quarks, and electrons. Collectively, the up, down, and strange quarks are frequently referred to as the light quarks.

Electromagnetic force	Weak force	Strong force
photon (γ) m = 0 GeV c = 0 1900	gauge bosons (W^+, W^-, Z^0) $m_{W^\pm} = 80.4$ GeV, $m_{Z^0} = 91.2$ GeV $c_{W^\pm} = \pm 1$, $c_{Z^0} = 0$ 1983	gluons (g) m = 0 GeV c = 0 1979

Table 2.1: Boson content of the Standard Model, along with each particle's common abbreviation, mass, charge, and year of discovery [26].

It is not a coincidence that the heaviest member of the Standard Model, the top quark, was also the last of the massive particles to be found [27, 28]. This is not only because of the experimental difficulties of producing such a heavy object, but also because experimentalists had limited guidance as to which mass range to probe. In fact, in the above description of the Standard Model, a key technicality was omitted. As presented, the exact symmetry of electroweak theory predicts massless gauge bosons, which have of course been repudiated by experiment. One possible mechanism for breaking this symmetry is the existence of a massive Higgs field that has a non-zero vacuum expectation value [29]. The existence of this field would break the exact symmetry, allowing the gauge bosons, and all other particles that interact with the Higgs field, to obtain masses. This Higgs boson has not yet been observed, but is widely considered the remaining missing piece of the Standard Model.

2.2 Perturbative QCD

The ability of QCD to describe the observed plethora of hadrons leaves several questions unanswered. Why do we never see free quarks or gluons outside of a hadron? And, on a

1st Generation	2nd Generation	3rd Generation
	Quarks	
up (u) m = 1.7-3.3 MeV c = 2/3 1964	charm (c) m = 1.27 GeV c = 2/3 1974	top (t) m = 172 GeV c = 2/3 1995
down (d) m = 4.1-5.8 MeV c = -1/3 1964	strange (s) 101 MeV c = -1/3 1964	bottom (b) 4.2 GeV c = -1/3 1977
	Leptons	
electron (e) m = 0.551 MeV c = -1 1897	muon (μ) m = 105.7 MeV c = -1 1936	tau (τ) m = 1.777 GeV c = -1 1975
electron neutrino (ν_e) m < 2 eV c = 0 1953	muon neutrino (ν_μ) m < 2 eV c = 0 1962	tau neutrino (ν_τ) m < 2 eV c = 0 2000

Table 2.2: Fermion content of the Standard Model, along with each particle's common abbreviation, mass (from QCD calculations and experimental measurements), charge, and year of discovery [26].

more practical note, how can this theory be used to make calculations that can be compared with experiment?

The answer to these questions lies in the complementary concepts of asymptotic freedom and confinement. The essence of asymptotic freedom is that the strong force couples particles together more strongly as the distance between them increases. This explains why quarks and gluons are only observed, at low energies, trapped together into color-neutral hadrons, in an effect is known as confinement. In very high-energy environments, such as the universe shortly after the big bang, quarks and gluons are only weakly linked by the strong force, forming what is called a quark-gluon plasma. A quantitative representation of the decreasing power of the strong force with increasing energy is given by the negative β-function of QCD [30, 31], which describes how the coupling constant of the force changes with energy. This variation of the strong coupling constant with energy is often referred to as the "running" of the coupling constant.

Since the coupling constant of QCD is large at small distance scales, analytic solutions are not possible for interactions on these scales. One method used to make QCD calculations for processes such as the confinement of quarks and gluons within hadrons and interactions between neighboring partons in a quark-gluon plasma is lattice QCD [32]. In lattice QCD, the complex equations of QCD are solved in small, discrete regions of space and time. Quarks are defined to be at the center of each of these regions, with gluon fields linking neighboring sites. Unfortunately, these solutions are incredibly computationally taxing.

In high-energy processes such as those at the LHC, the low value of the strong force coupling constant can be exploited, allowing perturbative techniques to be used to calculate physical processes. Each higher order of the perturbative expansion contains an additional factor of the strong coupling constant, α_s. Since the value of α_s varies with the energy, it must be evaluated at some energy scale close to the energy scale of the interaction. At energies of 15 GeV, α_s is $\sim$0.1, and the higher order terms can be ignored to yield an approximate solution. Thus from an expansion of an infinite number of terms, only a few need to be computed. The ultimate precision of the calculation that can be performed varies according to the complexity of the process. For example, predictions for the cross section for events with three partons in the final state are only available up to leading-order (LO). For inclusive parton production, calculations are typically performed at next-to-leading order (NLO).

To help organize the computation of the multitude of terms in perturbative calculations, the tool of Feynman diagrams is frequently used. Feynman diagrams are graphical representations of the terms of the perturbative expansion. The outer lines of the diagram correspond to incoming and outgoing particles, the inner lines correspond to virtual particles, and the vertices correspond to particle interactions. To each of these components of the diagram, a mathematical expression or operation is assigned. Each vertex corresponds to some power of α_s, so each increasing order in α_s of the perturbative expansion simply corresponds to a set of diagrams with the correct combination of vertices. By drawing all possible Feynman diagrams for a given order of perturbation theory, all the terms in the calculation can be read off. An example of diagrams corresponding to parton production at LO is shown in Figure 2.1. These leading-order diagrams are also known as "tree-level" diagrams.

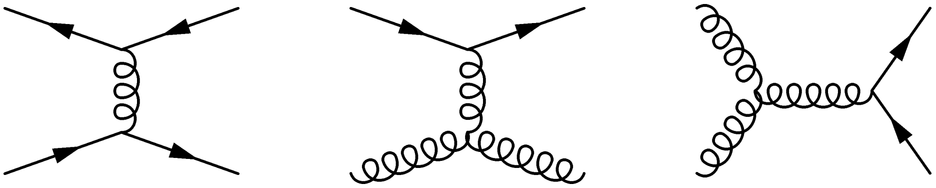

Figure 2.1: Sample leading-order diagrams corresponding to parton production from proton-proton collisions.

Using this formalism, the cross section for two partons to interact can be computed up to some fixed-order in perturbation theory, but there is a further complication. Colliders such as the LHC do not produce simple parton-parton interactions, but instead collisions of hadrons that consist of multiple partons.

The factorization theorem [33] allows the perturbative calculations for parton interactions to be extended into the complex world of hadron interactions. This theorem states that the total cross section for two hadrons to interact can be obtained by weighting and combining the cross sections for two particular partons to interact. This weighting is done using parton distribution functions, which state the probability for a certain parton to carry a momentum fraction x of the total hadron momentum. Thus the total cross section, at some momentum Q that characterizes the interaction, can be written as:

$$\sigma(P_1, P_2) = \sum_{i,j} \int dx_1 dx_2 f_i(x_1, \mu_f^2) f_j(x_2, \mu_f^2) \hat{\sigma}_{ij}(p_1, p_2, \alpha_s(\mu_r^2), Q^2/\mu_r^2, Q^2/\mu_f^2) \qquad (2.1)$$

Here, P_1 and P_2 are the momenta of the two incoming hadrons, x_1 and x_2 are the momentum fractions carried by the two interacting partons, and $p_1 = x_1 P_1$ and $p_2 = x_2 P_2$ are the momenta of the two interacting partons. The cross section $\hat{\sigma}_{ij}$, frequently referred to as the matrix element, is the cross section for two partons, i and j, to interact. This cross section is calculated to a fixed order in α_s, which is evaluated at some renormalization scale, μ_r. The total cross section is then obtained by summing over all possible parton flavors and integrating over all possible momentum fractions.

The parton distribution functions, f_i and f_j, are evaluated at a factorization scale, μ_f, which can be thought of as the scale that separates short-distance, perturbative physics from long-distance, non-perturbative physics. Any parton emitted with a momentum less than μ_f is considered part of the structure of the hadron, and thus absorbed into the parton distribution function. It is this separation that is at the heart of the factorization approach.

The two scale choices, μ_f and μ_r, are somewhat arbitrary, but need to be chosen at an appropriately high scale in order that the fixed-order calculations converge. As such, they should have no bearing on the physical cross section. Any differences in the calculated cross sections due to different choices of these scales can therefore be interpreted as an uncertainty due to the unknown higher-order corrections in the cross section calculation.

2.3 Parton Distribution Functions

In the simplest hadron picture, a proton is a combination of three quarks: two up quarks and one down quark. The reality, however, is much more complicated, with gluons constantly being emitted and absorbed, causing quark/antiquark pairs of many flavors to briefly fluctuate into and out of existence. The three static quarks of the standard hadron picture are called valence quarks, while the virtual quark/antiquark pairs are known as sea quarks. Both valence quarks and sea quarks, along with the gluons, share the total momentum of the hadron. The time-averaged probability for each of these constituents to carry a specific fraction, x, of the total momentum of the hadron is given by the parton distribution functions (PDFs) of Equation 2.1.

A sample PDF for a proton is shown in Figure 2.2. Note that the distribution of momenta inside the hadron depends strongly on the Q scale of the interaction, and in particular that with increasing Q, lower values of x are accessible. As one might intuitively expect, the valence quarks are much more likely to carry a high fraction x of the total momentum, with the two u quarks carrying approximately twice as much as the one d quark. Their sea quark counterparts, the $\bar{u}$ and $\bar{d}$ quarks, are much less likely to carry a high momentum fraction. The sea quarks of additional heavier flavors are even less likely to be at high x, with both quarks and antiquarks being equally likely to be found at any given x. The total momentum at low x is dominated by the gluon contribution, as can be noted by the scaling factor applied to the gluon contribution in Figure 2.2.

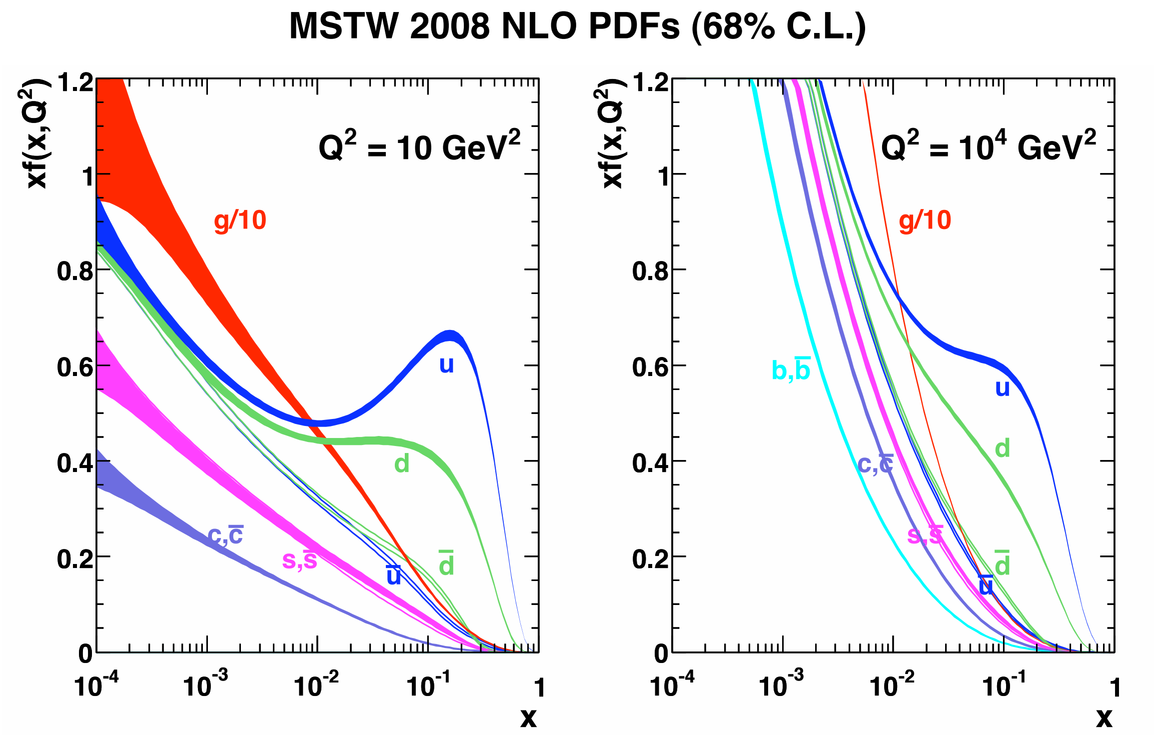

Figure 2.2: Parton distribution functions as a function of momentum fraction x, for $Q^2 = 10$ GeV^2 (left) and $Q^2 = 10^4$ GeV^2 (right), from the MSTW group [34]. The width of the bands for each parton corresponds to the uncertainty on the PDF prediction, in this case a 68% confidence level assignment.

The dependence of the PDF on Q is given by the DGLAP equations, published separately in the 1970s by Yuri Dokshitzer, Vladimir Gribov and Lev Lipatov, and Guido Altarelli and

Giorgio Parisi [35, 36, 37]. The DGLAP equations are derived by noting that the PDFs should be independent of the factorization scale μ_f. This gives a precise mathematical form to the dependence.

The dependence on x, on the other hand, must be obtained by fitting possible cross section predictions to data from hard scattering experiments. This inconvenience is in fact to be expected, since the structure inside the proton is a region of strong coupling constant α_s, and hence is not accessible with analytic non-perturbative calculations.

The uncertainties on these PDFs then come from uncertainties on the input experimental data and uncertainties on the fit to this data. In Figure 2.2, these uncertainties are depicted as the width of the lines for each parton, and correspond to a one-sigma variance, or 68% confidence level. Much of the input data for these fits come from deep inelastic scattering experiments, which use electrons, muons, or neutrinos to probe the structure of hadrons. Some of the most commonly used sets of such data come from the *e*-*p* experiments ZEUS and H1 at the HERA collider. Unfortunately, since electrons do not directly interact with gluons, these give poor constraints on the gluon PDF, particularly at high momentum fraction x. As a result, much of the data used to constrain high x gluon distributions come from Tevatron jet measurements, in particular the inclusive jet cross section analyses. At low x, below $\sim 10^{-3}$, there is only limited data from any experiment, and the PDFs are limited by experimental uncertainties. High x, conversely, has been very well constrained by fixed target experiments. A summary of the Q and x regions available to both fixed target and deep inelastic scattering experiments, as well as that available to the LHC experiments, is shown in Figure 2.3.

These constraints on the knowledge of the proton PDF are both a challenge and an opportunity for QCD measurements at the LHC. The LHC is able to probe regions of higher Q^2 and lower x than ever accessed by previous experiments. This means that comparisons to predictions in these regions are limited, since all PDFs are merely making extrapolations to LHC regions. On the other hand, this means that any jet measurement in this region will become an important input to future PDF sets.

Since PDFs are derived by fitting perturbative cross section calculations to data, they correspond to the particular order in perturbation theory that was used for the calculation. For example, if the comparison with a LO cross section calculation is used as an input to the fit, this will produce a LO PDF. When utilizing these PDFs, care must be taken to use

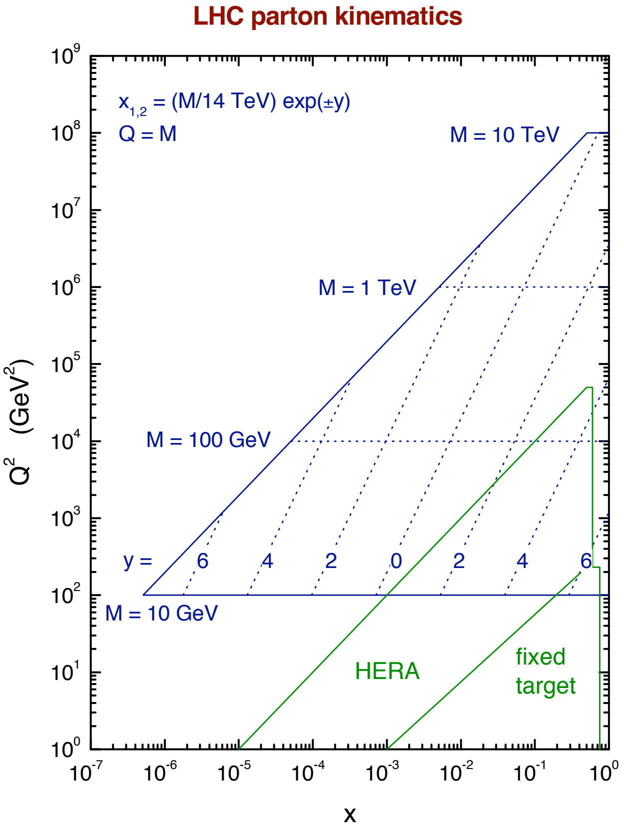

Figure 2.3: Regions of Q^2 and x probed by fixed target experiments, the deep inelastic scattering experiments of HERA, and LHC jet measurements at $\sqrt{s} = 14$ TeV. Different ranges of LHC access are shown according to mass (M) and absolute rapidity (y) of the jets measured. [34]

the appropriate order of PDF with the appropriate order of perturbative calculation. For NLO theory calculations, one must use an NLO PDF. Monte Carlo methods, described in Section 2.5, typically use LO calculations that poorly model many physics processes, for example the inclusive jet cross section. To improve the description of reality, many Monte Carlo generators therefore use modified LO (LO*) PDFs, which have been altered to better model NLO predictions.

Since the choice of PDF strongly affects the predictions of perturbative QCD calculations, especially in the high Q^2 and low x regions that will be probed by the inclusive jet measurement presented here, the main PDF sets used in this thesis are briefly introduced below.

CTEQ

The CTEQ [38], or Coordinated Theoretical-Experimental Project on QCD, group is a multi-institute collaboration of theorists and experimentalists that has provided PDF sets since the early 1990s. The main PDFs from this group that are used in this thesis are the CT10 [39] and CTEQ6.6 [40] sets.

As with almost all PDF sets, the CTEQ sets make extensive use of the precise deep inelastic scattering measurements from HERA and fixed target experiments. In addition, the CTEQ6.6 set includes the data from the Tevatron Run I inclusive jet cross section measurements of CDF and D0, which extend up to a p_T of $\sim$ 500 GeV and a rapidity of $|y| < 3$. The main feature of the CTEQ6.6 set, with respect to previous CTEQ sets, is that the gluon distribution is considerably harder. The new CT10 set includes both Run I and Run II Tevatron jet data, with the result that the distributions at high p_T and very forward rapidity are somewhat softer than for CTEQ6.6.

The errors on the CTEQ PDF sets are given as a group of variations around the central value that corresponds to a 90% confidence limit. More precisely, a basis of eigenvectors is constructed from combinations of the parameters used for the PDF fits, so correlations between the fit parameters are now removed in the new eigenbasis. Two error members are provided for each eigenvector, one in the positive and one in the negative direction from the central value. The total number of eigenvectors varies betwee CTEQ6.6, and CT10, but is close to 40 for both.

MSTW2008

The MSTW2008 set of PDFs is prepared by A.D. Martin, W.J. Stirling, R.S. Thorne, and G. Watt [34]. This set consists of LO, NLO, and NNLO PDFs produced explicitly for first LHC data-taking. The uncertainties are provided by sets of eigenvectors that correspond to a 90% confidence level, as with the CTEQ sets.

MSTW2008 incorporates a set of data very similar to that of CTEQ, but includes the Tevatron jet cross section measurements only from Run II and also adds neutrino deep inelastic scattering data from NuTeV and CHORUS. Because of these different inputs, in particular the different sets of jet data, there are systematic differences in the gluon distributions between MSTW2008 and the CTEQ6.6 PDFs. In the CTEQ6.6 sets, the gluon contribution at high x is constrained to be larger by the Tevatron Run I data and is correspondingly smaller at low x.

NNPDF 2.0

The NNPDF [41, 42] set uses a neural network technique to derive PDF fits to experimental data. In this technique, a set of artificial data is generated by producing events within a multi-gaussian distribution centered on the original data. The variance of this generated data is given by the systematic uncertainties on the experimental input. Typically, ~1000 replica data points are produced for each input data point. A set of PDFs parameterized by neural networks are then trained on this generated data by performing fits, evolving the PDFs from some starting scale to the scale of the experimental data. Rather than using the minimum χ^2 of the fit to choose the final PDF value, as other sets do, the NNPDF set is defined by choosing the fit which produces the χ^2 that is closest to that expected from the data uncertainties.

The input to this neural network technique is the standard set of fixed target and collider deep inelastic scattering data and inclusive jet Tevatron data. The result of the technique is typically a larger spread in the given PDF uncertainty, such that the NNPDF uncertainty frequently covers the differences observed between, for example, the CTEQ6.6 and MSTW PDF sets, which is not covered by the error bands of the two sets alone.

HERAPDF 1.5

The HERAPDF [43] set provides fits to the combined inclusive deep inelastic scattering data from both H1 and ZEUS experiments at HERA. Errors are delivered similarly to the method used by the CTEQ and MSTW groups, but this time the eigenvectors correspond to one-sigma variance, or a 68% confidence level. HERAPDF is an interesting PDF to use for comparisons to the inclusive jet cross sections of this thesis, because it contains a lower gluon density at high x, which is where most high-p_T jet processes occur.

2.4 Non-perturbative QCD

The last two sections detailed how to make perturbative QCD calculations of parton-scattering cross sections from hadron-hadron interactions. In order to compare these predictions with experiment, though, these parton collision products must be translated to stable particle quantities that can be observed by experiment.

The evolution from a single parton to an ensemble of hadrons occurs through the processes of parton showering and hadronization. Since the strong coupling constant grows with increasing distance between color charges, a strong color potential forms as the parton from the high Q^2, or “hard,” scattering process separates from the original hadron. This large potential causes quark/antiquark pairs to be created, each carrying some of the energy and momentum of the original partons. As these new partons move away from one another, yet more color potentials are formed, and the process repeats. Thus from one parton a shower of partons appears, travelling along the same direction as the original parton. This process continues until there is no longer enough energy to create additional quark/antiquark pairs, and instead the remaining partons combine to form stable hadrons. Since this progression involves successively lower energies and lower momentum transfers, perturbative QCD cannot describe the full process.

As a particular pair of partons undergo the hard interaction and parton shower, the other parton members of the colliding hadrons, separated from some of their original neighboring color charge, also feel a color field effect and may also produce a shower of partons. These left-behind partons, frequently referred to as spectator partons, may also undergo low Q^2, or “soft”, interactions with each other. This effect is known as multiple parton interactions. In addition, these partons may radiate some of their original energy, either before or after the hard interaction, in processes called initial state radiation and final state radiation. All of these parton interactions, which are not calculated from the hard scattering process, are grouped together in the term underlying event.

The cross section for these soft interactions grows quickly with increasing center-of-mass energy of the collisions, and is thus an important effect for LHC physics. This can be seen in Figure 2.2. The low-x component of the PDFs increases dramatically with increasing Q^2, and hence there is a much greater probability for low-momentum interactions to occur at the LHC than at previous collider experiments.

It should be stressed that these multiple parton interactions are a separate effect from the multiple proton interactions that may occur in each collision event at the LHC. These multiple proton collisions are referred to as pileup, and are not included in the definition of the underlying event.

2.5 Monte Carlo Generators

Monte Carlo generators are software programs capable of modeling the hard scattering for various physics processes. These generators can include phenomenologically motivated frameworks for parton showering and hadronization, which cannot be described by analytical calculations. In addition, the events produced by these programs can be passed through a detector simulation, which models the interactions that produced particles undergo when passing through the detector. Several different Monte Carlo generators are used for the analysis presented in this thesis.

NLOJET++ is a program that uses a Monte Carlo technique to calculate LO and NLO parton scattering cross sections for any given set of kinematic cuts. NLOJET++ is used, with appropriate input of PDF set, renomalization scale, factorization scale, and value of α_s, for the baseline inclusive jet cross section theory predictions, as described in Section 5.1. This program produces bare parton cross sections, and contains no methods for parton showering, hadronization, or underlying event.

The various Monte Carlo generators that do include descriptions of these non-perturbative processes all rely on similar techniques. To approximate the energy-evolution of the parton shower process, the same DGLAP equations that described the evolution of PDFs with changing energy scale can again be used. In order to avoid double-counting, the shower must be strictly ordered in some variable that prevents processes from being repeated as the parton shower evolves. The particular variable used varies between Monte Carlo generators, with the most popular choices being the p_T [44, 45] or angle [46, 47] of the outgoing parton. Each branching of the parton shower is weighted using Sudakov form factors, which give the probability for a branching between two energy scales to have *not* occurred [48]. This probabilistic technique is essential to making realistic Monte Carlo descriptions of parton showering. The showering continues until some p_T cutoff, which is a tuned parameter of the generator, is reached. The resulting partons are then grouped together into hadrons, with different Monte Carlo generators using different methods to define the grouping.

No precise model exists to reproduce the underlying event activity of a hadron collision. This underlying event activity, along with the p_T cutoff of the parton shower and many other parameters of each Monte Carlo generator, is instead adjusted to reproduce available experimental data. A specific set of chosen parameters for a generator is referred to as a "tune", with different tunes mimicking different sets of data. Data that are frequently used to model the underlying event include minimum bias charged particle multiplicity and angular distribution measurements. Measurements of energy production that is not correlated in direction with the hard collision products are also used to measure the average amount of underlying event energy.

In order to use the events produced by Monte Carlo generators to model events that one might observe with the ATLAS detector, the output of these generators is passed through a detector simulation model. ATLAS uses the GEANT4 [49] toolkit to simulate the passage of particles through the detector material. This includes models for the production of additional particles caused by inelastic scattering off of electrons and nuclei, as well as ionization and absorption by active detector elements. The description of the physics within GEANT4 has been tuned to mimic both ATLAS test beam and collision data, yet the detector simulation still represents one of the largest sources of uncertainty in the modeling of Monte Carlo events.

The two main Monte Carlo generators used in this measurement are described below.

Pythia

The Pythia Monte Carlo generator is used for the derivation of non-perturbative corrections to the parton cross section predictions of NLOJET++ and for many detector performance and jet reconstruction performance studies. ATLAS uses the Pythia 6.423 [44] version of the generator. Since Pythia implements LO perturbative QCD matrix elements, it is used with a modified LO PDF, MRST2007lomod [50].

Pythia uses a p_T-ordered parton showering, which ensures that the p_T of the produced partons decreases as the shower proceeds. After the parton showering, Pythia uses the Lund string model of hadronization to form particles [51]. In this model, the color force felt between partons is described as a string connecting them. As they separate, the potential in the string increases. When the potential is large enough, the string snaps into two, each broken end now linking a new parton to one of the original partons. If the string still contains sufficient tension, it will continue stretching and snapping, forming new partons. The process comes to a halt when the string and parton combinations no longer have enough energy to create new strings.

The baseline Pythia Monte Carlo used in this thesis has been tuned to emulate several ATLAS minimum bias and underlying event measurements. This tune, called the MC10 [52] tune, attempts to reproduce the ATLAS minimum bias charged particle multiplicity and angular distribution measurements and the ATLAS measurements of charged particle and p_T density observed collinear and transverse to high-energy activity. It also uses several CDF and D0 measurements that are sensitive to minimum bias and underlying energy distributions, though these measurements are given less importance than ATLAS measurements in the tuning procedure.

For systematic comparisons, a suite of additional tunes, called the Perugia tunes [53], are also used. These tunes utilize the minimum bias and p_T density measurements of CDF to model the underlying event, hadronic Z^0 decays from LEP to model the hadronization and final state radiation, and Drell-Yan measurements from CDF and D0 to model the initial state radiation. In particular, the Perugia 2010 tune, which produces improved jet shapes [54] and hadronic event shapes, has been used for this thesis.

Herwig++

The Herwig++ Monte Carlo generator is used to check the effect of varying parton shower, hadronization, and underlying event models. The version of Herwig++ used for this thesis is v2.2.1 [47], with the modified LO PDF MRST2007lomod [50].

Unlike Pythia, Herwig++ uses an angular-ordered parton showering. In this scheme, at each branching point the angle between the two produced partons is smaller than the angle at the previous branching point. In order to then form hadrons, Herwig++ utilizes the cluster model of hadronization [55]. After the parton branching ends, the remaining gluons are split into light quark/antiquark pairs. All quark pairs are then combined to form color-singlet clusters, and each cluster is then forced to decay into a pair of hadrons. If the cluster is too heavy to make two hadrons, the cluster is split by combining the quark constituents with a light quark/antiquark pair produced from the vacuum.

The underlying event in Herwig++ is modeled as soft gluon interactions, not color connected to the partons in the hard scatter. This description has recently been tuned by the Herwig++ authors to describe the underlying event measurements performed by ATLAS using 7 TeV collision data [56].

2.6 From Particles to Jets

Experiments are never able to observe the partons resulting from the hard scatter. Instead, they observe the group of hadrons that result at the end of the parton shower and hadronization processes. Some of these hadrons will decay before ever interacting with the detector, and some decay products, like neutrinos, will never leave a signature in ATLAS. The measurements presented in this thesis attempt to map the depositions of energy in the ATLAS calorimeter back to the original momentum of the group of hadrons. The partons produced by the hard scatter, the hadrons produced by the parton shower and hadronization, and the clusters of energy in the detector produced by the hadrons are all referred to as objects called jets [57]. In what follows, these objects will be referred to as parton-level jets, particle-level jets, and detector-level jets, respectively.

In a typical collision event, there are many sources of calorimeter energy deposition, and thus one main challenge is to accurately group detector signatures so that they correspond to the particle-level jets. Defining a grouping scheme is, in fact, not only an experimental problem, but also a complication of theoretical calculations. For example, when an outgoing parton emits some radiation, when is that radiation part of the same jet, and when does it form its own, new jet?

To solve these problems, a number of jet algorithms have been defined. A jet algorithm defines how the detector signatures, groups of hadrons, or outgoing partons from perturbative QCD calculations are grouped into jets. The kinematic properties of these jets can then be mapped back to the kinematic properties of the partons produced from the hard scattering process. This mapping process is known as a recombination scheme.

A good jet algorithm must satisfy several criteria [58]. It must not produce infinite divergences in theoretical calculations. In order to compare between theory and experiment, it must be equivalent at parton, particle, and detector levels and should be independent of the particular detector used for a measurement. Finally, to be of practical use, its execution must be computationally feasible for even systems with a large number of inputs to the jet algorithm.

The first requirement listed above can be re-worded to state that jet algorithms must be infrared and collinear safe. Infrared safety refers to the fact that perturbative calculations diverge to infinity in the limit of the emission of infinitely soft radiation. To be infrared safe, the emission of a small amount of additional soft radiation must not change the final jet clustering. Collinear safety refers to the fact that calculations also diverge if an outgoing parton splits into two partons traveling in parallel. Thus to be collinear safe, the final jet clustering must not be affected by a collinear splitting.

The Cone jet algorithm [58] is an example of a clustering algorithm that, while widely used for previous jet measurements, is both infrared and collinear *un*safe. This algorithm proceeds as follows. First a list of proto-jets is assembled. This could be a group of energy clusters in an experiment or a group of partons in a QCD calculation. In order for the algorithm to be computationally feasible, a proto-jet must have an energy above some seed threshold in order to be a part of this list. Using each of these proto-jets as a trial axis, all surrounding proto-jets within a cone of radius $R = \sqrt{\Delta y^2 + \Delta\phi^2}$[1]are clustered together. Next, the E_T-weighted centroid of the cone is calculated. This is now assigned to be the new axis, and the process is repeated until the axis is stable.

This algorithm contains several adjustable parameters. The first is the cone radius, R. The second is the number of iterations the algorithm will perform when attempting to find a stable axis. The third, called the split/merge scheme, refers to how overlapping cones are either separated into two jets, or merged into one jet. Typically, this proceeds by merging the jets if the overlapping region contains more than some fraction of the less energetic cone's energy, and splitting them if the overlapping region contains more than this fraction. This results in a new axis or axes, around which the Cone algorithm is re-run.

The Cone algorithm has been successfully used for jet measurements in a number of previous experiments, including both the CDF and D0 Run I measurements [1]. Its benefits include that it is a simple, intuitive algorithm with a well-defined shape. However, the algorithm is both infrared and collinear unsafe, as illustrated in Figure 2.4. The first two diagrams in Figure 2.4 show how a small amount of radiation, too small to form its own proto-jet, can through successive iterations of the algorithm pull the E_T-weighted centroid

---

[1] The rapidity, y, of an object has been defined in Equation 1.1. The azimuthal angle, ϕ, is defined around the axis of the incoming colliding particles.

of the cones towards each other enough that two jets merge to become one jet. The second two diagrams in Figure 2.4 show how one proto-jet that was above the seed threshold can collinearly split into two proto-jets that are below the seed threshold, causing no jet to be reconstructed.

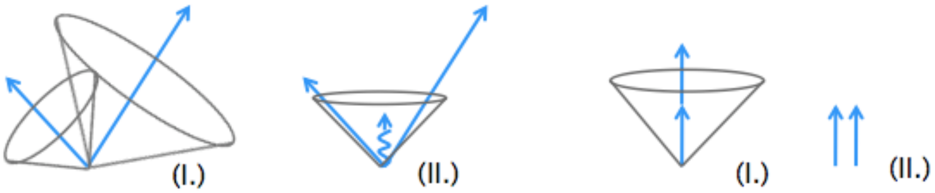

Figure 2.4: Examples of scenarios in which the addition of a small amount of radiation (left I. and II.) or a collinear splitting (right I. and II.) cause the Cone algorithm to give different jet results.

Because of this difficulty, for Tevatron Run II jet measurements, the Midpoint Cone algorithm was used [59]. This algorithm removes sensitivity to radiation as in the first two diagrams of Figure 2.4 by using the midpoints between proto-jets as proto-jets as well. Unfortunately, this only moves the sensitivity to infrared radiation to one higher order of perturbation theory, and does not solve the problem of collinear unsafety.

The anti-k$_t$ algorithm [60] is an example of a jet algorithm that solves both of these problems. This algorithm first starts with a list of proto-jets similar to the list assembled for the Cone algorithm, but with the important difference that no seed threshold is required. For all proto-jets, the quantities d_i and $d_{i,j}$ are defined, such that

$$d_i = p_{T,i}^{-2}, \tag{2.2}$$

and

$$d_{i,j} = min(p_{T,i}^{-2}, p_{T,j}^{-2})\frac{(\Delta R_{ij})^2}{R^2}, \tag{2.3}$$

where $p_{T,i}$ is the transverse momentum of the i^{th} proto-jet, $(\Delta R_{ij})^2 = \Delta y_{i,j}^2 + \Delta\phi_{i,j}^2$, and R is the size parameter of the algorithm. Next, the minimum of all d_i and $d_{i,j}$ are found. If the minimum is a $d_{i,j}$, the proto-jets i and j are merged into a new proto-jet. If the minimum is a d_i, then proto-jet i is identified as a final jet and removed from the list of proto-jets. This process is repeated until no proto-jets remain.

The net effect of the anti-k_t algorithm is to cluster nearby objects, as almost all jet algorithms do, but with the added feature that low-energy objects are first clustered with nearby high-energy objects before they are combined with each other. This results in very conical jets, but without the complications of a split/merge scheme or seed threshold. The variable R is a parameter which sets the size of the jet in $y-\phi$ space. Since it is theoretically safe and was shown in various ATLAS studies to yield good reconstruction and calibration performance, the anti-k_t algorithm is used for the measurement in this thesis.

As the jet algorithm successively combines proto-jets, the four-momenta of the original objects must be combined. There are two commonly used approaches to this recombination. The first approach treats all input objects as massless, and simply adds together all input four-momenta to form the final four-momentum of the jet. This is the scheme used by ATLAS. The second approach, called the Snowmass algorithm [58], calculates the transverse energy, E_T, and the angular coordinates of the jet as the E_T-weighted average of the input E_T and angular coordinates.

Note that in the jet algorithm definitions above, the final particles or energy depositions assigned to a jet may not correspond exactly to the particles produced from the hard-scattered parton. The underlying event may produce extra energy that overlaps with the defined jet, and the parton showering may be too wide to be totally captured within the radius R. Jets with different R parameters will feel each of these effects differently, with larger jets suffering more from underlying event energy addition and smaller jets suffering more from parton shower energy subtraction. For this reason, two different R parameters are used for the jet measurements presented here.

Chapter 3 The ATLAS Detector at the LHC

3.1 The LHC

The objective of the Large Hadron Collider (LHC) [61] is to provide high-energy, high-rate proton-proton and heavy ion collisions. It is designed to collide bunches of up to $\sim 10^{11}$ protons every 25 ns at a center-of-mass energy of 14 TeV, though it operated at a lower collision rate and lower energy throughout 2010. The accelerator facilities are based at CERN, located just outside of Geneva, Switzerland. The main accelerator is installed in a circular tunnel, 26.7 km in circumference, that originally housed the Large Electron Positron (LEP) [62] collider. The tunnel runs under areas of both Switzerland and France at a depth ranging from 45 to 100 m.

The LHC ring consists of eight arcs and eight straight sections. Four interaction points are arranged along four of these straight sections, each accommodating a separate detector system. Point 1, which is closest to the main CERN site, houses the ATLAS experiment. The other general purpose detector, CMS, is located at Point 5. Point 2 and Point 8 house ALICE, which is designed to investigate heavy ion collisions, and LHCb, which is designed to investigate rare decays of b-mesons. These points also house the two injection systems for the proton beams. The layout of these four experiments along the LHC ring is shown in Figure 3.1.

Proton beams are formed before insertion into the main LHC ring using a series of smaller accelerators, as also shown in Figure 3.1. In order to attain the desired high proton beam energy, the entire accelerator chain uses radio-frequency (RF) acceleration. In RF acceleration, particles travel through a series of time-varying electrical fields. Particles that enter with the correct phase are accelerated along their direction of motion, while those with the incorrect phase are decelerated. The result of a sequence of RF accelerations is several bunches of protons, each traveling with the desired energy. It is important to note that the phrase “LHC beams” in fact refers to many bunches of protons separated by some uniform distance.

The injection series consists of the LINAC 2 linear accelerator, the Proton Synchotron

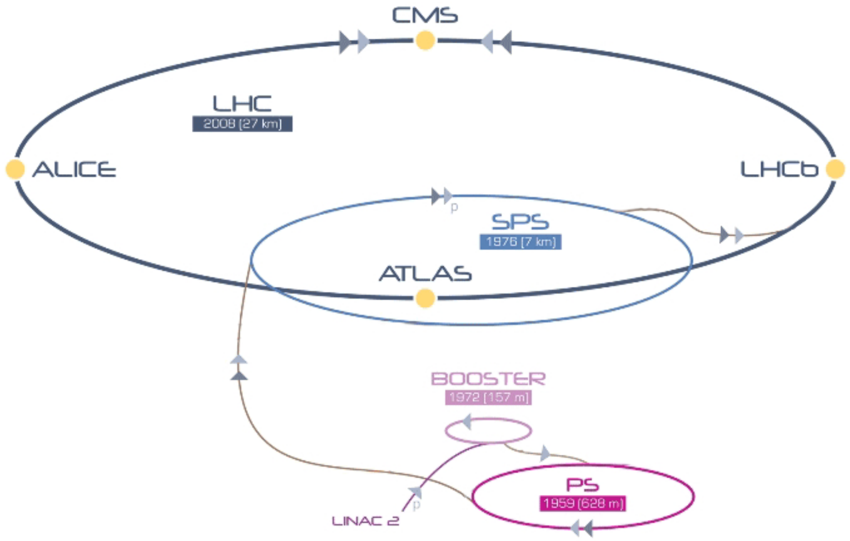

Figure 3.1: Schematic of the LHC complex, showing the injection system, along with each component's date of construction, and the placement of the four main experiments.

Booster (PSB), the Proton Synchotron (PS), and the Super Proton Synchotron (SPS). The chain begins as protons are separated from a duoplasmatron source and accelerated by LINAC 2 up to energies of 50 MeV. These are then injected into the PSB and further accelerated to 1.4 GeV. At design luminosity, six bunches of protons from the PSB are each split into three bunches upon entry to the PS, where they are accelerated to 25 GeV and split again into four. The bunch structure, known as a bunch train, now contains 72 bunches of protons. The SPS accumulates up to four fills of 72 bunches from the PS and accelerates them to 450 GeV, with a bunch spacing of $\sim$ 25 ns. Finally, the LHC receives 12 fills of SPS bunches, resulting in a total of 2,808 bunches with 25 ns spacing. At design strength, the LHC accelerates these bunches to an energy of 7 TeV, allowing collisions at a center-of-mass energy of 14 TeV. Typically, the LHC maintains these colliding bunches for several hours before dumping the beams and readying for another injection.

The rate of events produced by colliding beams depends on the luminosity of the collisions, which is a measure of the number of events per second per unit cross section, typically measured in units $\mathrm{cm}^2\mathrm{s}^{-1}$. The number of events of a particular process, then, is given by the product of the integrated luminosity, $\int dtL$, and the cross section of the process, σ_{event}. The integrated luminosities used in this thesis are typically quoted in units of inverse picobarns, $\mathrm{pb}^{-1} = 10^{36}$ cm^2. The most interesting physics processes probed by the LHC have tiny cross sections, and hence a very high luminosity is required to make measurements of these processes.

The luminosity of the collisions is given by the equation

$$L = \frac{N_b^2 n_b f_{rev} \gamma_r}{4\pi\sigma_x\sigma_y} \times F \tag{3.1}$$

where N_b is the number of protons per bunch, n_b is the number of bunches per beam, f_{rev} is the revolution frequency, γ_r is the relativistic gamma factor, σ_x and σ_y are the width and height of the proton beams, and F is the geometric luminosity reduction factor due to the crossing angle at the interaction point. The relativistic gamma factor and the geometric acceptance can by easily calculated from the beam parameters. The number of protons per bunch, the number of bunches per beam, and the revolution frequency are all set by the beam operators. The widths of the proton beams, though also controlled by the beam operators, can be measured more precisely in a process known as a Van der Meer scan [63]. In a Van der Meer scan, the two beams are swept across one another in well-defined steps of separation. The collision rate is measured as a function of this separation, and the width of a gaussian fit to the distribution yields the width of the beams in the direction of the separation. Five sets of Van der Meer scans were performed in 2010 and used to derive the total luminosity measurement used in this analysis [64].

A large magnetic field is needed to maintain highly-energetic particles in their circular orbits. As charged particles are deflected by this field, they emit synchotron radiation. The emitted power due to transverse acceleration over one orbit varies with the particle energy (E), particle mass (m), and radius of curvature (ρ) according to: $P \propto \frac{E^4}{m^4\rho^2}$. Because electrons are so much lighter than protons, they lose many orders of magnitude more energy per revolution than protons. In fact, if electrons were used at 7 TeV in the LHC, they would emit their entire energies before completing a single revolution. Antiprotons would not suffer from this high level of synchotron emission, but the high beam intensities required by the LHC make antiprotons impractical to use. Thus the LHC collides two counter-rotating beams of protons. The use of protons for both beams adds the complication that opposite magnetic fields are needed to keep the two beams in their circular paths.

Due to the space constraints in the LHC tunnel, a twin-aperture dipole magnet design is used to provide these two magnetic fields. This design consists of four sets of current-carrying coils running parallel to the beam direction. These coils form two beam channels separated by 194 mm, as shown in Figure 3.2(a). The currents through the coils produce magnetic fields perpendicular to the direction of motion of the protons, as shown in Figure 3.2(b), that deflect the protons into their circular orbits. Around the LHC ring there are 1,232 of these dipoles.

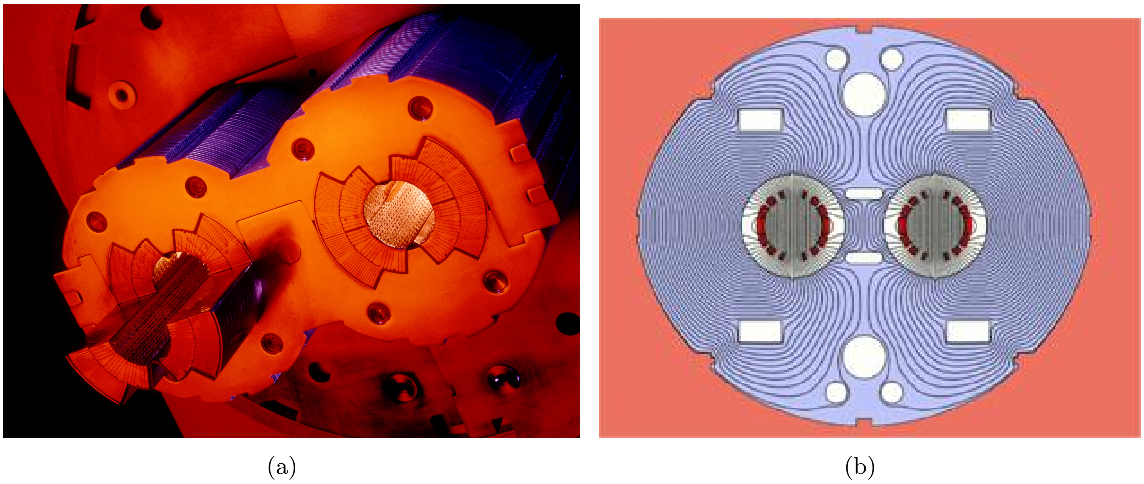
(a)

(b)

Figure 3.2: Photograph of a cross section of the an LHC dipole magnet (a) and an illustration of the magnetic field produced (b).

At a peak beam energy of 7 TeV, the dipoles need to produce an 8.33 T magnetic field, requiring a current of $\sim$ 12 kA. Superconducting NbTi coils are used to attain this high current. If the current density, magnetic field, or temperature of the coils is too high, they will lose their superconducting properties. A failure of this type is known as a magnet quench. In order to deliver the current densities and magnetic field required for 7 TeV proton beams, the magnets are kept at 1.9 K by circulating superfluid helium.

In addition to the deflecting dipole magnets, a system of quadrapole magnets is used to keep the beams focused as they circulate. There are ten of these focusing magnets in every straight section of the LHC. These are accompanied by approximately 3,500 orbit-corrector magnets distributed around the ring. This system of focusing and correcting magnets serves to reduce unwanted beam-beam interactions that may result as the beam sizes grow throughout the LHC orbit. Around each of the interaction points, additional systems of triplet magnets are used to further focus the beams before collision.

At nominal operating energy and intensity, approximately 7.6 MJ of energy is stored in each dipole magnet, and approximately 300 MJ of energy is stored in each beam. It is essential that this energy be controlled throughout the LHC cycle. In particular, if energy is added to the dipole magnet system, the system can heat up enough so that a quench is caused and the coils are no longer superconducting. Without protections, the temperature in a magnet after a quench would reach 1000 K in less than one second, destroying the magnet. Since quenches are an unavoidable part of accelerator operation, a sophisticated set of safeguards is installed that quickly dissipates the current in a quenched magnet. The stored beam must also be safely dumped at the end of each LHC fill or in the case of a magnet failure or other beam abort signal. To accomplish this, Point 6 is equipped with beam dump systems that deflect and defocus the beams using fast-pulsed "kicker" magnets. The beams are then deposited into dense blocks of graphite and concrete that can safely absorb the beam energy.

The very first proton-proton collisions produced by the LHC occurred on November 23, 2009 with a center-of-mass energy of 900 GeV. Very quickly after that, on December 8, 2009, the LHC was the highest energy accelerator in the world, colliding protons at an energy of 2.36 TeV. The incredibly rapid evolution of beam energy and intensity throughout the following year is a testament to the LHC team's rapid understanding of accelerator performance. This development took place in several phases throughout 2010. In February 2010, the LHC was commissioned once more with 450 GeV beams, and a series of tests were performed to ensure that the magnet systems could operate safely at the currents necessary to control 3.5 TeV beams. This was followed by the very first collisions at 7 TeV center-of-mass energy on March 30. The beam widths were squeezed to increase the beam intensity during three weeks in April, and the beam intensity was further increased by increasing the number of protons in each bunch during three weeks in June. Finally, the number of bunches in each beam was increased during a three week period in September. Table 3.1 summarize the basic beam parameters expected for design energy and luminosity and the progression of the beam parameters achieved during 2010. In particular, as the intensity, and hence delivered instantaneous luminosity, of the bunches increased, the mean number of interactions per crossing, also known as the rate of pileup, increased. This pileup rate can affect jet energy measurements, and is an important concern for the inclusive jet cross section measurement.

Between these commissioning periods, the LHC provided stable collisions to ATLAS, delivering a total of ~ 48 pb^{-1} of integrated luminosity. The total integrated luminosities provided by the LHC and recorded by ATLAS in the period from March 30, 2010 until November 3, 2010 are shown in Figure 3.3. These events form the dataset analyzed in this thesis.

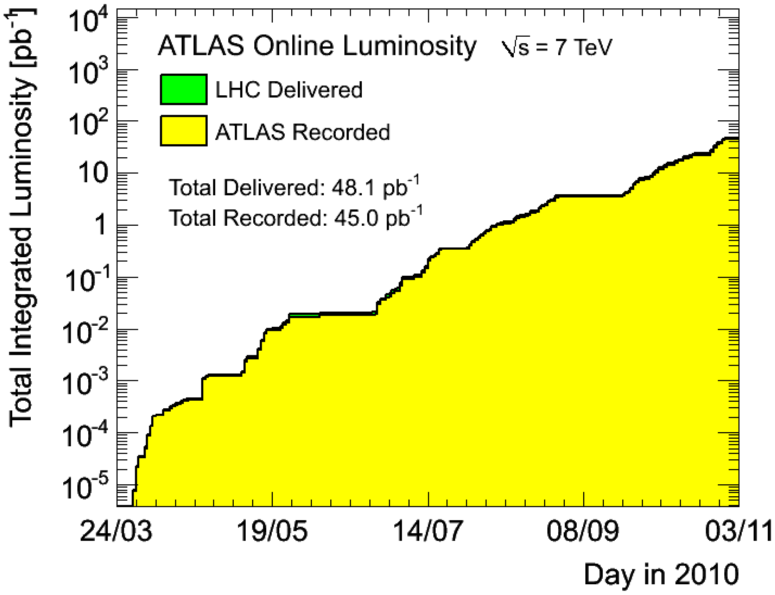

Figure 3.3: Total luminosity delivered by the LHC and recorded by ATLAS during the 2010 $\sqrt{s} = 7$ TeV proton-proton run, which took place from March 24 (24/03) to November 3 (03/11).

Parameter	2010 Runs	Design Performance
Center-of-mass energy [TeV]	7	14
Instantaneous luminosity [cm^{-2}s^{-1}]	$\sim 10^{27} - 10^{32}$	10^{34}
Bunches per beam	1-295	2808
Protons per bunch	$10^9 - 2 \cdot 10^{11}$	1.5×10^{11}
Mean interactions per crossing	0.01-3.8	23

Table 3.1: Summary of beam conditions during the 2010 7 TeV runs and those foreseen at design energy and luminosity.

3.2 ATLAS

The performance requirements of the ATLAS detector [65] were defined to encompass a range of possible Standard Model and new physics signatures that could be produced at the TeV scale. ATLAS must provide accurate charged particle identification and reconstruction, as well as measurements of jet energy and missing transverse energy. The LHC design places additional demands on the detector operation. The detector readout must be fast enough to handle the 40 MHz interaction rate, and all detector elements must be able to function in the high-radiation environment close to the LHC collisions. At even 7 TeV center-of-mass energy, the LHC interactions result in high particle multiplicity, requiring fine detector granularity, and particle production at forward rapidity, requiring large detector angular coverage.

To achieve these performance goals, a design consisting of multiple detector sub-systems with cylindrical symmetry around the incoming beams is used [66], as shown in Figure 3.4. Closest to the interaction point, the pixel detector, the semiconducting tracker (SCT), and the transition radiation tracker (TRT), collectively known as the inner detector, provide charged particle reconstruction. The entire inner detector is immersed in a solenoidal magnetic field to allow precision momentum measurements of these charged particles. Outside the solenoid, the electromagnetic and hadronic calorimeters perform electron, photon, tau, and jet energy measurements. Furthest from the interaction point, an array of muon drift chambers distributed within a toroid magnet system perform muon identification and momentum measurements.

The ATLAS detector coordinate system is used to describe the position of these subsystems within the full detector as well as the position of particles as they traverse the detector. It is a right-handed coordinate system, with z pointing along the beam direction, positive x pointing toward the center of the LHC ring, and positive y pointing up. The $x - y$ plane is referred to as the transverse plane, and the z direction as the longitudinal direction. Cylindrical coordinates are also frequently used, with z again pointing along the beam, $r = \sqrt{x^2 + y^2}$, and $\phi = tan^{-1}(\frac{y}{x})$. The angle of an object with respect to the beam axis is denoted θ, but in practice the pseudorapidity variable, $\eta = -ln[tan(\frac{\theta}{2})]$, is more commonly used. Regions of low η are referred to as "central," and regions of high η are referred to as "forward". In terms of momentum, pseudorapidity can be defined as

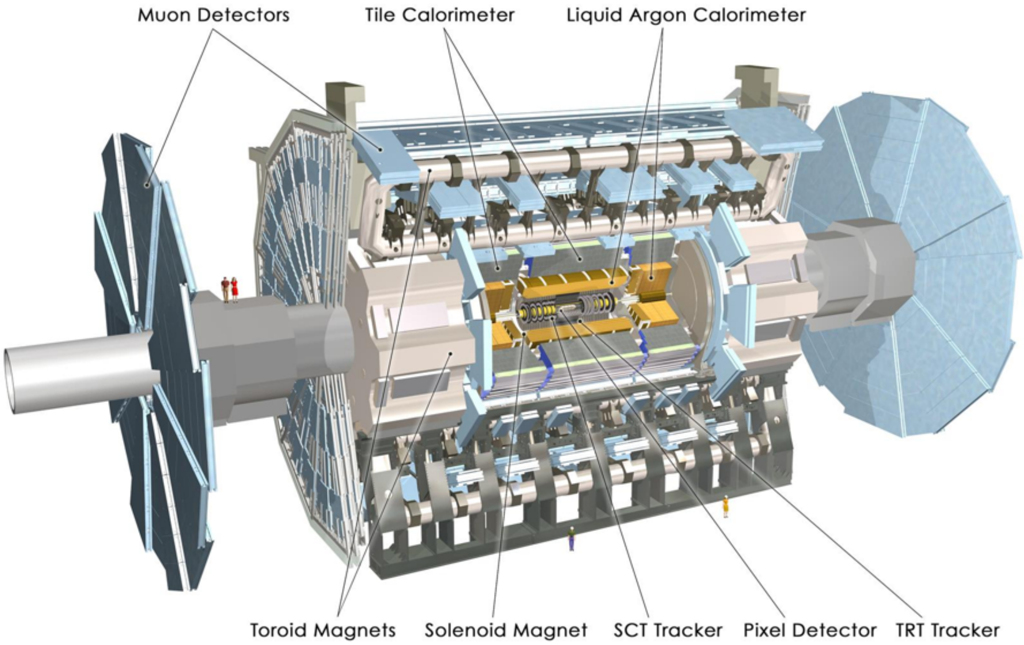

Figure 3.4: Overview of ATLAS sub-detector systems [66]. The total length of the detector is 46 m, and the total height is 25 m.

$\eta = \frac{1}{2} ln(\frac{|p|+p_z}{|p|-p_z})$, where p_z is the momentum along the beam axis. For particles with zero mass, an approximation that particles with very high momentum approach, pseudorapidity is numerically equal to rapidity, as was defined in Section 1.

3.2.1 Inner Detector

The goal of the pixel detector, SCT, and TRT is to provide charged particle trajectory reconstruction and momentum measurements within a coverage of $|\eta| < 2.5$. All three subdetectors are composed of sensors that register signals, referred to as “hits,” in response to the passage of charged particles. The paths of these charged particles are bent by a 2 T magnetic field, provided by a solenoid magnet that surrounds the entire inner detector. The positions of the registered hits are combined to form tracks, with the radius of curvature of the tracks providing a measurement of the particle’s transverse momentum.

At design luminosity, the LHC will deliver approximately 1000 particles in the region covered by the inner detector every 25 ns. The inner detector must have sufficient granularity to differentiate these separate tracks, as well as to associate these tracks to common interaction vertices. Due to damage induced by the high level of radiation close to the interacting beams, all three sub-detectors are planned to be replaced after five years of operation at design luminosity. The layer of pixels closest to the beam, which suffers the most radiation damage, will be replaced after only three years of design luminosity.

The pixel detector, SCT, and TRT sensors are arranged on concentric cylinders around the beam axis, known as barrel layers, and on disks perpindicular to the beam at either end of the barrel, known as end-caps. The layout of the inner detector is shown in Figure 3.5. With increasing distance from the interaction point, the granularity, and hence position resolution, of each of the sub-detectors decreases.

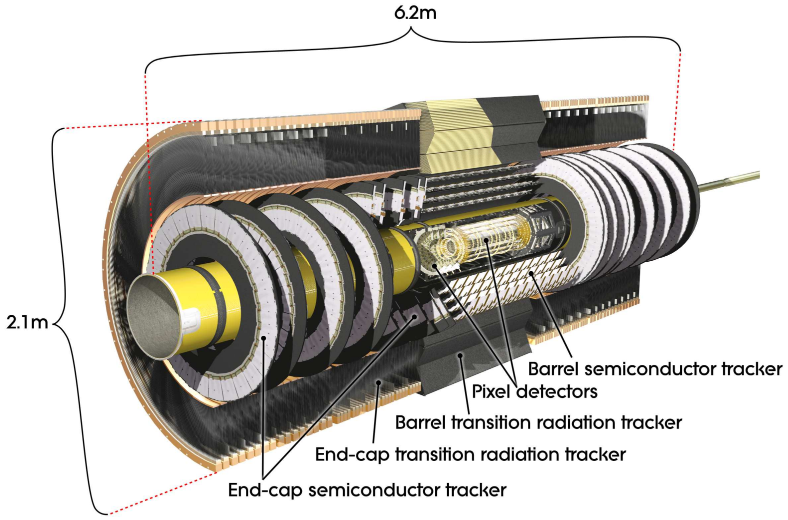

Figure 3.5: Layout of the ATLAS inner detector [66].

Closest to the beam is the pixel detector, whose innermost layer is ∼5 cm from the proton beams, followed by the SCT, whose innermost layer is ∼25 cm from the proton beams. To provide precision charge and position measurements in this high track density environment, both the pixel detector and the SCT utilize semiconducting silicon sensors. As a charged particle traverses the semiconductor it ionizes atoms, producing free electrons. The missing regions of negative charge within the lattice of silicon atoms that result from this are known as "holes." An applied voltage across the two ends of the sensor produces an electric field that directs the electrons and holes to the electrodes on the sensor surface. The initial applied voltage for both pixel and SCT sensors is 150 V, but this must increase with increasing radiation damage to the sensors. The flow of charge produces an analog pulse in the electrodes that can be recorded and processed by a further set of readout electronics.

To reduce inherent noise within the sensors, small amounts of positive and negative charge are induced in the silicon lattice of the pixel and SCT sensors in a process known as doping. Extra electrons are induced on one side of the silicon, referred to as n-type doping, and extra holes are induced on the other side, referred to as p-type doping. At the junction between the p-type and n-type doped silicon, any free negative charge flows to the p-doped side, and any positive charge flows to n-doped side. This results in the build up of a potential across the junction, which continues until the potential is too large to allow any charges to cross from one side to the other. Thus an extended region forms that is depleted of all free charge carriers that could produce background signals in the readout electronics.

The pixel detector is composed of 1,744 silicon sensors, with dimensions 19 mm×63 mm×250 μm. Every sensor has 46,080 readout channels, each channel connected to a pixel size of either 50×400 μm^2 or 50×600 μm^2. This yields a total of approximately 80 million readout channels, an order of magnitude more readout channels than the rest of ATLAS combined. These sensors are arranged on three barrel layers and three end-cap layers, producing typically three pixel position measurements per charged particle track. In practice, a charged particle traversing the pixel sensor will produce charge not just in one pixel, but in a group of neighboring pixels, forming what is known as a cluster. Information from the varying signal heights within this cluster yield an intrinsic position accuracy, assuming perfect knowledge of the pixel sensor positions within the ATLAS geometry, of 10 μm in r-ϕ and 115 μm along z in the barrel or along r in the end-caps. The pixel detector, including both barrel and end-caps, extends to a total length of $z \approx \pm 650$ mm and radius of $r \approx 150$ mm, providing good reconstruction efficiency for tracks up to $|\eta| < 2.5$.

The SCT consists of four barrel layers and nine end-cap layers surrounding the pixel detector, resulting in at least four hits along every charged particle track. The SCT barrel reaches to $z \approx \pm 750$ mm and $r \approx 515$ mm, while the end-cap covers out to $z \approx \pm 2720$ mm and $r = 560$ mm. There are 15,912 SCT sensors, each 12.8 cm long and approximately 285 μm thick. The sensors are read out as long strips, parallel to the beam axis in the barrel and along r in the end-caps, allowing for precision measurements of the ϕ coordinate of each hit. To improve the position resolution along the long edge of the strip, the sensors are stacked back-to-back, with the bottom sensor rotated by 40 mrad with respect to the top sensor. The intersection of two crossed strips thus provides an estimate of the position of the particle in z for the barrel and r in the end-caps. This yields an intrinsic accuracy for one stacked pair of SCT sensors of 17 μm in r-ϕ and 580 μm along the long side of the strips. In total, the SCT has approximately 6.3 million silicon strips.

A special Beam Conditions Monitor (BCM) is designed to prevent dangerous beam conditions from damaging the ATLAS detector, in particular the inner detector elements closest to the beam. Such conditions could result, for example, from a beam scraping the side of the beampipe or hitting the collimators in front of the detector, resulting in a spray of particles with dangerously high energy traveling toward the detector. The task of the BCM is to distinguish these events from events where the high particle flux results from healthy beam collisions and to trigger a beam abort in case of dangerous conditions. This is attained by using 8 radiation-hard diamond sensors arranged around the beampipe at $z = \pm 184$ cm. The time difference between signals in the detectors on either side of ATLAS distinguish stray particles from collision particles.

Even without damage due to beam accidents, the large amounts of radiation produced close to the LHC beam can damage the silicon lattice of these sensors. This effectively changes some regions of p-type doped silicon to n-type, and vice versa, leading to increased electronics noise due to the background current in the sensor. To minimize this noise, as well as to prevent the sensor electronics from overheating, both the pixel detector and the SCT are kept at a temperature of approximately -10° C by an evaporative cooling system using circulating C_3F_8.

The TRT, which is the furthest of the tracking detectors from the interaction point, is designed to give a large number of coarse position measurements. The TRT sensors are thin drift tubes consisting of cathode metal straws filled with an ionizing gas mixture of xenon, oxygen, and CO_2, with an anode wire running down the center of the straw. The passage of a charged particle through the gas produces positive ions and free electrons, which travel to the cathode and anode, respectively, under the influence of an applied voltage of 1600 V. Comparing the time that the signals are received at the cathode and the anode gives a drift time measurement that can be used to calculate the impact parameter of the particle. This method gives no information on the position along the length of the straw.

The TRT straws are arranged in one barrel cylinder, extending to $z \approx \pm 710$ mm and $r \approx 1060$ mm, and two end-cap cylinders, reaching $z \approx \pm 2710$ mm and $r \approx 1000$ mm. To give the best resolution of particle trajectories as they bend in the solenoidal field, the straws lie along the beam direction in the barrel and radially in the end-caps. The straw diameter of 4 mm causes a maximum drift time of approximately 48 ns and an intrinsic accuracy of 130 μm along the radius of the straw. There are approximately 351,000 readout channels in the TRT, distributed such that a particle with $|\eta| < 2.0$ will traverse at least 22 straws.

In addition to directly detecting charged particles produced by the collision, the TRT also measures the transition radiation induced by the passage of these particles through polypropylene sheets placed between the drift tube straws. Transition radiation refers to the photons emitted by charged particles as they pass from one material into another with a different dielectric constant. These photons yield a much larger signal amplitude than the charged particles, so separate thresholds in the electronics can be used to distinguish the two.

Since any xenon that may leak out of the straws would absorb the transition radiation photons before they reached the detectors, the environment of the TRT is filled with circulating CO_2. This circulating gas also helps to cool any heat dissipated by the detector electronics. Unlike the silicon sensors of the pixel detector and SCT, the TRT straws operate at room temperature.

The most important task of the inner detector for the inclusive jet cross section measurement is to provide accurate collision vertex identification, exploiting the excellent position resolution and tracking efficiency of the inner detector. Vertices are reconstructed by matching inner detector tracks with $p_T > 150$ MeV back to a common origin [67]. The presence of an interaction vertex is used to distinguish collision events from cosmic or beam-halo background events. In 2010 data, the efficiency to reconstruct a vertex was almost 100% for vertices with at least two tracks, with a fake rate around 1%. The presence of more than one interaction vertex is a measure of the number of pileup interactions in a given event, which has important effects on the jet energy calibration. Figure 3.6 shows the x and z position resolution of reconstructed vertices measured using 2010 collision data. In the later data-taking periods, when pileup was a concern, the typical spread of the z position of vertices was ~ 250 mm. The resolution is better than 40 μm for vertices with high sum track p_T^2, and not more than 2 mm for vertices with low sum track p_T^2. Thus, even in the presence of pileup interaction, the multiple vertices can be resolved. These issues are further as discussed in Section 4.1.2.

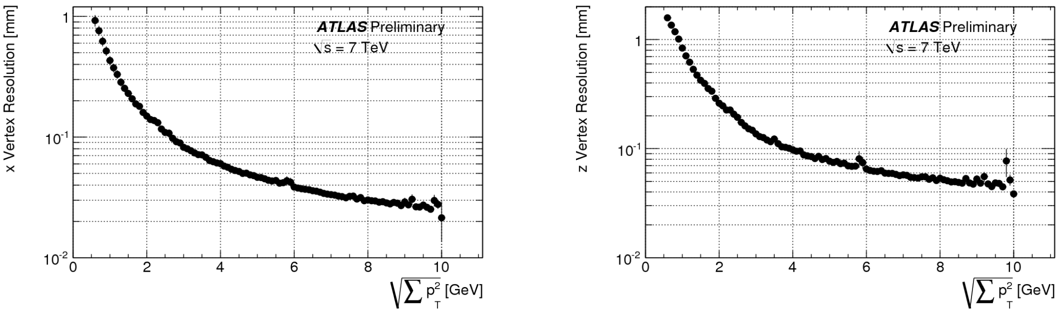

(a)

(b)

Figure 3.6: Distribution of the measured x position resolution (a) and the measured z position resolution as a function of the square root of the sum of the track p_T^2 associated to a vertex (b), as measured in early 2010 data [67].

3.2.2 Calorimeters

The purpose of the ATLAS calorimeter system is to measure the energy of electrons, photons, taus and hadrons within the pseudorapidity region of $|\eta| < 4.9$. The calorimeter system consists of electromagnetic (EM) calorimeter and hadronic calorimeter components. The EM calorimeters provide fine granularity measurements of electrons and photons. The hadronic calorimeters have a coarser granularity but contain more material to capture the full energy of high-momentum jets. All the ATLAS calorimeters are segmented transverse to the particle direction, to give position information, and along the particle direction, to chart the development of the induced particle shower. The calorimeter system also delivers fast, rough position and energy measurements to serve as trigger signals for photons, electrons, taus, jets, and missing transverse energy. The jet trigger, reconstruction, and energy calibration, based on cells of energy deposited in the calorimeters, form the backbone of the inclusive jet cross section analysis presented here. The layout of the various calorimeter components is shown in Figure 3.7.

The EM and hadronic calorimeters are sampling calorimeters, meaning they measure the energy deposited by a particle as it traverses several layers of absorber and active material. The absorber material consists of heavy atoms that cause energetic particles to interact and lose energy, and the active material produces signals in response to the deposited energy. This is in contrast to non-sampling calorimeters, such as exotic crystal detectors, which attempt to both induce energy loss and produce corresponding signals.

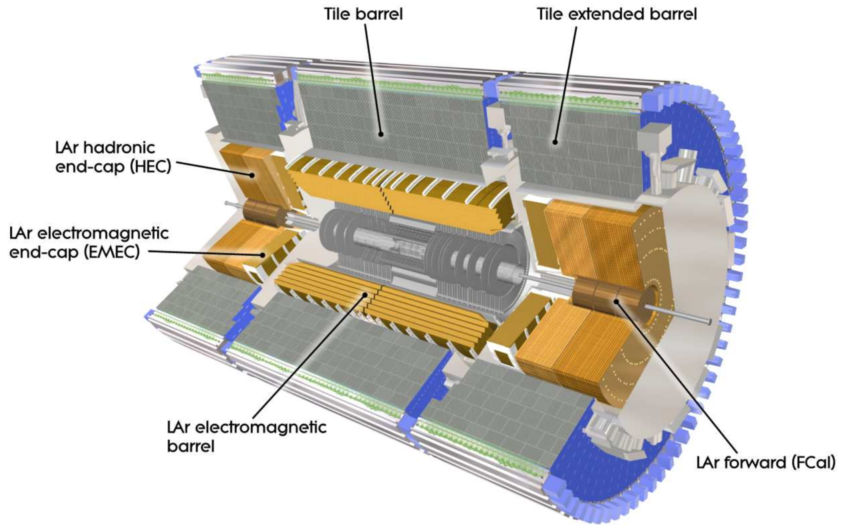

Figure 3.7: Layout of the ATLAS electromagnetic and hadronic calorimeter systems [66]. The total length is ~ 12 m, extending to a maximum radius of 4.25 m.

The EM calorimeter uses lead as the absorber and liquid argon (LAr) as the active material. A photon traversing the absorber will interact with the heavy nucleus via Compton scattering or the photo-electric effect, producing low-energy electrons, or pair production, producing electron/positron pairs. An electron or positron, in turn, can produce bremsstrahlung photons as it is deflected by the nuclei or produce more charged particles via ionization. Thus each incident photon, electron, or positron produces a shower of photons, electrons, and positrons that lose their energy through successive interactions in the absorber. The produced particles ionize the liquid argon, and the charge is collected by electrodes located in the liquid argon gap. These electrodes consist of three layers of copper sheets, the outer two kept at a high-voltage potential and the inner one used to readout the signal.

Liquid argon has been chosen for its radiation-hardness and its intrinsicly linear production of ionization charge as a function of incident charge. In order to maintain its liquid state, the liquid argon must be kept cold. In addition, variations in the temperature of the liquid argon affect the produced signal by altering its density and the drift velocity of charged particles through the material, resulting in a total signal decay of -2% for every 1 K increase in temperature [68]. To keep the liquid argon at a constant temperature of ~ 88 K, the EM and other liquid argon-based calorimeters are housed in three cryostats and ∼500 temperature probes are distributed throughout the system.

The EM calorimeter is divided into a barrel part, extending to $|\eta| < 1.475$, and two end-caps, extending to $1.375 < |\eta| < 3.2$, each housed in separate cryostats. Each end-cap has one outer wheel covering the region $1.375 < |\eta| < 2.5$ and one inner wheel covering the region $2.5 < |\eta| < 3.2$. In order to estimate the energy lost by electrons and photons upstream in the inner detector, the solenoid magnet, and the cryostat walls, a thin presampler layer extends out to $|\eta| = 1.8$. The presampler is made of interleaved cathode and anode electrodes attached between glass-fibre composite plates. Liquid argon fills the gaps, which are of size 1.1 cm in the barrel region and 0.5 cm in the end-cap region. To estimate the energy lost in the outer wall of the barrel cryostat, cryostat scintillators are attached to the outside of the end-cap cryostat, facing the barrel cryostats, covering the region $1.2 < |\eta| < 1.6$.

Also attached to the to the outer wall of the end-cap cryostat are the system of Minimum Bias Trigger Scintillators (MBTS). These scintillators are used to form trigger signals corresponding to minimum bias events during low-luminosity data taking, and were used to collect the initial and low-p_T data used for this inclusive jet cross section analysis. They consist of two sets of 16 scintillating counters, covering the region $2.09 < |\eta| < 3.84$.

To provide full coverage in ϕ without any cracks, an accordion-shaped absorber and electrode geometry is used. The accordion waves run radially in the barrel, the folding angle increasing with r in order to keep the width of the liquid argon-filled gap constant. The gap on each side of electrode is 2.1 mm, yielding a maximum drift time of 450 ns for an operating voltage of 2000 V. In the end-cap, the waves run along z, the gap increasing with r. Since the drift gap varies with η, the applied voltage varies in steps to approximate a constant drift time.

The position resolution of the EM calorimeter is driven by the readout geometry, consisting of rectangular cells in $\eta \times \phi$ space. There are three layers of these cells, segmented along the particle's direction of motion. A schematic of a ϕ slice of the barrel EM calorimeter, with the cell dimensions of each of the three layers highlighted, is shown in Figure 3.8. The ϕ segmentation comes from grouping the accordion-shaped electrodes together into a common readout channel. The η and r segmentation is achieved by etching on the electrodes. In the EM end-cap, the cells of all three layers are 0.025×0.025. Towers of readout cells with coarser granularity, 0.1×0.1 in the barrel, sum the energy in all three layers of cells and feed information to the trigger system.

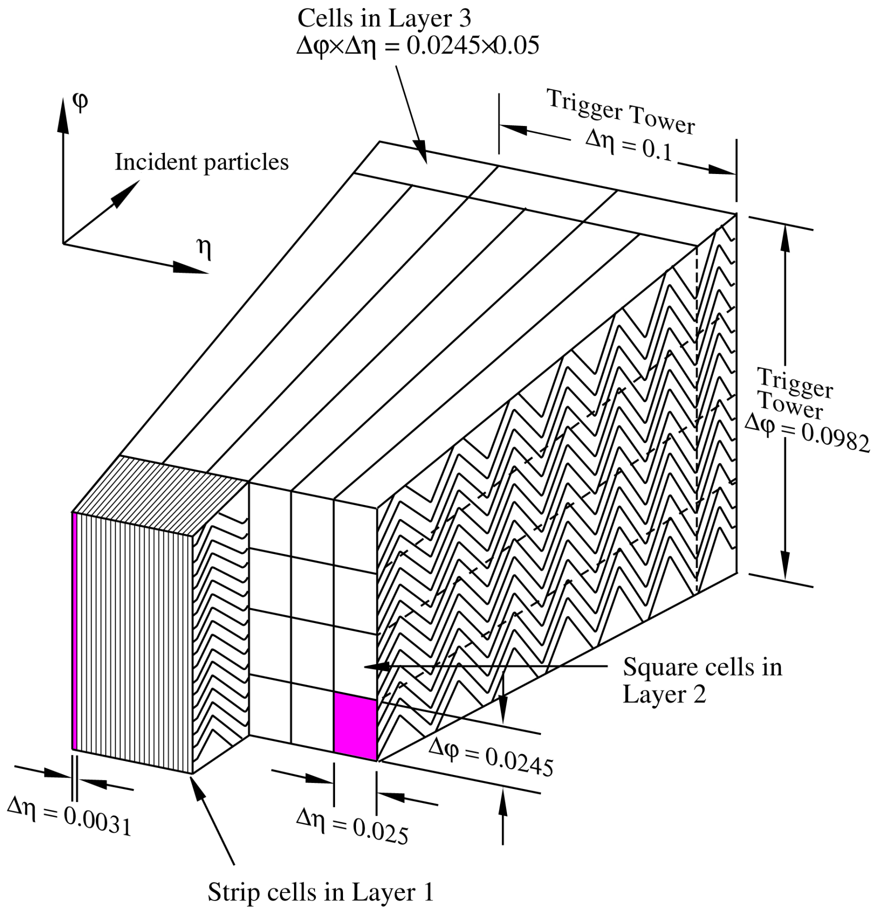

Figure 3.8: Diagram of a slice of the barrel EM calorimeter [68]. The first layer, closest to the interaction point, consists of the presampler strips. The second layer is readout as square cells of size $\Delta\eta = 0.025$ and $\Delta\phi = 0.025$. The third layer is readout as cells of size $\Delta\eta = 0.05$ and $\Delta\phi = 0.0245$. The inputs to the trigger algorithms are towers consisting of the cells in all three layers, with size$\Delta\eta = 0.1$ and $\Delta\phi \approx 0.1$.

Outside of the EM calorimeter lies the system of hadronic calorimeters. The barrel portion, known as the tile calorimeter, uses iron absorber slabs interspersed with scintillating tiles. The hadronic end-cap and the forward calorimeter, which need to absorb the more energetic particles that are produced at large $|\eta|$, are made of copper and tungsten absorbers, respectively, with liquid argon as the active material.

The tile calorimeter is composed of 3 mm thick scintillating tiles, arranged to lie parallel to the incoming particle direction, interleaved with 14 mm thick iron plates, as shown in Figure 3.9. It is divided into the barrel calorimeter, covering $|\eta| < 1.0$, and two extended barrel calorimeters, covering $0.8 < |\eta| < 1.7$. Each tile is read out by two wavelength-shifting fibers, which convert the scintillator signal to visible light. The readout fibers of several tiles are grouped to a single photomultiplier tube, forming cells in $\eta \times \phi$ space. As in the EM calorimeter, these cells are segmented into three layers, the first two of size $\Delta\eta = 0.1$ and $\Delta\phi = 0.1$ and the last of size $\Delta\eta = 0.2$ and $\Delta\phi = 0.1$. Towers to provide information to the trigger system are formed from 0.1×0.1 groupings of all three layers, with the energy from cells that are larger than this split evenly between two towers.

To allow for inner detector cabling and EM calorimeter power supplies and cabling, there are gaps between the tile calorimeter and the extended tile calorimeters. Gap scintillators are attached to the extended tile calorimeter boundary in order to provide an estimate of energy lost in this material for $1.0 < |\eta| < 1.2$.

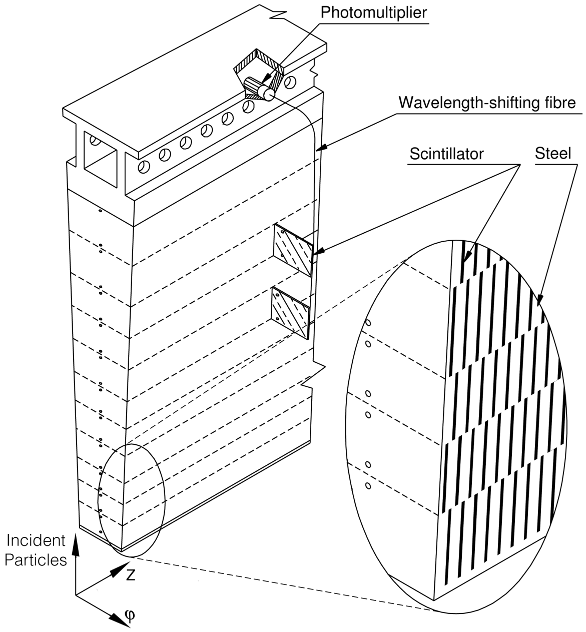

Figure 3.9: Diagram of a slice of the hadronic tile calorimeter [66]. Incoming particles are incident on the bottom of the slice. The scintillating tiles are arranged parallel to the incoming particle, and are read out via wavelength-shifting fibres connected to photomultiplier tubes.

The hadronic end-cap comprises two cylindrical wheels located directly behind the EM end-caps. It covers the region $1.5 < |\eta| < 3.2$, overlapping slightly with both the forward calorimeter and tile calorimeter. Planes of copper plates serve as the absorber material. The gaps between these plates are filled with liquid argon and three separate electrodes, forming four separate 1.8 mm drift zones. For a nominal voltage of 1800 V, the maximum drift time is approximately 430 ns. Readout cells are etched into the electrodes in each gap, forming 0.1×0.1 cells in the region $|\eta| < 2.5$ and 0.2×0.2 cells elsewhere.

The forward calorimeter extends to cover the region $3.1 < |\eta| < 4.9$. Since it is the only calorimeter that covers this very forward region, it must provide both electromagnetic and hadronic measurements. In addition, the high particle fluxes in this region necessitate a finely granulated design. The detector must also be very dense due to the constrained space in the forward region, which must provide room for inner detector cabling and other services. The EM layer is composed of 18 vertical copper plates separated by liquid argon gaps. These plates are punctuated with 12,260 holes containing co-axial copper rods and tubes aligned along z that act as electrodes. The two hadronic layers each consist of two copper end-plates, again bridged by copper tubes and filled with liquid argon, but here tungsten, which is dense enough to contain the full shower of very energetic particles, is used for the electrode rods. These rods are read out in groups of four, six, or nine for the EM, first hadronic, or second hadronic component, respectively, yielding readout cells in the $x - y$ plane corresponding to cells of roughly $|\eta| \times |\phi| = 0.2 \times 0.2$.

The combination of EM barrel, EM end-cap, tile barrel, tile extended barrel, hadronic end-cap, and forward calorimeters, each with several sampling layers, forms a complex map of overlapping detectors. To quantify the amount of material needed to capture a particle's energy, the unit of an interaction length, which is the distance over which a high energy charged particle loses $1 - \frac{1}{e} \approx 63\%$ of its energy, is commonly used. Figure 3.10 shows the number of interaction lengths of each detector as a function of pseudorapidity, summarizing the η coverage of the calorimeter system.

To minimize noise and increase speed, the first level of analog readout for the calorimeters is located on the detector, just outside of the cryostats for the liquid argon calorimeters and in drawers on the external support structures for the tile calorimeters. These front-end electronics amplify and shape the signals. A sample analog pulse measured in the the liquid argon calorimeter and an ideal reference pulse for the tile calorimeter are shown in Figure 3.11. A separate analog readout goes directly to the Level-1 calorimeter hardware, located off the detector in the ATLAS cavern, as described in Section 3.2.5.

To translate these analog signals to digital signals that can be transmitted long distances to the next stage of the readout system, the pulse shape is measured over several 25 ns time intervals, known as samples. The challenge of calorimeter calibration is to map these measured signals to the energy deposited in the active detector medium, known as the visible

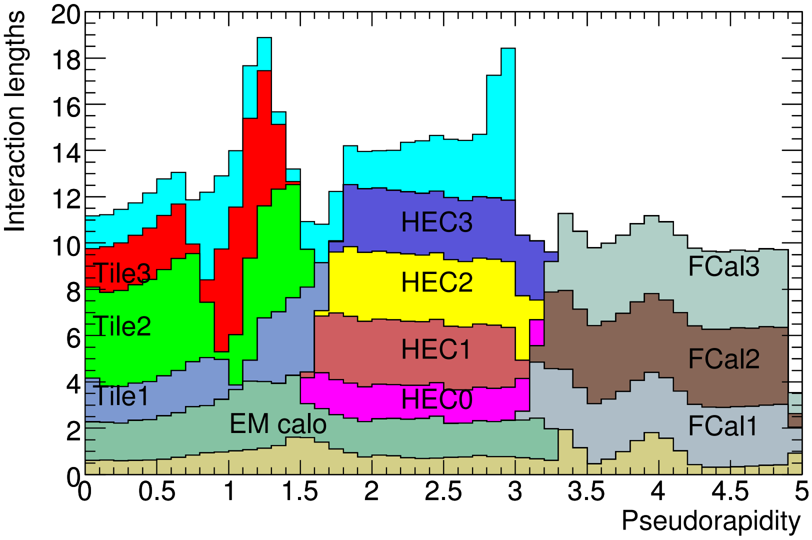

Figure 3.10: Distribution of calorimeter material as a function of psuedorapidity [66]. The top shaded region indicates the material in the first layer of the muon system, and the bottom shaded region indicates the material in the inner detector.

energy. The measured signal in the liquid argon calorimeters is translated to deposited energy via the equation [69]:

$$E^{cell} = \frac{1}{f_{I/E}} \cdot F \cdot \sum_{sample=1}^{N} OF_{sample}(S_{sample} - P). \tag{3.2}$$

N is the number of samples taken of the pulse, typically five for collision data, but up to 32 for calibration purposes. S_{sample} is the signal height, measured in ADC counts, for each sample. The pedestal noise level, P, is derived from data taken taken during periods when no signal events are expected, The optimal filtering coefficients, OF_{sample}, are derived from the expected shape of the analog pulse [70]. They are used to reduce any inherent jitter in the signal shape due to factors such as cross-talk between channels and underlying noise. It is important to note that since these coefficients attempt to reconstruct a signal over a small number of samplings assuming an ideal pulse shape, it is possible for them to cause a negative value of energy to be reconstructed. The observed ADC counts are converted to a current by the factor F, which is determined during calibration by injecting with a well-known current into the readout cell. Finally, $f_{I/E}$ performs the translation from measured current to energy. Due to the complexities of the structure of the electric

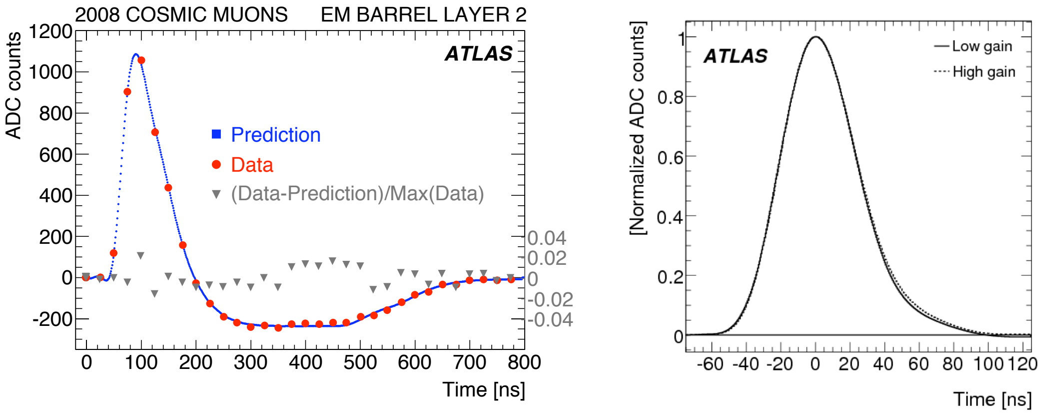

(a) (b)

Figure 3.11: Examples of a measured signal pulse in the EM barrel calorimeter (a), as measured from cosmic muon data and compared to a predicted signal shape [68], and reference tile calorimeter pulses for two gain scales, as measured from test beam data.

field and the showering inside the detector, this factor is difficult to calculate, and is thus derived from detailed data and Monte Carlo comparisons, test beam injection of electrons with well-defined energies, and reconstruction of the Z mass peak in $Z \rightarrow ee$ decays.

The tile calorimeter must map the analog signal from the photomultiplier tubes to visible energy. As in the liquid argon detectors, the signal is measured in several discrete time intervals. The measured signal amplitude is then related to the energy deposited in a cell via the equation:

$$E_{cell} = F \cdot f_{I/E} \cdot C_{Cs} \cdot C_{laser} \cdot \sum_{sample=1}^{N} OF_{sample} S_{sample} \tag{3.3}$$

The signal amplitude, S_{sample}, the optimal filtering coefficients, OF_{sample}, the ADC-to-current conversion factor, F, and the current-to-energy conversion factor, $f_{I/E}$, are all defined and derived analogously to the case for a liquid argon calorimeters. The additional factors, C_{Cs} and C_{laser}, correct for any additional variations between detector elements. C_{Cs} corrects for deviations between cells, as observed by exposing all cells to a Cesium radioactive source integrated into the detector. C_{laser} adjusts for deviations in photomultiplier tube response, as measured by a laser calibration system located on the detector. Typically, the number of samplings is seven times for collision data, but up to nine for calibration purposes.

Since the length of the pulses produced by both the liquid argon and tile calorimeters are much longer than the 25 ns interaction spacing, the time of the cell energy deposition is defined at the leading edge of the pulse shape. The measured pulse shape may have some inherent jitter, as discussed above, so an additional set of optimal filtering coefficients are used to define the phase shift with respect to the 25 ns clock that would be measured assuming an optimal pulse. The cell time is then defined taking into account the known delay of each cell due to the length of the readout cables.

The ATLAS hadronic calorimeters are non-compensating calorimeters, meaning that the signal response for incident electromagnetic and hadronic particles is different. The above formulation is designed to return the energy deposited in a cell by an electromagnetic particle. This is known as the EM energy or EM-scale energy. This difference for hadronic objects, such as jets, must be accounted for when reconstructing the final object energy in a separate step after the signal reconstruction. The procedure for translating the measured EM energy to the correct hadronic scale is detailed in Section 4.3.

3.2.3 Muon System

Since muons have a much smaller cross section to interact in material than electrons or hadrons, they are typically the only charged particles that penetrate the calorimeters. The muon system is designed to detect charged particles within $|\eta| < 2.7$ that do not deposit all their energy in the calorimeters. Because many new physics signatures involve high-momentum muons, the system is also required to provide trigger signals based on the particle p_T for $|\eta| < 2.4$.

To provide a momentum measurement, the muons trajectories are bent in a toroidal magnetic field. This field is provided by one large barrel toroid and two large end-cap toroids, each toroid consisting of eight coils arranged symmetrically around the beam axis. The toroid system produces a magnetic field that is typically oriented in the ϕ direction, though the exact direction is complicated by the overlapping toroid geometry, the non-uniformity of the toroid coil coverage, and the distribution of metal throughout the ATLAS cavern. To accurately measure this complicated field, over 1800 Hall sensors are placed throughout the magnets. Under the influence of this field, muons are deflected in the $r-z$ plane, the radius of curvature of the tracks giving the transverse momentum of the muons. Since the highly-energetic muons bend very little even in this high magnetic field, the muon system is the largest of all the ATLAS sub-detectors, covering a radius from ~ 4.5 m to ~ 12.5 m.

The muon system, consisting of four different detector technologies, is shown in Figure 3.12. A system of Monitored Drift Tube chambers (MDTs) and Cathode Strip Chambers (CSCs) are used to provide precision momentum measurements. The MDTs utilize a detector technology very similar to the TRT straws, consisting of anode wires running down the centers of cathode tubes filled with $\mathrm{Ar/CO_2}$ gas. The passage of a charged particle ionizes the gas atoms, creating free charges that drift to the anode. The time difference between signal at the tube and signal at the wire gives the radial distance of the incident muon track to the wire. The tube diameter of ~ 30 mm and the operating voltage of 3080 V results in a maximum drift time of 700 ns.

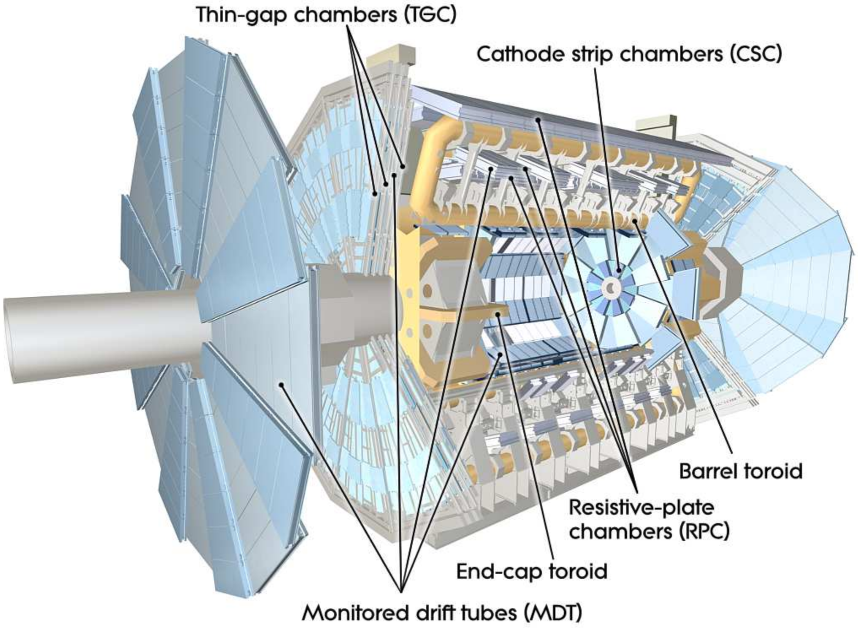

Figure 3.12: Layout of the ATLAS muon systems [66]. The total length is 46 m, extending to a maximum radius of ~ 12.5 m.

The MDTs are arranged in three cylindrical shells at 5 m, 7.5 m, and 10 m from the beampipe and four disks perpedicular to the beam axis in front of and behind the end-cap toroids, ranging from 7.5 m to 21.5 m away from the interaction point. This provides a total coverage up to $|\eta| < 2.7$. The position resolution of each drift tube is 80 μm along the radius of the tube. The tubes are stacked into layers and aligned along ϕ to give position measurements in the bending plane of the toroidal magnetic field.

The CSCs are mulit-wire proportional chambers constructed from two parallel metal sheets with one plane of parallel wires running in between. The metal sheets are segmented into cathode strips, one sheet having strips aligned parallel to the direction of the wires and the other having strips aligned perpendicular. To minimize multiple scattering, the planes are made of a light polyurethane foam with thin copper coats on each surface acting as electrodes. The chambers are filled with ionizing $\mathrm{Ar}/\mathrm{CO}_2$ gas, and a voltage of 1900 V is applied. The ionization charge produced around the anode wire induces a charge distribution on the the two cathode planes. The planes are oriented transverse to the beam direction, so that the peaks of these distributions along the two sets of strips gives position information in η and ϕ.

The CSCs are used for the first layer of the end-cap region $2.0 < |\eta| < 2.7$, where the rate of produced particles is too high to be handled by the MDTs. They are arranged, on two disks of eight chambers each, located approximately 7 m along z from the interaction point. Each chamber is composed of four wire planes, providing four position measurements for each particle that are used to resolve different tracks before they are bent by the magnetic field.

To form trigger signals for muons, detectors with narrow timing resolution, fast signal readout, good momentum discrimination, and coarse position information are necessary. This performance is provided by a combination of Resistive Plate chambers (RPCs) and Thin Gap chambers (TGCs).

The RPCs are constructed from two resistive plates separated by 2 mm of ionizing gas mixture, with a 9.7 kV voltage applied across the gap. They lie in three cylindrical layers around the beam axis, each containing two RPC detectors, covering the region $|\eta| < 1.05$. The charges produced as particles ionize the gas are readout by capacitive coupling to metal strips on the outer surfaces of the plates.

The TGCs provide high-rate information for the end-cap muon trigger. Similar to the CSCs, they are mulit-wire proportional chambers formed by two metal plates, segmented into readout strips, with a plane of parallel metal wires in between. The wires are aligned along ϕ, to provide coordinates in the bending plane of the magnets. Unlike in the CSCs, the strips of both metal plates are perpendicular to the wires, along r. This provides a ϕ position measurement that complements the $r - z$ position measurement given by the MDTs. The high applied voltage, ~ 2900 V, and the small wire-to-cathode distance, $\sim$1.8 mm, gives the TGC detectors their excellent timing resolution and small signal latency. The inner MDT layer has 2 corresponding TGC layers, and the middle MDT layer has 7 corresponding TGC layers, providing a total TGC coverage of $1.05 < |\eta| < 2.4$.

3.2.4 Forward Detectors

ATLAS is equipped with several forward detectors that monitor collision conditions and provide instantaneous luminosity estimates. Precise knowledge of the luminosity delivered to the ATLAS detector is necessary for cross section measurements, such as the inclusive jet cross section measurement presented in this thesis. An explanation of the procedure to obtain this luminosity is given in Section 4.6, but the necessary detector elements are briefly described below.

LUCID (LUminosity measurement using Cerenkov Integrating Detector) is the closest to the interaction point, at $z = \pm 17$ m, reaching to an $|\eta|$ of approximately 5.8. It is composed of ten aluminum tubes located on each side of the detector, surrounding the beampipe and pointing toward the interaction point, each filled with C_4F_{10}. The Cerenkov radiation produced by particles as they traverse the gas is measured by photomultiplier tubes. The principle of LUCID is to detect inelastic $p-p$ scattering in the forward direction, exploiting the fact that the number of particles detected is proportional to the total, both primary and pileup, interactions in a bunch-crossing. LUCID thus provides a relative luminosity measurement, in which the detected number of particles must be translated to the total number of proton-proton interactions via calibration runs.

The goal of the ALFA (Absolute Luminosity For ATLAS) detector, on the other hand, is to measure the absolute luminosity delivered to ATLAS. ALFA measures the elastic scattering of particles at small angles to the beam direction. The optical theorem can then be used to exactly relate the measured forward scattering cross section to the total collision scattering cross section. The detector consists of scintillating fiber trackers placed at $z = \pm 240$ m in several “roman pots,” which allow movement of the detector as close to beam as possible during stable LHC beams, but far away from the beam during LHC commissioning.

The Zero Degree Calorimeter (ZDC) is located between LUCID and ALFA, at $z = \pm 140$ m, covering the region $|\eta| > 8.3$. The purpose of the ZDC is to detect forward neutrons during heavy ion collisions, and also to provide an additional minimum bias trigger to ATLAS. It is composed of one EM calorimeter and two hadronic calorimeter components, each composed of tungsten plates that cause particles to produce Cerenkov light. The ZDC, which provides an orthogonal trigger to that given by the MBTS, was used to verify the trigger efficiency for low-p_T jets.

3.2.5 Data Acquisition and Trigger

At design luminosity, the LHC will deliver approximately 40 million collision events every second. With an average ATLAS event size of $\sim$1.5 MB, this is far more information than can be saved into the finite data storage resources available. The goal of the trigger system is to move interesting physics events to permanent storage, while rejecting the vast majority of other events. This is accomplished using a three-tiered trigger system: a hardware-based Level 1 trigger (L1), followed by a software-based Level 2 trigger (L2) and event filter (EF). The L1 trigger is designed to reduce the 40 MHz collision rate to a 75 kHz rate of accepted events. The L2 trigger is designed to reduce this rate further to 3.5 kHz, with the EF further reducing it to the ultimate data-recording rate of 200 Hz. However, due to the low total integrated luminosity throughout 2010, the EF was often run with an output rate of up to 400 Hz, to capture as many events as possible. The L2 trigger and EF are known collectively as the high-level trigger (HLT).

The L1 trigger is designed to accept high-p_T muons, electrons, photons, jets, and taus, referred to below as "objects," as well as events with large missing transverse energy or sum energy. It uses signals from the TGCs and RPCs for muon triggers and reduced-granularity calorimeter information for electron, photon, jet, tau, and total energy triggers. In addition, it generates minimum bias trigger decisions based on signals from the MBTS, ZDC, or LUCID and several zero bias triggers based on random signals or designated time spacings. The calorimeter trigger system, which maintains a fast readout independent from the remainder of the calorimeter, is known as the Level-1 Calorimeter (L1Calo). The discussion below will focus on elements necessary for jet triggers, since they are a crucial ingredient of the jet cross section measurement.

The L1Calo constructs object transverse energy, scalar sum energy, and multiplicity information from approximately 7200 analog trigger towers of size $\Delta\eta = \Delta\phi = 0.1$, spanning both the EM and hadronic calorimeters. Jet trigger elements are 2×2 groupings of these towers. The jet trigger is divided into the central jet trigger, which uses towers within $|\eta| < 3.2$, and the forward jet trigger, which uses forward calorimeter towers within $3.2 < |\eta| < 4.9$.

Level-1 jets can then be defined as 2×2, 3×3, or 4×4 combinations of these elements, corresponding to cells within $\Delta\eta \times \Delta\phi$ regions of 0.4×0.4, 0.6×0.6, or 0.8×0.8. This jet window is defined to be centered on the 2×2 combination of jet elements that contains the local maximum of energy. The midpoint of this 2×2 combination defines the jet coordinates. The jet energy is defined by subjecting the calorimeter signals to very basic noise suppression and pedestal subtraction and an extremely rudimentary calibration based on a look-up table. When defining the jet time, it is essential to assign the trigger signal to the correct bunch crossing. The L1Calo algorithm reads out the calorimeter signals in five samples, finds the peak, then uses the known peaking time to derive the incident signal time.

The electron, photon, and tau triggers also use the L1Calo elements, applying combinations of transverse energy thresholds and isolation criteria to groups of trigger towers to identify candidate objects. The muon triggers require a coincidence of signals in layers of the RPC and TGC to define a candidate muon.

The Central Trigger Processor, then combines information from different trigger objects and makes the final trigger decision. This decision could require a simple transverse energy threshold, a certain multiplicity objects, or a combination of different objects. This decision includes the possible application of a prescale, which is an additional rejection factor necessary to reduce the rate of certain high-frequency triggers. The Timing and Trigger Control system distributes this decision, along with the 40 MHz clock signal, to the individual sub-detector readouts.

While waiting for the L1 decision, detectors store information in front-end electronics boards on or near the detector. If an event is accepted, selected information is moved to the L2 processors, while the full information is sent to a series of Readout Buffers that store the information while waiting for the L2 decision. If an event is rejected by the L1 trigger, the data corresponding to that event is lost forever.

The L2 trigger applies additional energy thresholds and multiplicity requirements using the Regions of Interest (RoIs) around triggered L1 objects. Using only information in regions surrounding L1 objects limits the amount of data that must be transferred in order to make a trigger decision. For example, the L2 jet trigger retrieves the data from cells surrounding the L1 RoI and constructs jets using a simplified cone jet algorithm. The L2, as well as the EF, can also be run in “pass-through” mode, meaning that they do not apply any further decisions after L1, but simply pass the data on to storage. This mode was used in much of 2010, as the trigger elements were still being commissioned. If L2 is not in pass-through mode, the L2 trigger starts by confirming the L1 trigger decision, then requests additional information from sub-detectors as needed to formulate the L2 decision.

If no L2 trigger is satisfied, then the contents of the Readout Buffers are discarded. If a trigger is satisfied, the event information is sent to the EF processing farms. The EF applies decisions to fully-reconstructed events, including, for the first time in the trigger process, full information from the inner detector. It consists of a processing farm running standard ATAS event reconstruction and analysis software. Jets in the EF are reconstructed using the anti-k$_t$ jet algorithm, as used in offline analysis. During all of 2010, the EF jet triggers were being commissioned, so the EF operated in pass-through mode for the entire data-taking period.

Events that are not rejected by the EF are moved to CERN permanent storage. Immediately at the output of the EF, the event information is in the byte-stream format that results from the detector readout. This data, known as RAW data, is first sent to the Tier-0 computing facilities located at CERN. The data is grouped according to the trigger requirement or requirements that the particular events passed. These collections are known as trigger streams, and are typically associated according to common trigger objects. For example, the “L1Calo” trigger stream was an early trigger stream that grouped all events that passed any level-1 calorimeter trigger requirement, and the “Egamma” trigger stream collects any events that pass an HLT electron or photon trigger. Each of these files is further labelled by the unique ATLAS run number, which typically corresponds to one LHC run.

At Tier-0, the byte-stream data is converted to an object-oriented data format using the standard ATLAS reconstruction software. This software is grounded in the ATHENA [71] software framework. The objects that result correspond to physics objects, such as tracks, muons, missing transverse energy, or jets.

This reconstructed data is stored in a variety of formats, varying in level of detail and size, and distributed to Tier-1 and Tier-2 computing facilities located all over the world. The data can then be retrieved from these facilities via the worldwide computing GRID [72], which is a global network of computers accessible by all ATLAS members. The original RAW data is maintained at Tier-0 so that further improvements to reconstruction algorithms or fixes to bugs in the reconstruction code can be applied during some later data reprocessing.

The most detailed format typically used for 2010 data analysis was the Events Summary Data (ESD) format, which consisted of POOL ROOT files [72]. For many analyses, a more convenient data format is the Derived Physic Data (DPD) format. These are small ROOT n-tuples that are made from ESDs, but store a limited number of reconstruction objects. These files are easily analyzed outside of the ATHENA framework using ROOT.

3.2.6 Detector Operation in 2010

The total number of channels for each ATLAS sub-detector and the percentage of these channels that were operational in 2010 are shown in Table 3.2.6. The main cause of inefficiencies for the inner detector is silicon sensors that are not read out due to high-voltage failures and failures in segments of the cooling system that do not allow the electronics to be operated. For the liquid argon calorimeters, the main detector problem was the break down of several dozen of the laser transmitters that send data from the on-detector front-end electronics to the Read Out Buffers. This was corrected for in the reconstruction of these cells by using the slightly noisier, reduced-granularity measurement from the L1Calo trigger towers. The trigger towers cover the same regions of the detector, but only utilize an analog readout and hence do not suffer from these transmitter problems. The main problem for the tile calorimeters was the failure of several of the drawers that house low-voltage power supplies and readout for an entire ϕ wedge either the barrel or one of the extended barrel calorimeters. The ϕ wedges cover an area of 1/64 of the total ϕ coverage. Since the majority of a shower's energy is deposited in the EM calorimeters, these failures are not critical and were corrected for using the average of the energy deposited in neighboring tile cells. The small inefficiencies in the muon system are due mainly to problems with the high-voltage power supplies.

Also shown is the percentage of good quality delivered by each of the ATLAS sub-detectors, measured relative to the total luminosity delivered to ATLAS. The recorded data is flagged as "good" if any problems in the sub-detector during the data delivery are understood and accounted for in the offline analysis. To prevent damage to the silicon sensors, the pixel and SCT systems are only fully-powered once a stable beam signal is given by the LHC. This results in an additional data taking inefficiency of $\sim 2\%$, which is not included in this table. The inefficiencies in the EM calorimeter are due mainly to isolated high voltage supply trips, and those in the hadronic end-cap calorimeter are predominantly due to bursts of noise.

Sub-detector	Total readout channels	Operational (%)	Good data (%)
Pixel	8.0×10^7	97.2	99.1
SCT	6.3×10^6	99.2	99.9
TRT	3.5×10^5	97.5	100
EM calorimeter	1.7×10^5	99.9	90.7
Hadronic end-cap calo.	5600	99.8	96.6
Forward calorimeter	3500	99.9	97.8
Hadronic tile calorimeter	9800	98.8	100
MDT muon chambers	3.5×10^5	99.8	99.9
RPC muon chambers	3.7×10^5	97.0	99.8
TGC muon chambers	3.2×10^5	99.1	99.8
CSC muon chambers	3.1×10^4	98.5	96.2

Table 3.2: Total number of readout channels, percentage of readout channels that were operational, and luminosity-weighted relative percentage of good quality data delivered for each of the ATLAS detector sub-systems during the 2010 proton-proton run.

Chapter 4 Data Analysis

This chapter details the various corrections and selections applied to the gathered data to form the inclusive jet cross section measurements. The event selection will be summarized in Section 4.1. Next, the jet reconstruction, calibration, and selection procedure will be described in Sections 4.2-4.4. An essential element of both the event and jet selection scheme is the combination of data from appropriate triggers, which is detailed in Section 4.5. Related to the trigger selection is the luminosity used to normalize the measured jet distributions, as described in Section 4.6. Section 4.7 discusses the unfolding, or deconvolution, procedure that is applied to correct for detector resolution and inefficiencies. Finally, a summary of the various uncertainties on the measured cross sections is presented in Section 4.8, with particular emphasis on the dominant uncertainty due to the jet energy scale calibration.

In the following, it is useful to note that jet reconstruction and calibration studies are usually quoted in terms of detector pseudorapidity, η, while the final measurement and corrections applied to this measurement are quoted in terms of jet rapidity, y. This is motivated by the fact that the varying calorimeter technology and coverage dictate the jet reconstruction performance, but the underlying physics distributions should be detector independent. The two quantities are typically very similar, and though differences increase for higher $|\eta|$, lower jet p_T, and jet origins displaced along z, they are typically smaller than the jet angular resolution.

To show clearly the separate effects caused by different calorimeter regions, studies are usually presented in the seven different pseudorapidity ranges listed in Table 4. The final cross section results will be shown in the same bins, but defined in terms of jet rapidity. Typically, the term "central" will be used to describe the pseudorapidity/rapidity regions covered by the barrel calorimeters, and "forward" will be used to describe the regions covered by the end-cap and forward calorimeters.

The results in this chapter are usually only shown for one jet size, either $R = 0.4$ or $R = 0.6$, in order to maintain brevity in the total number of figures. Differences, where relevant, will be noted in the text, and figures of particular importance will be included in the appendices.

$\lvert\eta\rvert$ region	ATLAS calorimeter coverage
$0 \leq \lvert\eta\rvert < 0.3$ $0.3 \leq \lvert\eta\rvert < 0.8$	Barrel EM and barrel tile calorimeters
$0.8 \leq \lvert\eta\rvert < 1.2$ $1.2 \leq \lvert\eta\rvert < 2.1$	Transitions between barrel, extended tile barrel, and hadronic end-cap calorimeters
$2.1 \leq \lvert\eta\rvert < 2.8$	End-cap calorimeters
$2.8 \leq \lvert\eta\rvert < 3.6$	Transition from hadronic and EM end-caps to forward calorimeter
$3.6 \leq \lvert\eta\rvert < 4.4$	Forward calorimeter

Table 4.1: Detector $|\eta|$ regions that define the binning of performance studies and final cross section results.

4.1 Event Selection

4.1.1 Data Selection

The inclusive jet cross section measurement detailed in this analysis utilizes the full 2010 data set of proton-proton collisions $\sqrt{s} = 7$ TeV. However, different subsets of this data are used for different kinematic regions of the measurement, as dictated by the varying detector and beam conditions, the latter of which allowed the instantaneous luminosity delivered by the LHC to increase throughout the year. ATLAS runs that collected data under similar beam and detector configurations are grouped into periods, labelled Period A-I. A description of the beam configuration and the total integrated luminosity collected in each data period is given in Table 4.2. The integrated luminosity quoted in this table, and throughout this thesis, is given in units of inverse picobarns, $\text{pb}^{-1} = 10^{36}$ cm^2. This entire data set was reprocessed at Tier-0 using a coherent set of reconstruction software in Autumn 2010, consisting of the software tags AtlasProduction_16.0.2.3 and AtlasProduction_16.0.2.5.

For jets with $p_T < 60$ GeV, only data from Periods A-C are used. This data was collected without a significant rate of multiple-proton, or pileup, interactions, which deposit small amounts of energy throughout the calorimeter that can significantly distort the measurement of low-p_T jets. Also, throughout these periods, the minimum bias triggers were allocated a large share of the trigger rate. This was particularly useful for the collection of low-p_T jets, which are not fully-efficient with respect to the available jet triggers. In the later periods, the minimum bias triggers were heavily prescaled due to their high rates.

Measurements of jets with $p_T \geq 60$ GeV and $|y| \geq 2.8$ are performed using data from from late Period E (run 161118) onwards. In early Period E, commissioning activities within the L1Calo hardware improved the timing of the forward jet triggers, which cover $|\eta| > 3.2$. Before this commissioning, the poor timing of the forward jet triggers caused large inefficiencies, and hence jets collected by these triggers before the timing improvement are not used.

Measurements of jets with $p_T \geq 60$ GeV and $|y| < 2.8$ are made using data from all periods. The one exception is that several runs in Period E are not used to measure jets with $1.2 \leq |y| < 2.1$, due to commissioning activity that caused inefficiencies for triggers in the region $|\eta| = 1.45$.

Period	Run Range	Lumi. [pb^{-1}]	Beam Configuration
A	152166 -153200	0.4×10^{-3}	Initial collisions at $\sqrt{s} = 7$ TeV, beam width squeezed from 60-30 μm, from 2 to 13 bunches per beam, $\sim$1-2$\times10^{10}$ protons per bunch
B	153565 -155160	9.0×10^{-3}	
C	155228 -155697	9.5×10^{-3}	
D	158045 -159224	0.3	Number of bunches per beam increased from 3 to 50, increase to $\sim 10^{11}$ protons per bunch, first amount of significant pileup with average interactions per crossing > 1.5
E	160387 -161948	1.2	
F	162347 -162882	2.0	
G	165591 -166383	9.0	Bunch trains with 150 ns spacing, total bunches per beam increasing from 8 to 368, $\sim 1.5 \times 10^{11}$ protons per bunch
H	166466 -166850	9.3	
I	167575 -167844	23.0	

Table 4.2: Data periods of the 2010 proton-proton LHC run, with corresponding ATLAS run numbers, integrated luminosity delivered to ATLAS, and relevant beam configuration changes.

Within each ATLAS run, data quality flags are assigned to ensure that only reliably collected and reconstructed data is used for analysis [73]. Flags are assigned to each detector sub-system, as well as to the reconstruction software performance. These flags are defined for the time interval of a luminosity block, which is the shortest coherent timescale of the ATLAS data acquisition system, typically a few minutes long. Initially, they are set by the team of control room and offline shifters, but later they are confirmed by the ATLAS Data Quality group.

The ATLAS data quality flag system consists of five colors: black, yellow, red, green, and gray. Black is used to label a detector element that is entirely off. Data marked as red is not suitable for analysis. This flag is assigned if, for example, large portions of a sub-detector are off or malfunctioning, or there are non-recoverable problems within the data acquisition system. Yellow data corresponds to a subsystem that is known to be flawed, but could be recovered by proper treatment during offline analysis or further reprocessing. Green signifies that the data is suitable for analysis, though some imperfections may remain. For example, small regions of a sub-detector could be malfunctioning or off, as long as their impact on reconstruction is understood. If a run is too short to assess the quality of data or if there are malfunctions in the data quality monitoring software, the gray flag is assigned. Luminosity blocks with gray flags are re-assessed offline in order to determine the appropriate permanent color.

The data quality flags from each run are used to form Good Run Lists (GRLs), which define the luminosity blocks over which a relevant set of detector and reconstruction elements were functioning properly. The analysis presented in this thesis requires that events pass the GRL requirements recommended by the ATLAS Standard Model jet working group. These require that flags be set to green for the central trigger processor, L1Calo, solenoid magnet, inner detectors (Pixel, SCT, and TRT), calorimeters (barrel, end-caps and forward calorimeters), luminosity detectors, and tracking, jet, and missing energy reconstruction performance. Data-quality flags for the high-level trigger are are also required to be green for Periods G-I, when the HLT was activated.

4.1.2 Vertex Selection

The presence of a reconstructed primary vertex, which marks the interaction point of a proton-proton collision, is required to reject events due to cosmic rays or beam background. A secondary vertex, on the other hand, is the point of decay of a long-lived particle that was produced from the primary proton-proton interaction, such as a hadron containing a b-quark. These two types of vertices can be distinguished by noting their distance from the beam-spot, with primary vertices located within the beam-spot and secondary vertices displaced by typically several mm.

Vertices are reconstructed by matching several tracks back to a common origin. To ensure that only good quality tracks are associated to a vertex, the ATLAS vertex reconstruction uses only tracks that satisfy:

- $p_T > 150$ MeV,
- $|d_0| < 4$ mm,
- $\sigma(d_0) < 5$ mm,
- $\sigma(z_0) < 10$ mm,
- at least 4 hits in the SCT detector,
- and a total of at least 6 hits in the pixel and SCT detectors.

Here, d_0 is the minimum radial impact parameter of the track with respect to some origin, and z_0 is the minimum longitudinal impact parameter of the track with respect to some origin. These parameters are restricted in order to separate primary from secondary vertices. The uncertainties on these parameters are $\sigma(d_0)$ and $\sigma(z_0)$, as given by the quality of the fit used for track reconstruction.

Before a list of primary vertices to be used for physics analysis is compiled, the coordinates within ATLAS of the beam-beam interaction region, known as the beam-spot, are determined. The exact position is based on a distribution of preliminary primary vertices, defined as follows. First, a vertex seed is defined by taking the global maximum of all tracks that satisfy the above criteria, using the detector origin, $(x, y, z) = (0,0,0)$, to determine d_0 and z_0 for each track. An adaptive vertex fitting algorithm [74] is then executed, in which the tracks with the largest χ^2 contributions to the vertex fit are removed one by one and a new vertex is defined. This process is repeated until no tracks with $\chi^2 > 49$ remain, or until only 2 tracks are associated to the vertex. The remaining tracks are then used to find new vertices, until no unassociated tracks remain or no new vertices can be formed. The beam-spot is then extracted by applying an unbinned maximum likelihood fit to the distribution of primary vertices, which returns coordinates of the center of the interaction region and the transverse and longitudinal widths.

The beam-spot is re-calculated throughout an ATLAS run, in order to account for the varying beam crossing positions and widths throughout the LHC fill cycle. It is usually measured every five luminosity blocks, or about every 10 minutes. The assignment of a beam-spot, however, requires at least 100 primary vertices. If fewer than this number of vertices is accumulated in a given interval, the position $(x, y, z) = (-0.2$ mm,1 mm,0 mm$)$ is assigned with the large transverse and longitudinal widths of 3 cm and 50 cm.

After an event beam-spot location is defined, the final list of primary vertices is compiled by performing the same vertex fitting procedure described above, but using the beam-spot coordinates to constrain both the input tracks and final vertex fit.

An event vertex can then be defined as the primary vertex with the highest associated $\sum p^2_{T,track}$. The high amount of track p_T associated with this vertex identifies it as the origin of a hard scattering. Events used in this analysis are required to have an identified event vertex with at least five associated tracks, chosen to eliminate fake vertices that can be formed from a small number of tracks and to be compatible with the vertex definition used to derive the jet energy correction due to piluep. The efficiency for collision events to pass these vertex requirements, as measured in a sample of events passing all other event and jet selection requirements, is well over 99%. The z distribution of the event vertex, after GRL selection applied to jet-triggered events, is shown in Figure 4.1(b), for various similar data periods and for the full data set. The RMS of the distribution in different data periods illustrates how the beam-spot expanded due to the increasing number of protons in each bunch, and the offset of the peak illustrates that detector origin does not always reflect the collision point. The total number of primary vertices, N_{PV}, with at least five tracks in each event, after GRL selection applied to jet-triggered events, is shown in Figure 4.1(a). The mean number of primary vertices in each event, which is a measure of the pileup interaction rate, is 2.19, averaged over the full data set.

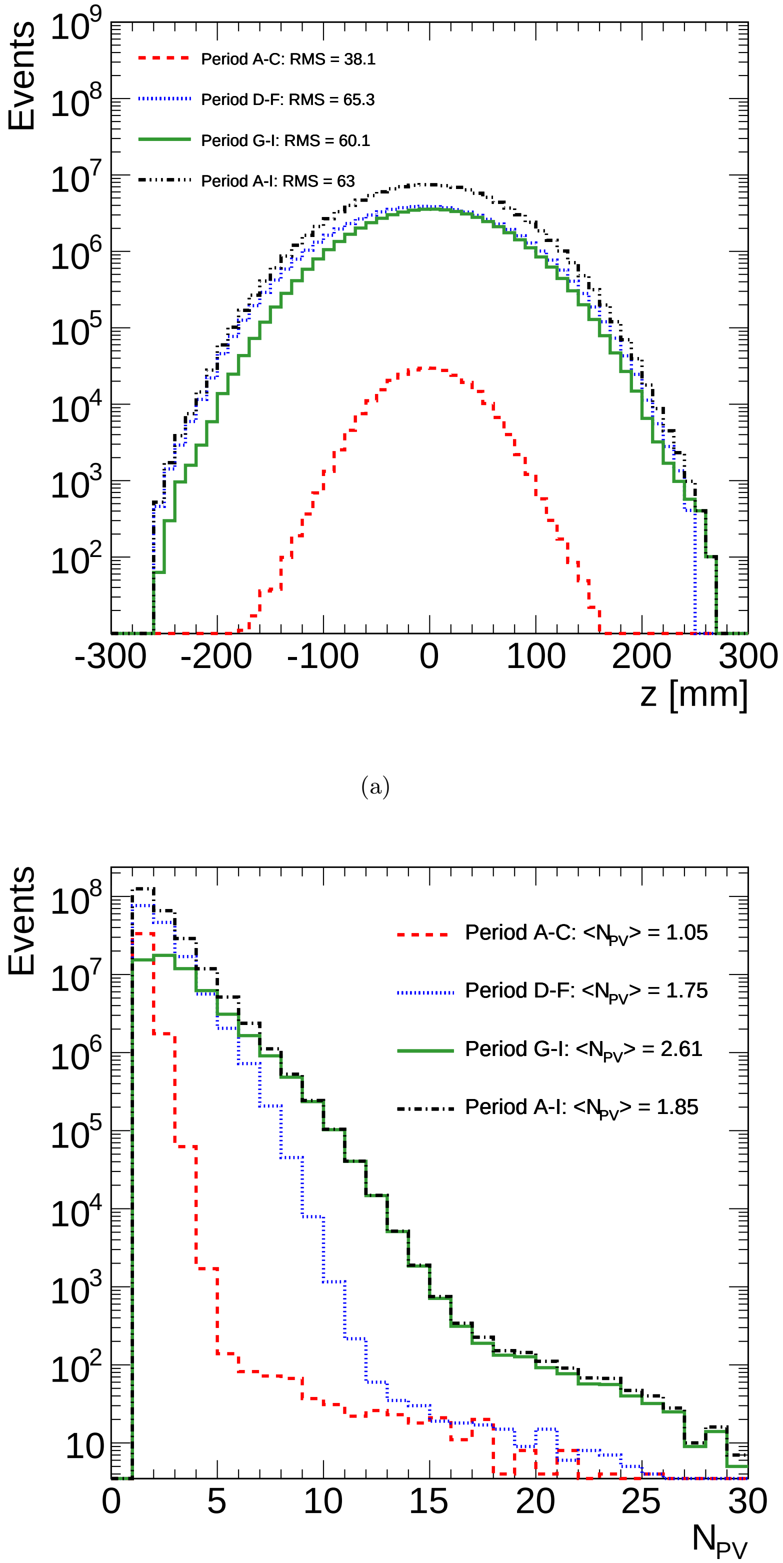

(a)

(b)

Figure 4.1: Position in z of identified primary vertices with at least five tracks (a) and the number of primary vertices, N_{PV}, with at least five tracks (b) for events in throughout the 2010 data set. The RMS of the z distribution and the mean of the primary vertex distribution are indicated.

4.2 Jet Reconstruction

As discussed in Section 2.6, a jet can be formed from a variety of possible constituent objects. The main jets used for this analysis are constructed from energy in three-dimensional clusters of calorimeter cells, though jets built from other experimentally-measured objects are used for supporting jet energy calibration and reconstruction performance studies. The jets are built using the anti-k$_t$ algorithm, as defined in Section 2.6, with the FastJet software package [75]. The four-momentum of each jet is constructed by vectorially summing the four-momenta of its constituents. In ATLAS, jets are reconstructed using two different size parameters: $R = 0.4$, for narrow jets, and $R = 0.6$, for wider jets. Other jet algorithms have been implemented and studied in the ATLAS software in the past, but are not used for the current analysis [76].

In order for the reconstructed jets to correspond to particles produced by the proton collisions, detector signals that do not originate from particle interactions must be properly constrained. This procedure is known as noise suppression. For jets built from calorimeter input objects, the noise levels are assessed by recording calorimeter signals in periods where no beam is present in the LHC. These periods are typically dedicated calibration runs or gaps in the LHC cycle. Both the mean measured energy and the standard deviation, σ, around this mean are recorded for each layer of the calorimeter as a function of the η position of the cells. The mean measured energy is used as the pedestal value when defining the reconstructed cell energy, as detailed in Equation 3.2. The σ around this mean is interpreted as the noise of the calorimeter cell. Permanently noisy cells are “masked” during jet reconstruction, meaning they are never used as inputs to the jet clustering algorithm. Cells that are only occasionally noisy, however, could still contain useful signals and must be dealt with using a more sophisticated noise suppression scheme.

The jets used for the inclusive jet cross section analysis are built from noise-suppressed topological clusters, also known as “topo-clusters,” of energy in calorimeter cells. The formation of these clusters begins by identifying calorimeter cells that have energy depositions at least 4σ above each cell's mean noise, according to the relation $|E_{cell}/\sigma| > 4$. Next, any neighboring cells that have an energy at least 2σ above their mean noise, according to $|E_{cell}/\sigma| > 2$, are added to the cluster. Finally, a single layer of cells neighboring the cluster, regardless of signal-to-noise ratio, are added. The result of this process is a three-dimensional cluster of energy that takes advantage of the fine granularity of the ATLAS calorimeter system. The position of the cluster is assigned as the energy-weighted centroid of all constituent cells, and the cluster four-momentum is then used as an input to the jet algorithm. Jets built from these topological clusters are known as "topo-jets." Unless otherwise noted, the jets referred to in this thesis are all topo-jets.

One disadvantage of jets built from topological clusters is that they lack an easily-defined area in $\eta - \phi$ space. Such an area is useful, for example, to perform corrections due to the low energy density distributed throughout the calorimeter that results from pileup interactions. For the study of pileup, jets built from projective towers of $\Delta\eta \times \Delta\phi = 0.1 \times 0.1$ groups of calorimeter cells, extending through both the EM and hadronic calorimeter layers, are instead used. The position of these towers is fixed by the 0.1×0.1 grid, and their total energy is constructed using only the cells within this area that are part of topological clusters. If a cell coincides with more than one tower, its energy is divided proportionally to the cell area that falls inside each tower. These towers thus exploit the noise suppression of topological clusters, but maintain a constant area. The use of these "tower-jets" to derive the energy correction due to pileup is discussed further in Section 4.3.

To validate the detector reconstruction with respect to the "true" jet position and energy, jets in Monte Carlo simulated events can be constructed using either the partons resulting from the event generation or the stable particles that result from the parton shower and hadronization, initial and final state radiation, and pileup interactions. The kinematic properties of these parton or particle jets, known as truth jets, are calculated with respect to their generation vertex, before any interactions with the detector. Throughout this thesis, the phrases "truth jets," particle-jets, and particle-level jets will be used to refer to particle jets formed from Monte Carlo event generation. Jets formed from partons will be referred to as parton-jets or parton-level jets.

An event recorded by ATLAS in August 2010 with five topo-jets, reconstructed using $R = 0.6$, is shown in Figure 4.2. The cells that contribute to clusters in the EM and hadronic calorimeters are highlighted in yellow. Charged particle tracks pointing toward these energy depositions are clearly visible in the inner detector. The jets are shown as circles in the $\eta - \phi$ plane in the bottom left panel, with the EM-scale energy assigned to each jet shown on the vertical axis.

Understanding of the efficiency and purity of the reconstruction procedure outlined

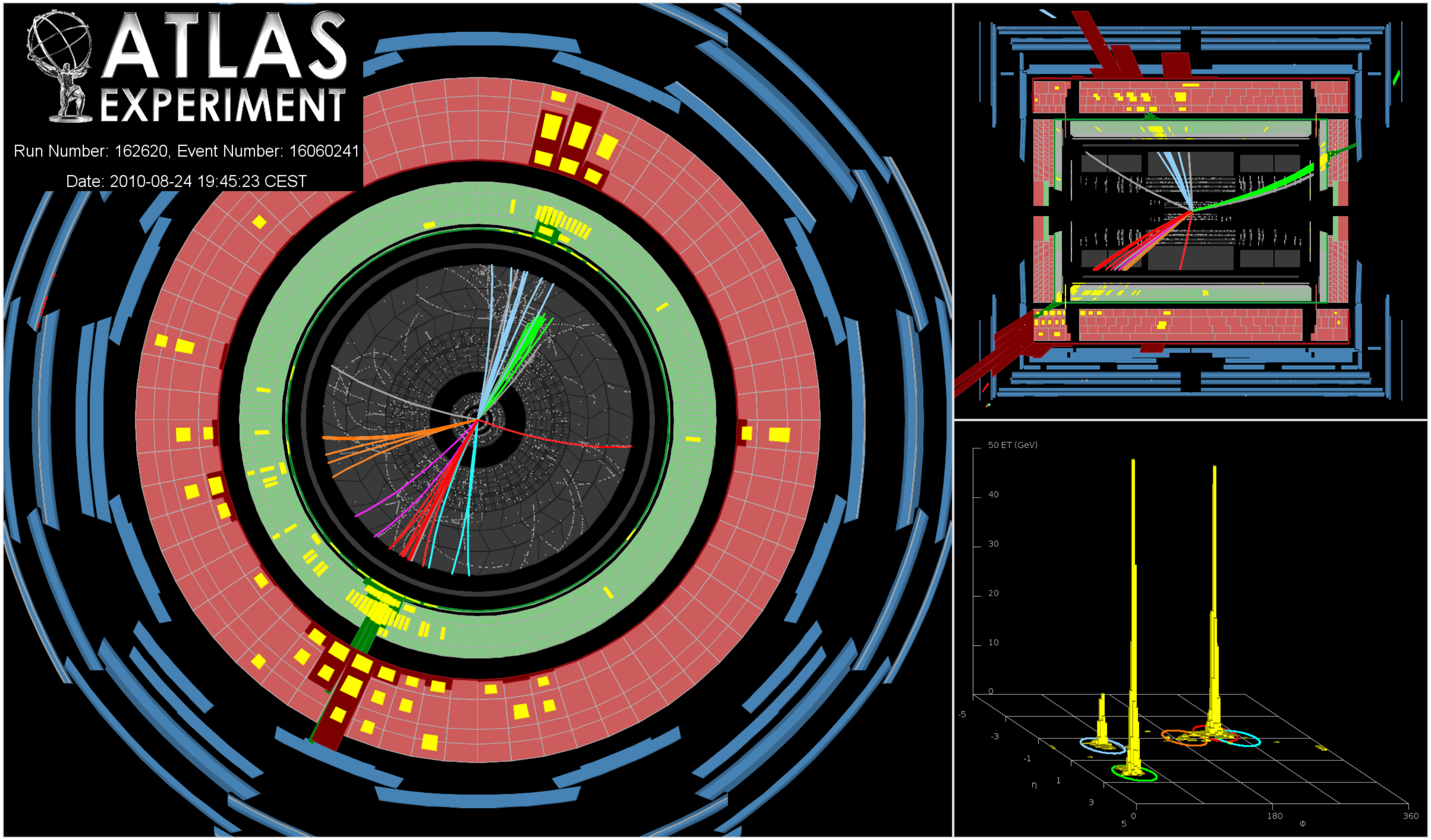

Figure 4.2: Event display of an event with five reconstructed topo-jets. The reconstructed objects are shown in the $x - y$ cross section of the barrel of the detector (left panel) and the $y - z$ cross section of the full detector (top right panel). The innermost portion shows the tracks reconstructed by the inner detector. The next two layers show the clusters of energy reconstructed by the EM and hadronic calorimeters. The outermost layers illustrate the activity recorded by the muon system. The EM-scale jet energies are shown in the $\eta - \phi$ plane in the bottom left panel.

above is an essential element of the inclusive jet cross section analysis. The jet reconstruction efficieniency and purity are defined as:

$$\text{efficiency} = \frac{\#\text{ of truth jets matched to a reconstructed jet within } \Delta R^1 < R_{match}}{\#\text{ of truth jets}} \tag{4.1}$$

$$\text{purity} = \frac{\#\text{ of reconstructed jets matched to a truth jet within } \Delta R < R_{match}}{\#\text{ of reconstructed jets}} \tag{4.2}$$

The reconstruction efficiency and purity for topo-jets with $R = 0.6$, as measured in Pythia Monte Carlo events with a matching radius of $R_{match} = 0.3$, is shown in Figure 4.3. In general, the reconstruction efficiency and purity for $R = 0.4$ jets at a given p_T will be higher than that for $R = 0.6$ jets at the same p_T. To reach the same p_T, a narrower jet must have a greater energy density, which is more likely to produce a cluster in the calorimeter. Similarly, the reconstruction efficiency and purity are higher for jets located at higher $|\eta|$, since a jet in the forward η region with a given p_T will have an energy typically an order of magnitude higher than that of a jet in the central η region with the same p_T. The drop in efficiency at low p_T is mainly due to jets that, as a result of jet energy resolution smearing, have energies below the 7 GeV threshold that is required by the ATLAS software in order to reconstruct jets. Jets in all η regions with calibrated $p_T > 30$ GeV are greater than 99% efficient and pure, except in the transition region between barrel and extended barrel of the tile calorimeter at $0.8 \leq |\eta| < 1.2$. In this region, the poor calorimeter coverage, as illustrated in Figure 3.10, leads to poor angular resolution that causes jets to fall outside the matching radius.

To verify these Monte Carlo measurements, a tag-and-probe method [77] was used to measure *in-situ* the topo-jet reconstruction efficiency relative to jets reconstructed using tracks in the inner detector. These jets, known as track-jets, are assembled by using the measured four-momentum of tracks as inputs to the jet algorithm. Track-jets have very similar performance in both data and Monte Carlo [78]; because track-jets and topo-jets are measured using independent ATLAS sub-detectors, a good agreement between data and Monte Carlo for the efficiency to match topo-jets to track-jets is a verification that the absolute topo-jet reconstruction efficiency in Monte Carlo models that in data.

The track-jets are reconstructed using the anti-k_T algorithm with $R = 0.6$. They are

---

[1] $\Delta R = \sqrt{(\phi^{reconstructed} - \phi^{truth})^2 + (\eta^{reconstructed} - \eta^{truth})^2}$

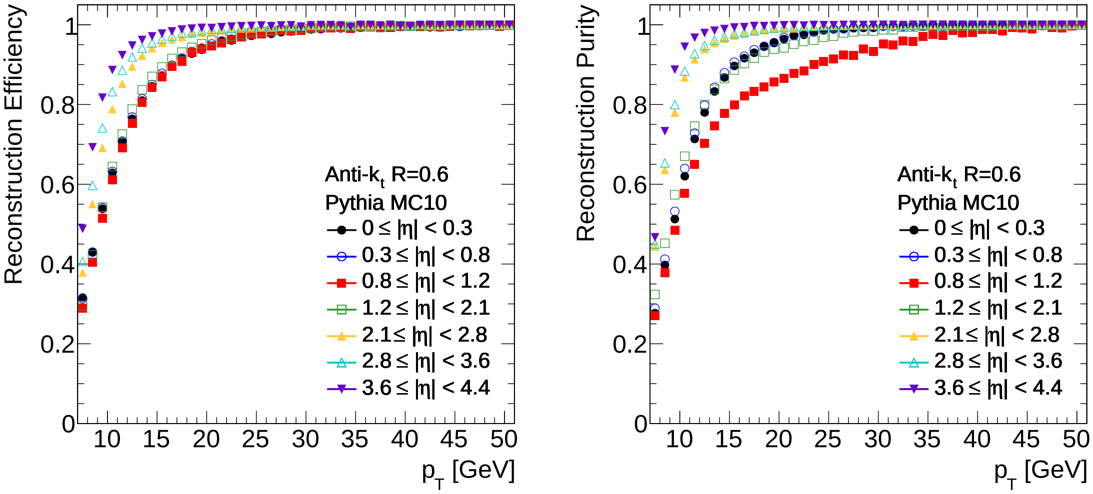

(a)

(b)

Figure 4.3: Jet reconstruction efficiency as a function of calibrated jet p_T (a) and purity as a function of true jet p_T (b) as measured in Monte Carlo events for jets in several detector $|\eta|$ regions.

required to be composed of at least two tracks, each with $p_T^{track} > 500$ MeV, at least one pixel detector hit, at least 6 SCT hits, $d_0 \leq 1.5$ mm, and $z_0 \leq 1.5$ mm, where d_0 and z_0 are the transverse and longitudinal impact parameters of the track with respect to the beam-spot. In order to be fully contained in the efficient tracking region, the track-jets are required to have $|\eta| < 1.9$. Topo-jets and track-jets are reconstructed with p_T thresholds of 7 GeV and 4 GeV, respectively.

To identify di-jet events, the highest p_T track-jet in the event is defined as the tag object, and a second track-jet balancing this in ϕ, with $\Delta\phi > 2.8$ between the two jets, is defined as the probe object. In order to provide an unambiguous matching candidate, the event is rejected if more than one probe jet is identified in the $\Delta\phi$ window. A matching efficiency is then defined as:

$$\text{efficiency} = \frac{\#\text{ of track-jets at a given } p_T \text{ that match a topo-jet within } \Delta R < 0.4}{\#\text{ of track-jets at a given } p_T} \quad (4.3)$$

Due to the $|\eta| < 1.9$ restriction on track-jets and the matching requirement of $\Delta R < 0.4$, the measurement is only valid for topo-jets with $|\eta| < 2.3$. However, as discussed above,

---

[1] $\Delta R \equiv \sqrt{(\phi^{track-jet} - \phi^{topo-jet})^2 + (\eta^{track-jet} - \eta^{topo-jet})^2}$

the efficiency is expected to only increase with increasing η.

Figure 4.4(a) shows the efficiency to match topo-jets to track-jets in data and Monte Carlo. The total error, indicated by the hatched region, is the quadratic sum of the statistical and systematic errors. Bayesian statistical errors are assigned independently to each bin in p_T, and are negligible for all but the highest p_T bins. Systematic uncertainties are obtained by varying the minimum p_T of the tag track-jet, the $\Delta\phi$ window for the probe track-jet, and the ΔR matching radius between the probe track-jet and the topo-jet. The values used for these variations are $p_T > 20$ GeV, $\Delta\phi < 2.6$ and 2.9, and $\Delta\mathrm{R} < 0.3$ and 0.5, respectively. The largest source of systematic uncertainty comes from the choice of tag track-jet p_T, which contributes up to 5% for the lowest p_T bins.

The ratio between the efficiency relative to track-jets for data and for Monte Carlo is shown in Figure 4.4(b). The uncertainty on this ratio is dominated by systematic effects at low p_T and statistical errors at high p_T. Excellent agreement is shown across the full measured range, with in particular a less than 2% disagreement in the region where efficiency is less than 99%. Because of this similarity between data and Monte Carlo reconstruction performance, corrections due to reconstruction inefficiencies are performed during the Monte Carlo-based unfolding procedure, as detailed in Section 4.7.

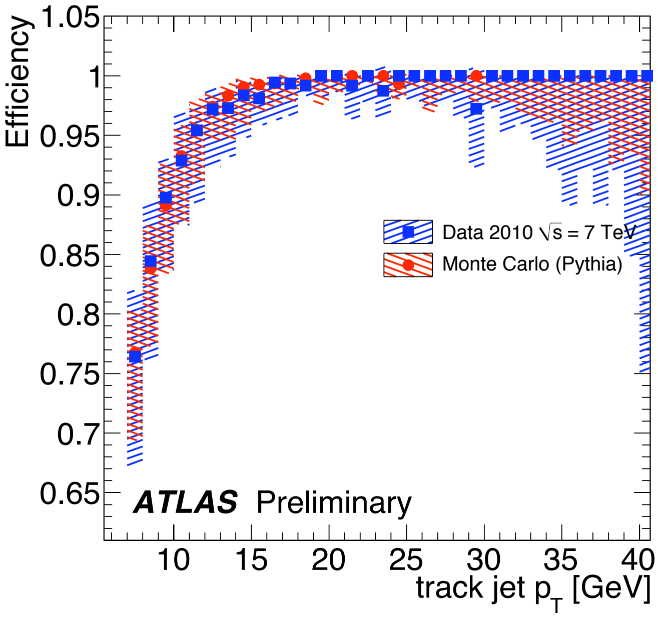

(a)

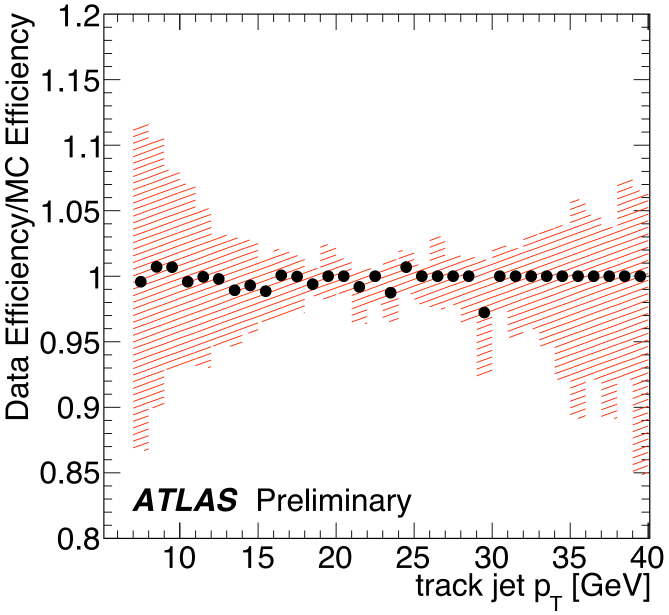

(b)

Figure 4.4: Relative reconstruction efficiency for calorimeter jets, measured with respect to track-jets, as a function of track-jet p_T for data and Monte Carlo (a) and the ratio of this efficiency measured in data to that measured in Monte Carlo (b). Quadratic sum of statistical and systematic errors are indicated by the hatched regions.

4.3 Jet Energy Scale

Because of the steeply-falling nature of the jet p_T spectrum, even small shifts in the jet energy calibration can produce large shifts in the measured jet cross section. For this reason, the accurate assignment of a jet energy calibration and understanding of its uncertainties with early ATLAS data are of paramount importance to the inclusive jet cross section analysis, and were the major focus of the ATLAS Jet performance group throughout 2010.

The jet energy is first reconstructed from the constituent cell energies at EM-scale. These cells have been calibrated to return the energy corresponding to electromagnetic showers in the calorimeter, based on test-beam injection of electrons and pions [69], measurements of cosmic muons [79], and reconstruction of the Z mass peak in $Z \rightarrow ee$ decays. Cells are combined to form clusters, as described in Section 4.2, which are by construction massless objects. The cluster four-momenta are then vectorially summed to yield the final jet four-momentum, with its energy at EM-scale.

The purpose of the jet energy calibration, or jet energy scale, is to correct this measured EM-scale energy to the energy of the particles within a jet. These include π^0s' and η's, which decay to photons that produce high-energy EM cascades, as well as $\pi^{\pm}$'s and p's, which interact via ionization and strong interactions with nuclei. The nuclear interactions can knock free additional protons and neutrons or produce recoiling nuclei in excited states, which emit photons upon de-excitation. To complicate matters further, frequently no calorimeter signature is left by the nuclear recoils and neutrons of a hadronic shower. The jet energy calibration must also account for energy lost in in-active regions of the detector, such as in the cryostat walls or cabling; energy that escapes the calorimeters, such as that of highly-energetic particles that "punch-through" to the muon system; energy of cells that are not included in clusters, due to inefficiencies in the noise-suppression scheme; and energy of clusters not included in the final reconstructed jet, due to inefficiencies in the jet reconstruction algorithm. The muons and neutrinos that may be present within the jet are not expected to interact within the calorimeters, and are not included in this energy calibration.

Due to the varying calorimeter coverage, detector technology, and amount of upstream in-active material, the calibration that must be applied to each jet to bring it to the hadronic scale varies with its η position within the detector. This can be seen in the corresponding variation of the EM-scale jet response, as shown in Figure 4.5. The jet response is defined in Monte Carlo as $\mathcal{R} = E^{EM}_{jet}/E_{truth}$, where each reconstructed jet at EM-scale is matched to a truth jet within $\Delta R < 0.3$. In particular, the dips in jet response at $0.8 < |\eta| < 2.1$ correspond to the transition between barrel and end-cap calorimeters, and those at $2.8 < |\eta| < 3.6$ correspond to the transition between hadronic end-cap and forward calorimeters. The goal of the jet energy calibration is to bring the calibrated jet response to $\mathcal{R} = 1$, flat across all η.

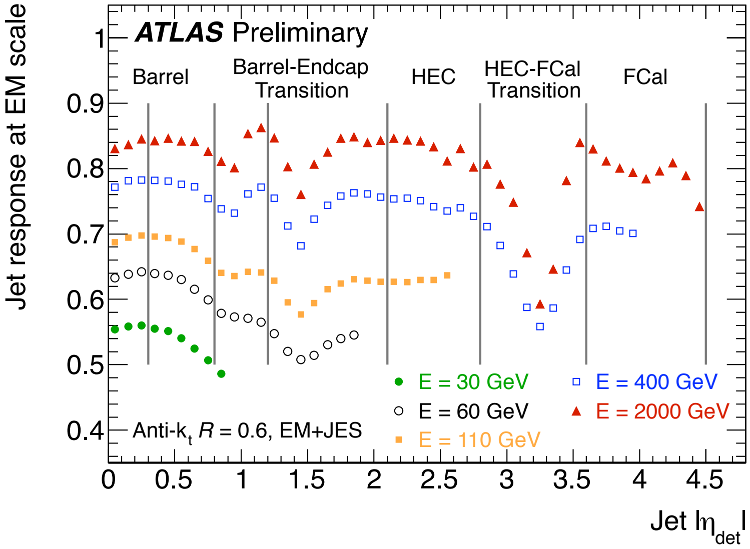

Figure 4.5: Simulated jet energy response at EM-scale as a function of detector pseudorapidity, $|\eta_{det}|$, for several bins of jet energy [80].

The calibration applied to jets for 2010 data analysis is derived from a combination of *in situ* studies and comparisons of reconstructed and truth jets in Monte Carlo events. This calibration, known as the "EM+JES" calibration scheme [80], consists of three separate corrections:

1. The offset correction subtracts the average extra energy deposited in the calorimeter by pileup interactions from the EM-scale jet energy [81].
2. The four-momentum of the jet is corrected to point back to the hard-interaction vertex, instead of to the detector origin.
3. The jet energy and position are corrected using E^{EM} and η dependent factors derived from comparisons of reconstructed and truth jets in Monte Carlo simulations.

The first step in the calibration, the offset correction, is based on the observation that extra pileup interactions produce low-energy deposits dispersed throughout the calorimeter. The amount of energy deposited depends on the number of additional interactions, which is quantified by the number of reconstructed primary vertices in the event. It also depends on the η position in the calorimeter, due to the underlying angular distribution of particles produced by the soft interactions and the varying calorimeter coverage. The average amount of pileup energy that falls inside a jet, as a function of the η position of the jet and number of primary vertices, N_{PV}, is subtracted from the jet energy according to:

$$E_T^{corrected} = E_T^{EM} - \mathcal{O}(\eta, N_{PV}) \tag{4.4}$$

The offset correction, $\mathcal{O}$, could in principle also be affected by the time between colliding bunches, τ_{bunch}, since signals in the calorimeter extend over many hundreds of nanoseconds. If two collisions occur within this same window, signals from earlier bunch crossings could interfere with signals from later crossings. The spacing between bunches within a bunch train was small enough to produce such interference from Period G onwards. Since the last bunch in the train, which sees the effect of several previous bunches, is more influenced than first bunch, which should see no effect, the possible offset dependence on τ_{bunch} was studied by measuring the average cluster energy in jets as a function of the event position within bunch train. No bias was observed in the bunch train settings used in 2010, so no correction applied for τ_{bunch} is applied to this dataset, though the further decrease in bunch spacing in 2011 may cause this to be necessary.

The value of the offset applied to each jet is derived by measuring the average energy deposited in $\Delta\eta \times \Delta\phi = 0.1 \times 0.1$ calorimeter towers, with no noise suppression applied in order to remain sensitive to low-energy deposits. This average energy was measured as a function of the number of reconstructed primary vertices in the event that have at least five associated tracks and as a function of the η position of the tower within the calorimeter. Next, the average number of towers in each jet is measured, also as a function of η. Finally, the applied correction is defined as the product of the average energy per tower and the average number of towers per jet, according to:

$$E_T^{corrected} = E_T^{EM} - \mathcal{O}_{tower-based}(\eta, N_{PV}) \times \langle N_{towers}^{jet} \rangle . \tag{4.5}$$

For central jets, the total offset is approximately 0.2 GeV in events with 2 vertices, increasing to 1 GeV in events with 5 vertices. For forward jets, the offset is higher due to the higher amount of pileup energy in this region, approximately 1 GeV in events with 2 vertices and 4 GeV in events with 5 vertices.

After the offset correction is applied to the jet EM-scale energy, the four-momentum of each topocluster in a jet is corrected to point back to the vertex with the highest associated $\sum p_{T,track}^2$. The jet four-momentum is then the redefined as the vector sum of the cluster four-momenta. This mainly improves the jet angular resolution, but also introduces small, $< 1\%$, shifts in the jet p_T.

Next, a calibration factor is extracted from Monte Carlo that corrects the EM-scale jet energy to the energy of the truth jet, using a technique known as numerical inversion [82]. The procedure to define this calibration factor starts by matching isolated reconstructed jets to isolated truth jets within $\Delta R < 0.3$. Subsequently, the EM-scale jet response, $\mathcal{R}$, is measured in bins of truth jet energy and reconstructed jet η, defined with respect to the detector origin. The peak response, as obtained from a gaussian fit to the response distribution, and the average EM-scale reconstructed jet energy are calculated for each bin of truth energy and η. The response is then fit as a function of EM-scale energy to a logarithmic function, and the final calibration factor is the inverse of this function. The corrected jet energy is then given by:

$$E^{corrected} = E^{EM} \times \frac{1}{\mathcal{F}(E^{EM})|_{\eta}}. \tag{4.6}$$

The calibration factors that are applied to the EM-scale jet energy are shown in Figure 4.6, as a function of EM-scale p_T for several bins of detector $|\eta|$. These factors are largest at low p_T, due to the combination of several effects. Most importantly, low energy hadronic particles are less likely to interact in the EM calorimeter. This means a higher fraction of their energy is deposited in the hadronic calorimeter, which in turn causes a lower jet response due to calorimeter non-compensation. Low p_T jets also tend to be wider, and hence the effects of energy falling outside of the reconstructed jet radius is greater, and the noise suppression scheme can cause low-energy deposits to not form clusters that can seed jets. The calibration factors must also account for the large fraction of energy lost by low p_T particles in the inner detector, cryostat wall, and cabling before reaching the calorimeter, as well as for the low p_T particles that never reach the calorimeter due to these interactions.

The calibration factors are lower at high $|\eta|$ than for corresponding p_T bins at low η, due to the large amount of energy needed to produce a sizable p_T in the forward region. Jets at high $|\eta|$ are thus less likely to lose energy due to noise suppression and more likely to be narrow, and hence fully-contained within the jet radius. Additionally, there is less inactive material at high $|\eta|$ that could absorb portions of the jet energy.

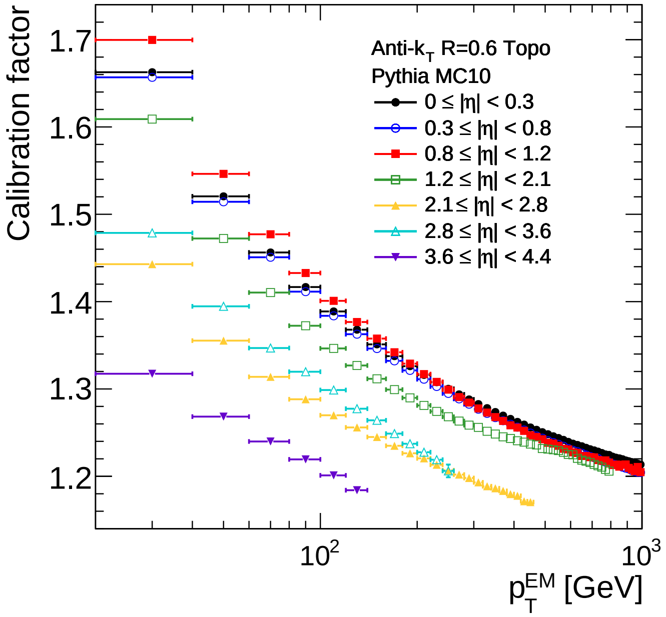

Figure 4.6: Calibration factor applied to jets as a function of EM-scale jet p_T for several detector $|\eta|$ bins.

Finally, the origin-corrected η of the jet is further corrected to account for the fact that poorly-instrumented regions of the calorimeter tend to reconstruct lower energy deposits than their neighboring calorimeter regions. This systematic underestimation of energy causes jets to be biased to point towards the adjacent high-energy deposits in the better-instrumented regions. This η correction, defined as $\Delta\eta = \eta_{truth} - \eta_{origin-corrected}$, is derived from Monte Carlo in bins of E_{truth} and detector η and applied as a function of corrected jet energy and detector η. The correction $\Delta\eta$ is less than 0.01 for most regions, but is as high as 0.04 for jets falling in the region between the hadronic end-cap and the forward calorimeter.

The uncertainty on this calibration scheme, referred to as the jet energy scale uncertainty, is assessed using a combination of *insitu* studies and Monte Carlo variations. The various components of the jet energy scale uncertainty are derived as follows:

- The uncertainty on the Monte Carlo-based calibration method is derived by applying the calibration factors to Monte Carlo jets. The deviation of the jet response from unity is then taken as the relevant uncertainty. This effect, known as the non-closure of the method, comes from approximations implied by using the peak response and average reconstructed EM-scale energy in deriving the calibration factors. It is also caused by the bias induced by shifting the energy of the jet four-momentum, but leaving its mass constant. In the central region, this uncertainty is 2% for $p_T <$ 30 GeV and $<$ 1% for $p_T >$ 30 GeV. In the forward region, it amounts to $<$ 1% for $p_T >$ 20 GeV.

- The uncertainty from the modeling of the calorimeter response in the Monte Carlo simulation is derived by comparing E/p studies in data and Monte Carlo [83]. E/p studies measure the ratio of energy deposited by a particle in the calorimeter to the corresponding momentum of a charged particle in the inner detector. A comparison of E/p measured in data and in Monte Carlo gives the difference in calorimeter response to single particles. The mapping of particles to jets in Monte Carlo is then used to assess how the single particle response affects the jet response. The uncertainties on this method come from the variation of the single particle response in Monte Carlo, variations of the charged particle composition of jets, and various acceptance effects. Due to statistical constraints and the poor momentum resolution for high-momentum tracks, these E/p measurements are only applicable for particles with $p <$ 20 GeV. For particles with $p >$ 20 GeV, uncertainties on the single particle energy resolution are taken from test beam measurement. The large uncertainty on particles with $p >$ 400 GeV, where no measurements exist, causes the largest contribution to the total jet energy scale uncertainty in high-p_T region. The total contribution from E/p is 1.5-4%.

- The uncertainty due to the difference in noise thresholds between data and Monte Carlo, which can affect cluster reconstruction, is assessed by varying the noise threshold in Monte Carlo to correspond to the spread of the noise, σ, measured in data.

These thresholds are shifted by ±5, 7, and 10% of σ, and the maximal change induced in the jet response is taken as the contribution to the jet energy scale uncertainty. The contribution is 1(2)% for $20 \leq p_T < 30$ GeV for $R = 0.4 (R = 0.6)$, 1% for $30 \leq p_T < 45$ GeV, and negligible for $p_T < 45$ GeV.

- The variation of the jet energy scale due to the amount of inactive detector material, known as "dead material", is assessed by adding material to the detector simulation in Monte Carlo events. In particular, ≤ 0.1 radiation length of additional material is added to the inner detector, the presampler and first layer of EM calorimeter, the cryostat before and after the barrel EM calorimeter, and the region between EM barrel and EM end-cap. In general, the uncertainty due to these variation is less than 3% for $p_T < 45$ GeV and less than 2% elsewhere.

- The uncertainty due to Monte Carlo modeling of fragmentation, underlying event, and hard and soft sub-processes is assessed by using Alpgen [84], which can simulate $2 \rightarrow 5$ processes, to generate matrix elements, Herwig [85] to perform the parton shower and hadronization, and Jimmy [86] to model the underlying event. Pythia with the Perugia2010 [53] tune is also used, as described in Section 2.5.

The final jet energy scale uncertainty is only provided for jets with $p_T > 15$ GeV. To determine this uncertainty, reconstructed jets with p_T as low as 7 GeV were used for the studies of Monte Carlo variations. The calibration factors, however, are only provided for jets with $E^{EM} > 10$ GeV, due to the non-gaussian response distributions below this threshold. The same calibration factors are therefore applied to all jets with $E^{EM} \leq 10$ GeV, meaning that low energy jets are under-corrected. These low energy jets are also very close to the generation threshold of the Monte Carlo and the reconstruction threshold of the ATLAS software. For these reasons, the inclusive jet cross section measurement detailed in this thesis only uses jets with $p_T > 20$ GeV.

Aside from the uncertainty due to non-closure, which is measured in each η region, the uncertainties measured in the region $0.3 \leq |\eta| < 0.8$ are propagated to the more forward η regions using studies of the relative transverse momentum balance in di-jet events, a method known as eta-intercalibration [87]. The use of $0.3 \leq |\eta| < 0.8$ to define a baseline uncertainty accounts for the better knowledge of the detector geometry in the central region and the lack of test-beam measurements in the forward regions. Two methods for measuring this balance are used: one which requires one jet to be in the central region and studies the balance with respect to a jet outside this region, and another, the so-called matrix method, in which the two jets are in different η regions. The latter method gives better statistical precision, so is used to quote the final intercalibration results. The agreement in response between central and forward jets is better than 2% for jets with $|\eta| < 1.8$, better than 5% for jets with $1.8 < |\eta| < 2.8$ and approximately 10-15% for jets with $|\eta| > 2.8$. The difference in response is added to the baseline uncertainty for the region $0.3 \leq |\eta| < 0.8$.

An additional uncertainty due to the offset correction is estimated for events with more than one primary vertex. This uncertainty is obtained from closure tests in Monte Carlo simulations, variations of the trigger selection used to select events when deriving the correction, and variations of the number of towers assumed for each jet. Another component comes from differences observed when mapping track-jets, which are matched back to the hard event vertex and are thus not susceptible to pileup, to calorimeter jets as a function of N_{PV}. For events with two measured primary vertices, the uncertainty is up to 2.5% for jets with $20 \leq p_T < 30$ GeV and $3.6 < |\eta| < 4.4$, less than 1% for jets with $20 \leq p_T < 30$ GeV and $0.3 < |\eta| < 0.8$, and less than 1% everywhere for jets with $p_T > 60$ GeV.

The total uncertainty, for events with $N_{PV} = 1$, is shown for the central, end-cap, and forward regions in Figures 4.7-4.9. For the barrel region, the total uncertainty is as high as ~4.5% for $p_T < 60$ GeV, decreasing to ~2% for $p_T \approx 100$ GeV. The uncertainty is higher in the end-cap region due to the additional uncertainty derived from the eta-intercalibration. The total uncertainty ranges from ~7% for $p_T < 30$ GeV to ~2.5% at $p_T \approx 100$ GeV. The highest uncertainties occur in the forward calorimeter, ranging from ~12.5% for $p_T < 30$ GeV to ~2.5% $p_T \approx 100$ GeV.

The main correction of the jet response in the EM+JES scheme is totally Monte Carlo-based. However, it has been validated with a number of *in situ* jet response measurements. Perhaps the most canonical *in situ* jet response measurement is the so-called direct γ-jet balance technique, which exploits the transverse momentum balance in photon-jet events [88]. Photons interact electromagnetically, and are thus inherently measured better by the calorimeter system. After corrections to the EM-scale derived from $Z \rightarrow ee$ measurements, the uncertainty on the measured photon energy is less than 0.5% for $|\eta| < 0.6$, between -0.4% and +0.8% for $0.6 \leq |\eta| < 1.0$, and between -0.4% and +1.4% for $1.0 \leq |\eta| < 1.37$ [88]. The photon transverse momentum is thus taken as the reference, "true"

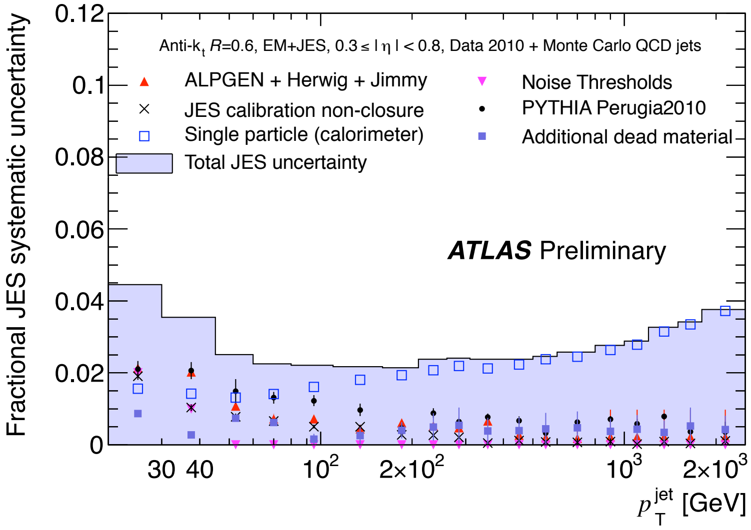

Figure 4.7: Fractional jet energy scale systematic uncertainty as a function of p_T for jets in the pseudorapidity region $0.3 \leq |\eta| < 0.8$ [80].

energy of the jet, and the response is defined as the ratio of p_T^{jet} to p_T^{γ}. A comparison of this response as measured in data and in Monte Carlo gives an estimate of the uncertainty on of the jet response as modeled in the Monte Carlo, and thus a validation of the jet energy calibration procedure.

In the γ-jet analysis, it is essential to select only well-measured photons resulting from hard collisions. To eliminate non-collision background events, events in which the vertex with highest $\sum p_T^{tracks}$ has less than five associated tracks are rejected. The highest p_T photon in the event is required have $p_T > 25$ GeV, in order to avoid bias from the photon trigger selection, and be located within $|\eta_\gamma| < 1.37$, in order to be entirely in the EM barrel calorimeter. Additional photon identification criteria based on the longitudinal and transverse shape of the EM shower [89] is applied, and the photon is required to be isolated from other energy deposited in the calorimeter, with no more than 3 GeV present in the surrounding calorimeter region.

The photon must be clearly balanced in the transverse plane by the highest p_T jet in the event, with $\Delta\phi(jet, \gamma) > \pi - 0.2$ rad. This jet must have $|\eta_{jet}| < 1.2$, in order to be fully-contained in the barrel tile calorimeter[2], and all jets in the event are required to be of good quality, as outlined in Section 4.4. To avoid events where soft radiation can cause

---

[2] The response of jets with $|\eta| > 1.2$ is verified *in situ* using the eta-intercalibration technique.

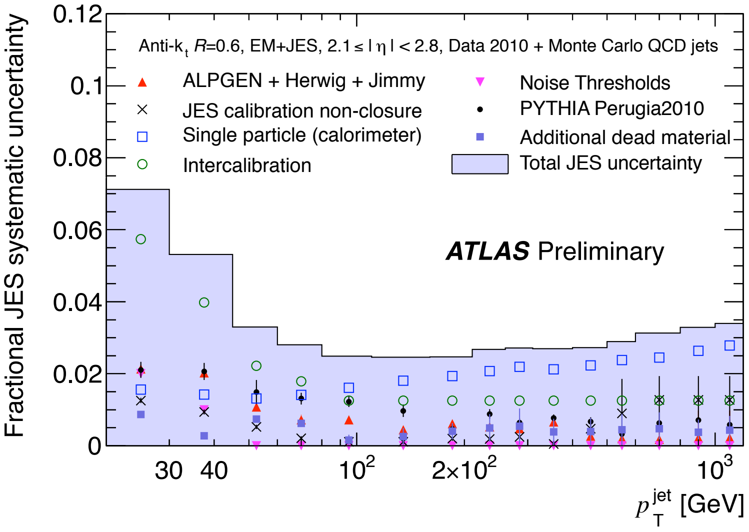

Figure 4.8: Fractional jet energy scale systematic uncertainty as a function of p_T for jets in the pseudorapidity region $2.1 \leq |\eta| < 2.8$ [80].

an inherent imbalance between the photon and the jet, the ratio of the p_T of the second leading jet to the p_T of the photon must satisfy: $p_T^{jet2}/p_T^{\gamma} < 0$.

The result of this response measurement in data and in Monte Carlo is shown in Figure 4.10(a), with the ratio of the data to the Monte Carlo response shown in the bottom panel. The two response measurements are consistent within 3% for most of the measured range. The 5% difference for the lowest p_T bin is most probably due to the use of Monte Carlo without pileup interactions.

Systematic uncertainties on this measurement are assigned for the presence of pileup interactions, background contamination of the photon sample, soft radiation effects, and the photon energy scale uncertainty. The effect of pileup is studied by comparing the response measured in data events with only one vertex to that measured in events with multiple vertices. The uncertainty due to the presence of soft radiation is assessed by varying the $\Delta\phi(jet, \gamma)$ and p_T^{jet2}/p_T^{γ} criteria, and that due to the photon energy scale is assessed by varying photon energy scale within its uncertainties. The photon background uncertainty is obtained by convoluting the estimated photon purity with the response variation due to mis-identified photons. The rate at which a jet is falsely identified as a photon is measured in our sample by using a sideband technique [89] and by relaxing the photon selection criteria in data. The photon purity is estimated to be approximately 0.6 at $p_T^{\gamma} = 25$ GeV,

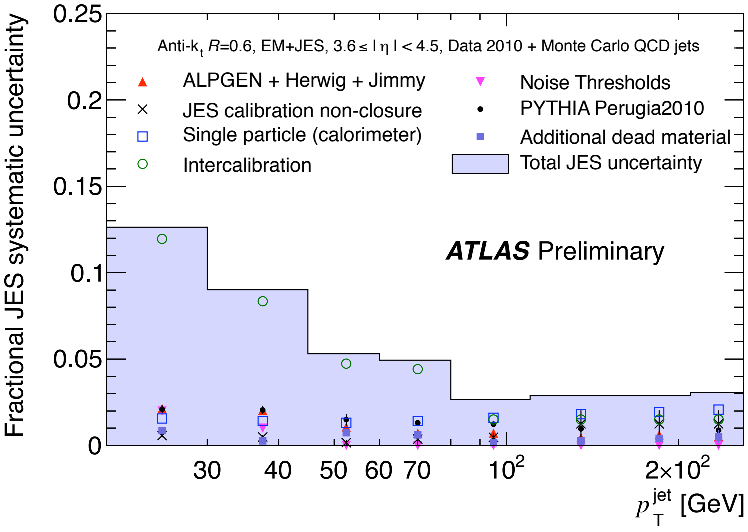

Figure 4.9: Fractional jet energy scale systematic uncertainty as a function of p_T for jets in the pseudorapidity region $3.6 \leq |\eta| < 4.5$ [80].

increasing to 0.95 for high p_T. The response variation due to a jet being identified as the photon is obtained using di-jet Monte Carlo samples that have been filtered to events where one jet resembles a photon. The uncertainty due to background contamination of the photon sample is then given by:

$$\epsilon = (\frac{R_{dijet} - R_{\gamma-jet}}{R_{\gamma-jet}}) \times (1 - P), \tag{4.7}$$

where P is purity measured from data, R_{di-jet} is the response measured in a filtered di-jet sample, and $R_{\gamma-jet}$ is the response in the nominal photon-jet sample. The total systematic uncertainty on the ratio shown in Figure 4.10(b).

The direct γ-jet balance measurements, as well as measurements employing balance of jet energy against missing energy [88], track-jets, and multi-jet systems [90] have all confirmed the JES systematic uncertainties shown in Figure 4.10 within the systematic uncertainties on these methods.

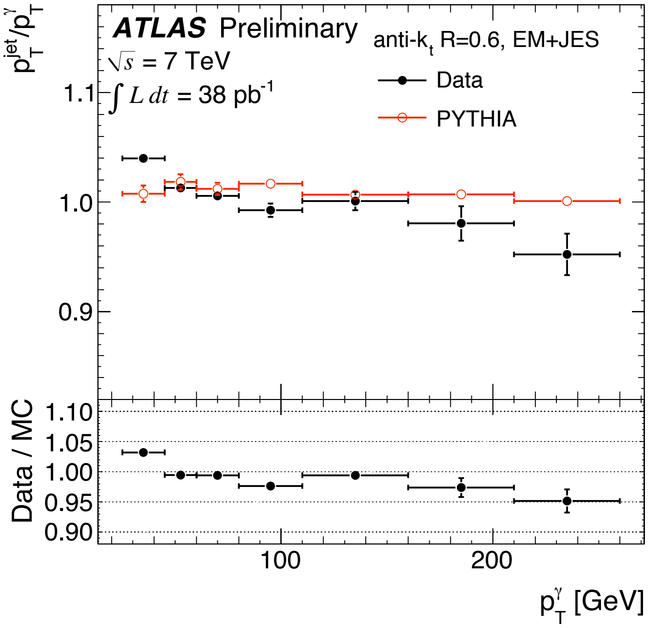

(a)

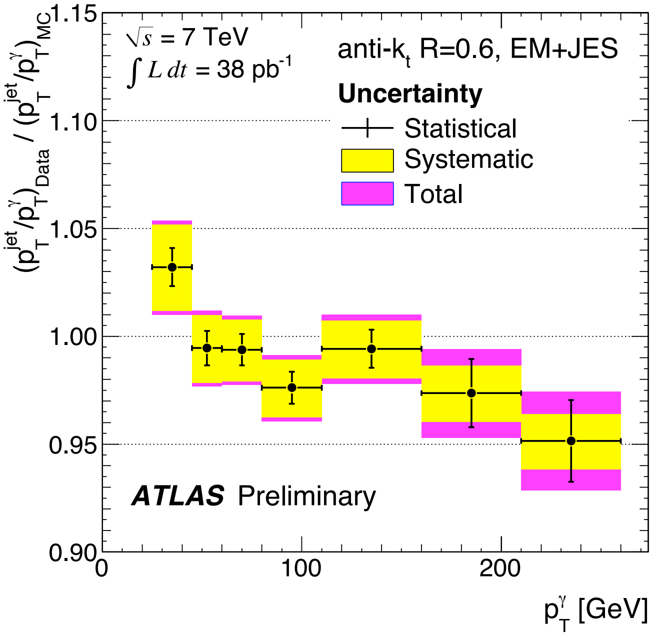

(b)

Figure 4.10: Jet response as determined using the direct p_T-balance technique in γ-jet events as a function of photon transverse momentum for both data and Monte Carlo (a) and the ratio of response in data to the response in Monte Carlo, illustrating both statistical and systematic uncertainties (b) [88].

4.4 Jet Selection

A series of jet quality selections, also known as jet cleaning cuts, are implemented to remove jets reconstructed from calorimeter signals that do not originate from particles produced in the hard collision. Note that since this analysis aims to make an inclusive jet measurement, only individual jets are removed from the data sample by these cleaning cuts, not entire events. Many of these jets are already removed by the event vertex requirement, but those that are coincident with an actual collision require dedicated elimination.

The main causes of these non-collision "fake" jets in the 2010 data sample were bursts of noise in the hadronic end-cap calorimeter and coherent noise in the EM calorimeter. Fake jets can also be produced by non-collision particle interactions. Sources of these calorimeter signals include cosmic rays traversing the detector, beam protons interacting with residual beam gas left in the beampipe, and beam protons interacting with material, such as the beam collimators, producing muons or pions traveling in the halo of the beam. These last two effects are known as beam-gas collisions and beam-halo, respectively, and constitute the main sources of beam background in ATLAS.

The set of jet cleaning cuts described below has been optimized by ATLAS by studying distributions of variables related to particular sources of fake jets. These distributions were compared in samples of good jets, chosen from clear di-jet events where the two jets are balanced back-to-back in ϕ, and in samples of bad jets, chosen from events with a large ratio of missing E_T to the sum E_T of the event, indicating a jet was reconstructed with no energy to balance it in the transverse plane. The exact values of the cuts were chosen to maximize both the efficiency to retain jets resulting from collision particles and the rejection of fake jets. The procedure used to derive these cuts is detailed in Reference [91], though the exact variables used have evolved since the writing of this document.

In the case of jets reconstructed from hadronic end-cap noise, most of the energy of the jet will be in one cell of the hadronic end-cap calorimeter, with a small amount of energy in neighboring cells due to cross-talk. Thus these jets will have high values of the variable HEC fraction, or $HECf$, which is the fraction of the jet's energy at EM-scale that originates from cells in the hadronic end-cap. In addition, the signal shape resulting from this noise is different than the signal shape expected from true particle energy deposition. This is quantified by the cell quality factor, which is a measure of how badly the observed signal varies from the reference signal used to reconstruct the cell energy:

$$\text{cell quality} = \sum_{i=samples} (a_i^{observed} - a_i^{reference})^2, \tag{4.8}$$

where a_i is the signal amplitude at a particular sampling. This cell quality factor is then used to form a hadronic end-cap quality factor, denoted HEC quality or $HECq$, which is defined as the fraction of the jet's energy, at EM-scale, that is located in hadronic end-cap cells with quality greater than 4000. A high value of $HECq$ means there is poor average agreement with the reference signal, and hence the jet likely originated from a non-particle signal.

As discussed in Section 3.2.2, the translation of a signal to a cell energy can cause a negative value of energy to be reconstructed. This is more likely to occur for noisy cells, which receive a signal pulse that is very different in shape than that used to derive the optimal filtering coefficients. A large total energy originating from negative energy cells, denoted $negE$, is thus an indication that the jet was reconstructed due to cell noise.

Based on these observations, a jet is rejected from the measurement sample if:

- $HECf > 1 - HECq$, or
- $|negE| > 60$ GeV

The distribution of HEC fraction vs. HEC quality for jets that pass all other event and jet selection criteria is shown in Figure 4.11(a). The cut value is indicated by the red line. This cut isolates the jets with high HEC fraction and high HEC quality, in particular the pocket of clearly fake jets with HEC fraction and HEC quality greater than 0.8. The distribution of $negE$ as a function of calibrated jet p_T is shown in Figure 4.11(b), again for jets that pass all other selection cuts. This cut removes the few remaining jets with poorly-reconstructed signals that remain after the HEC fraction and HEC quality cut. As with all jet cleaning variables that will be shown as a function of p_T, the distribution is slightly discontinuous at $p_T = 60$ GeV due to the smaller data sample that is used to measure the low-p_T region.

Similar to jets caused by noise in the hadronic end-cap calorimeter, jets caused by noise in the EM calorimeter are likely to have a large fraction of their energy originating from one EM cell or from cells with poor quality. To quantify these effects, the variables EM

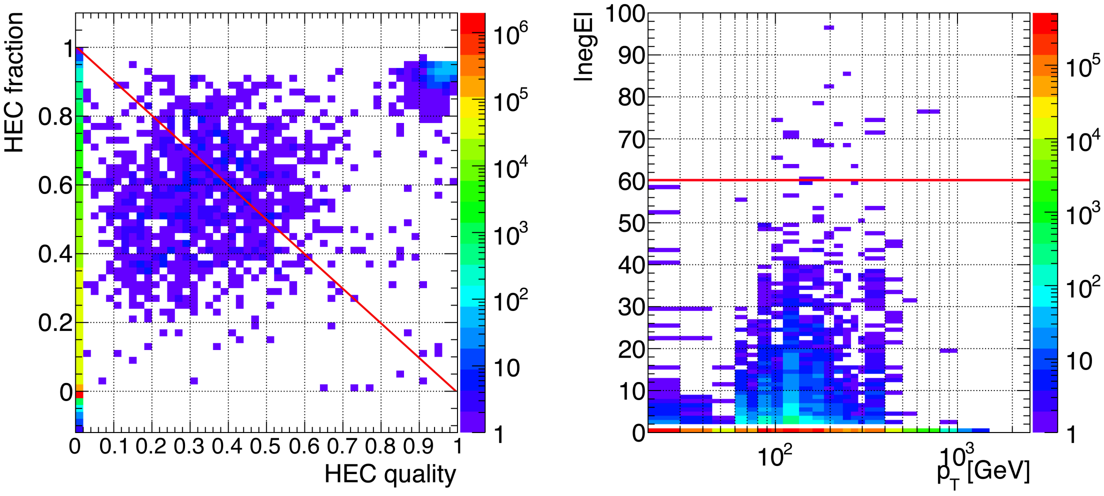

(a)

(b)

Figure 4.11: Distributions of HEC fraction vs. HEC quality (a) and negative energy (b) for $R = 0.6$ jets in the region $|\eta| < 4.4$ that pass all other event and jet selection. The cuts applied are indicated by the red lines.

fraction, or EMf, and LAr quality are defined analogously to the variables' HEC fraction and HEC quality. High energy jets in the forward region have cell signals that are not well modeled by the quality variable, so no cut is applied in this region.

To remove jets reconstructed from noise in the EM calorimeter, a jet is rejected if:

- $EMf > 0.9$ and $|\text{LAr quality}| > 0.8$ and $|\eta_{jet}| < 2.8$

The distribution of EM fraction vs. LAr quality for jets with $|\eta| < 2.8$ that pass all other selection criteria is shown in Figure 4.12. Analogous to the HEC fraction and HEC quality cut, this removes jets in the region of high EM fraction and high quality.

There are four variables that have been optimized to reject cosmic ray and beam background processes. The first is the jet time, which is the mean time with respect to the bunch crossing clock of the signals recorded in each cell of a jet, weighted by the squared energy of the cell. The arrival of cosmic rays and beam background events is uncorrelated to the collision time, so large jet times are an indication of non-collision signals.

The second variable is the charged fraction, or Chf, defined as the ratio of the sum of the p_T of the tracks pointing towards a jet to the calibrated jet p_T. Since the track reconstruction algorithms are designed to form tracks originating from the interaction point,

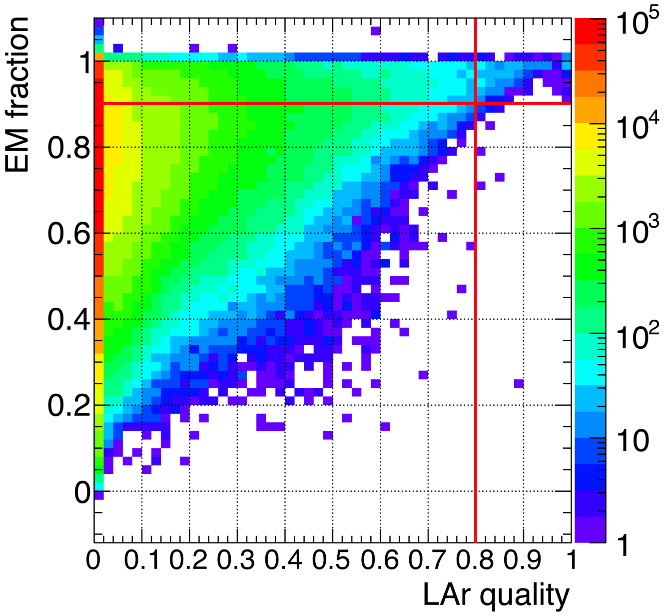

Figure 4.12: Distribution of EM fraction vs LAr quality for $R = 0.6$ jets in the region $|\eta| < 2.8$ that pass all other event and jet selection. The cuts applied are indicated by the red lines.

a cosmic muon passing through the inner detector will generally not have a corresponding reconstructed track, and thus a low charged fraction. Jets resulting from collision events, however, will generally have many tracks caused by the charged-particles of the hadronic shower, as seen in Figure 4.2.

The remaining two variables exploit the fact that cosmic ray and beam background events tend to deposit energy in just one sub-detector of the calorimeter system. Details of the detector in which the muon deposited its energy thus provide additional discriminating information. A cosmic muon will pass through many interaction lengths of the hadronic calorimeter before ever reaching the EM calorimeter. For this reason, it is more likely to undergo a bremsstrahlung interaction in the hadronic calorimeter, losing energy before ever reaching the EM calorimeter and resulting in jets with low EMf. If a muon does interact in the EM calorimeter, it will produce a jet which has almost no energy in the hadronic calorimeter and thus has a very high EMf. Beam background events can cause jets to be reconstructed out of energy deposited only in the presampler. The variable $Fmax$, or the maximum fraction of the jet energy at EM-scale that can be formed from just one calorimeter layer, is designed to remove these jets. Since the presampler only extends to $|\eta| = 1.8$, the cut is only applicable for jets with $|\eta| < 2$.

The optimized version of cuts to remove cosmic and beam background jets dictates to reject a jet if:

- $|\text{time}| > 10$ ns, or
- $EMf < 0.05$ and $Chf < 0.1$ and $|\eta| < 2$, or
- $EMf < 0.05$ and $|\eta| \geq 2$, or
- $EMf > 0.95$ and $Chf < 0.05$ and $|\eta| < 2$, or
- $Fmax > 0.99$ and $|\eta| < 2$

Distributions of EM fraction vs. charged fraction and EM fraction, $Fmax$, and time as a function of calibrated jet p_T are shown in Figures 4.13 and 4.14.

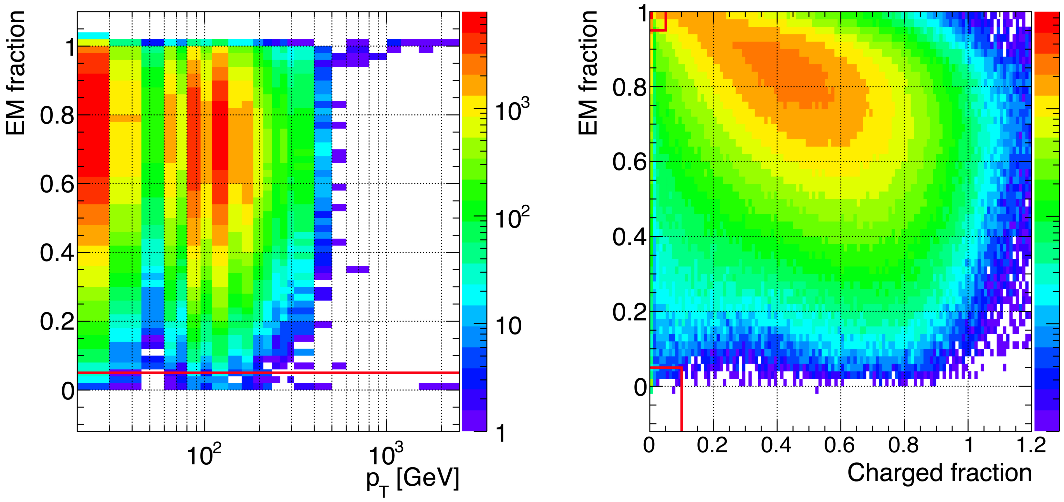

(a)

(b)

Figure 4.13: Distributions of EMF as a function of calibrated jet p_T (a) for $R = 0.6$ jets in the region $|\eta| \geq 2$ and EMF vs. charged fraction (b) for $R = 0.6$ jets in the region $|\eta| < 2$, both shown for jets that pass all other event and jet selection. The cuts applied are indicated by the red lines.

Many of the jet cleaning variables are poorly modeled in the Monte Carlo, so inefficiencies introduced by these cuts must be assessed in data. The jet cleaning efficiency has been studied in ATLAS *in-situ* using a tag-and-probe technique. A sample consisting of

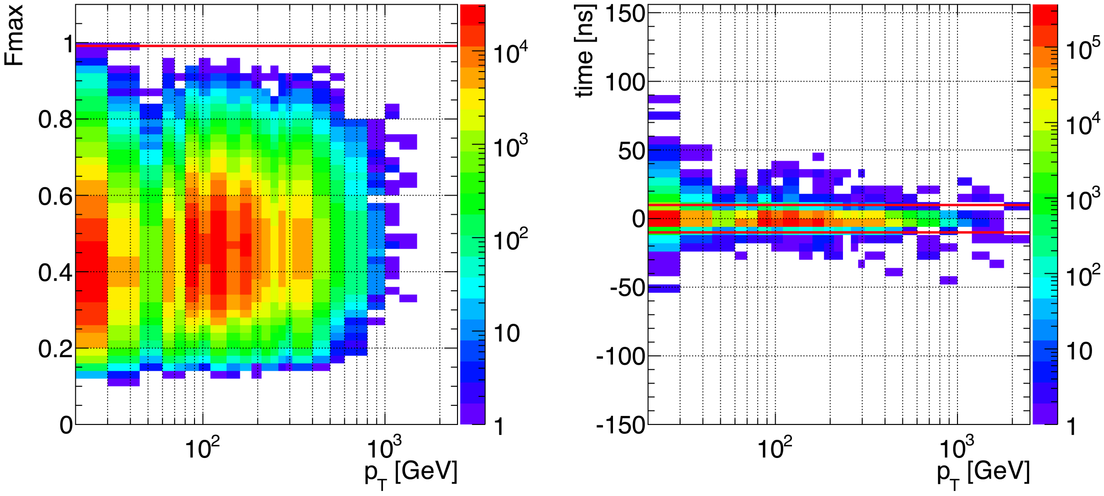

(a)

(b)

Figure 4.14: Distributions of $Fmax$ (a) for $R = 0.6$ jets in the region $|\eta| < 2$ and time (b) for $R = 0.6$ jets in the region $|\eta| < 4.4$, both shown for jets that pass all other event and jet selection. The cuts applied are indicated by the red lines.

real collision jets is assembled by requiring there be a tag jet within $|\eta| < 2$ that passes a tightened version of the cleaning cuts outlined above. A probe jet is identified that balances the tag jet in ϕ and p_T, according to $\Delta\phi > 2.6$ and $\frac{p_{T,1}-p_{T,2}}{p_{T,avg}} < 0.4$, where $p_{T,avg} = \frac{p_{T,1}+p_{T,2}}{2}$. The efficiency is then measured for this probe jet to pass the cleaning criteria, defined, in bins of p_T and η, as:

$$\text{efficiency} = \frac{\#\text{ of jets in this bin after all jet cleaning cuts}}{\#\text{ of jets in this bin before all jet cleaning cuts}} \tag{4.9}$$

For jets with $|\eta| < 2.1$, this efficiency is greater than 99% for jets with $p_T > 90$ GeV. The efficiency decreases below this point, with the lowest efficiency being $\sim 90\%$ for jets with $p_T < 30$ GeV in the region $0.8 \geq |\eta| < 1.2$. For jets with $|\eta| \geq 2.1$, the efficiency is everywhere greater than 99%.

Systematic uncertainties were derived by applying looser and tighter selections to the tag jet, and are found to be everywhere less than 2%. As an additional cross check on the method, the efficiency measured by applying this method to jets in Monte Carlo was compared to the efficiency measured as the fraction of Monte Carlo jets rejected by cleaning. Since Monte Carlo events have no noise spikes, cosmic rays, or beam background interactions, these two efficiencies should be the same. The result is an uncertainty on the method of less than 0.2%, well within the measured systematic uncertainties

These efficiencies are used to correct the measured jet p_T spectrum in regions where the efficiency is $< 99\%$. The systematic uncertainty on the efficiencies is used as an additional systematic uncertainty on the final jet cross section measurement.

In addition to the fake jets detailed above, there also exist jets whose energies are inherently poorly measured. Poor energy measurements result from the gap scintillators located between the barrel and end-cap tile calorimeters, as well as calorimeter cells that are flagged as "bad" and whose energy is extrapolated using the energy of their neighboring cells. A jet is removed from this data sample if has a high fraction of energy originating from the tile gap scintillators, TileGap3Frac, or from energy-corrected bad cells, BCH_CORR_CELL, according to:

- TileGap3Frac > 0.5, or
- BCH_CORR_CELL > 0.5

The distributions of TileGap3Frac and BCH_COR_CELL as a function of the calibrated p_T of the jet for jets that pass all other selection cuts are shown in Figure 4.15. The cut on BCH_COR_CELL removes a total of eight jets, none with a p_T greater than 300 GeV. The cut on TileGap3Frac removes 3573 jets, $\sim 0.1\%$ of the sample, but predominantly in the lowest p_T bins, which have abundant statistics and are most susceptible to large variations in energy due to isolated calorimeter problems. Because of the very small impact on the overall data sample, no correction is applied to account for these cuts.

Very occasionally, jets that clearly originate from noise bursts in the liquid argon calorimeters survive the jet cleaning criteria outlined above. These jets are then removed by the additional requirement that the "larError" flag for each event not be set to "Warning." This flag is set if at least six front-end electronics boards are found with at least 30 channels producing bad quality signals. This cut removes six additional jets from the data sample, all of which have been inspected in event displays and validated to be caused by noise bursts.

The number of measured jets as a function of jet p_T in the dataset used for this analysis is shown in Figure 4.16, both before and after applying the jet cleaning cuts. The uneven nature of the p_T spectrum is due to the combination of events from various trigger streams,

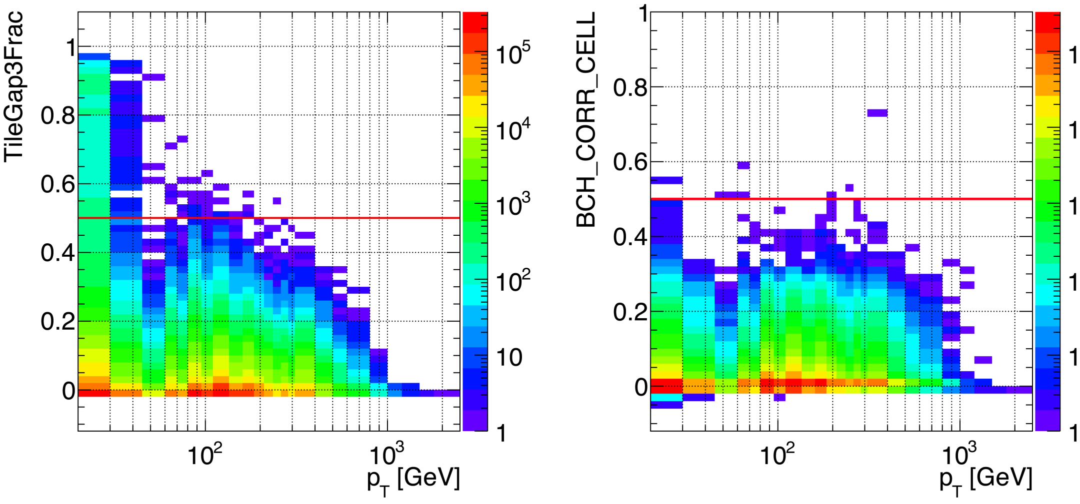

(a) (b)

Figure 4.15: Distributions of TileGap3Frac (a) and BCH_CORR_CELL (b) as a function of calibrated jet p_T for $R = 0.6$ jets in the region $|\eta| < 4.4$ that pass all other event and jet selection. The cuts applied are indicated by the red lines.

each with a varying prescale, as described in the following section. The cleaning procedure removes almost the full high-p_T tails of the jet p_T distributions, which in fact extend far beyond the 3.5 TeV kinematic limit. All high p_T jets, as defined by occupying the highest several occupied p_T bins in each y region of the measurement, that have been removed have been inspected in event displays and found to be fake. Very little effect is seen in the rest of the distribution, and the small inefficiencies at low p_T are corrected in the final measurement as described above.

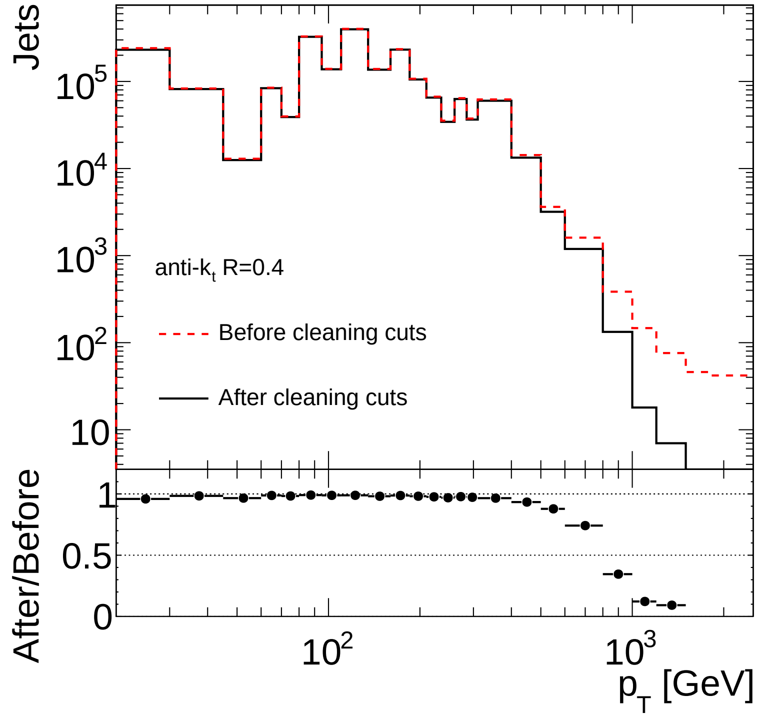

(a)

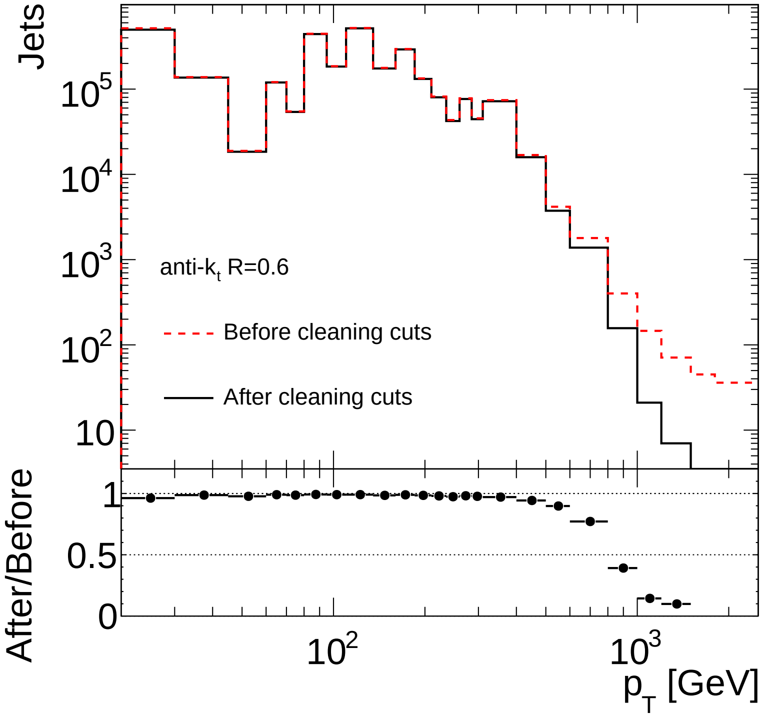

(b)

Figure 4.16: Measured jet p_T distribution before and after cleaning procedure, including all other event and jet selection, for $R = 0.4$ (a) and for $R = 0.6$ (b) jets with $|y| < 4.4$.

4.5 Trigger Combination

Jets are only recorded by ATLAS if the event passes a particular trigger requirement, known as a trigger item, as described in Section 3.2.5. Each trigger item has an associated rejection factor, known as a prescale, applied to events that satisfy the trigger requirement in order to control total trigger output rate. This prescale is defined for each trigger item in each luminosity block, and is in practice tuned during detector operation to ensure that the total trigger rates remain steady throughout the varying beam conditions of an ATLAS run. To derive a cross section measurement, which aims to describe the total number of produced jets, both the number of jets observed and the prescale that was applied to these jets must be known.

To ensure that the jets in each bin of the measurement are corrected by the proper prescale, only one trigger is used to select jets for each p_T and y bin for a given ATLAS run. This is true for jets in all regions *except* the region $2.8 \leq |y| < 3.6$, which is more complicated due to the fact that it overlaps with both the central and forward jet trigger regions and will be discussed in detail below. The prescale for all regions is then taken into account during the calculation of the luminosity that is used to normalize each p_T bin. Bins that are populated by triggers with higher prescale factors will have correspondingly lower effective luminosities, assuring that the cross section, $\sigma \propto N_{jets}/\mathcal{L}$, is properly scaled.

In this formulation, it is important to note that the ATLAS trigger system selects events to record, not individual jets. However, in the offline analysis, a particular trigger requirement is imposed on each jet, for the reasons described above. Throughout this discussion, when a jet is referred to as passing a trigger, this in fact means that the jet must be in an event that passed a trigger.

The choice of which trigger item to use for which p_T bin depends on the efficiency of each trigger, as well as its prescale. To avoid corrections for inefficient regions, which may be poorly-modelled in Monte Carlo and, due to available statistics, poorly-measured in data, each trigger is only used in regions where it is $> 99\%$ efficient. To maximize the statistical accuracy of the measurement, the trigger with the smallest prescale is chosen from the available fully-efficient triggers for each bin. Since, to control total trigger rates, triggers with lower E_T thresholds are more heavily prescaled than triggers with higher E_T thresholds, each bin is filled by the trigger with the highest E_T threshold that is fully-efficient across the entire bin.

The highest E_T, fully-efficient trigger that is available, however, varies according to which triggers were applied during the different stages of the 2010 run. Jet triggers were slowly commissioned throughout the year, with first only Level-1 triggers used to reject events in Periods A-F, and then Level-2 triggers becoming active for Periods G-I. The event filter was never used to enforce trigger decisions in 2010, but additional prescales could be applied at this level whenever the Level-2 trigger was active.

A combination of minimum bias, Level-1 jet, and Level-2 jet triggers are used to select the jets in this analysis. The utilized jet trigger items at Level-1, Level-2, and Event Filter are listed in Table 4.3. Each trigger item is identified by the trigger level it applies to, i.e. "L1" for Level-1, "L2" for Level-2, or "EF" for the Event Filter. The trigger items marked with "J" or "j" are central single-jet triggers, which cover the region $|\eta| \leq 3.2$, while those marked "FJ" or "fj" are forward single-jet triggers, which cover the region $|\eta| > 3.2$. After the central or forward jet trigger designation, the E_T threshold, in GeV, that is applied to jets is indicated. Throughout 2010, these thresholds were applied to the EM-scale jet energy, though rudimentary calibrations are possible within the various trigger levels and may be applied in the future. For example, "L1_J5" requires that the event have at least one Level-1 jet with an $E_T > 5$ GeV at EM-scale located within $|\eta| < 3.2$. Since no jet trigger decisions were applied by the Event Filter in 2010, items at this level are marked with the tag "jetNoEF".

In order for an event to pass a given Level-2 or Event Filter trigger, it must also pass the associated Level-1 trigger, including any prescale that was applied. The rows of Table 4.3 indicate the corresponding Level-1, Level-2, and Event Filter triggers, referred to as trigger chains. For example, in periods when the HLT was active, an event must pass L1_FJ10 and L2_fj25, with their prescales, in order to also pass EF_j30_jetNoEF. To ensure that high-p_T jets were never lost due to possible inefficiencies in the HLT, the two highest Level-1 thresholds, L1_J95 and L1_J115, never had additional HLT decisions or prescales applied, and hence have no corresponding Level-2 or Event Filter item.

The jets in this analysis with $p_T < 60$ GeV are only taken from Periods A-C, as described in Section 4.1.1. These jets are below the fully-efficient region of the jet triggers and are instead selected using signals generated by charged particles traversing the Minimum Bias Trigger Scintillators (MBTS). The particular trigger used, L1_MBTS_1, requires that

Level-1	Level-2	Event Filter
L1_J5	L2_j15	EF_j20_jetNoEF
L1_J15	L2_j30	EF_j35_jetNoEF
L1_J30	L2_j45	EF_j50_jetNoEF
L1_J55	L2_j70	EF_j75_jetNoEF
L1_J70	L2_j90	EF_j95_jetNoEF
L1_J95	n/a	n/a
L1_J115	n/a	n/a
L1_FJ10	L2_fj25	EF_j30_jetNoEF
L1_FJ30	L2_fj45	EF_j50_jetNoEF
L1_FJ55	L2_fj70	EF_j75_jetNoEF

Table 4.3: Corresponding Level-1, Level-2, and Event Filter trigger items. Items marked with "J" or "j" are central jet trigger items, while those marked with "FJ" or "fj" are forward jet trigger items. The label "_jetNoEF" indicates that no Event Filter decision was used to reject events. The Level-2 and Event Filter items were only available from Period G onwards.

a signal be recorded by at least one of these scintillators. Although the MBTS only covers the region $2.09 \leq |\eta| < 3.84$, the additional soft radiation that accompanies the production of jets ensures that this signal is fully-efficient for jets produced in any region of the detector [92]. This trigger had a low prescale during the initial, low-luminosity phase of ATLAS operation, and hence collected abundant statistics to populate the region $p_T < 60$ GeV and $|y| < 4.4$.

The MBTS trigger was also used to collect jets in all p_T ranges for all data taken before run 152777, consisting of only eight early runs. Before this run, poor timing within the L1Calo hardware caused large inefficiencies for all jet triggers. Jets collected from run 152777 onwards utilize the full set of available Level-1 jet triggers.

Before assigning triggers to select jets with $p_T \geq 60$ GeV, the efficiencies of each trigger must be measured. A trigger efficiency is generally defined as the probability to record an observable, such as an event, a muon at a certain η, a photon with a certain p_T, etc., given a particular trigger condition:

$$\text{efficiency} = \frac{\text{\# of observables that satisfy trigger requirement}}{\text{\# of observables}} \tag{4.10}$$

The observable of interest for the inclusive jet cross section measurement is a single jet in a bin of p_T and y. Therefore, the relevant efficiency is defined as:

$$\text{efficiency} = \frac{\#\text{ of jets in given } p_T \text{ and } y \text{ bin that satisfy trigger requirement}}{\#\text{ of jets in given } p_T \text{ and } y \text{ bin}} \tag{4.11}$$

This efficiency, referred to in the following as the inclusive jet trigger efficiency, is equivalent the ratio of the jet p_T spectra composed without any trigger selection to the jet p_T spectra composed from jets that pass the trigger selection. In Monte Carlo events, it is straightforward to define the jet spectra before trigger selection. In data, however, events are only recorded that pass some trigger requirement, so care must be taken to define an unbiased sample for measuring the efficiency.

The inclusive jet trigger efficiency is measured for each jet trigger used, in each measured bin of rapidity, using a combination of orthogonal and bootstrap methods. In the orthogonal method, an independent trigger, such as a minimum bias or muon trigger, is used to select jets to fill the denominator of the efficiency. The numerator is then defined as the subset of these jets that pass the given jet trigger requirement. In the bootstrap method, a jet trigger with a lower E_T threshold is used to select jets to fill the denominator of the efficiency for a higher E_T threshold. The numerator, again, is defined as the subset of these jets that pass the higher E_T threshold. The total efficiency is then the product of this efficiency and the efficiency for the lower E_T threshold trigger. The choice of lower threshold trigger used in the bootstrap method is driven by which trigger streams will yield sufficient statistics, after prescales, to perform an accurate efficiency measurement.

The inclusive jet trigger efficiencies for the various Level-1 and Level-2 jet trigger items are shown in Figure 4.17, for $R = 0.6$ jets in the region $0 \leq |y| < 0.3$. The Level-1 efficiencies are measured in the periods when only Level-1 decisions were used to reject events, Periods A-F. The L1_J5 and L1_J15 efficiencies were measured with respect to the orthogonal trigger L1_MBTS_1. The remaining efficiencies were measured using the bootstrap technique, with L1_J30 and L1_J55 measured with respect to L1_J5; L1_J75 with respect to L1_J15; L1_J95 with respect to L1_J30; and L1_J115 with respect to L1_J55. In all of these bootstrap measurements, the higher-threshold trigger is assessed in the region where the lower threshold trigger is already greater than 99% efficient.

The Level-2 efficiencies are measured in Periods G-I, and are defined as the efficiency to satisfy both the Level-2 and corresponding Level-1 trigger decision. For these efficiencies, L2_j30 and L2_j45 were bootstrapped from L2_j15, and L2_j70 and L2_j90 were bootstrapped from L2_j30. The lowest threshold Level-2 jet trigger, L2_j15, is not shown, since the minimum bias stream was heavily prescaled in the periods when the Level-2 triggers were active, and thus there are not sufficient statistics to make a precise measurement from an orthogonal trigger stream. However, since the same energy calibration is applied to all jets at Level-2, and the point at which the Level-2 triggers reach $> 99\%$ efficiency is only offset by a few GeV for the L2_j30 trigger with respect to its corresponding Level-1 trigger, it is safe to assume the L2_j15 plateaus a few GeV past where L1_J5 reaches its full efficiency.

These data measurements were compared to efficiencies measured in Monte Carlo events, and, though discrepancies exist below the full-efficient regions, each point of $> 99\%$ efficiency found in data is consistent with that found in Monte Carlo.

It may be surprising to note that the lowest threshold Level-1 jet trigger, which applies a nominal threshold of 5 GeV at EM scale, does not become fully-efficient until almost 45 GeV of calibrated jet energy. If this difference were purely due to the jet energy calibration and jet energy resolution smearing, the efficiency should rise above 99% by ~15 GeV, far below the measured turn-on region. In fact, this difference is due to a complicated set of factors, in addition to the jet energy scale. First, the "EM scale" calibration applied at Level-1 is not the same as the offline EM scale calibration. Instead, the energy at Level-1 is measured in units of ADC counts, with one ADC count corresponding to 280 MeV, which then are roughly translated into an EM-scale measurement. This rough calibration affects the trigger efficiencies for all the available jet triggers. Secondly, the size of the jets used to assess L1_J5 are $\eta \times \phi = 0.4 \times 0.4$, which is smaller than the offline jet size. This implies that the amount of energy falling in the Level-1 jet will be smaller than the energy clustered into the offline jet, and hence the trigger will not be fully efficient until higher values of offline jet p_T. One might naively ask why the E_T threshold applied is not simply lowered or why a larger jet size is not used at Level-1, in order to improve the efficiency. Unfortunately, significantly lowering the threshold or expanding the jet size would cause noise rates that would quickly overwhelm the Level-1 readout.

Analogous to the jet reconstruction efficiency, the jet trigger efficiency for $R = 0.4$ jets is in general higher than that for $R = 0.6$ jets at the same p_T. This is due to the smaller jet size having a correspondingly smaller reconstructed jet energy, meaning that the same measured efficiency corresponds to a lower p_T. Also analogous to the jet reconstruction

p_T range	Period A*-F	Period G-I
60-80	L1_J5	EF_j20_jetNoEF
80-110	L1_J15	EF_j35_jetNoEF
110-160	L1_J30	EF_j50_jetNoEF
160-210	L1_J55	EF_j75_jetNoEF
210-260	L1_J75	EF_j95_jetNoEF
260-310	L1_J95	L1_J95
310+	L1_J95	L1_J115

Table 4.4: Triggers used to select jets in the region $|y| < 2.8$, *excluding* $1.2 \leq |y| < 2.1$, in each p_T bin of the measurement. Period A* refers to runs in Period A from run 152777 onwards. Jets with $p_T < 60$ GeV are all selected by the minimum bias trigger L1_MBTS_1 in Periods A-C only.

efficiency, jets in more forward η regions will be have a higher efficiency than jets in the central η regions for the same p_T. This is due to the fact that at higher η, more energy is required to reach the same p_T, and this higher energy is more likely to pass a given E_T threshold. The inclusive jet trigger efficiencies for both jet sizes and for all rapidity regions are included in Appendix A.

An exception to the general rule that jets in forward regions have higher trigger efficiencies occurs in the region $1.2 \leq |y| < 2.1$, as shown in Figure 4.18. The trigger efficiencies in this region do not become fully efficient until a higher calibrated p_T point than in the central region, due to larger difference between EM scale and calibrated p_T for jets in this region, and because the gap and inter-cryostat scintillators, which improve energy measurements in this region, are not part of the L1Calo trigger towers.

The assignment of a central single-jet trigger to each p_T region is shown for jets in the regions $|y| < 1.2$ and $2.1 \leq |y| < 2.8$ in Table 4.4. Since the efficiencies are slightly worse for jets in the region $1.2 \leq |y| < 2.1$, a different scheme is used, as shown in Table 4.5. For each range of p_T, care was taken to ensure that only triggers with efficiency $> 99\%$ are used, including an extra safety factor to account for the jet energy scale uncertainty in assigning the p_T efficiency point. Although no decision was applied by the Event Filter during 2010, additional prescales were applied at this level, so the Event Filter trigger corresponding to the fully efficient Level-2 trigger is used to select jets in the Periods G-I.

In the region $|\eta| > 3.2$, forward jet triggers apply. Due to miscalibrations of the timing of the forward jet triggers before run 161118, no jets with $p_T > 60$ GeV are used from periods before this run. The inclusive jet forward trigger efficiencies, measured after the

p_T range	Period A*-F	Period G-I
60-80	L1_J5	EF_j20_jetNoEF
80-110	L1_J5	EF_j20_jetNoEF
110-160	L1_J15	EF_j35_jetNoEF
160-210	L1_J30	EF_j50_jetNoEF
210-260	L1_J55	EF_j75_jetNoEF
260-310	L1_J75	EF_j95_jetNoEF
310-400	L1_J95	L1_J95
400+	L1_J95	L1_J115

Table 4.5: Triggers used to select jets in the region $1.2 \leq |y| < 2.1$, in each p_T bin of the measurement. Period A* refers to runs in Period A from run 152777 onwards. No jets are selected from Period E before run 16118. Jets with $p_T < 60$ GeV are all selected by the minimum bias trigger L1_MBTS_1 in Periods A-C only.

p_T range	Period E*-F	Period G-I
60-80	L1_FJ10	EF_fj30_jetNoEF
80-110	L1_FJ30	EF_fj30_jetNoEF
110-160	L1_FJ55	EF_fj50_jetNoEF
160+	L1_FJ55	EF_fj75_jetNoEF

Table 4.6: Triggers used to select jets in the region $3.6 \leq |y| < 4.4$, in each p_T bin of the measurement. Period E* refers to runs in Period E from run 161118 onwards. Jets with $p_T < 60$ GeV are all selected by the minimum bias trigger L1_MBTS_1 in Periods A-C only.

timing improvements, are shown in Figure 4.19 for $R = 0.6$ jets with $3.6 \leq |y| < 4.4$. For the Level-1 efficiencies, each trigger is measured with respect to the previous, fully-efficient trigger, with the lowest threshold trigger measured with respect to the minimum bias trigger. These measurements utilize data from Periods A-F, when only the Level-1 trigger was active. Data collected when the Level-2 trigger was active suffers from poor statistics due to heavy prescales. Thus, efficiencies for the Level-2 triggers are measured by reconstructing a Level-2 decision in Period F data. In this scheme, the event passes the Level-2 trigger if there exists a Level-2 jet with E_T above the trigger's threshold that matches a Level-1 Region of Interest with E_T above the corresponding Level-1 threshold. An additional complication occurs due to the presence of one one dead trigger tower on one side of the forward calorimeter. However, as can be seen in Figure 4.19, this has minimal effect on the trigger efficiency since there is frequently another jet in the event that causes the trigger to be satisfied. The final selection of trigger chains used to fill each p_T bin in each period of data taking is shown in Table 4.6.

p_T range	Period E*-F	Period G-I
60-80	L1_J10 or L1_FJ10	n/a
80-110	L1_J10 or L1_FJ10	L1_FJ_30 or EF_fj30_jetNoEF
110-160	L1_J30 or L1_FJ30	EF_j50_jetNoEF or EF_fj50_jetNoEF
160-210	L1_J55 or L1_FJ55	EF_j50_jetNoEF or EF_fj50_jetNoEF
210+	L1_J55 or L1_FJ55	EF_j75_jetNoEF or EF_fj75_jetNoEF

Table 4.7: Triggers used to select jets in the region $2.8 \leq |y| < 3.6$, in each p_T bin of the measurement. Period E* refers to runs in Period E from run 16118 onwards. Jets with $p_T < 60$ GeV are all selected by the minimum bias trigger L1_MBTS_1 in Periods A-C only.

For jets falling near the $|\eta| = 3.2$ boundary between forward and central jet triggers, no one trigger alone is fully-efficient in a given p_T bin. Instead, jets are required to satisfy a logical "OR" of two triggers, one central and one forward, in order to provide a selection that is $> 99\%$ efficient. The efficiency for $R = 0.6$ jets with $2.8 \leq |y| < 3.6$ to pass either of the two chosen triggers is shown in Figure 4.20. Here, the efficiency for each trigger combination was bootstrapped from events that passed either of the corresponding lower-E_T central or forward jet triggers, with the lowest E_T threshold combination measured with respect to the minimum bias trigger. The Level-2 efficiencies are assessed by reconstructing the Level-2 decision, as was done for the Level-2 efficiencies in the region $3.6 \leq |y| < 4.4$

The triggers used to select jets with $2.8 \leq |y| < 3.6$ in each p_T range are listed in Table 4.7. For jets with $60 \leq p_T < 80$ GeV, no set of Level-2 triggers is safely efficient, and so no data from Periods G-I are used. The use of more than one trigger to populate a single p_T bin leads to complications in accounting for the proper prescale factor during the luminosity calculation, as will be discussed in the following section.

Very occasionally, an event will require a longer processing time to evaluate a particular trigger item than the time allocated to the HLT. These events are stored in a separate "debug" trigger stream, which is re-processed offline to formulate a proper HLT decision. Of the ∼40,000 events in the "debug_hltacc" trigger stream, 931 $R = 0.6$ jets and 823 $R = 0.4$ jets are found that pass all event and jet selection. The p_T spectrum of these $R = 0.6$ jets in each rapidity bin is shown in Figure 4.21. Approximately one-third of these events were studied in detail, revealing that the dominant cause of time-out was a large amount of activity in the muon system due to very high-energy jets that penetrate through the transition regions from barrel to extended barrel or extended barrel to the end-cap calorimeters. These are thus valid jet events and are included into the jet cross section measurement. This inclusion is important since, although the total number of jets from the debug stream is relatively small, jets from the debug stream constitute up to 10% of the total number of jets in the highest p_T bins.

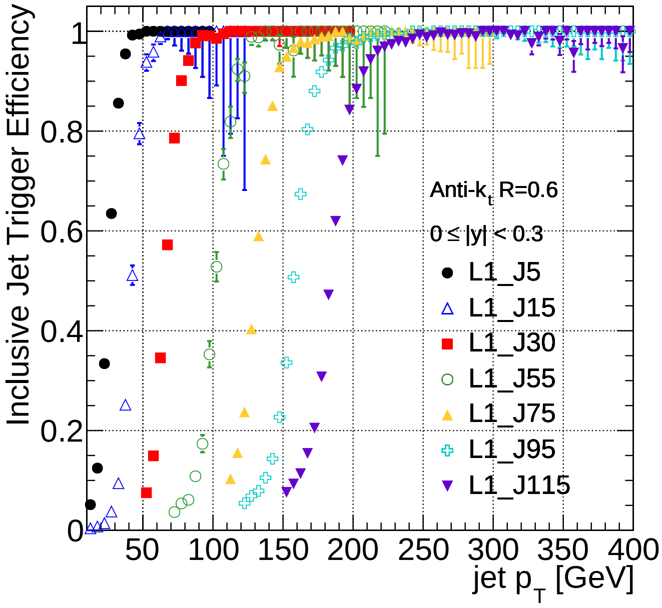

(a)

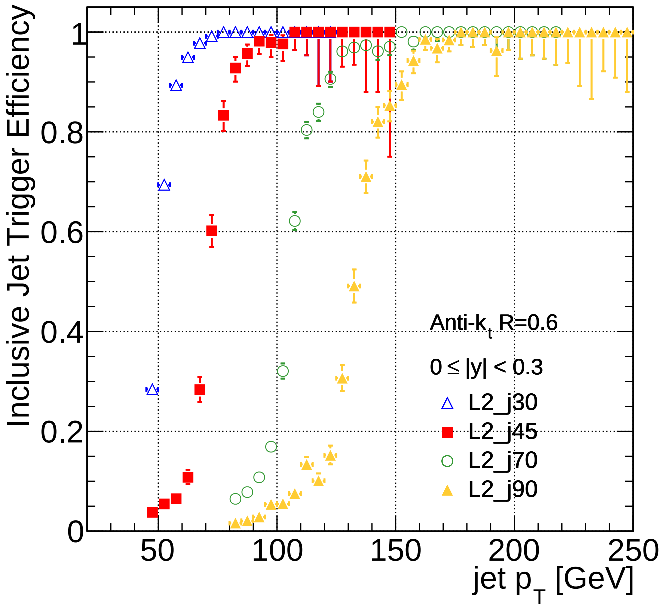

(b)

Figure 4.17: Inclusive jet trigger efficiencies for $R = 0.6$ jets in the region $0 \leq |y| < 0.3$, shown for the Level-1 (a) and Level-2 (b) jet trigger items used for this analysis.

.

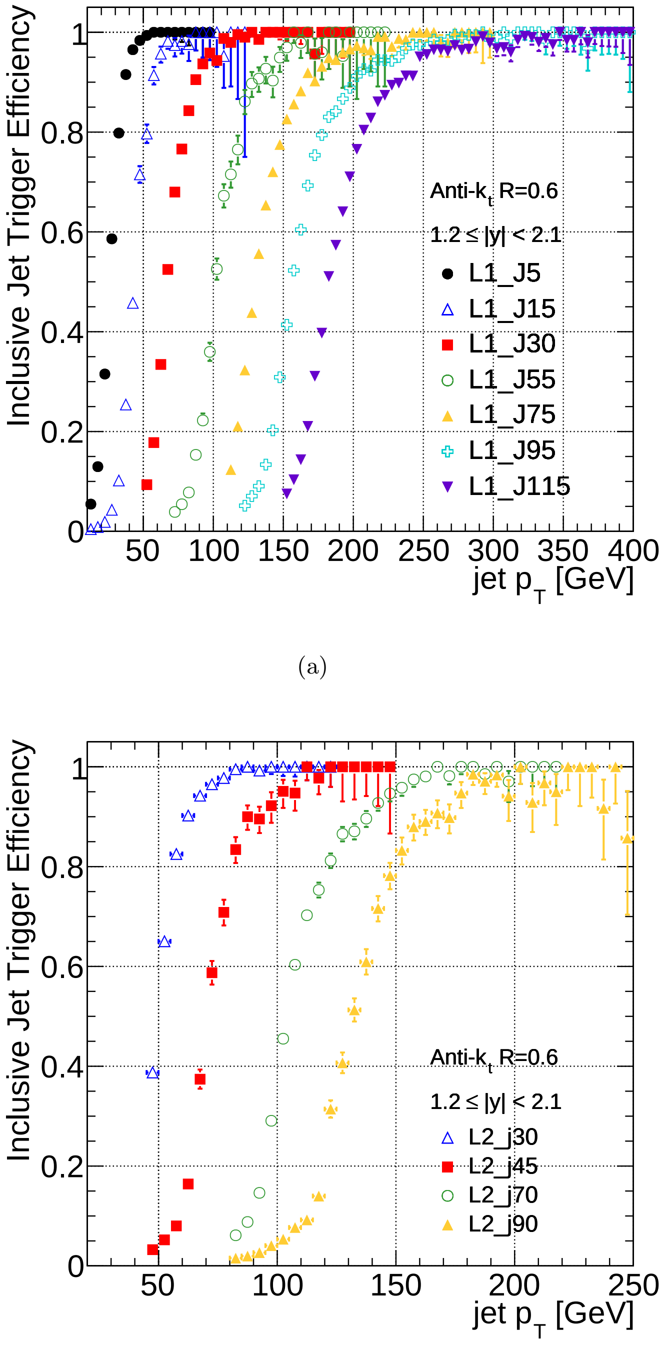

(a)

(b)

Figure 4.18: Inclusive jet trigger efficiencies for $R = 0.6$ jets in the region $1.2 \leq |y| < 2.1$, shown for the Level-1 (a) and Level-2 (b) jet trigger items used for this analysis.

.

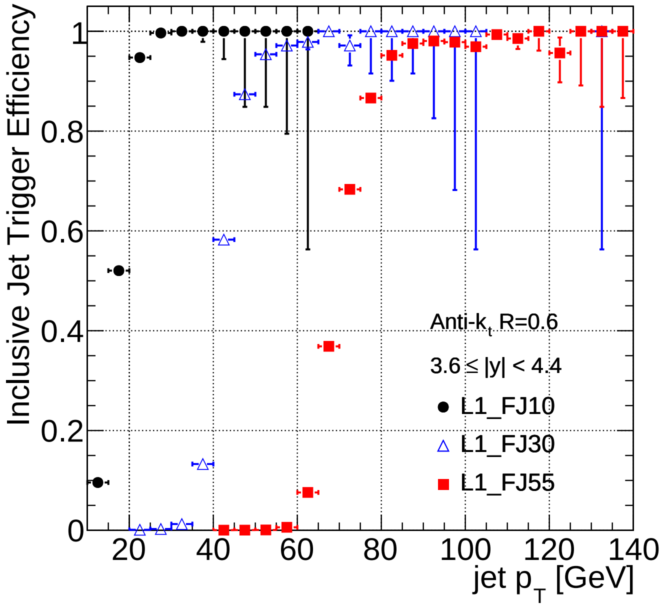

(a)

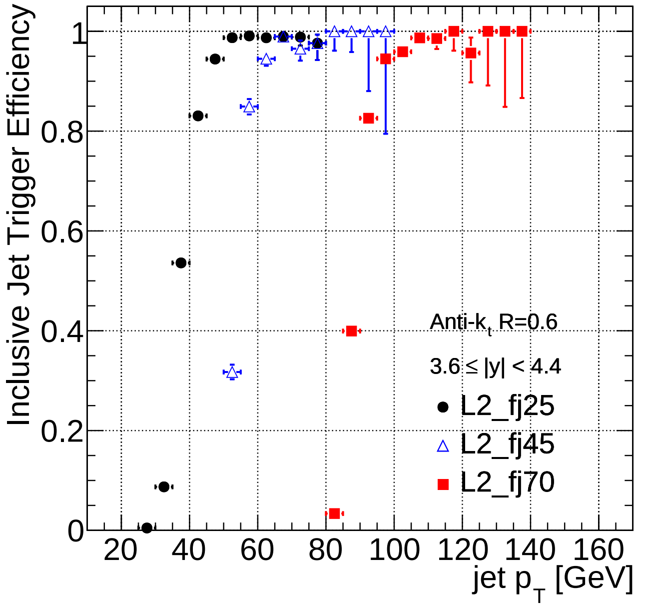

(b)

Figure 4.19: Inclusive jet trigger efficiencies for $R = 0.6$ jets in the region $3.6 \leq |y| < 4.4$, shown for the Level-1 (a) and Level-2 (b) jet trigger items used for this analysis.

.

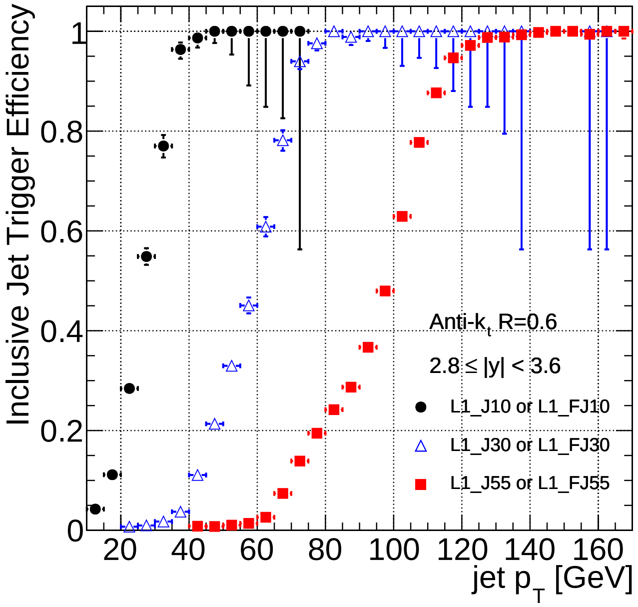

(a)

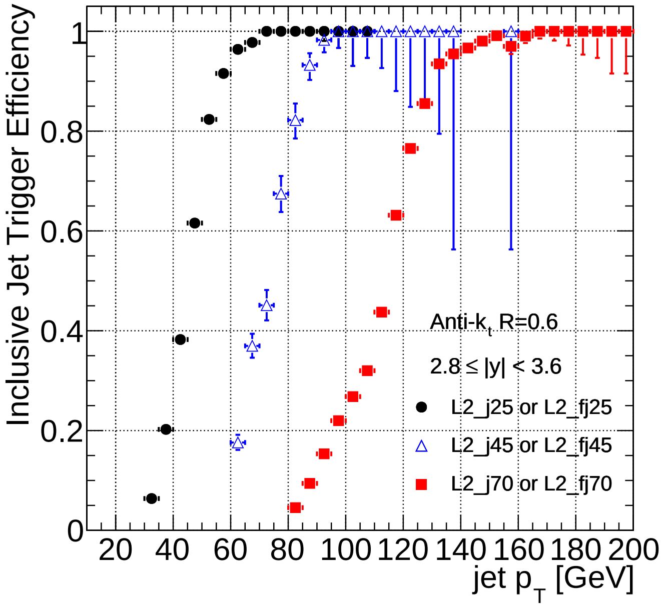

(b)

Figure 4.20: Inclusive jet trigger efficiencies for $R = 0.6$ jets in the region $2.8 \leq |y| < 3.6$, shown for the Level-1 (a) and Level-2 (b) jet trigger items used for this analysis.

.

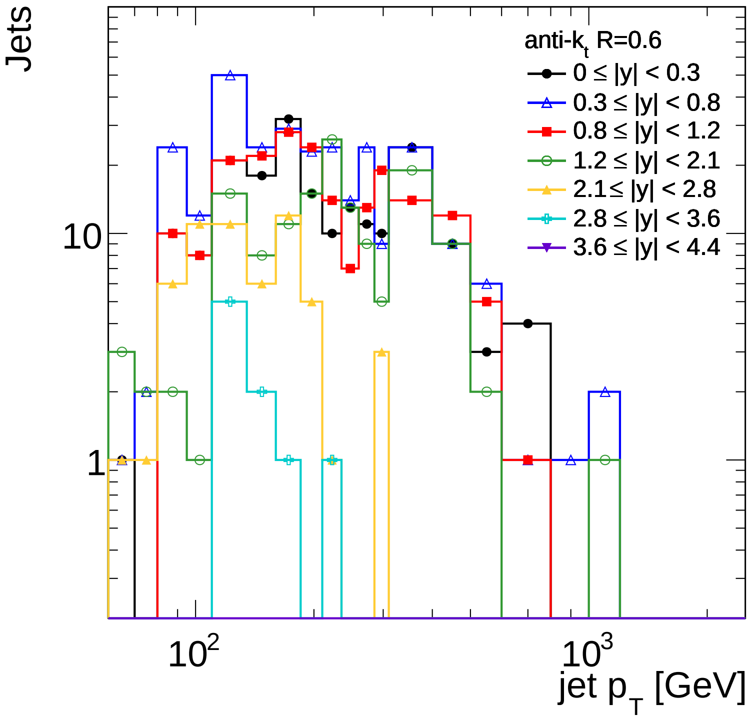

Figure 4.21: Number of $R = 0.6$ jets from the "debug_hltacc" trigger stream that pass all jet and event selection, shown for each rapidity bin of the measurement.

4.6 Luminosity Calculation

The instantaneous luminosity of proton-proton collisions is given by

$$\mathcal{L} = \frac{\mu n_b f_r}{\sigma_{inel}}, \tag{4.12}$$

where μ is the average number of interactions per bunch crossing, n_b the number of colliding bunches per beam, f_r the frequency of rotation, and σ_{inel} is the total inelastic cross section for proton-proton collisions. At the Tevatron, σ_{inel} was given by Monte Carlo simulations, and the instantaneous luminosity was derived by measuring μ. At the LHC, however, Monte Carlo simulations poorly models the interaction rate at the unprecedented center-of-mass energy of 7 TeV, and this method yields uncertainties on the luminosity calculation of up to 20%.

To provide more precise luminosity estimates, ATLAS instead combines measurements made by a complementary group of luminosity detectors, described in Section 3.2.4 and throughout Section 3.2, with a calibration derived from runs taken with specific beam parameters [93] [94]. The luminosity is estimated from the observed interactions in these detectors using the following equation, analogous to Equation 4.12:

$$\mathcal{L} = \frac{\mu^{meas} n_b f_r}{\sigma_{vis}} \tag{4.13}$$

Here, μ^{meas} is the measured average number of interactions per bunch crossing measured by one of the luminosity detectors, and σ_{vis} is the visible cross section, which is the product of the efficiency of this detector and total σ_{inel}.

This σ_{vis}, also known as the detector normalization, is determined *in-situ* using measurements of the beam conditions. This exploits the equivalence between the luminosity defined by Equation 4.13 and that determined purely from beam parameters, given by:

$$\mathcal{L} = \frac{n_b f_r I_1 I_2}{2\pi \sigma_x \sigma_y} \tag{4.14}$$

Here, I_1 and I_2 are the bunch currents, or the number of protons in each bunch of each beam, and σ_x and σ_y are the widths of the beams in x and y. These widths are determined during sets of Van der Meer scans [63], in which the two beams are swept across one another in the transverse plane in steps of separation. The rate of interactions produced by the crossing beams, as measured by one of the ATLAS luminosity detectors, is recorded for each step. Figure 4.22 shows the interaction rate as measured with the LUCID_EventOR algorithm, which counts the number of events that have at least one hit on either side ($+z$ or $-z$) of the LUCID detector. The beam width in the direction of separation is then defined as the standard deviation of a gaussian fit to this distribution.

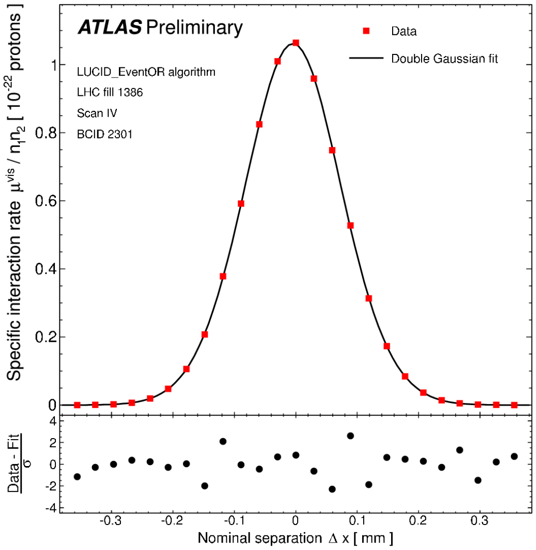

Figure 4.22: Interaction rate measured by the LUCID_EventOR algorithm as a function of beam separation [94]. This interaction rate is normalized to the product of the charges in each bunch of each beam ($n_1 n_2$), measured in units of (10^{11} protons)^2. The bottom panel illustrates the residual deviation of the data from the fit.

The normalization for each detector can then be extracted from the luminosity given by Equation 4.14 by noting that the maximum observed interaction rate, R_{MAX}, is related to the maximum luminosity, i.e. that at zero beam separation, by $R_{MAX} = \sigma_{vis}\mathcal{L}_{MAX}$. Therefore,

$$\sigma_{vis} = \frac{R_{MAX}}{\mathcal{L}_{MAX}} = R_{MAX}\frac{2\pi\sigma_x\sigma_y}{n_b f_r I_1 I_2} \tag{4.15}$$

This detector normalization can then be used in Equation 4.13 to provide an estimate of the instantaneous luminosity given any observed rate of interactions.

The main detector algorithm used for the luminosity determination of the 2010 dataset was the LUCID_eventOR algorithm, as described above. This was chosen because it can operate with high instantaneous luminosities, is independent of any malfunctions in the

ATLAS data acquisition system, and has a low background rate. Other detector algorithms, such as coincidence counting in the Minimum Bias Trigger Scintillators, counting of events with reconstructed vertices, or counting of events observed by the BCM, were used as cross checks for the luminosity obtained with LUCID.

The total systematic uncertainty on the luminosity obtained from the above procedure is 3.4% [94]. The dominant component of this uncertainty comes from the uncertainty in the amount of charge for each bunch used to determine σ_{vis}, which contributes 3.1%. This uncertainty is due to ambiguities in the calibration of the bunch current monitors. Other sources of uncertainty include possible transverse correlations between the estimated beam widths, such as would occur if the beams were ellipsoid in shape, the possible growth in beam size through a run, and the possible dependence of μ^{meas} on the total rate of proton-proton interactions.

During normal ATLAS operation, the luminosity is determined about once per second. The total integrated luminosity is then recorded for every luminosity block of an ATLAS run. The final luminosity used in any analysis, though, depends on the trigger that is used to select events and its associated prescale. An offline luminosity calculator is therefore used to correct the total luminosity for the prescale of a given trigger, as well as any dead time of the data acquisition system. This returns an effective luminosity, defined as:

$$\mathcal{L}_{eff} = \sum_{LB} \frac{\mathcal{L}_{LB}}{PS_{LB}^{trig}}, \tag{4.16}$$

where $\mathcal{L}_{LB}$ is the luminosity for a given luminosity block (LB), as determined by Equation 4.13 excluding any dead time of the data acquisition system, and PS_{LB}^{trig} is the prescale of a given trigger in the same luminosity block. For periods when the HLT was active, PS_{LB}^{trig} is the product of the prescales applied at Level-1, Level-2, and Event Filter. Since a new luminosity block is started anytime a trigger prescale is adjusted, this correctly takes into account all prescales used over a set of runs.

The luminosity calculation for most bins of the inclusive jet cross section measurement is straightforward, since only one trigger is used to fill each bin of p_T and y. Jets in the region $2.8 \leq |y| < 3.6$, however, could have passed either the appropriate forward jet trigger or the corresponding central jet trigger (see Section 4.5), each having a different prescale. The luminosity for the bins in this region is calculated by separating the jets in each bin into three categories: those from events that passed only the central jet trigger, those from events that passed only the forward jet trigger, and those from events that passed both central and forward jet triggers. The effective luminosity for the jets that pass only the central or the forward jet trigger is then given by Equation 4.16. The effective luminosity for jets that pass both the central and the forward trigger is derived by noting that the probability for an event to pass the prescale of at least one of N_{trig} different trigger items, given that the event passed the trigger decision, is:

$$P = 1 - \Pi_{i=1}^{N_{trig}}(1 - \frac{1}{PS^{trig}}). \tag{4.17}$$

For our case, in which there are only two prescaled trigger items for each bin, this simplifies to

$$P = \frac{PS^J + PS^{FJ} - 1}{PS^J PS^{FJ}}, \tag{4.18}$$

where PS^J is the prescale of the central jet trigger and PS^{FJ} is the prescale of the forward jet trigger. Normalizing the luminosity for jets in events that satisfy both central and forward triggers by this probability yields:

$$\mathcal{L}_{eff} = \sum_{LB} \frac{\mathcal{L}_{LB}}{PS^J_{LB} PS^{FJ}_{LB}/(PS^J_{LB} + PS^{FJ}_{LB} - 1)}. \tag{4.19}$$

The cross section for jets in the region $2.8 \leq |y| < 3.6$ is then given by the sum of the three categories, each normalized by the appropriate effective luminosity.

The effective luminosity used for each p_T bin in the regions $0 \leq |y| < 0.3$ is shown in Figure 4.23(a), demonstrating the lower effective luminosity that is assigned to bins filled by highly-prescaled low-E_T triggers. The effective luminosities computed for each of the three categories of jet in region $2.8 \leq |y| < 3.6$ is shown in Figure 4.23(b).

4.7 Detector Unfolding

To allow direct comparison with measurements made using different detectors, and to allow comparison with theoretical predictions that may be developed in the coming years, the inclusive jet cross section measurements are corrected for all detector effects to yield particle-jet cross sections. The correction procedure must account for detector efficiencies and

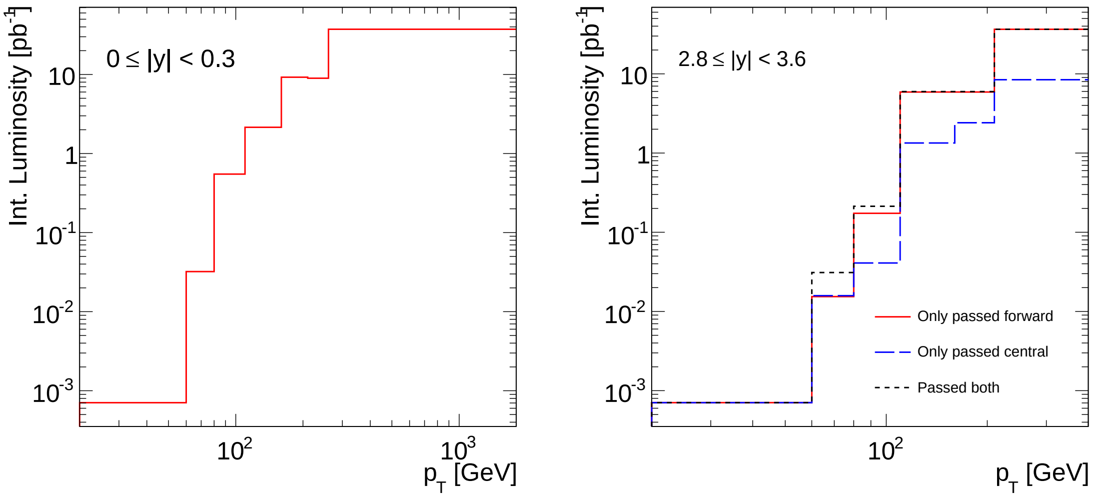

(a)

(b)

Figure 4.23: Effective luminosities used to normalize the measured jet p_T distributions for jets in the region $0 \leq |y| < 0.3$ (a) and for the three categories of jets, described in the text, in the region $2.8 \leq |y| < 3.6$ (b).

resolutions, such as the jet reconstruction efficiency, the jet p_T resolution, and the jet angular resolution, but not the jet trigger efficiency, as each trigger is used in a region where it is >99% efficient. This process is known as unfolding or deconvolution.

Unfolding attempts to determine a true distribution, $f(x)$, given a measured distribution, $g(y)$, that is related to $f(x)$ via:

$$g(y) = \int R(y,x) f(x) dx \tag{4.20}$$

Here, $R(x,y)$ accounts for the inefficiencies and resolution smearing that are induced by the detector measurement. In practice, only a finite number of measurements exist, usually in bins of the measured quantity y, such that Equation 4.20 corresponds to

$$\boldsymbol{y} = R\boldsymbol{x}, \tag{4.21}$$

where $\boldsymbol{y}$ is the vector representing the measured histogram, $\boldsymbol{x}$ is the vector representing the true histogram, and R is the matrix that contains the information of how the true quantities in $\boldsymbol{x}$ are altered by detector effects to produce the measured quantities. R is known as the response or transfer matrix, with, in the case of the jet cross section, element R_{ij} reflecting the probability to measure a jet in bin i given that the true jet occurs in bin j.

The problem of unfolding would then appear to consist merely of inverting this response matrix and applying it to the measured histogram. However, complications arise due to the lack of precise knowledge of the true distribution x. In most applications, R is determined from Monte Carlo simulations that model as accurately as possible the relationship between the underlying true distribution and the reconstructed distribution. Additional complications then arise due to the limited statistical precision of the produced Monte Carlo.

The various unfolding techniques typically applied then vary in how they combine the detector effects as modeled in Monte Carlo and the limited measurement statistics to estimate the underlying true distribution. One of the most straightforward techniques is to define a correction factor that is applied to each bin of the measurement. In the inclusive jet cross section analysis, this correction factor is defined as the ratio of the Monte Carlo cross section of the particle-level truth jets, in each bin of p_T and rapidity, to the Monte Carlo reconstructed jet cross section, in the same bin of p_T and rapidity. Assuming that the same events are used to construct both true and reconstructed cross sections, any normalization factors in the cross sections cancel, and this can be written in terms of the number of truth or reconstructed jets in a given bin as:

$$C = \frac{N^{MC}_{truth}}{N^{MC}_{reco}}. \tag{4.22}$$

The final estimated number of truth jets estimated by data in a given bin is then given by:

$$N^{est}_{truth} = C \cdot N^{data}_{reco}. \tag{4.23}$$

This method, known as bin-by-bin unfolding, is conceptually equivalent to projecting the response matrix onto only diagonal elements.

The bias of this unfolding method, defined as the difference between the truth estimated from data, $N^{est,data}_{truth}$, and the actual truth, N_{truth}, is then:

$$\text{bias} = (\frac{N^{MC}_{truth}}{N^{MC}_{reco}} - \frac{N_{truth}}{N^{data}_{reco}})N^{data}_{reco} \tag{4.24}$$

This bias, rather than depending solely on the size of the correction factors or the absolute difference between number of jets in data and in Monte Carlo, instead depends directly on the relation between the reconstructed and the truth spectra in Monte Carlo and that in data. The bias is thus affected by anything that changes the modeling of this relation in Monte Carlo. The effects of differing p_T resolution and spectrum shape are particularly important for the inclusive jet cross section measurement, where the cross section distribution falls very steeply across p_T. For any given bin, the much higher number of jets in lower-p_T neighboring bins than in higher-p_T neighboring bins means that more jets are transfered by jet energy resolution smearing into the bin from low p_T than out of the bin to low p_T. This leads to an overall shift of the spectrum to higher p_T values, with any slight changes in either the shape of the distribution or the size of the resolution affecting the amount of shift.

The effect of any bias in the bin-by-bin unfolding procedure is to pull the final result towards the Monte Carlo distribution. For example, if $N^{MC}_{truth}/N^{MC}_{reco} > N_{truth}/N^{data}_{reco}$, the overall bias will be positive, effectively pulling the estimated truth distribution closer to the higher values predicted by the Monte Carlo. Thus the impact of any biases must be evaluated and assigned as systematic uncertainties on the bin-by-bin unfolding correction factors.

Another concern in assessing the unfolding performance is the existence of large fluctuations between bins in the final unfolded spectrum caused by large variances in the correction factors. These large variances could be caused by large off-diagonal elements in the response matrix that are not correctly accounted for in the bin-by-bin method. This problem is largely avoided by using p_T bin sizes that are everywhere at least twice as large as the value of the p_T resolution, with the boundaries of the bins still dictated by the available triggers, as described in Section 4.5. The p_T resolution varies from ∼25% at $p_T = 20$ GeV to ∼5% at $p_T = 1$ TeV, for $R = 0.6$ jets in the central region. This resolution varies as $1/\sqrt{E_{jet}}$, so jets in the forward region, which require larger energy to reach the same p_T, will in general have smaller resolutions compared to the central region for the same p_T. Due to the effect of jet energy falling outside of the jet radius, $R = 0.4$ jets tend to have slightly worse resolution, ranging from ∼28% at $p_T = 20$ GeV to ∼6% at $p_T = 1$ TeV for jets in the central region. These p_T resolutions have been confirmed by both data and Monte Carlo studies [77], and small differences between the two are accounted for in the assignment of systematic uncertainties to the unfolding factors.

The final p_T bin boundaries used for the inclusive jet cross section measurement, taking into account both jet p_T resolutions and jet trigger effiencies, are: 20, 30, 45, 60, 80, 110, 160, 210, 260, 310, 400, 600, 800, 1000, 1200, and 1500 GeV. The rapidity bins that are used, as listed in Table 4, are much larger than the jet angular resolutions, and thus smearing of the reconstructed jet rapidity is a much smaller concern.

In order to minimize any bias due to differences in the p_T spectrum shape, a weighting factor is applied to the Monte Carlo jet p_T spectra to improve the agreement between the Monte Carlo reconstructed jet distribution and the measured data distribution. This weighting factor is defined as the ratio of the next-to-leading order (NLO) predicted cross section, derived using the MSTW2008 NLO PDF, to the cross section predicted using leading order matrix elements with the MRST 2007 LO* PDF (see Section 2.3). Since the Monte Carlo distribution is obtained by leading order event generation using the LO* PDF, the multiplication by these weights helps pull the distribution closer to that predicted by NLO calculations, which are in turn closer to the spectra observed in data. The derived weights for $R = 0.6$ jets are shown in Figure 4.24. Since the underlying predicted cross sections for $R = 0.4$ and $R = 0.6$ jets are very similar, the weights used for the two different jet sizes are almost indistinguishable. A linear interpolation of the weights, which helps smooth large weight variations between bins, is then applied to both the truth and reconstructed jet p_T spectra, as a function of the Pythia event parameter $\hat{p_T}$, which is related to the energy of the underlying hard scatter.

The final agreement between the jet p_T spectrum measured in data and that modeled in Monte Carlo is shown for $R = 0.6$ jets in three rapidity bins in Figure 4.25-4.27. The data distributions have been normalized by the appropriate effective luminosity, as described in Section 4.6, to give the correct, steeply-falling spectrum shape. The number of entries in the Monte Carlo distributions has been normalized to the number of entries in the corresponding data distributions to eliminate any differences caused by the total number of jets in each distribution, which, as discussed above, do not impact the bias. The weighting procedure helps everywhere to bring the Monte Carlo distribution closer to that in data, though differences still exist that must be accounted for during the assignment of systematic uncertainties.

The final correction factors that are applied to the data are then derived using Equation 4.22. These correction factors for three bins of rapidity are shown in Figures 4.28-4.30. The corrections are in general largest at low p_T, due to the large fractional resolutions and

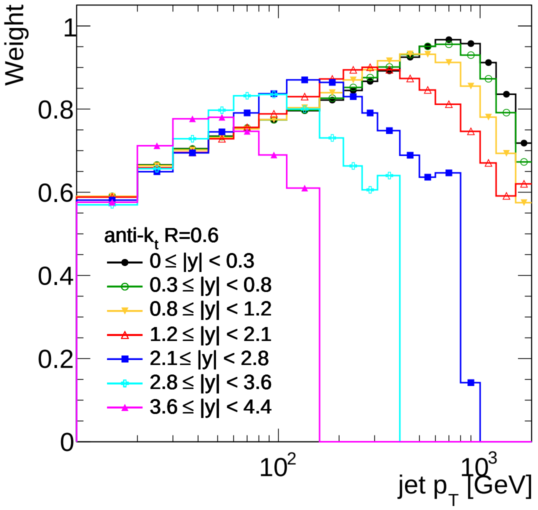

Figure 4.24: Weights applied to Monte Carlo jets, defined as the ratio of the next-to-leading order cross section predicted using an NLO PDF to the cross section predicted by leading order event generation using an LO* PDF.

large jet reconstruction inefficiencies in this region. They are also large for jets with energies near the kinematic limit for jet production at $\sqrt{s} = 7$ TeV. In this region, the cross section is more steeply falling, so the effect of resolution smearing is larger. In regions of high p_T and high rapidity, the accuracy of the correction factors begins to be limited by the available statistics in the Monte Carlo simulation. These statistical errors are derived by correctly taking into account correlations between the number of Monte Carlo reconstructed and truth jets in each bin, as described in Appendix C.

The systematic uncertainties on these correction factors, also shown in Figures 4.28-4.30, are assessed by varying the Monte Carlo p_T and angular resolutions, as well as the cross section shape, and comparing the resulting correction factors with the default correction factors. From di-jet balance and E/p studies of single hadrons, the p_T resolution modeled in Monte Carlo has been verified to within 10% [77]. For jets with $p_T < 20$ GeV, no measurement exists in data to verify the resolution modeled in Monte Carlo. Therefore a conservative resolution difference of 30% is assigned to jets in this region. To assess the impact of these potential differences between the simulated and real energy resolution, the resolution in the Monte Carlo is artificially worsened. This is done by applying an additional smearing to the reconstructed jet p_T, on top of the smearing that already exists in the Monte

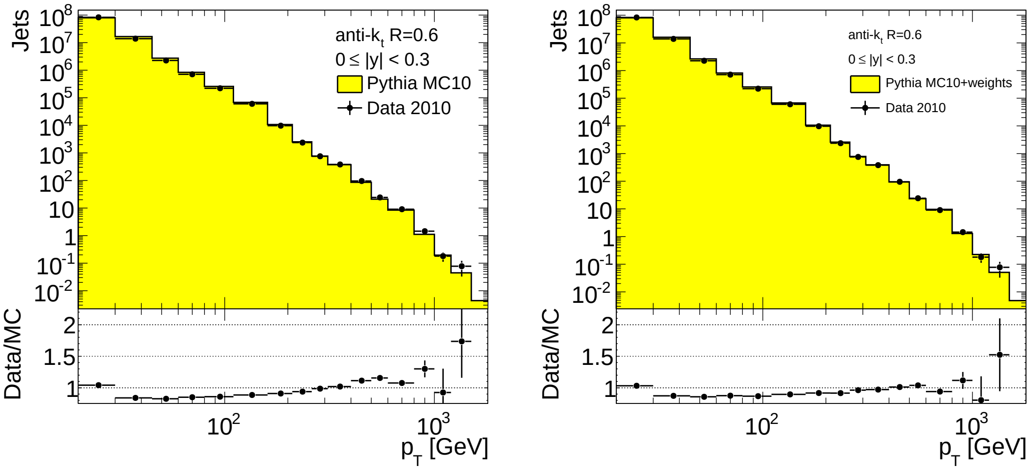

(a)

(b)

Figure 4.25: Comparison of reconstructed jet p_T spectra shapes in data and Monte Calro for $R = 0.6$ jets with $0 \leq |y| < 0.3$, shown before applying weights (a) and after applying weights (b). The Monte Carlo distributions are normalized to the total number of events in the data distribution.

Carlo. First an additional resolution factor, σ'_{MC}, is defined for each jet, such that

$$\sqrt{\sigma'^2_{MC} + \sigma^2_{MC}} = (1 + x)\sigma_{MC}, \tag{4.25}$$

where σ_{MC} is the p_T resolution of this jet in the Monte Carlo and x is the amount by which the resolution should be worsened, in this case either 10% or 30%, depending on the jet p_T. A gaussian distribution of width σ'_{MC} centered at zero is then formed, and a random amount of energy is sampled from this gaussian and added to the p_T of the jet. This process is repeated ten times for each jet, to avoid any statistical fluctuations. The observed uncertainty on the correction factors due to jet p_T resolution is as high as ~25% for the first p_T bin, which is affected by the large uncertainty for jets with $p_T < 20$ GeV, but generally less than 5% for the remaining p_T bins. Since the resolution cannot be improved using this method, this uncertainty is applied symmetrically. This is justified by the observed linear change of the correction factors as a function of the increasing additional smearing.

The angular jet resolution is much smaller in comparison to the bin size than the p_T resolution, with $|y_{reco} - y_{truth}|$, as determined in the Monte Carlo simulation, less than 0.05 for jets with $p_T = 20$ GeV, decreasing to ~0.01 for jets with $p_T = 1$ TeV. A conservative

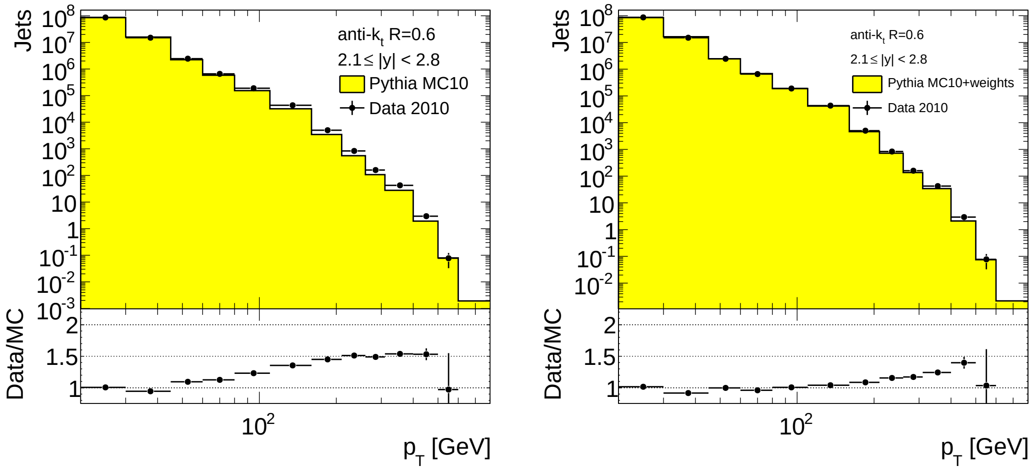

(a) (b)

Figure 4.26: Comparison of reconstructed jet p_T spectra shapes in data and Monte Calro for $R = 0.6$ jets with $2.1 \leq |y| < 2.8$, shown before applying weights (a) and after applying weights (b). The Monte Carlo distributions are normalized to the total number of events in the data distribution.

uncertainty of 10% is assigned to this angular resolution [95], and the impact on the unfolding factors is assessed using a similar procedure as outlined for the jet p_T resolution. This leads to an uncertainty on the correction factors that is $< 1\%$ for most regions, but up to $\sim$2% for the forward regions at high and low p_T.

Systematic uncertainties due to the shape of the p_T distributions are assessed by applying additional weighting factors, on top of the default weighting factor, to alter both the truth and reconstructed jet spectra. The three functions used for this variation are:

- $w_1 = 1 + (\hat{p}_T - 17) \cdot 1.9/1500$
- $w_2 = 1 + (\hat{p}_T - 17) \cdot 0.6/1500$
- $w_3 = 1 + (\hat{p}_T - 17) \cdot 1.7/1000 + 0.15e^{((\hat{p_T} - 52.5)/5)^2}$

These variations were chosen to bracket the observed differences in the p_T spectra in data and Monte Carlo. The first two functions effectively increase the high-p_T region, while the last function also increases region near 52.5 GeV, which in several rapidity regions differs from data more than the surrounding bins. The uncertainty on the correction factors is taken as the envelop of the uncertainties resulting from each of these three variations. This final uncertainty is as high as 10% for the first p_T bin, but generally $< 5\%$ for all other bins.

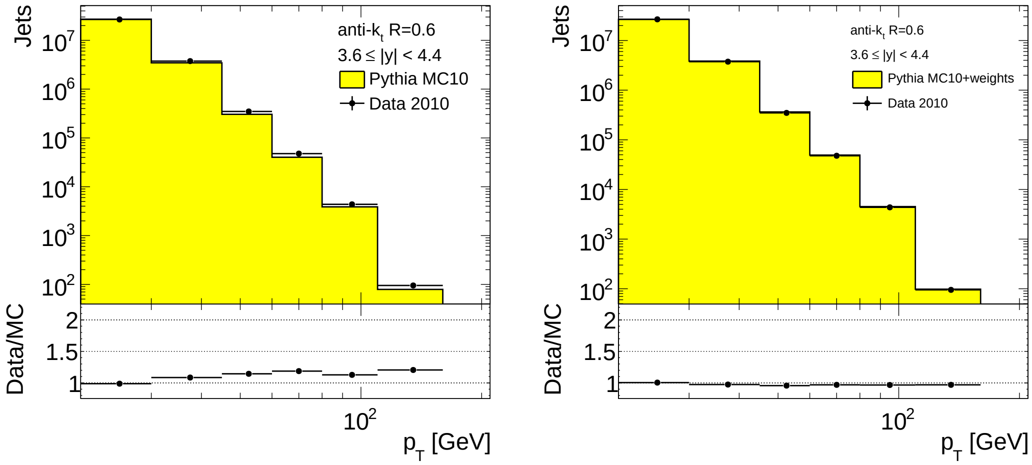

(a) (b)

Figure 4.27: Comparison of reconstructed jet p_T spectra shapes in data and Monte Calro for $R = 0.6$ jets with $3.6 \leq |y| < 4.4$, shown before applying weights (a) and after applying weights (b). The Monte Carlo distributions are normalized to the total number of events in the data distribution.

The jet reconstruction efficiency has been shown by data measurements to be well-modelled in Monte Carlo [77]. A small additional uncertainty is only assigned to regions where the efficiency is $< 99\%$, which only occurs in the bin covering the region 20-30 GeV. The uncertainty on the efficiency is $^{+2}_{-1}\%$. It is translated to an uncertainty on the correction factors by noting that the total number of reconstructed jets in Monte Carlo is the product of the efficiency in Monte Carlo times the original number of jets, $N^{MC}_{reco} = \epsilon N$. the correction factor with the default efficiency and that with the efficiency altered by some uncertainty is then:

$$C = \frac{N^{MC}_{true}}{\epsilon N}, \text{ and } C' = \frac{N^{MC}_{true}}{(\epsilon + \Delta\epsilon)N} \tag{4.26}$$

the difference between the two correction factors is thus:

$$C' - C = \frac{N^{MC}_{true}}{N}\left(\frac{1}{\epsilon + \Delta\epsilon} - \frac{1}{\epsilon}\right) = \frac{N^{MC}_{true}}{N}\left[\frac{-\Delta\epsilon}{\epsilon(\epsilon + \Delta\epsilon)}\right] = -C\frac{\Delta\epsilon}{\epsilon + \Delta\epsilon}, \tag{4.27}$$

and the relative uncertainty induced on the correction factor is then:

$$\text{Relative uncertainty } = \frac{C' - C}{C} = -\frac{\Delta\epsilon}{\epsilon + \Delta\epsilon} \tag{4.28}$$

The sign of this uncertainty is important, since any increase in efficiency will increase the number of reconstructed jets, which will in turn decrease the final correction factor.

The total uncertainty on the correction factors, indicated by the green band in Figures 4.28-4.30, is obtained by assuming the uncertainties due to statistics, p_T resolution, angular resolution, spectrum shape, and jet reconstruction efficiency are uncorrelated, and using the quadratic sum of all contributions as the final uncertainty.

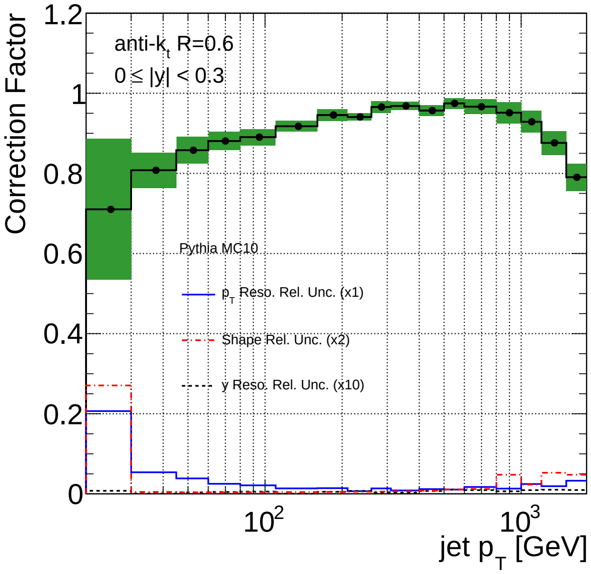

Figure 4.28: Unfolding correction factors as a function of jet p_T for $R = 0.6$ jets with $|y| < 0.3$. Relative uncertainties due to jet p_T and angular resolutions and the spectrum shape are shown. Statistical uncertainties are indicated by the black error bars. The shaded region indicates the quadratic sum of the systematic and statistical uncertainties.

4.8 Cross Section Uncertainty

The derivation of many of the experimental errors relevant for the inclusive jet cross section measurement, such as the uncertainty on the jet energy calibration, the jet selection efficiency, and the luminosity, have been detailed in the previous sections. These uncertainties, however, must be propagated into a corresponding uncertainty on the cross section itself and combined to form a total systematic uncertainty.

The dominant source of systematic uncertainty for this inclusive jet cross section analysis, as it was for previous measurements performed at CDF [3] and D0 [2], is the jet energy

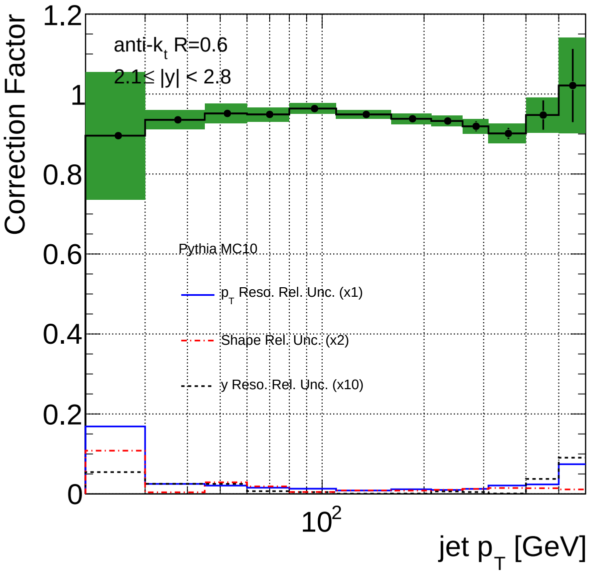

Figure 4.29: Unfolding correction factors as a function of jet p_T for $R = 0.6$ jets with $2.1 \leq |y| < 2.8$. Relative uncertainties due to jet p_T and angular resolutions and the spectrum shape are shown. Statistical uncertainties are indicated by the black error bars. The shaded region indicates the quadratic sum of the systematic and statistical uncertainties.

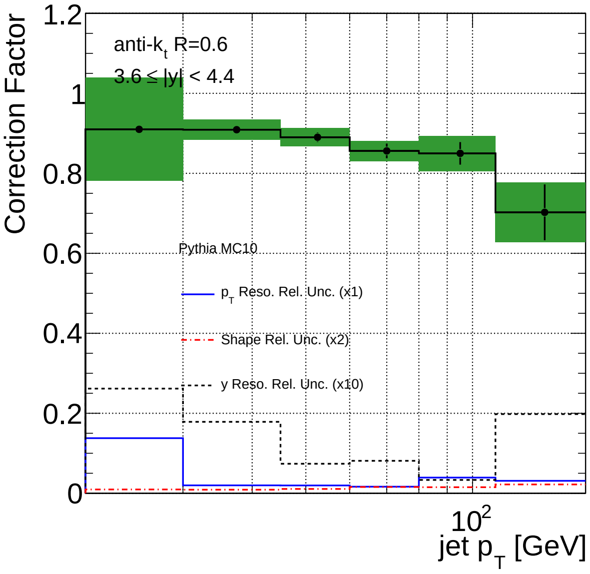

Figure 4.30: Unfolding correction factors as a function of jet p_T for $R = 0.6$ jets with $3.6 \leq |y| < 4.4$. Relative uncertainties due to jet p_T and angular resolutions and the spectrum shape are shown. Statistical uncertainties are indicated by the black error bars. The shaded region indicates the quadratic sum of the systematic and statistical uncertainties.

scale uncertainty. Due to the steeply-falling nature of the inclusive jet cross section, small variations in the jet energy scale lead to large uncertainties on the measured cross section. As discussed in Section 4.3, the uncertainty on the jet energy scale ranges from ∼2-4.5% in the central region to ∼3-12.5% in the most forward region, as has been validated with a number of *in-situ* studies. In addition to this baseline uncertainty, there is an additional uncertainty due to the correction that removes pileup energy. This uncertainty is especially important for data taken in later periods, in which there were, on average, more than two interactions in every beam crossing. Since every additional interaction leads to a larger amount of energy deposited in the calorimeter, and hence a larger correction, the uncertainty on the pileup correction increases with the number of primary vertices in the event.

The simplest approach to transfer the jet energy scale uncertainty to an uncertainty on the cross section is to shift the p_T of each jet in data up and down by the appropriate absolute uncertainty, recalculate the cross sections resulting from each shift, and find the relative difference between these variations and the default cross section. However, this leads to a double-counting of the statistical uncertainty on the measurement, and the low statistics in the highest p_T bins cause large fluctuations in the estimated uncertainties for this region. Another approach is to fit the observed data spectrum to a smooth function. Each p_T bin of the measurement is then divided into many smaller sub-bins, and the average p_T of each sub-bin is fluctuated up or down by the jet energy scale uncertainty. A new histogram is filled with the p_T corresponding to this variation, weighted by the number of jets estimated in this sub-bin by the smooth function. Unfortunately, this method suffers from the difficulty of finding an appropriate function that can fit the measured data spectrum over the full p_T range.

Instead, the uncertainty on the cross section is evaluated by varying the p_T of the jets in Monte Carlo and evaluating the relative difference of the produced spectrum with respect to the nominal spectrum. The size of the variation for each jet is one standard deviation of the jet energy scale uncertainty for the given bin of p_T and rapidity. To minimize differences between the shape of the p_T spectrum in Monte Carlo and in data, which could affect how many jets migrate between bins due to jet energy variations, the Monte Carlo is weighted by the factors described in Section 4.7. This approach is equivalent to evaluating the jet energy scale uncertainty as an additional uncertainty on the unfolding factors, as was done for the jet energy resolution. However, since this is the dominant uncertainty on the measurement, it is treated separately here in order to illustrate the separate effects.

This procedure accounts for the baseline jet energy scale uncertainty in a quite straightforward manner. An additional complication arises, though, when incorporating the uncertainty due to the pileup correction. The amount of pileup varied throughout 2010, and, due to use of different triggers with varying prescales, jets in different p_T regions contain different amounts of data from each period. In contrast, the Monte Carlo used to assess the impact of jet energy scale variations has only one primary interaction in each event. To attain a final uncertainty number that correctly accounts for the varying amount of pileup, first the distribution of the number of primary vertices, N_{PV}, in data events is recorded for each bin of jet p_T and rapidity. The uncertainties on the cross section that would result from differing levels of pileup, corresponding to $N_{PV} = 1, 2, ..., 7+$, are then evaluated in Monte Carlo using the technique described in the previous paragraph. The resulting uncertainties are shown in Figure 4.31, for $R = 0.6$ jets in the central and forward regions. These uncertainties are then combined, weighting each one by the fraction of jets in each p_T and rapidity bin that resulted from events with the corresponding N_{PV}. The final uncertainty on the cross section that results from this weighted combination is indicated by the black points in Figure 4.31.

The almost totally negligible final uncertainty due to pileup can be understood as follows. Jets at low p_T, which are the most susceptible to variations due to small amounts of pileup energy, were measured predominantly in events with very few pileup vertices. This nicely illustrates the importance of using only data from Periods A-C for the measurements of jets with $p_T < 60$ GeV. In the most forward bin, if all the jets with $p_T < 30$ GeV were produced in events with three primary vertices, the uncertainty on the cross section due to pileup would be over 10%; however, less than 2% of all jets in this bin come from events with more than one vertex. At slightly higher p_T, the majority of jets in the 60-80 GeV bin were collected in the early data periods when the low E_T triggers had small prescales. In the central region, ~25% of all jets in this p_T bin come from events with more than one vertex. Although the percentage of jets affected by pileup is significant, the affect of pileup on these higher-p_T jets is smaller. For bins of p_T greater than 310 GeV, the majority of jets occur in events with more than one vertex, but the affect of pileup on these jets is negligibly small. Thus, although there was a large amount of pileup in later data periods, this mostly affected high-p_T jets that are relatively immune to pileup affects.

To further validate that no large uncertainties are induced by the presence of pileup, cross sections measured using data from different periods are compared. The cross section derived using the full dataset and that derived using data from Periods A-C, D-F, and G-I are shown in Figure 4.32 for $R = 0.6$ jets with $0 \leq |y| < 0.3$ and $2.1 \leq |y| < 2.8$. The ratio of each of these cross sections to the final measured cross section, shown in the bottom panels, is stable across the various data periods. This validates that jet energies measured in periods when there was significant pileup are consistent with those measured in periods when there was virtually no pileup.

The total relative uncertainty on the inclusive jet cross section due to the jet energy scale, as evaluated using the Monte Carlo technique outlined above, is shown in Figure 4.33 for $R = 0.6$ jets in the regions $0 \leq |y| < 0.3$ and $2.1 \leq |y| < 2.8$. The black points indicate the uncertainty that is estimated using the totally data-driven technique of fluctuating each jet in data up and down by the proper uncertainty. This data-based method intrinsically accounts for the correct amount of pileup, but causes large fluctuations in the low-statistic bins, as seen in the high-p_T region of Figure 4.31(a). In the low-p_T region, it appears that the Monte Carlo-based method slightly underestimates the uncertainty, as compared to that obtained from data. This difference is due to the difference in p_T spectrum shape in data and Monte Carlo, and is accounted for in the uncertainty on the unfolding factors, as described in Section 4.7.

In addition to the baseline and pileup jet energy scale uncertainties described above, other factors in the data sample could influence the jet energy scale. For example, the uncertainty due to energy lost in dead cells of the liquid argon and tile calorimeters, which is corrected for as described in Section 3.2.6, could be underestimated. These dead regions are mimicked in the Monte Carlo, and any deterioration of response for jets in these regions is taken into account, on average, by the Monte Carlo-derived baseline jet energy scale uncertainty. However, the number of dead calorimeter regions increased throughout 2010, and additional average jet energy variations could exist if large regions of dead calorimeter components were not included in the particular Monte Carlo used to derive the baseline uncertainty. Figures 4.34 and 4.35 show the location in η and ϕ of the dead cells present in data collected during one of the final runs of 2010 and those present in the Monte Carlo used to derive the baseline jet energy scale uncertainty. Since there are only small differences in the dead regions in data and Monte Carlo, and since *in-situ* measurements, such as the direct γ-jet balance analysis [88], observed no deterioration in response for jets located in the dead calorimeter regions, no additional uncertainty is assigned.

The z position of the event vertex could also affect the jet energy scale uncertainty. The jet energy calibration is derived as a function of electromagnetic energy and η for jets produced near the origin of the detector, with the η dependence driven by the varying detector coverage. As can be seen in Figure 4.1(b), however, jets in data were produced from vertices as far as 250 mm away from the detector origin. For jets that are created very far from the origin, the jet η could be very different from the detector η used to derive the calibration. As a result, an inappropriate calibration factor could be applied to these jets, causing a corresponding decrease in jet response. The possible effect of vertex displacement on the jet response was studied in Monte Carlo as a function of the z position of the event vertex, as shown in Figure 4.36. No statistically significant change in response is observed, and hence no additional uncertainty is applied.

The sources of uncertainty other than the jet energy scale uncertainty are propagated to the cross section as follows:

- Unfolding : The uncertainty on the unfolding factors, as described in Section 4.7, accounts for uncertainties on the p_T and angular resolutions, the p_T spectrum shape, and the jet reconstruction efficiency. Since the unfolding correction factors are simple multiplicative factors that are applied to the measured cross section to define the final cross section, any relative uncertainty on the unfolding factors is equivalent to a relative uncertainty on the final cross section.

- Jet selection efficiency : Corrections for the jet selection efficiency, as detailed in Section 4.4, are only applied in regions where the efficiency is $< 99\%$. In these regions, the uncertainty on the jet selection efficiency is propagated to the final cross section analogously to the manner in which the jet reconstruction efficiency was propagated, i.e. via Equation 4.28.

- Trigger efficiency : No correction due to the trigger efficiency is applied, since each trigger selection is only applied in regions where it is $> 99\%$ efficient. During the derivation of the unfolding correction factors, no trigger selection was applied as this efficiency was implicitly assumed to be 100%. To account for small inefficiencies which may exist, a ±1% uncertainty is assigned to the trigger efficiency. Similar to the uncertainties on the jet reconstruction efficiency and the jet selection efficiency, this efficiency uncertainty is translated into an uncertainty on the cross section using Equation 4.28.

- Luminosity : The uncertainty on the luminosity is 3.4%, as described in Section 4.6. The final cross section is inversely proportional to the luminosity, $\sigma \propto 1/\mathcal{L}$, and the change in cross section due to a change in luminosity is thus $\Delta\sigma \propto 1/(\mathcal{L}+\Delta\mathcal{L}) - 1/\mathcal{L}$. Similar to the derivation of Equation 4.28, this then leads to a relative uncertainty on the cross section of:
$$\frac{\Delta\sigma}{\sigma} = -\frac{\Delta\mathcal{L}}{\mathcal{L}+\Delta\mathcal{L}} \tag{4.29}$$

- Background : The main possible non-collision sources of observed jets are cosmic muon and beam background events, as discussed in Section 4.4. To assess the impact of possible background contamination on the final cross section, the full jet and event selection criteria are applied to a sample of events selected to contain an enhanced number of background signals. Possible contamination from cosmic sources was studied using events from the “Cosmic_Calo” trigger stream, which contains events that give calorimeter timing signals consistent with cosmic muons, and events that pass the “L1_J5EMPTY” trigger item, which selects events that satisfy the L1_J5 trigger during empty bunch crossings. The effect of beam backgrounds was studied using events that pass the “L1_J10UNPAIRED” trigger item, which selects events that satisfy the L1_J10 trigger when only one bunch was traversing ATLAS. In all, data corresponding to ∼2 pb^{-1} was studied. Of the roughly five million events from the Cosmic_Calo stream, no jets survive the event and jet selection. Additionally, no jets survive from the L1_J5EMPTY sample. The contribution from beam background was slightly higher, with 191 jets, predominantly at low p_T, surviving all selection out of the 10 million events investigated. Due to these low rates of background acceptance, the uncertainty on the measured cross section due to background sources is taken to be negligible.

The total relative uncertainty on the inclusive jet cross section, for $R = 0.6$ jets, is shown along with each individual uncertainty contribution in Figures 4.37-4.40. As all sources of error are considered uncorrelated, the final uncertainty is the quadratic sum of the individual uncertainties. The jet energy scale is everywhere the dominant uncertainty. For central jets, the uncertainty on the cross section ranges from $\sim^{+30}_{-26}\%$ at 20 GeV and 1500 GeV, to less than ±10% at 100 GeV. The most forward region has the largest total uncertainty, due to the large jet energy scale uncertainty, reaching as high as +80% in the bin from 30 to 45 GeV and as low as -50% in the bin from 20 to 30 GeV. The relative uncertainties on the inclusive jet cross sections for $R = 0.4$ jets are included in Appendix D. In general, they are comparable in size, but are slightly smaller for the low p_T regions. This is due to the fact that the smaller jet size is less affected by energy deposited by the underlying event, which is modeled differently by the different Monte Carlo generators used to assign the jet energy scale uncertainty.

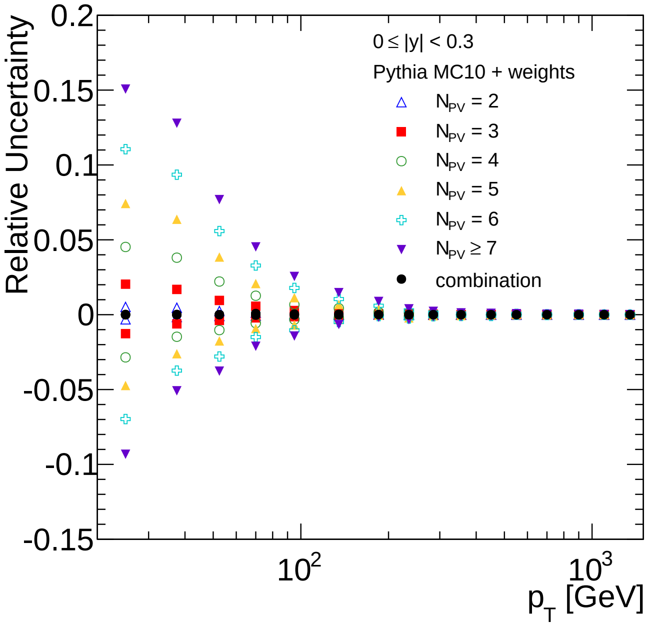

(a)

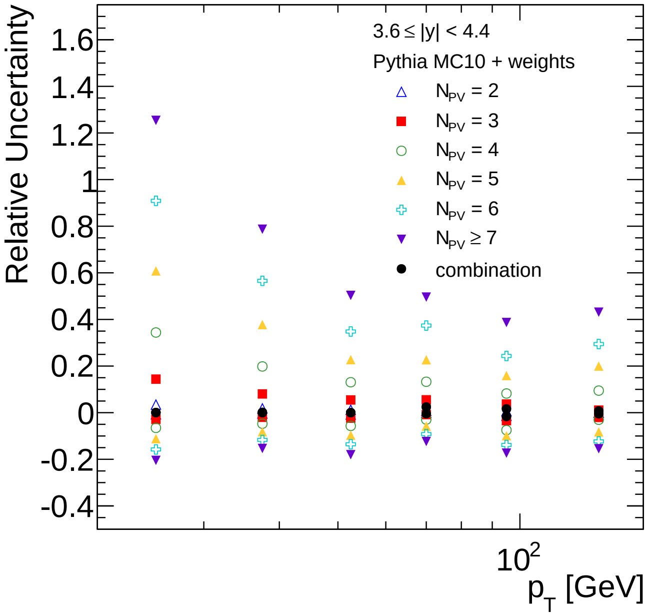

(b)

Figure 4.31: Relative uncertainty on the inclusive cross section for $R = 0.6$ jets due to pileup, as a function of p_T and number of primary vertices in the event, for jets in the region $0 \leq |y| < 0.3$ (a) and $3.6 \leq |y| < 4.4$ (b). The black points indicates the total uncertainty due to pileup estimated from the primary vertex distribution in data.

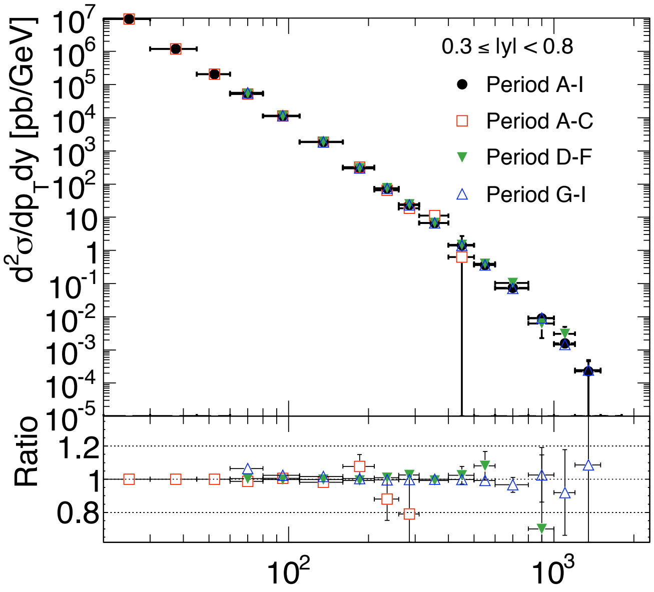

(a)

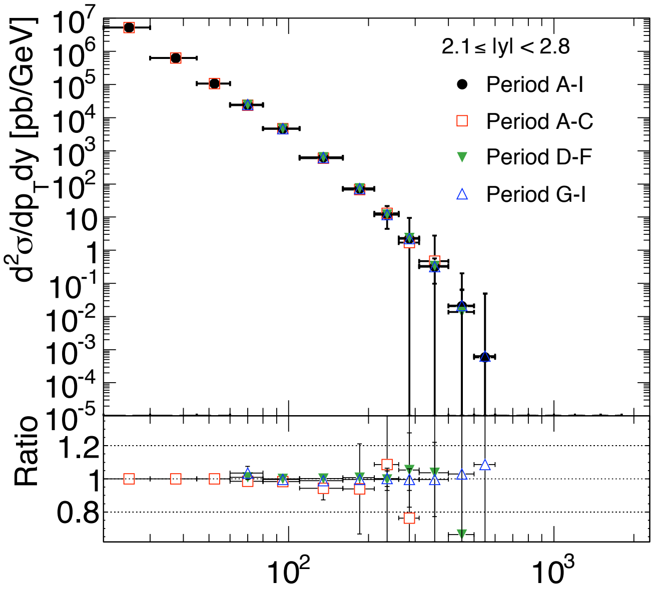

(b)

Figure 4.32: Cross sections as measured using data from Periods A-I, A-C, D-F, and G-I for $R = 0.6$ jets with $0 \leq |y| < 0.3$ (a) and $2.1 \leq |y| < 2.8$ (b). The ratio of each of these cross sections to the final measured cross section, from Period A-I, is shown on the bottom panel.

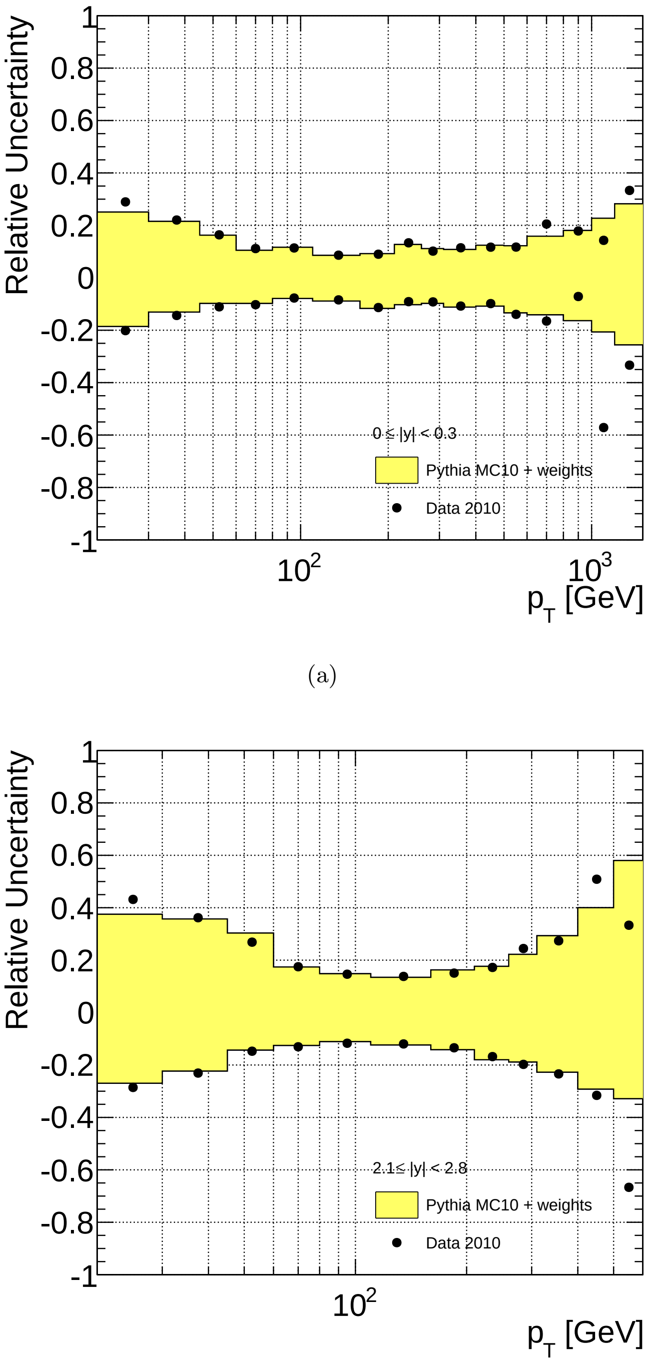

(a)

(b)

Figure 4.33: Relative uncertainty on the inclusive cross section for $R = 0.6$ jets due to the total jet energy scale uncertainty, for jets in the region $0 \leq |y| < 0.3$ (a) and $3.6 \leq |y| < 4.4$ (b). The shaded region indicates the uncertainty derived from the Monte Carlo procedure. The black points indicates the uncertainty derived by fluctuating the jets in data by the appropriate uncertainty.

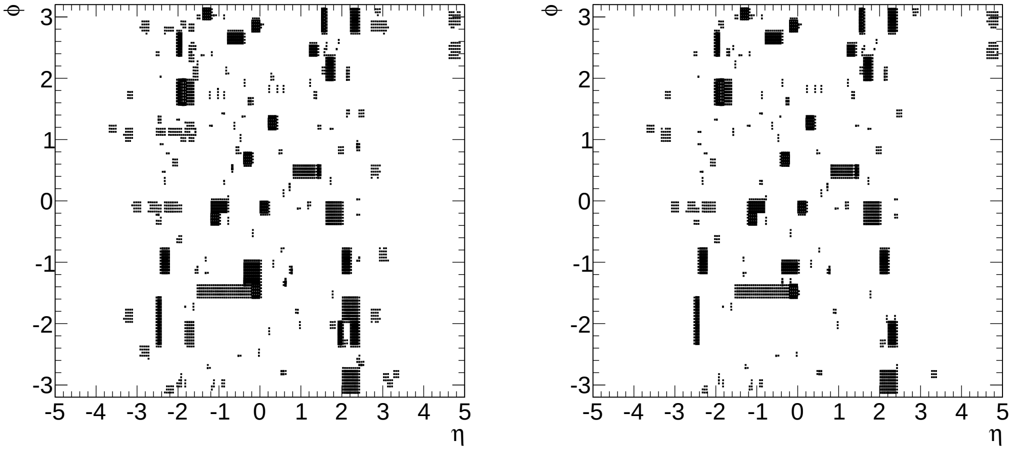

(a) (b)

Figure 4.34: Location in η and ϕ of dead cells in the liquid argon calorimeters in data (a) and modeled in Monte Carlo (b). Energy lost in these cells is corrected for using the energy measured neighboring cells in the various calorimeter layers.

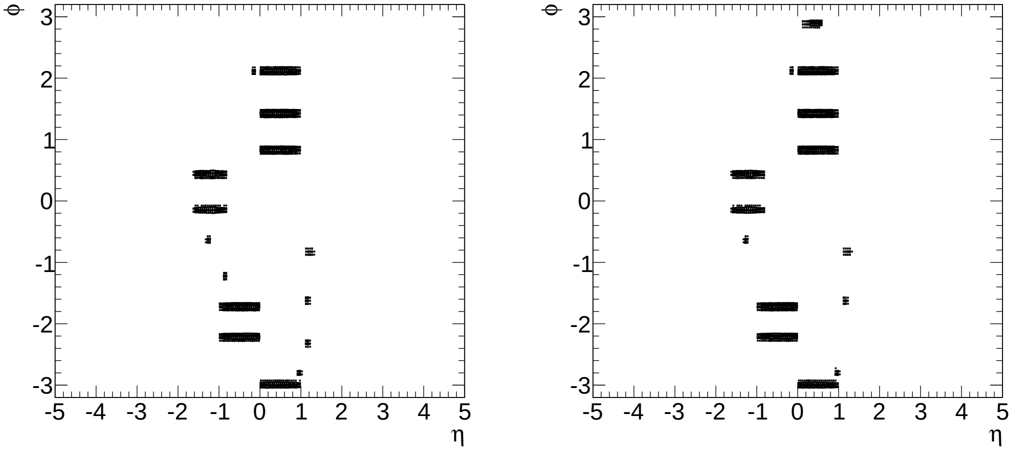

(a) (b)

Figure 4.35: Location in η and ϕ of dead cells in the tile calorimeters in data (a) and modeled in Monte Carlo (b). Energy lost in these cells is corrected for using the energy measured neighboring cells in the various calorimeter layers.

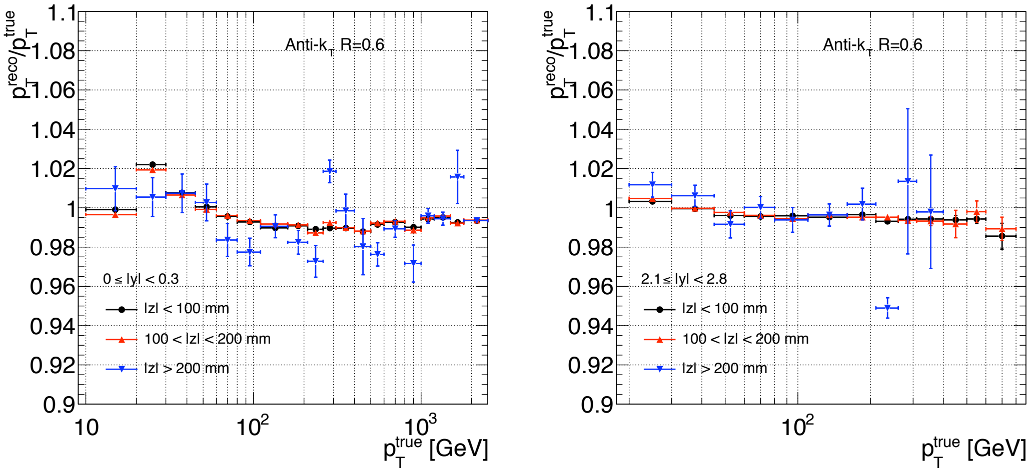

(a) (b)

Figure 4.36: Jet response as a function of true jet p_T for jets in events where the event vertex is within $|z| < 100$ mm, $100 < |z| < 200$ mm, and $|z| > 200$ mm, for $R = 0.6$ jets in the regions $0 \leq |y| < 0.3$ (a) and $2.1 \leq |y| < 2.8$ (b).

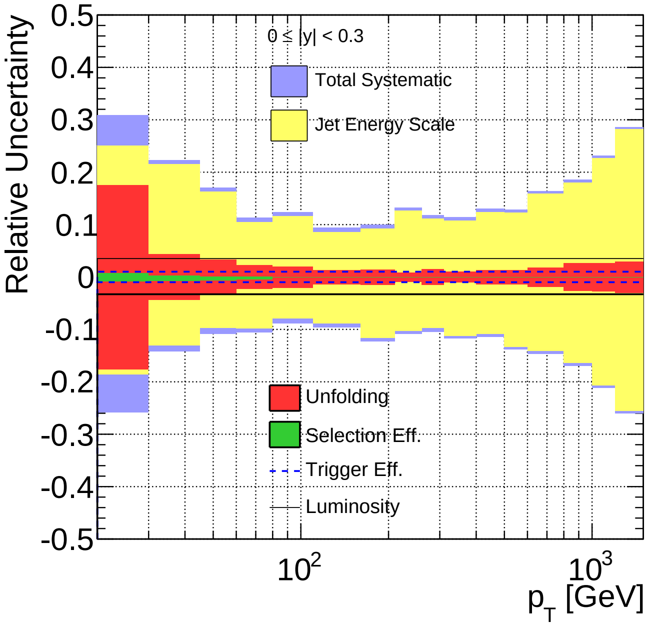

(a)

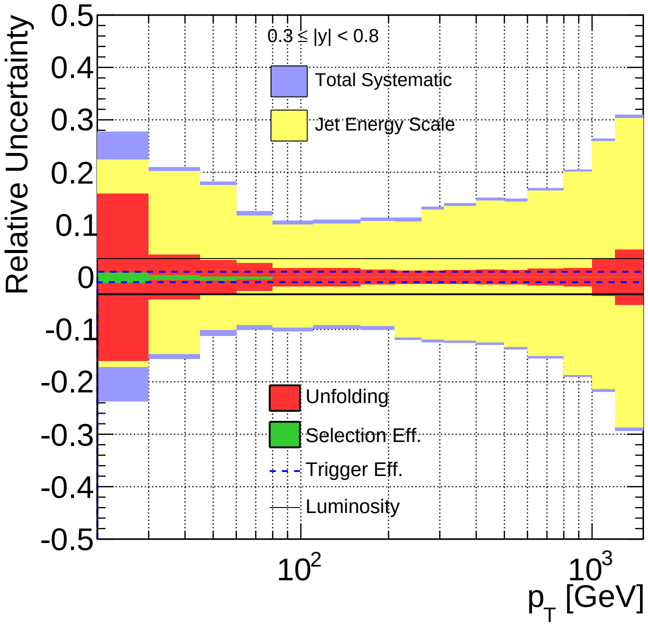

(b)

Figure 4.37: Total relative uncertainty on the inclusive jet cross section and contribution from each uncertainty source, for $R = 0.6$ jets in the region $0 \leq |y| < 0.3$ (a) and $0.3 \leq |y| < 0.8$ (b).

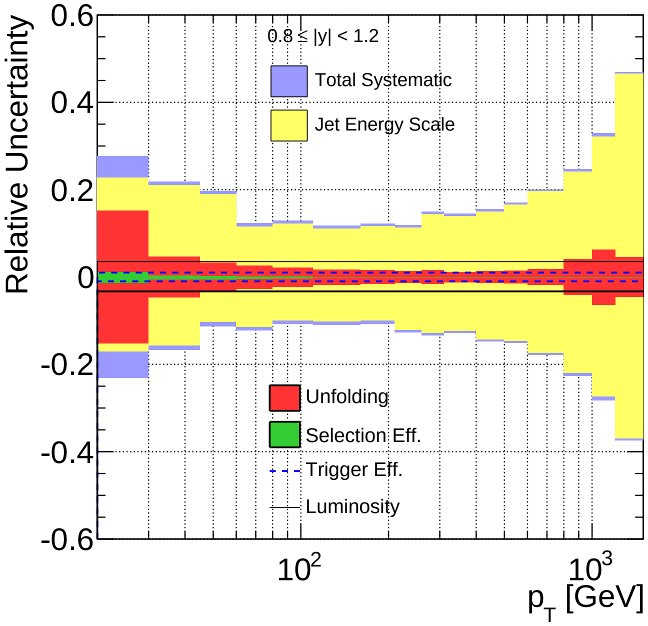

(a)

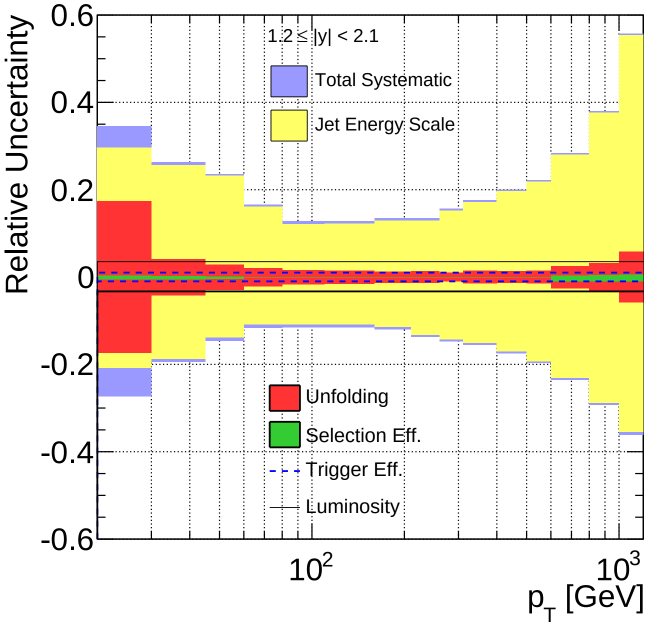

(b)

Figure 4.38: Total relative uncertainty on the inclusive jet cross section and contribution from each uncertainty source, for $R = 0.6$ jets in the region $0.8 \leq |y| < 1.2$ (a) and $1.2 \leq |y| < 2.1$ (b).

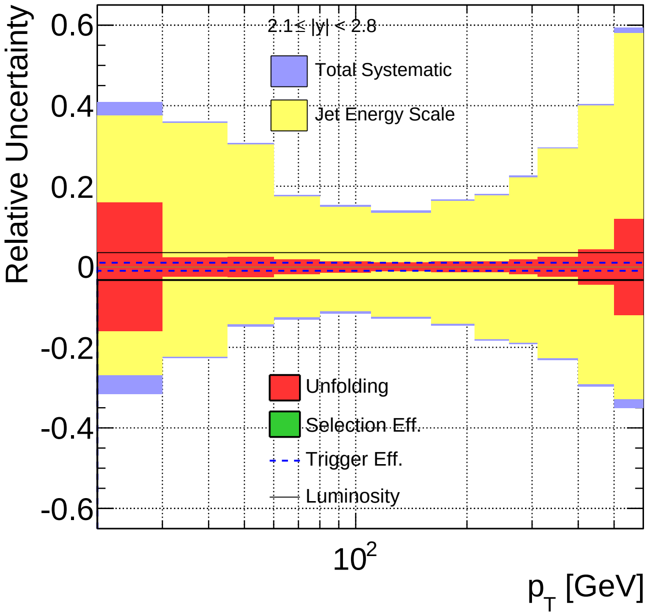

(a)

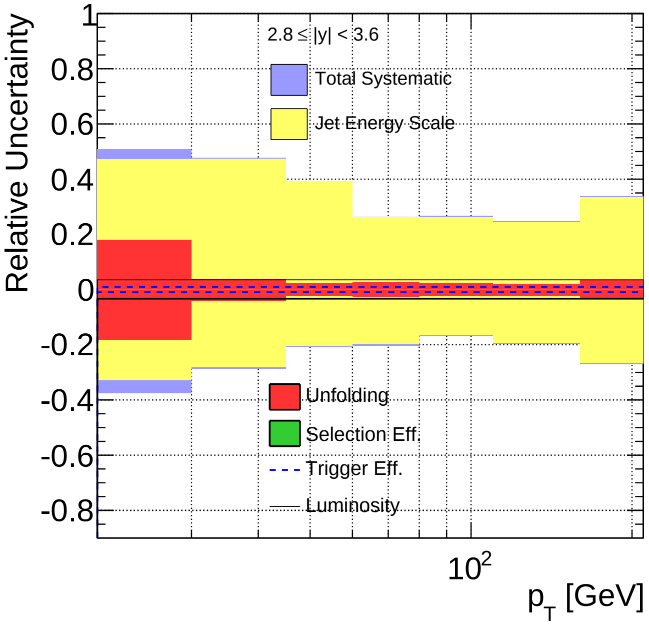

(b)

Figure 4.39: Total relative uncertainty on the inclusive jet cross section and contribution from each uncertainty source, for $R = 0.6$ jets in the region $2.1 \leq |y| < 2.8$ (a) and $2.8 \leq |y| < 3.6$ (b).

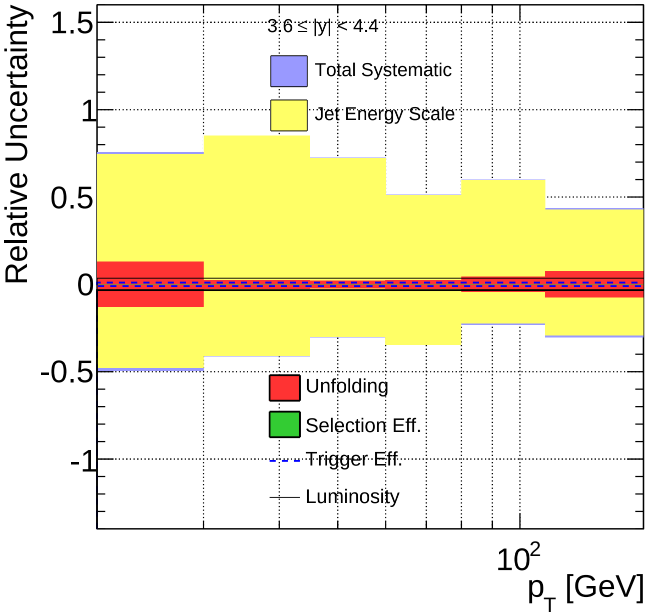

Figure 4.40: Total relative uncertainty on the inclusive jet cross section and contribution from each uncertainty source, for $R = 0.6$ jets in the region $3.6 \leq |y| < 4.4$.

Chapter 5 Theoretical Predictions

5.1 NLO Predictions

The measured cross sections, corrected for detector effects to particle-jet level, are compared to NLO perturbative QCD predictions, corrected for the non-perturbative effects of underlying event and hadronization. The NLOJET++ program [96] is used for all baseline NLO calculations. Main comparisons are performed with respect to predictions obtained using the CT10 [39] NLO PDFs, which utilize the most up-to-date set of Tevatron jet measurements within the well-validated PDF derivation procedure of the CTEQ group. Additional comparisons are made to predictions using the CTEQ 6.6 [40], MSTW2008 [34], HERAPDF 1.5 [43], and NNPDF 2.1 [41] PDF sets.

Key uncertainties on the NLO prediction are due to the uncertainties on the PDF central value, the choice of factorization and renormalization scales, and the uncertainty in the value of the strong coupling constant, α_s. To allow for fast and flexible evaluation of the impact of these uncertainties on the predicted cross section, the APPLGRID [97] software is interfaced with NLOJET++. APPLGRID replaces the numerical integration of Equation 2.1 with a sum over many phase space points. The value at each point is factorized into contributions from the PDF, α_s, and an overall event weight. These event weights are calculated only once, during an initial NLOJET++ event generation, and stored in look-up tables, indexed by the momentum transfer and interaction scale points. The convolution of these event weights with a particular choice of PDF, α_s, and renormalization and factorization scale is then easily performed *a posteriori* to obtain the systematic variations of the predicted cross section.

The procedure for propagating the PDF uncertainties to the cross section calculation depends on the particular PDF set used. Each set has a central member, used for the baseline calculation, that represents the best fit to the input experimental data and a set of additional error PDFs, used to evaluate uncertainties. The CTEQ, MSTW and HERAPDF error PDFs are defined as a basis of eigenvectors formed from the free parameters of the PDF fit. Two error members are provided for each eigenvector, one in the positive direction and one in the negative direction from the central value. The asymmetric uncertainty on a predicted observable for these PDFs is given by:

$$\Delta X^{+} = \sqrt{\sum_{i=1}^{N}[max(X_i^{+} - X_0, X_i^{-} - X_0, 0)]^2} \tag{5.1}$$

$$\Delta X^{-} = \sqrt{\sum_{i=1}^{N}[max(X_0 - X_i^{+}, X_0 - X_i^{-}, 0)]^2} \tag{5.2}$$

where X_0 is the predicted values of the observable calculated with the central PDF, and $X_i^{\pm}$ is that predicted with each of the positive and negative variations. For the MSTW and CTEQ PDFs, the uncertainty provided by these equations corresponds to a 90% confidence estimate; for HERAPDF, it corresponds to a 1σ uncertainty. In order to make comparisons coherent across PDF sets, the uncertainties for MSTW and CTEQ were scaled down by the factor $C_{90} = 1/1.64485$.

The prescription for obtaining uncertainties using the NNPDF set is slightly different. The NNPDF group derives a family of PDFs from many sets of replica data, as described in Section 2.3. The central prediction of an observable is defined as the average value of the observable obtained using each of the derived PDFs. The uncertainty on an observable is then given by the standard deviation of these predictions,

$$\Delta X = \sqrt{\frac{1}{N_{rep} - 1}\sum_{k=1}^{N_{rep}}[X_k - \langle X \rangle]^2}, \tag{5.3}$$

where N_{rep} is the number of replica data sets, X_k is the value of the observable using the PDF derived from replica set k, and $\langle X \rangle$ is the average value of the observable across all PDFs.

The uncertainty on the $R = 0.6$ inclusive jet cross section due to PDF errors is shown, for predictions obtained using the CT10 PDFs, in Figures 5.1-5.4. At low p_T, where the PDF fits are well-constrained by experimental data, the uncertainty on the cross section is $\sim 3\%$. At high p_T and forward rapidity, where only limited previous measurements exist, this uncertainty becomes the dominant theoretical uncertainty, reaching $> 10\%$ for jets with $P_T > 1$ TeV in the central region and $> 50\%$ for jets with $p_T > 100$ GeV in the most forward region. The uncertainties on the $R = 0.4$ inclusive jet cross sections are similar, as shown in Appendix E.

The uncertainty due to the chosen value of the strong coupling constant, α_s, is evaluated following the recommendation of the CTEQ group [98]. In this method, the cross section is re-calculated using a set of PDFs that were derived from fits assuming positive and negative variations of the coupling from its best estimate. The values of α_s used are $\alpha_s = 0.118 \pm 0.002$ for the CTEQ PDFs; $\alpha_s = 0.120^{+0.003}_{-0.004}$ for MSTW; $\alpha_s = 0.1176 \pm 0.002$ for HERAPDF; and $\alpha_s = 0.119 \pm 0.002$ for NNPDF. The uncertainty on the cross section prediction due to uncertainty on α_s is then given by:

$$\Delta\sigma = \frac{1}{2}\sqrt{(\sigma_{\alpha_s^+} - \sigma_{\alpha_s^-})^2}, \tag{5.4}$$

where $\sigma_{\alpha_s^\pm}$ is the cross section calculated using the PDF derived using positive and negative variations of α_s. This uncertainty is shown for $R = 0.6$ jets in Figures 5.1-5.4 and for $R = 0.4$ jets in Appendix E. In the most central region, the uncertainty ranges from 3% at low p_T to 4% at high p_T; in the most forward region, this increases to 5% at low p_T and 7% at high p_T.

The renormalisation and factorisation scales (μ_R and μ_F, respectively) used for the baseline calculations are defined, for each event generated by NLOJET++, as the p_T of the hardest jet in the event. To estimate the uncertainty on the prediction due to the neglected higher-order terms of the perturbative expansion, the cross section was calculated using renormalisation scales varied by a factor of two with respect to the default choice. Similarly, to estimate the sensitivity to the choice of energy at which the PDF evolution is separated from the matrix element, the factorisation scale was separately varied by a factor of two. Thus the total set of renormalisation and factorisation scales used is:

$$(\frac{\mu_R}{\mu_R^{default}}, \frac{\mu_F}{\mu_F^{default}}) = (\frac{1}{2}, 1),\ (2, 1),\ (1, \frac{1}{2}),\ (1, 2),\ (\frac{1}{2}, \frac{1}{2}),\ (2, 2)$$

The total uncertainty due to scale is assigned to the envelop of the uncertainties resulting from these variations. This uncertainty ranges from typically +5% to -10%. The asymmetry is due to the fact that the NLO calculation is more unstable as you lower μ_R, causing calculations to start to diverge, and lower μ_F, causing more physics to be accounted for by the PDFs, than it is as you raise them.

5.2 Non-perturbative Corrections

The NLO calculations described above predict parton-level jet cross sections. To meaningfully compare these predictions with the measured particle-level jet cross sections, they must be corrected for the non-perturbative effects of underlying event and hadronization. This is performed, in a process similar to that used for the detector unfolding, by defining a correction factor for each bin of the predicted cross section. The correction factor is defined as the ratio of the cross section obtained from Monte Carlo generation that includes hadronization and underlying event to that obtained from Monte Carlo generation with these effects turned off , i.e.

$$C = \frac{\sigma^{MC}_{with\ hadronization\ and\ UE}}{\sigma^{MC}_{without\ hadronization\ and\ UE}}. \tag{5.5}$$

The final predicted cross section is then the product of this correction factor and the cross section calculated with NLOJET++.

The Pythia event generator with the MC10 parameters was used to derive the baseline correction, since this has been extensively tuned to early ATLAS data. The uncertainty on this correction is estimated as the maximum difference between the baseline factors and the factors obtained from Pythia with the Perugia2010 parameters, which have been shown to best reproduce the shape of jets observed with ATLAS [54], and from Herwig++ with the recently developed UE7.1 parameters, which have been tuned to reproduce the ATLAS underlying event measurements at 7 TeV [56]. The Rivet [99] software program was used to interface with these generators, allowing to set the particular tuning parameters, cross section binning, jet definitions, and underlying event and hadronization settings.

To smooth the fluctuations that result from limited generated statistics, the correction factors for each rapidity bin are fit as a function of p_T. For the correction factors obtained from Pythia, the function $A + Be^{C \cdot p_T}$ was found to give the best fit. The correction factors obtained from Herwig++, which have slightly different behavior as discussed below, were fit with the function $A + B/[C \cdot log(p_T)]$. To give the best agreement across the full p_T range, the lowest p_T point was omitted from the fitting procedure for the Herwig++ factors.

The non-perturbative correction factors obtained with these different tunes are shown for both $R = 0.4$ and $R = 0.6$ jets in one central and one forward rapidity bin in Figures 5.5 and 5.6. The correction factors for all bins are included in Appendix F. A comparison of the baseline correction factors for the two jet sizes reveals the differing dominant non-perturbative effect for each one. The baseline correction for the smaller jet size is dominated by the effect of hadronization spreading energy outside of the jet area, leading to correction factors that are less than one at low p_T. For this smaller jet radius, both Perugia2010 and Herwig++ predict narrower jets than the MC10, producing correction factors that are closer to one at low p_T. The correction for the larger jet size is dominated by underlying event energy falling inside of the jet area, leading to correction factors that are greater than one at low p_T. The default PDF used by Herwig++ has a significantly higher low-x gluon contribution than the PDF used by Pythia, causing much more underlying event activity and correspondingly higher low-p_T correction factors. For jets with $p_T > 100$ GeV, non-perturbative effects are small in comparison to the scale of the hard scatter, and the correction factors are $\sim$1. Conversely, for jets with $p_T < 100$ GeV, the uncertainty on the non-perturbative correction is the dominant uncertainty on the theoretical calculation, as shown in Figures 5.1-5.4.

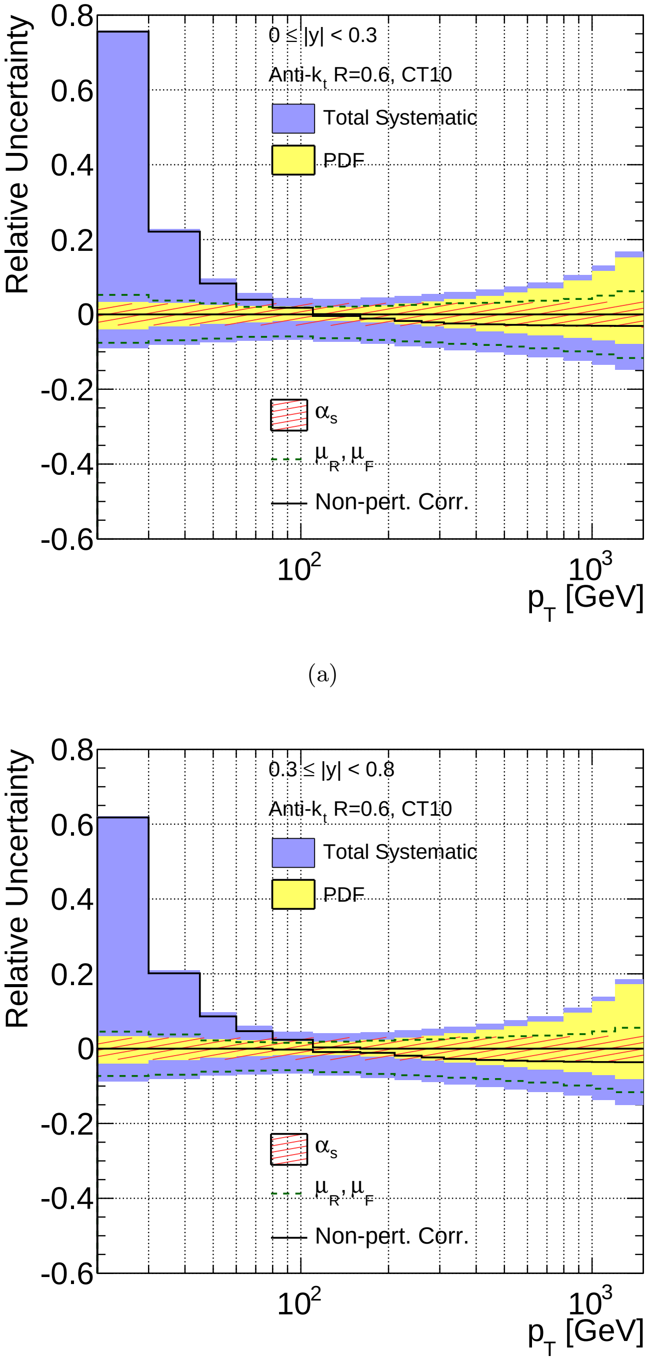

(a)

(b)

Figure 5.1: Total relative uncertainty on the predicted NLO inclusive jet cross section and contribution from each uncertainty source, for $R = 0.6$ jets in the region $0 \leq |y| < 0.3$ (a) and $0.3 \leq |y| < 0.8$ (b). The total uncertainty is given by the quadratic sum of the individual uncertainties.

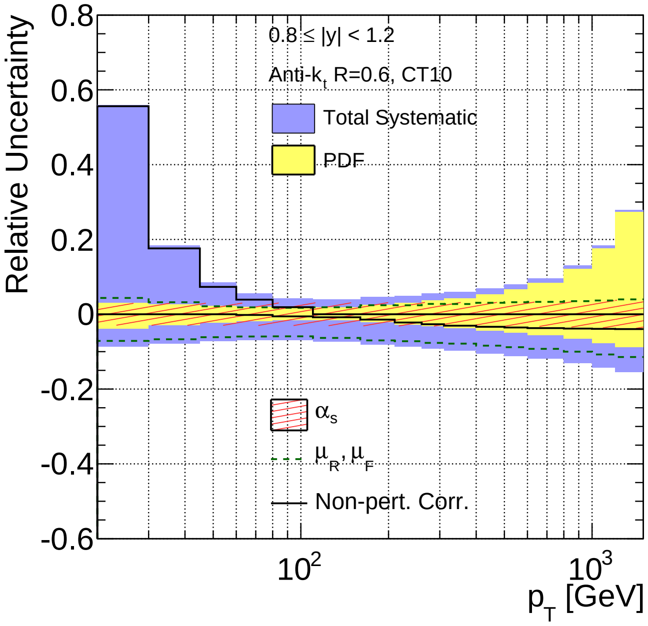

(a)

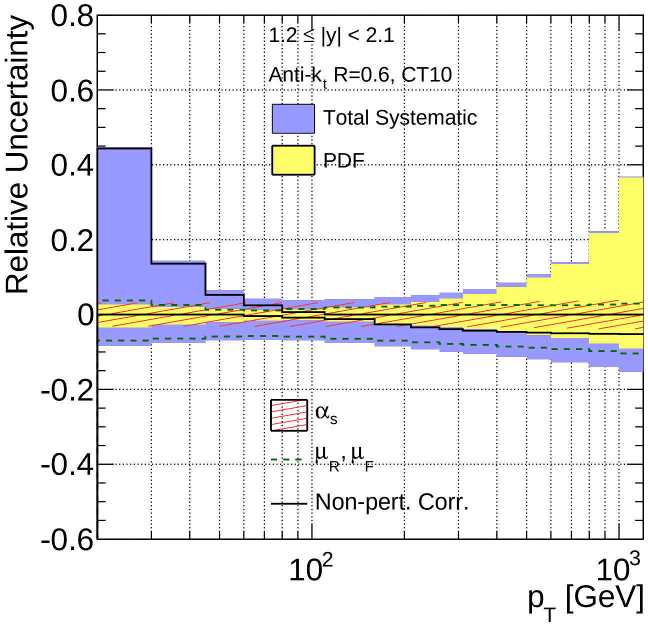

(b)

Figure 5.2: Total relative uncertainty on the predicted NLO inclusive jet cross section and contribution from each uncertainty source, for $R = 0.6$ jets in the region $0.8 \leq |y| < 1.2$ (a) and $1.2 \leq |y| < 2.1$ (b). The total uncertainty is given by the quadratic sum of the individual uncertainties.

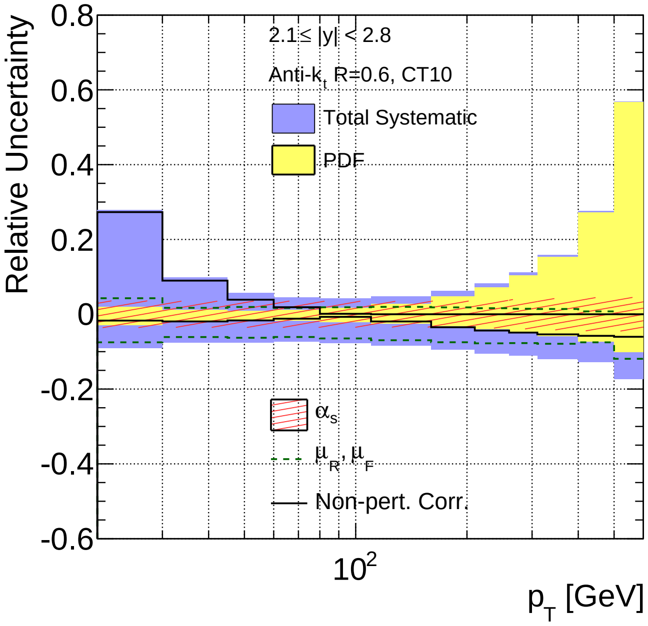

(a)

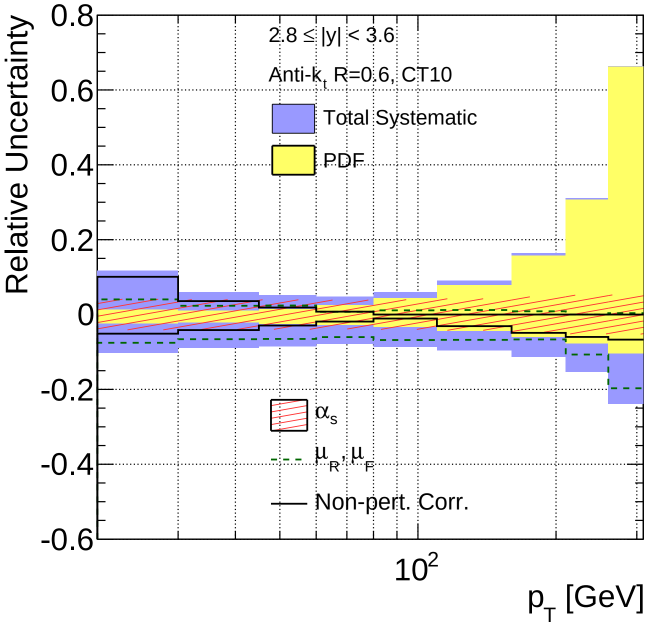

(b)

Figure 5.3: Total relative uncertainty on the predicted NLO inclusive jet cross section and contribution from each uncertainty source, for $R = 0.6$ jets in the region $2.1 \leq |y| < 2.8$ (a) and $2.8 \leq |y| < 3.6$ (b). The total uncertainty is given by the quadratic sum of the individual uncertainties.

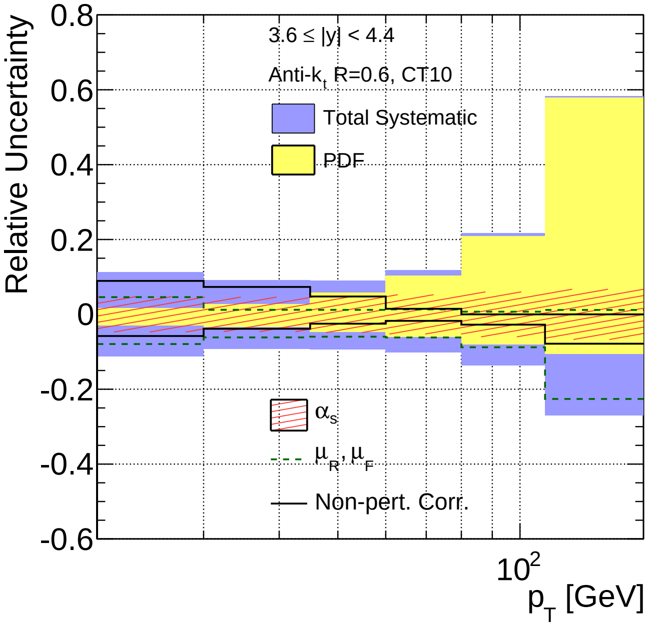

Figure 5.4: Total relative uncertainty on the predicted NLO inclusive jet cross section and contribution from each uncertainty source, for $R = 0.6$ jets in the region $3.6 \leq |y| < 4.4$. The total uncertainty is given by the quadratic sum of the individual uncertainties.

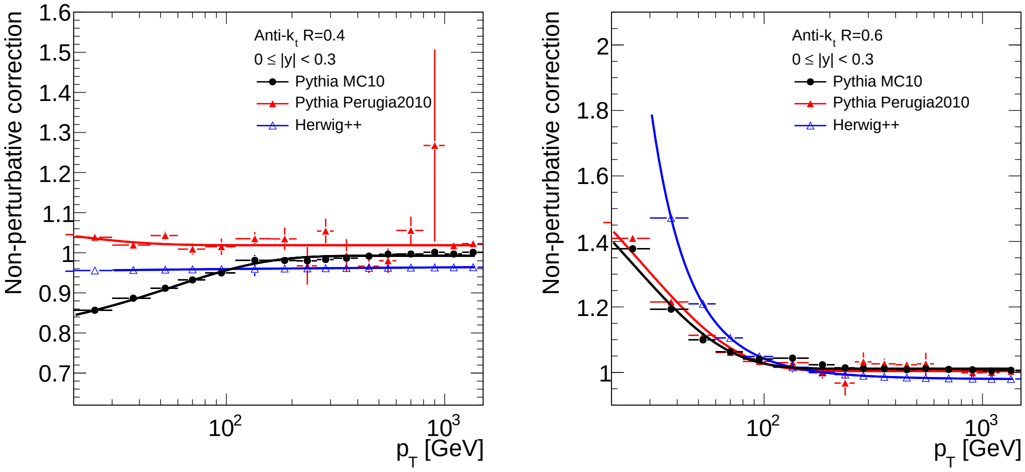

(a) (b)

Figure 5.5: Baseline non-perturbative corrections obtained from Pythia MC10 and systematic variations obtained from Pythia with the Perugia2010 tune and Herwig++, for $R = 0.4$ jets (a) and for $R = 0.6$ jets (b) with $0 \leq |y| < 0.3$.

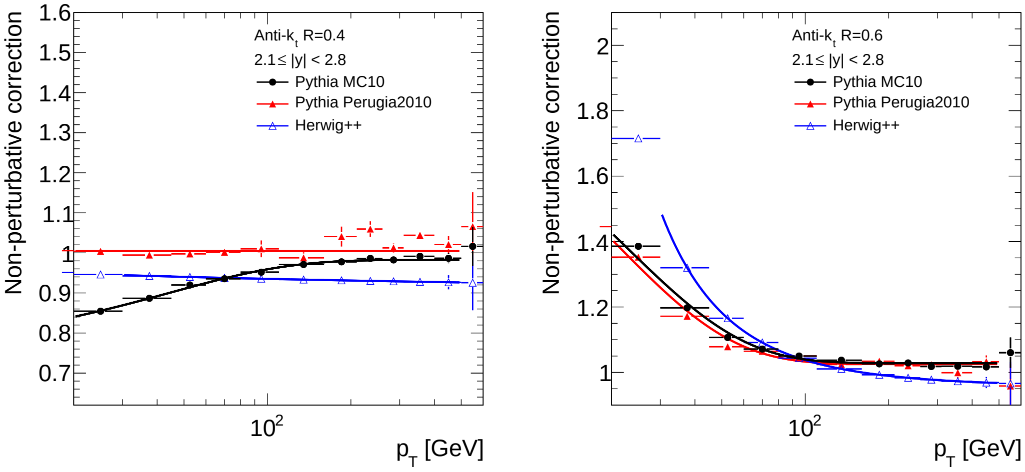

(a) (b)

Figure 5.6: Baseline non-perturbative corrections obtained from Pythia MC10 and systematic variations obtained from Pythia with the Perugia2010 tune and Herwig++, for $R = 0.4$ jets (a) and for $R = 0.6$ jets (b) with $2.1 \leq |y| < 2.8$.

Chapter 6 Results

The inclusive jet double-differential cross sections are shown, as a function of jet p_T in the seven regions of $|y|$, for anti-k$_t$ jets with $R = 0.6$ and $R = 0.4$ in Figures 6.1 and 6.2. To clearly separate the results from different rapidity regions, each cross section is multiplied by the factor indicated in the legend. The black points are the measured cross sections, corrected for detector effects to particle-jet level, along with the statistical errors. The light shaded bands indicate the quadratic sum of all systematic uncertainties, dominated by the jet energy scale uncertainty. The dark shaded bands indicate the cross sections predicted by NLO perturbative QCD, corrected for the non-perturbative effects of hadronization and underlying event, along with the quadratic sum of the uncertainties due to PDF, scale choice, value of α_s, and non-perturbative modeling. The CT10 PDF set is used for the baseline prediction and derivation of associated uncertainties. The number of measured jets in each bin of p_T and rapidity along with the measured cross section, total systematic uncertainties, predicted cross section, and total theoretical uncertainties are given in Appendix G.

The measured cross sections fall by 18 orders of magnitude over the covered kinematic range. In the regions $|y| < 1.2$, measurements extend to the unprecedented energy of 1.5 TeV. In the most forward region, the measurement extends to within 50 GeV of the kinematic limit for jet production at $\sqrt{s} = 7$ TeV.

On this logarithmic scale, good agreement can be observed between the measured and predicted cross section values. Inspection of the ratio of the values measured in data to those predicted by theory, however, is more useful to track possible disagreements. This ratio is shown in Figures 6.3-6.6, for $R = 0.6$ and $R = 0.4$ jets in each bin of rapidity. Excellent agreement is seen between data and theory across the full p_T range for both jet sizes in the region $|y| < 2.8$. For high p_T jets in the more forward regions, the data begins to be systematically lower than the theoretical prediction, though still generally consistent with the given uncertainties. The slight disagreement for the highest p_T jets at most forward rapidity could indicate that the available PDFs, which are derived from data that extends to only to $|y| < 3.0$, do not adequately describe this region. The systematically lower value of the measured cross section as compared to the predicted cross section for $R = 0.4$ jets, though still consistent within uncertainties, could signify a slight over-correction during jet energy calibration for energy falling outside of the jet radius, but further investigation is necessary.

The measured cross sections are also compared to the cross sections predicted using the CTEQ6.6, MSTW2008, HERAPDF 1.5, and NNPDF 2.1 PDFs, as shown in Figures 6.7-6.14. The ratio of the prediction obtained with a given PDF, along with associated uncertainties, to that obtained with the CT10 PDF is indicated by the hatched lines. In general, the predictions from CTEQ6.6 are very similar to those from CT10, but with slightly smaller stated uncertainties. MSTW2008, HERAPDF, and NNPDF all predict smaller cross sections at high p_T than those predicted by the CTEQ PDFs, giving slightly better agreement with the data in the forward regions. HERAPDF, which includes only data from deep inelastic scattering at HERA, produces the best agreement with the measured cross sections at high p_T and high rapidity.

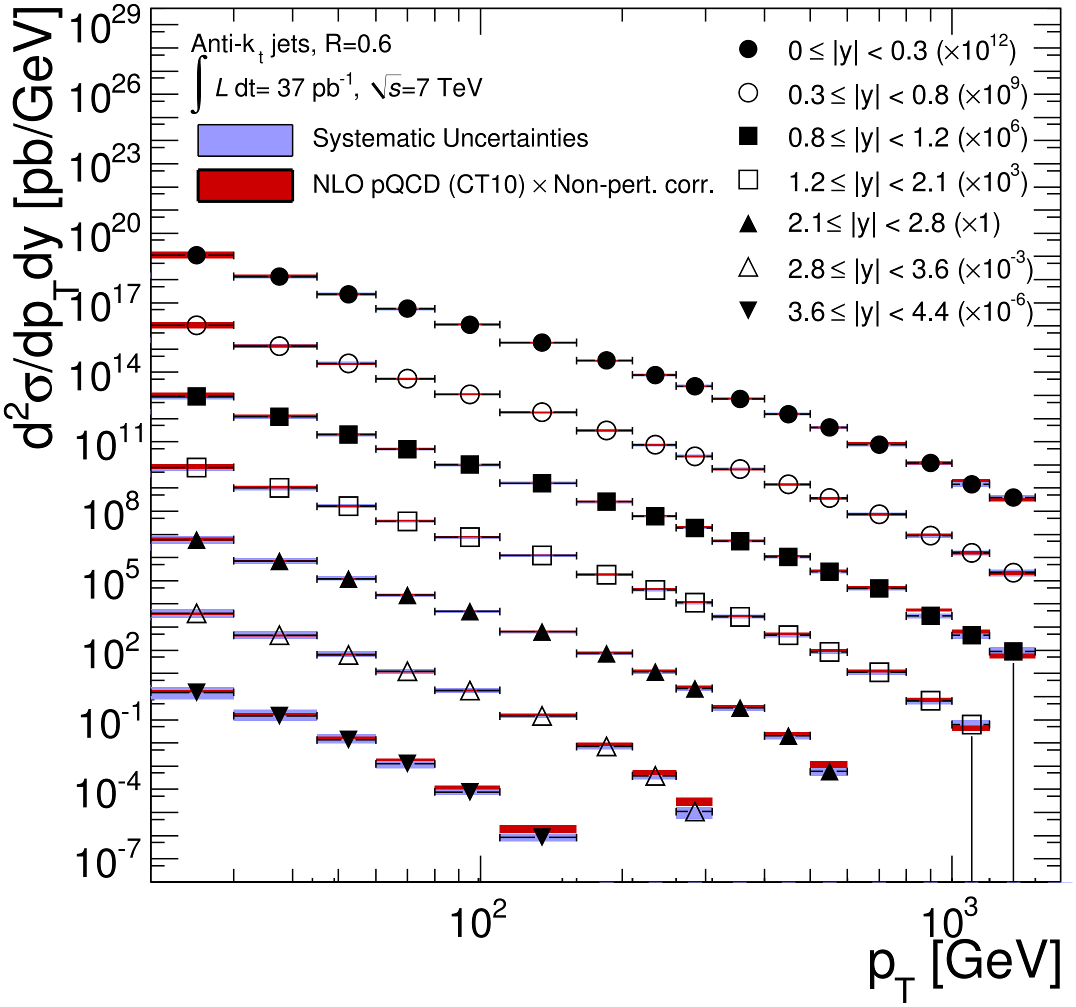

Figure 6.1: Inclusive jet double-differential cross section as a function of jet p_T in different regions of absolute rapidity for jets identified using the anti-k$_t$ algorithm with $R = 0.6$. For clarity, the cross sections are multiplied by the factors indicated in the legend. The data are compared to NLO perturbative QCD calculations to which non-perturbative corrections have been applied. The error bars indicate the statistical uncertainty on the measurement, and the light shaded bands indicate the quadratic sum of the experimental systematic uncertainties, which is dominated by the jet energy scale uncertainty. The baseline theoretical predictions are performed with the CT10 parton distribution functions. The theory uncertainty, indicated by the dark shaded bans, is the quadratic sum of uncertainties from the choice of parton distribution functions, renormalisation and factorisation scales, α_s, and the modeling of non-perturbative effects.

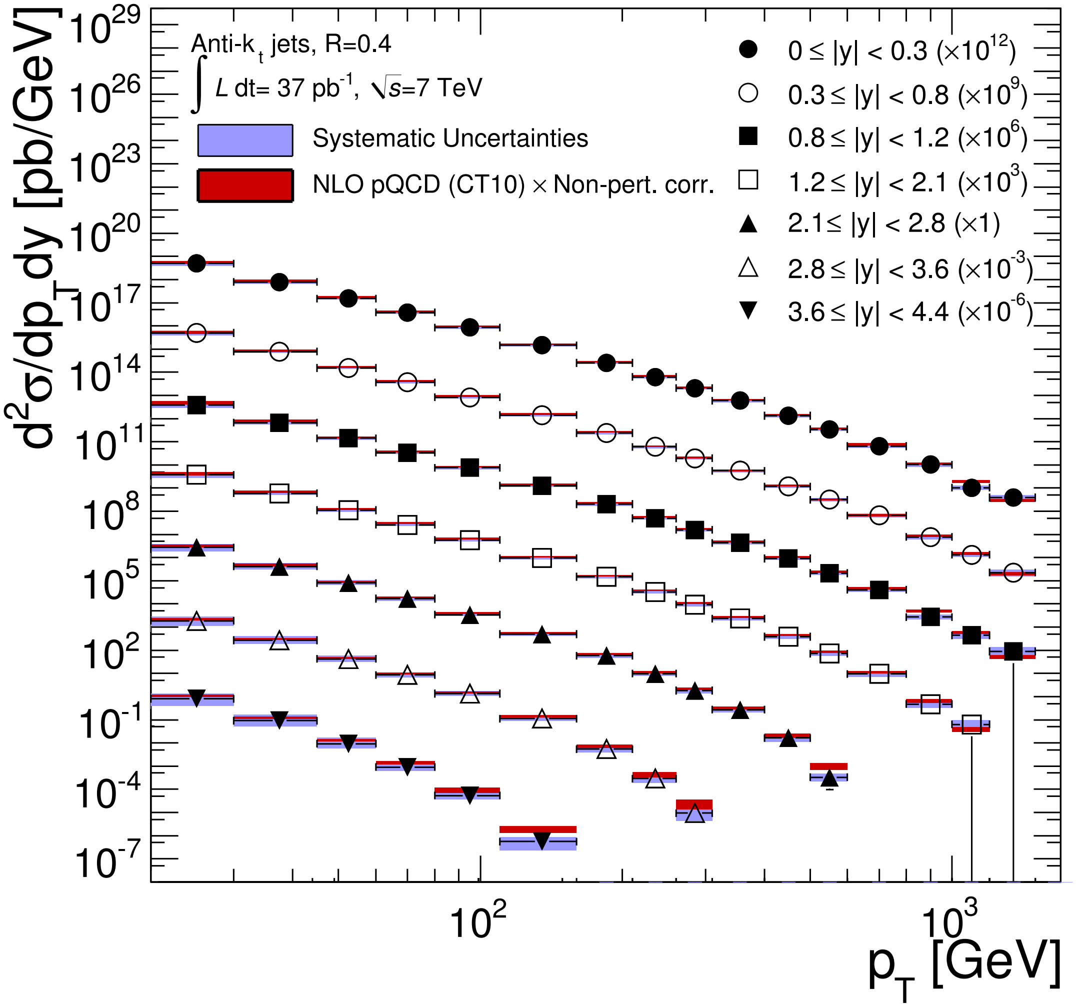

Figure 6.2: Inclusive jet double-differential cross section as a function of jet p_T in different regions of absolute rapidity for jets identified using the anti-k$_t$ algorithm with $R = 0.4$. For clarity, the cross sections are multiplied by the factors indicated in the legend. The data are compared to NLO perturbative QCD calculations to which non-perturbative corrections have been applied. The error bars indicate the statistical uncertainty on the measurement, and the light shaded bands indicate the quadratic sum of the experimental systematic uncertainties, which is dominated by the jet energy scale uncertainty. The baseline theoretical predictions are performed with the CT10 parton distribution functions. The theory uncertainty, indicated by the dark shaded bans, is the quadratic sum of uncertainties from the choice of parton distribution functions, renormalisation and factorisation scales, α_s, and the modeling of non-perturbative effects.

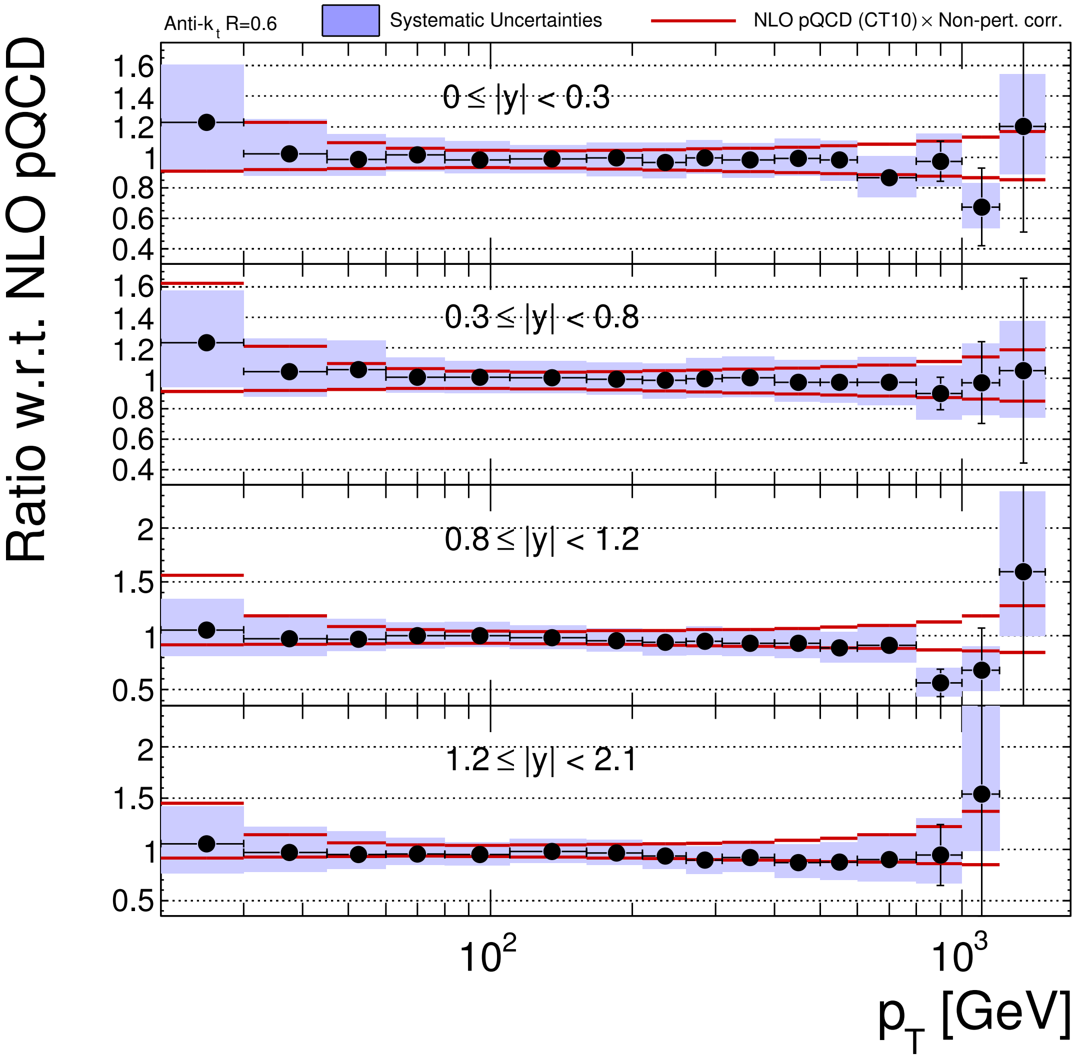

Figure 6.3: Inclusive jet double-differential cross section as a function of jet p_T in different regions of absolute rapidity for jets identified using the anti-k$_t$ algorithm with $R = 0.6$. The ratio of the data to the theoretical prediction obtained using the CT10 parton distribution function is shown, and the total systematic uncertainties on the theory and measurement are indicated. The theoretical and experimental uncertainties are calculated as described in Figure 6.1.

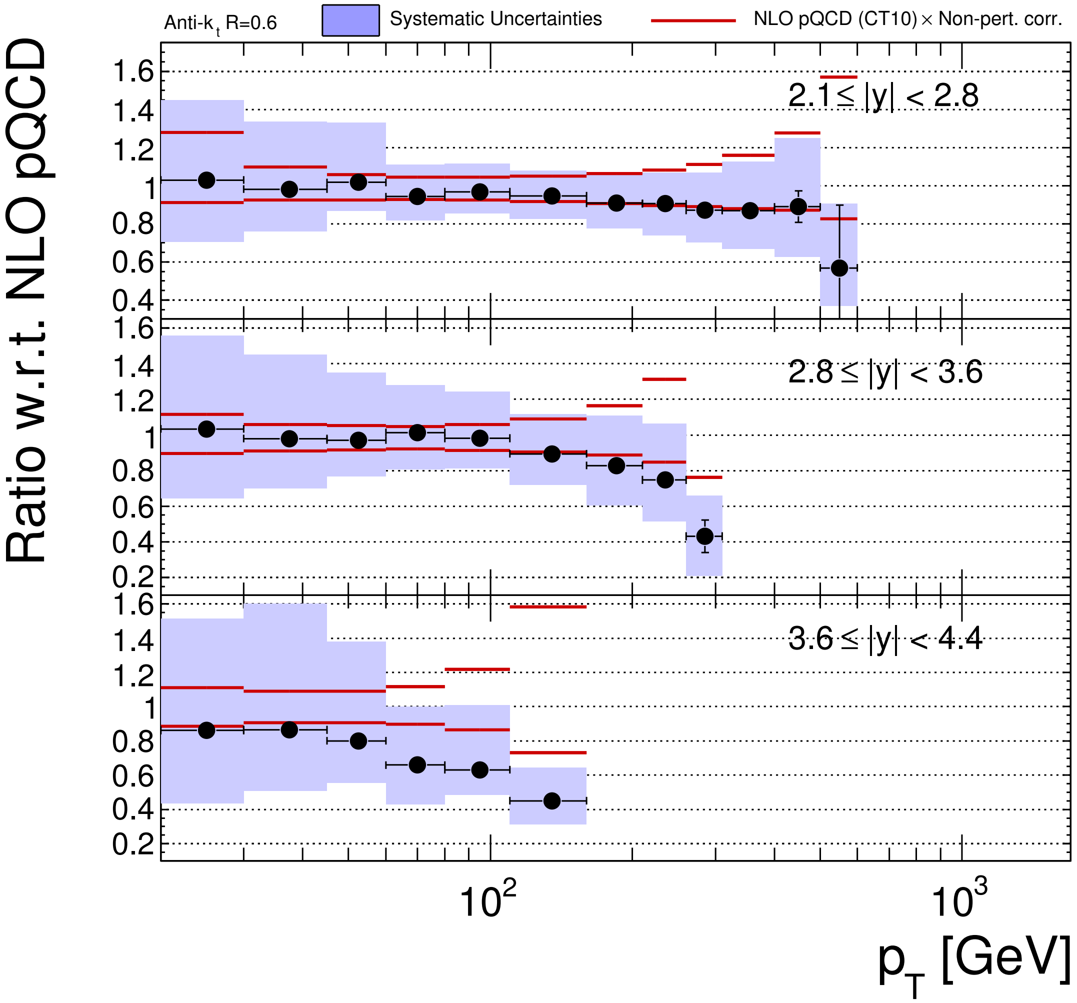

Figure 6.4: Inclusive jet double-differential cross section as a function of jet p_T in different regions of absolute rapidity for jets identified using the anti-k$_t$ algorithm with $R = 0.6$. The ratio of the data to the theoretical prediction obtained using the CT10 parton distribution function is shown, and the total systematic uncertainties on the theory and measurement are indicated. The theoretical and experimental uncertainties are calculated as described in Figure 6.1.

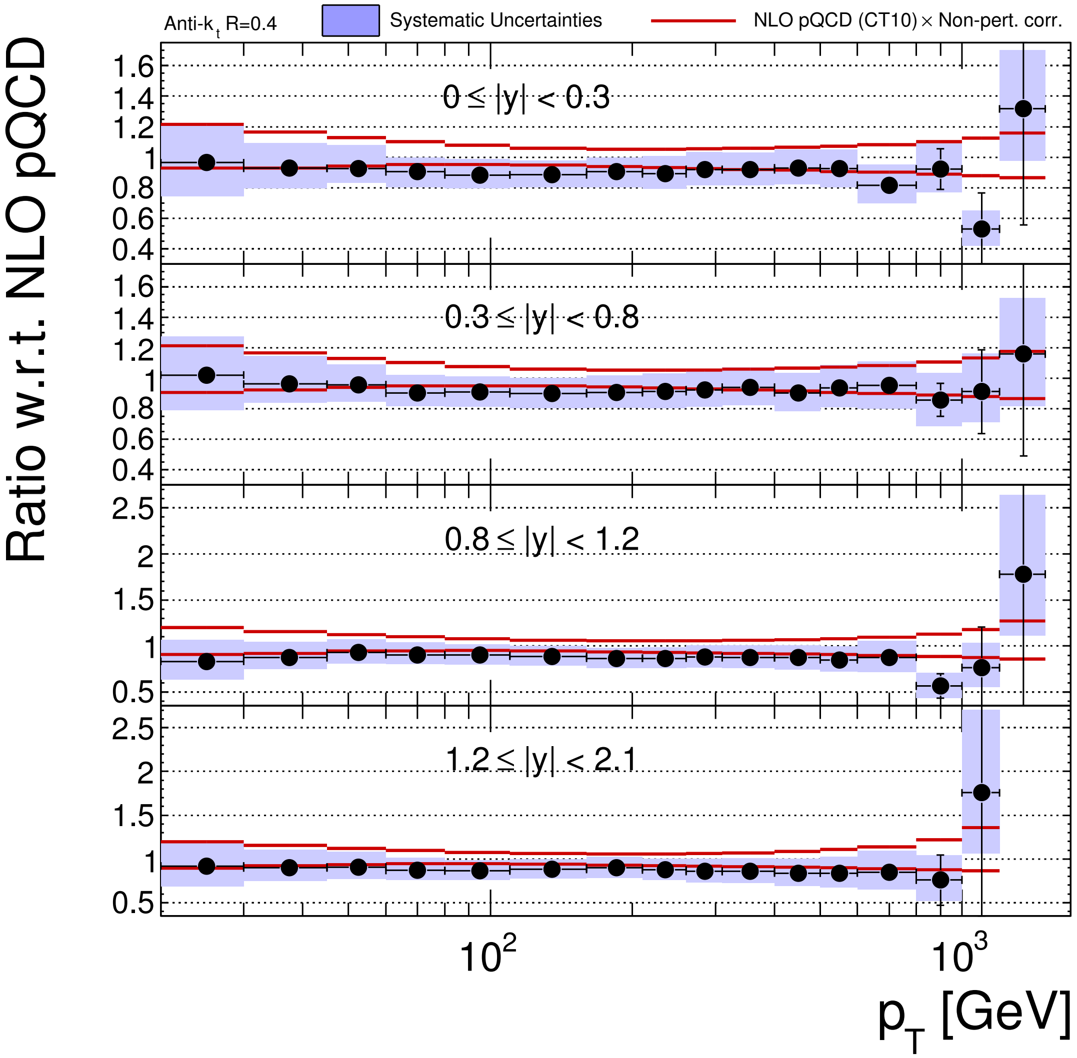

Figure 6.5: Inclusive jet double-differential cross section as a function of jet p_T in different regions of absolute rapidity for jets identified using the anti-k$_t$ algorithm with $R = 0.4$. The ratio of the data to the theoretical prediction obtained using the CT10 parton distribution function is shown, and the total systematic uncertainties on the theory and measurement are indicated. The theoretical and experimental uncertainties are calculated as described in Figure 6.2.

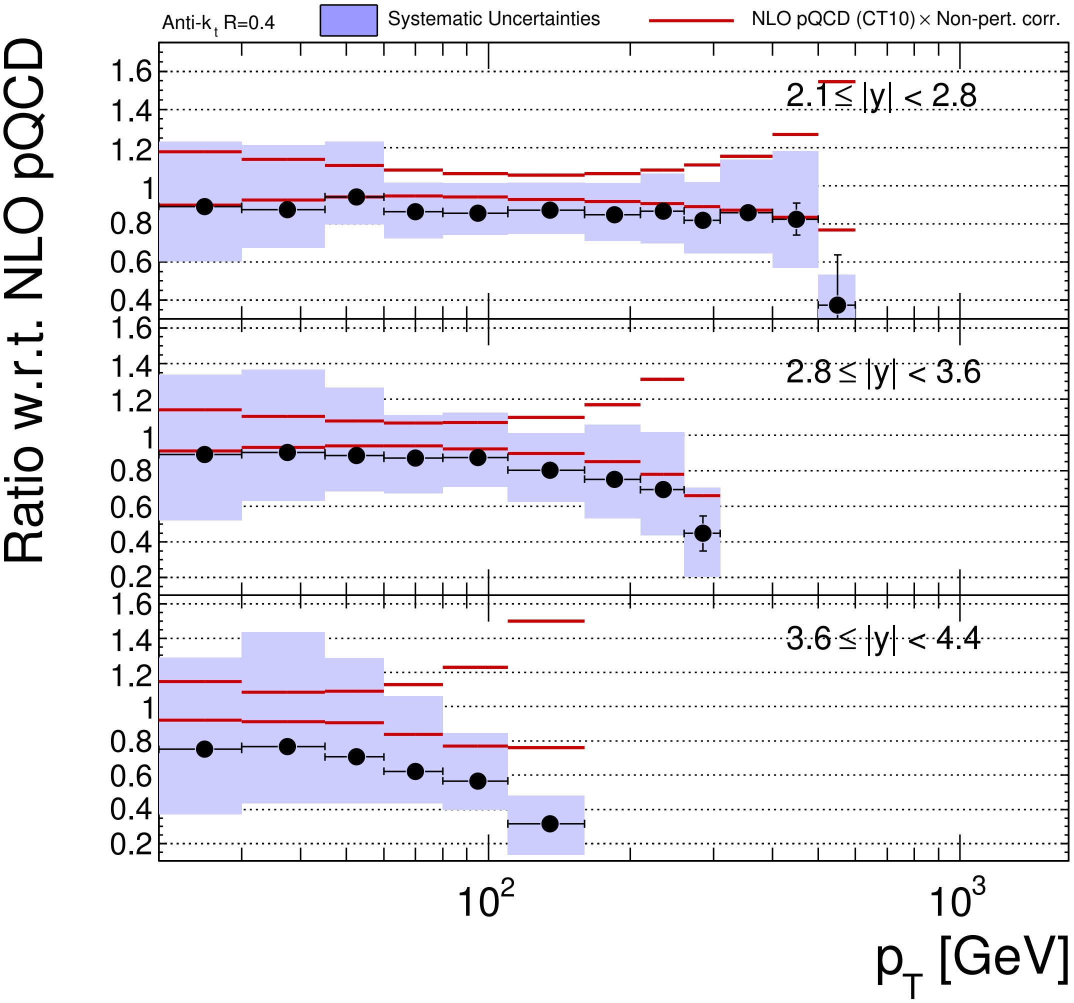

Figure 6.6: Inclusive jet double-differential cross section as a function of jet p_T in different regions of absolute rapidity for jets identified using the anti-k$_t$ algorithm with $R = 0.4$. The ratio of the data to the theoretical prediction obtained using the CT10 parton distribution function is shown, and the total systematic uncertainties on the theory and measurement are indicated. The theoretical and experimental uncertainties are calculated as described in Figure 6.2.

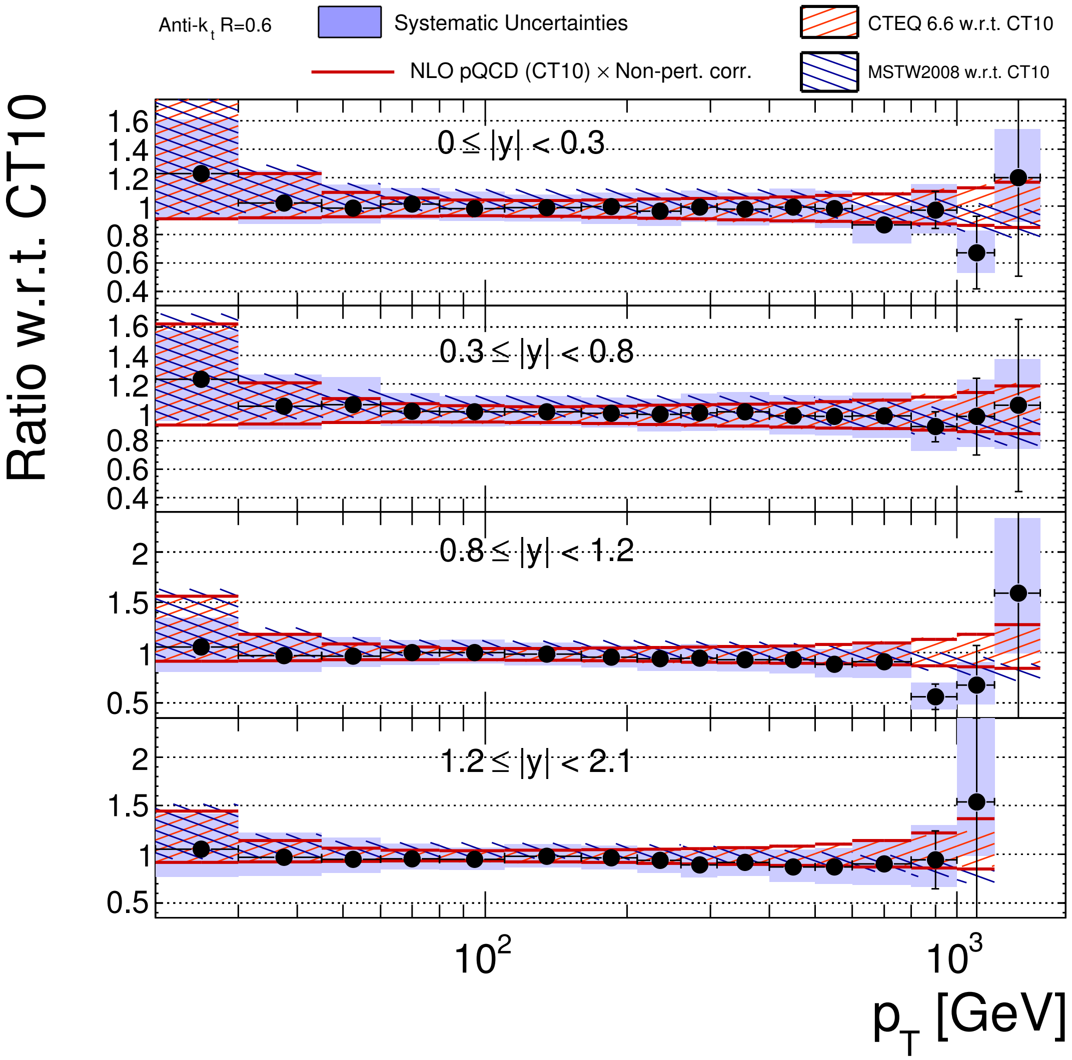

Figure 6.7: Inclusive jet double-differential cross section as a function of jet p_T in different regions of absolute rapidity for jets identified using the anti-k$_t$ algorithm with $R = 0.6$. The ratio of the data to the theoretical prediction obtained using the CT10 parton distribution function is shown, and the total systematic uncertainties on the theory and measurement are indicated. The theoretical and experimental uncertainties are calculated as described in Figure 6.1. The ratios of the theoretical predictions, with accompanying uncertainties, obtained using the CTEQ 6.6 and MSTW2008 parton distribution functions to the baseline CT10 predictions are also shown.

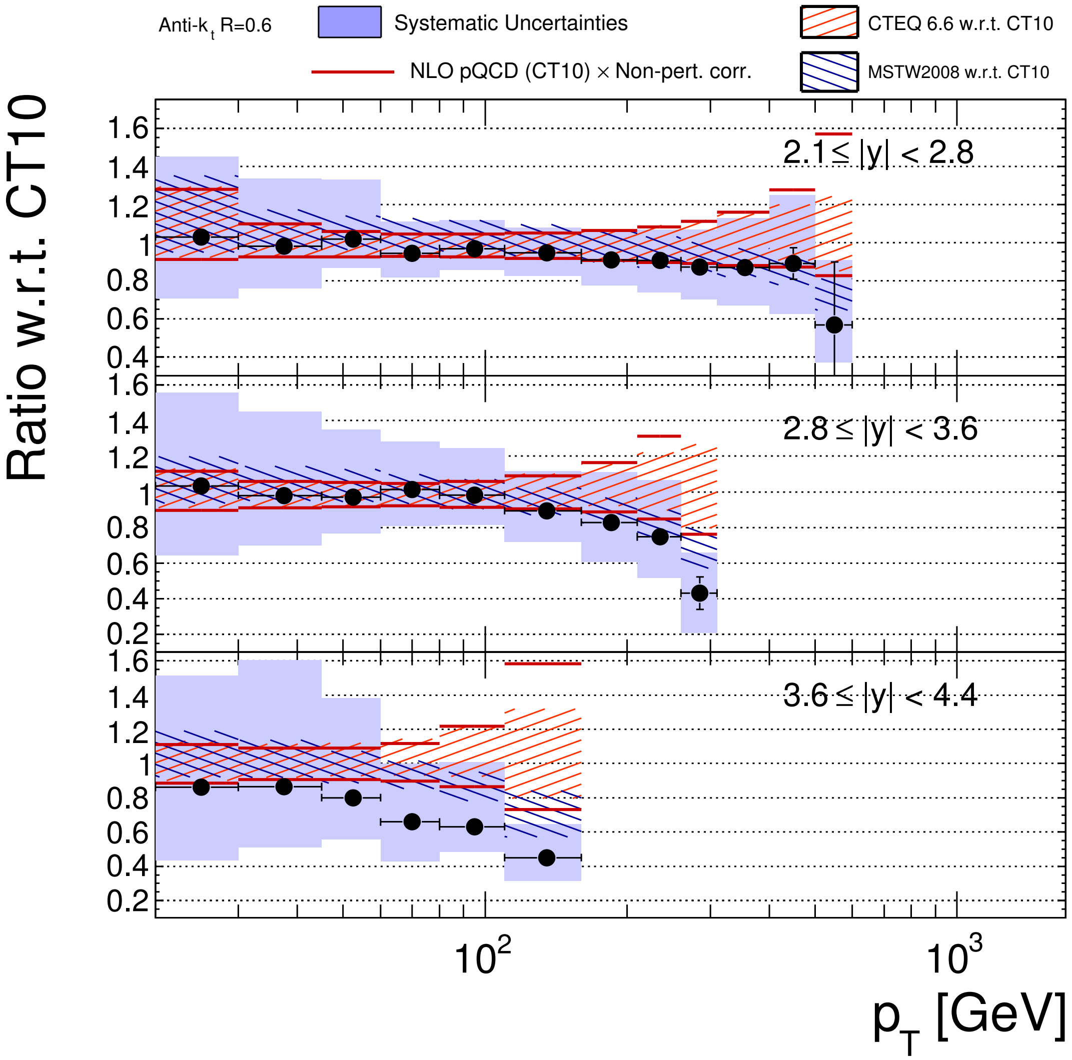

Figure 6.8: Inclusive jet double-differential cross section as a function of jet p_T in different regions of absolute rapidity for jets identified using the anti-k$_t$ algorithm with $R = 0.6$. The ratio of the data to the theoretical prediction obtained using the CT10 parton distribution function is shown, and the total systematic uncertainties on the theory and measurement are indicated. The theoretical and experimental uncertainties are calculated as described in Figure 6.1. The ratios of the theoretical predictions, with accompanying uncertainties, obtained using the CTEQ 6.6 and MSTW2008 parton distribution functions to the baseline CT10 predictions are also shown.

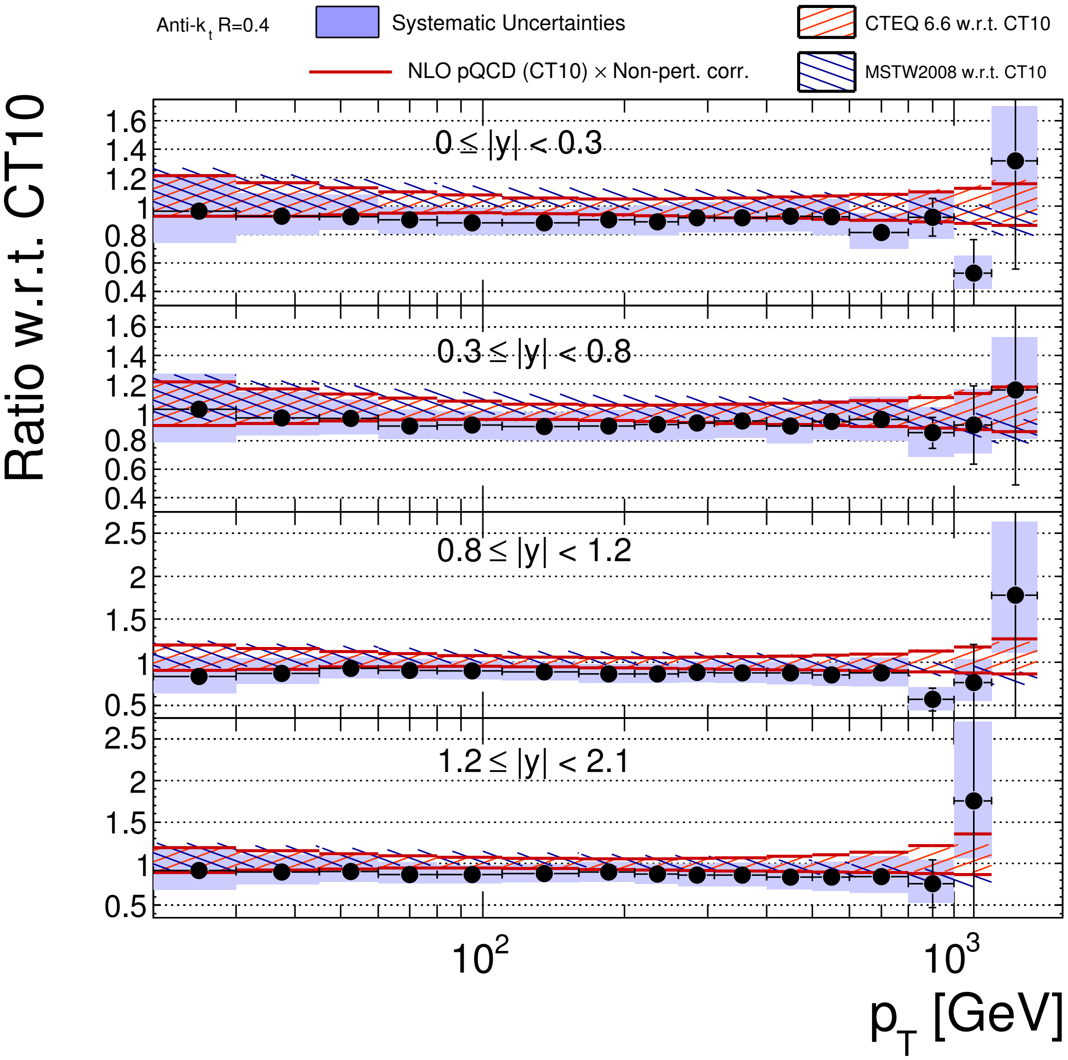

Figure 6.9: Inclusive jet double-differential cross section as a function of jet p_T in different regions of absolute rapidity for jets identified using the anti-k$_t$ algorithm with $R = 0.4$. The ratio of the data to the theoretical prediction obtained using the CT10 parton distribution function is shown, and the total systematic uncertainties on the theory and measurement are indicated. The theoretical and experimental uncertainties are calculated as described in Figure 6.2. The ratios of the theoretical predictions, with accompanying uncertainties, obtained using the CTEQ 6.6 and MSTW2008 parton distribution functions to the baseline CT10 predictions are also shown.

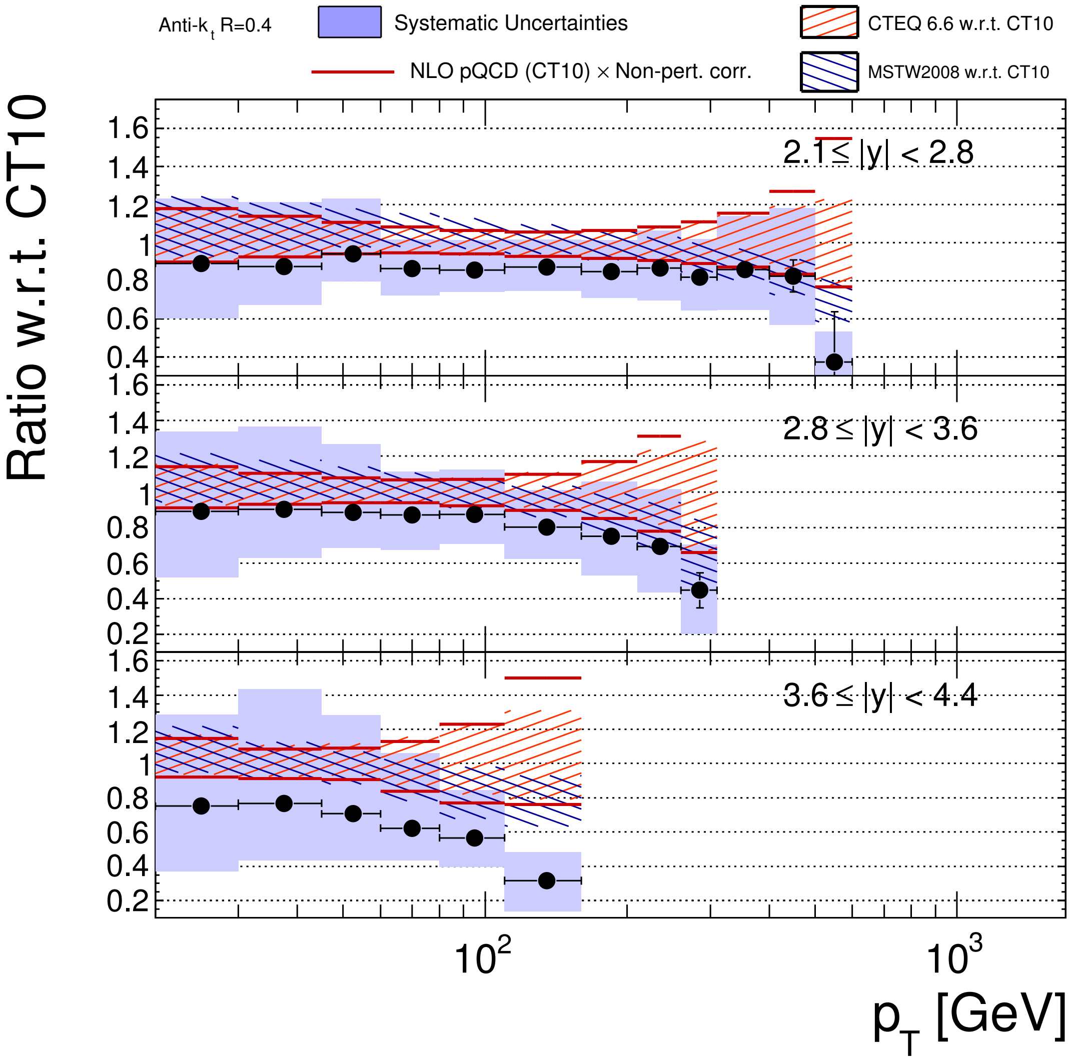

Figure 6.10: Inclusive jet double-differential cross section as a function of jet p_T in different regions of absolute rapidity for jets identified using the anti-k$_t$ algorithm with $R = 0.4$. The ratio of the data to the theoretical prediction obtained using the CT10 parton distribution function is shown, and the total systematic uncertainties on the theory and measurement are indicated. The theoretical and experimental uncertainties are calculated as described in Figure 6.2. The ratios of the theoretical predictions, with accompanying uncertainties, obtained using the CTEQ 6.6 and MSTW2008 parton distribution functions to the baseline CT10 predictions are also shown.

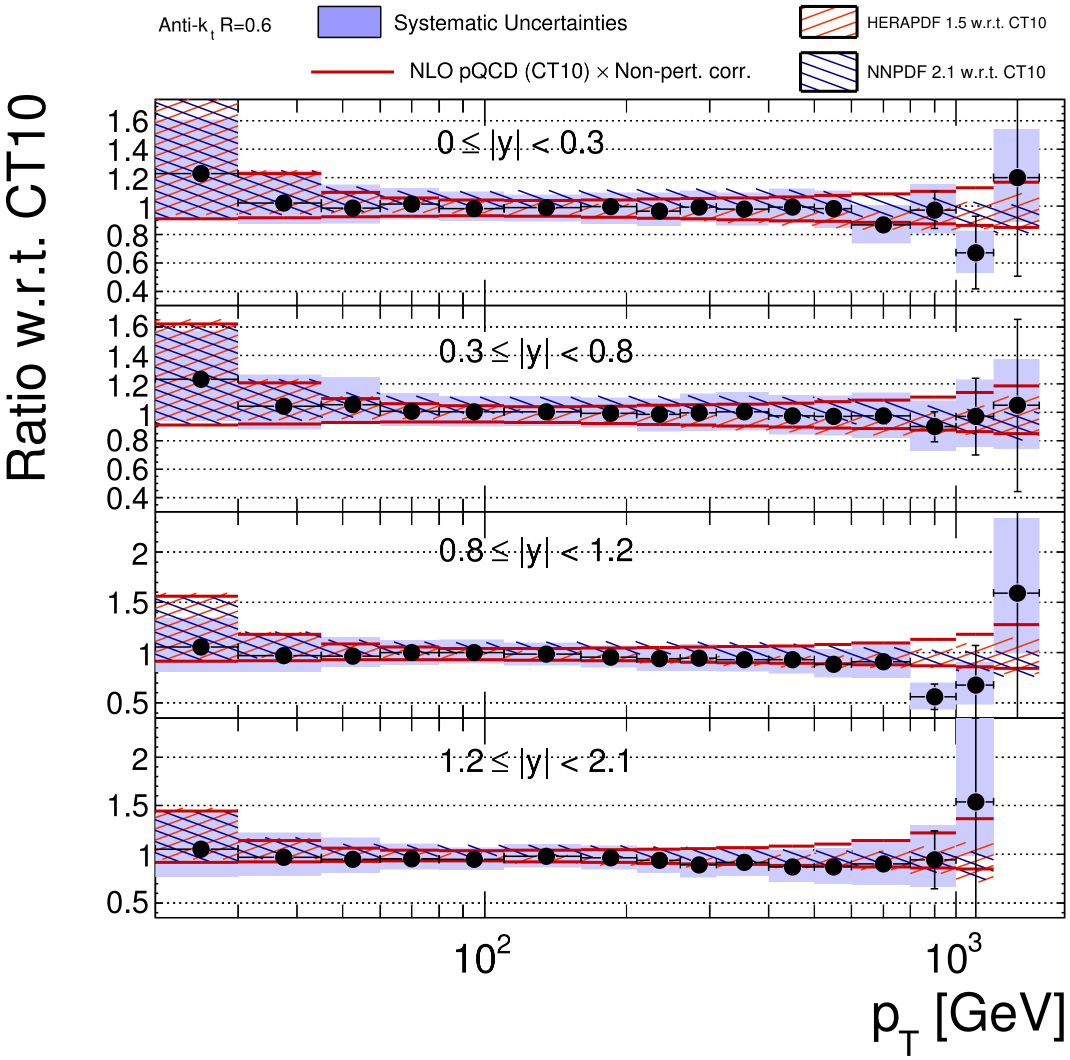

Figure 6.11: Inclusive jet double-differential cross section as a function of jet p_T in different regions of absolute rapidity for jets identified using the anti-k$_t$ algorithm with $R = 0.6$. The ratio of the data to the theoretical prediction obtained using the CT10 parton distribution function is shown, and the total systematic uncertainties on the theory and measurement are indicated. The theoretical and experimental uncertainties are calculated as described in Figure 6.1. The ratios of the theoretical predictions, with accompanying uncertainties, obtained using the HERAPDF 1.5 and NNPDF 2.1 parton distribution functions to the baseline CT10 predictions are also shown.

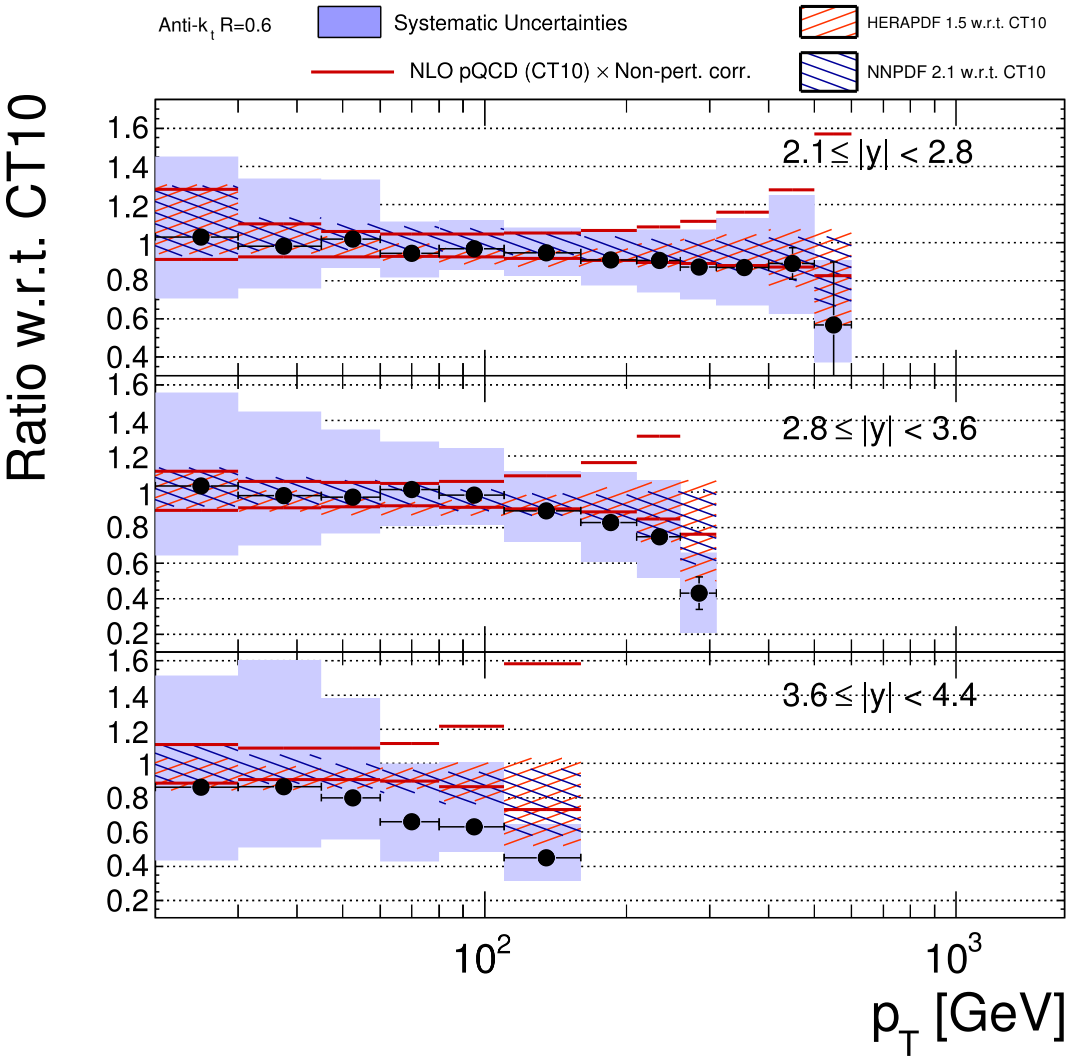

Figure 6.12: Inclusive jet double-differential cross section as a function of jet p_T in different regions of absolute rapidity for jets identified using the anti-k$_t$ algorithm with $R = 0.6$. The ratio of the data to the theoretical prediction obtained using the CT10 parton distribution function is shown, and the total systematic uncertainties on the theory and measurement are indicated. The theoretical and experimental uncertainties are calculated as described in Figure 6.1. The ratios of the theoretical predictions, with accompanying uncertainties, obtained using the HERAPDF 1.5 and NNPDF 2.1 parton distribution functions to the baseline CT10 predictions are also shown.

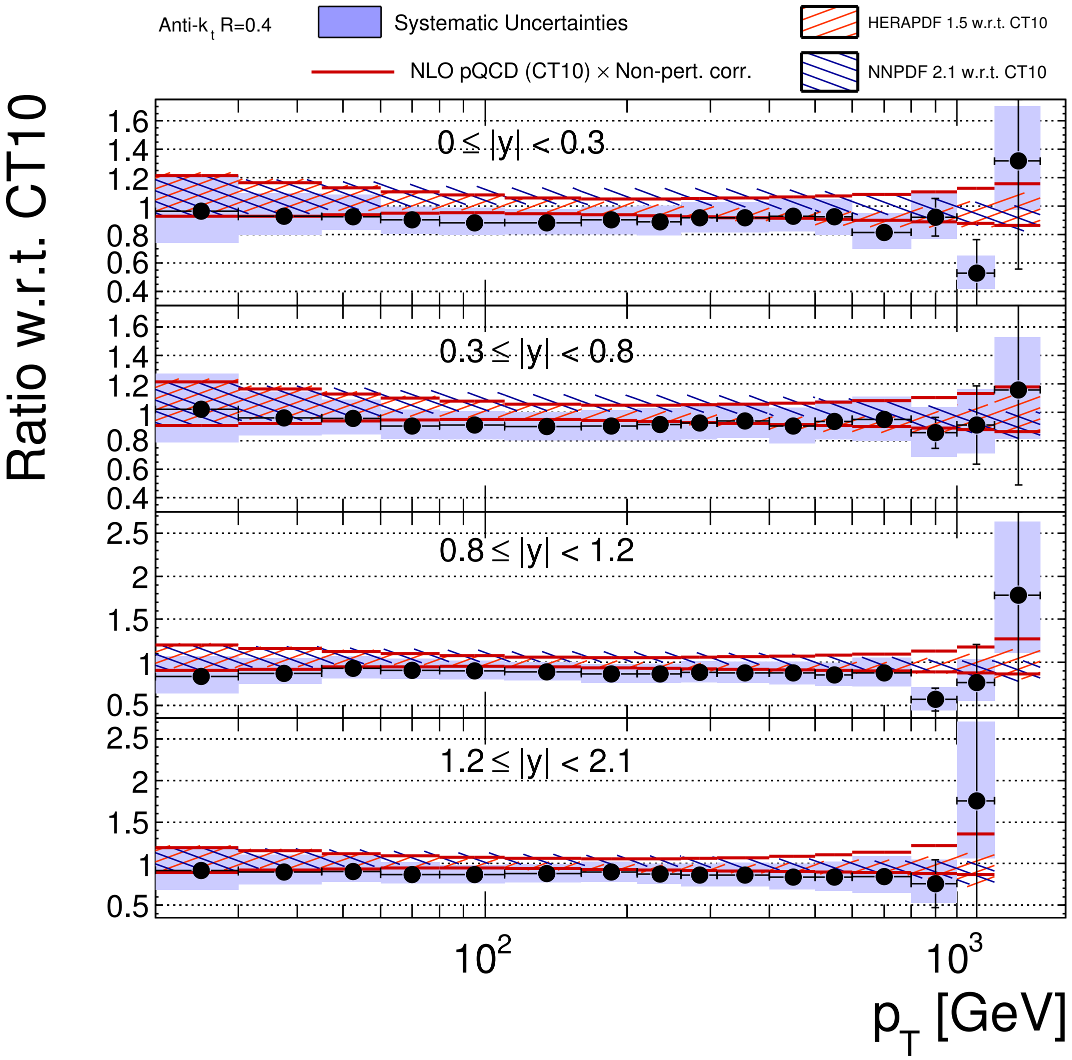

Figure 6.13: Inclusive jet double-differential cross section as a function of jet p_T in different regions of absolute rapidity for jets identified using the anti-k$_t$ algorithm with $R = 0.4$. The ratio of the data to the theoretical prediction obtained using the CT10 parton distribution function is shown, and the total systematic uncertainties on the theory and measurement are indicated. The theoretical and experimental uncertainties are calculated as described in Figure 6.2. The ratios of the theoretical predictions, with accompanying uncertainties, obtained using the HERAPDF 1.5 and NNPDF 2.1 parton distribution functions to the baseline CT10 predictions are also shown.

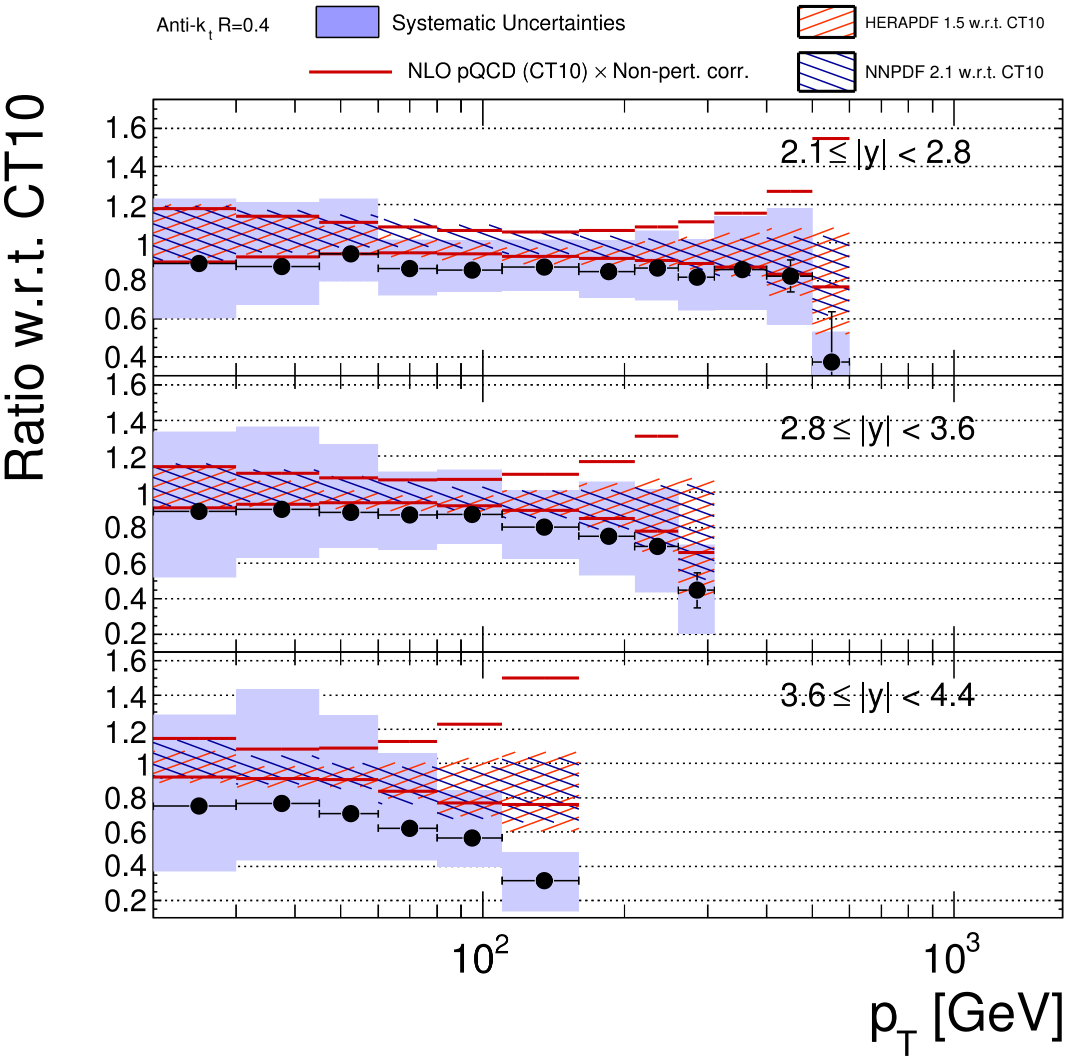

Figure 6.14: Inclusive jet double-differential cross section as a function of jet p_T in different regions of absolute rapidity for jets identified using the anti-k$_t$ algorithm with $R = 0.4$. The ratio of the data to the theoretical prediction obtained using the CT10 parton distribution function is shown, and the total systematic uncertainties on the theory and measurement are indicated. The theoretical and experimental uncertainties are calculated as described in Figure 6.2. The ratios of the theoretical predictions, with accompanying uncertainties, obtained using the HERAPDF 1.5 and NNPDF 2.1 parton distribution functions to the baseline CT10 predictions are also shown.

Chapter 7 Future Prospects

In addition to the comparisons with NLO perturbative QCD predictions to which non-perturbative corrections have been applied, a new generation of Monte Carlo generators are beginning to make possible comparisons to NLO predictions that coherently incorporate non-perturbative effects in the event generation. The first such Monte Carlo generator that has become available for jet production is Powheg [100]. Powheg includes NLO matrix elements within its event generation, and then uses existing Monte Carlo generators to directly perform showering and hadronization of the outgoing partons and incorporate underlying event. Thus, rather than the NLO calculation and non-perturbative effects being accounted for in two separate steps, they are coherently treated with the same set of events.

The ratios of data and Powheg predictions to NLO predictions corrected for non-perturbative effects are shown in Figures 7.1-7.4, for both $R = 0.6$ and $R = 0.4$ jets. Both the NLO prediction and the Powheg matrix element calculation use the MSTW2008 PDF set. The Powheg events are then showered separately using Pythia and Herwig[1], utilizing the particular PDF incorporated in each generator. Each generator uses an underlying event tune based on ATLAS data, with Pythia using the AMBT1 [52] tune and Herwig using the AUET1 [101] tune.

The predictions of Powheg with Pythia and Powheg with Herwig are both consistent with the data, within the present uncertainties. Since the underlying NLO matrix elements are the same for both Powheg implementations, the differences between the two predictions are entirely due to the differing parton shower, hadronization, and underlying event implementations. Powheg with Herwig in general predicts smaller cross sections than Powheg with Pythia, except in the low p_T and forward rapidity regions that are affected by the stronger underlying event in Herwig. Both Powheg cross section predictions are larger than the NLO predictions and the data at low p_T. At high p_T, the Powheg predictions are smaller than the NLO predictions, but more consistent with the data. This promising agreements motivates Powheg as a potential new standard for QCD jet predictions.

---

[1] Herwig [85] is the earlier, Fortran version of Herwig++. Like Herwig++, it utilizes an angular-ordered parton shower and cluster model of hadronization.

To further improve the precision of the cross section measurements, work is ongoing to decrease the dominant sources of systematic uncertainty, specifically the uncertainties from the jet energy scale and the unfolding. In the coming year, the dramatic planned increase in luminosity delivered by the LHC will provide enough photon events to extend the direct γ-jet balance measurements to higher p_T and more forward rapidity. These increased statistics will improve both the accuracy of the response measurement itself and the estimation of associated systematic uncertainties. The additional data will also allow for improvements in the *in-situ* multi-jet balance measurements, which are able to probe the highest values of jet p_T. These response measurements will allow ATLAS to tune the current Monte Carlo-based jet energy calibration to data, reducing the total uncertainty on the calibration.

The main contributions to the unfolding uncertainty are the uncertainty due to the p_T resolution and, at low p_T, the uncertainty on the p_T spectrum shape as modeled in Monte Carlo simulations. These will be lowered as *in-situ* jet energy resolution measurements are extended to $p_T < 20$ GeV and as both the measured resolution and the measured spectrum shape become better reproduced by the Monte Carlo. On a shorter timescale, more sophisticated unfolding techniques than the simple bin-by-bin method utilized here are being investigated. Two techniques that attempt to solve the problem of matrix inversion posed by Equation 4.21 are the iterative unfolding methods, such as that based on Bayes' theorem [102], that update possible solutions until a stable solution is reached and the regularized unfolding methods, such as SVD unfolding [103], that attempt to smooth possible fluctuations in the inverted result using *a priori* knowledge of the result. However, both techniques still rely on the accuracy of the response matrix as constructed by Monte Carlo simulations and require care in the choice of unfolding parameters, such as when to halt iteration and the form of the regularization function.

With decreasing a jet energy scale uncertainty at high p_T, meaningful comparisons can be made not only to perturbative QCD models, but also to new physics models such as those that predict that quark substructure. In analogy with the scattering experiments that probed the nucleus and hadron substructure, these models predict the production of high-p_T jets in excess of the QCD prediction due to additional hard scatters within the quark [104]. Searches within the inclusive jet spectrum for signatures of this quark substructure would complement searches already performed using the dijet mass spectrum [105].

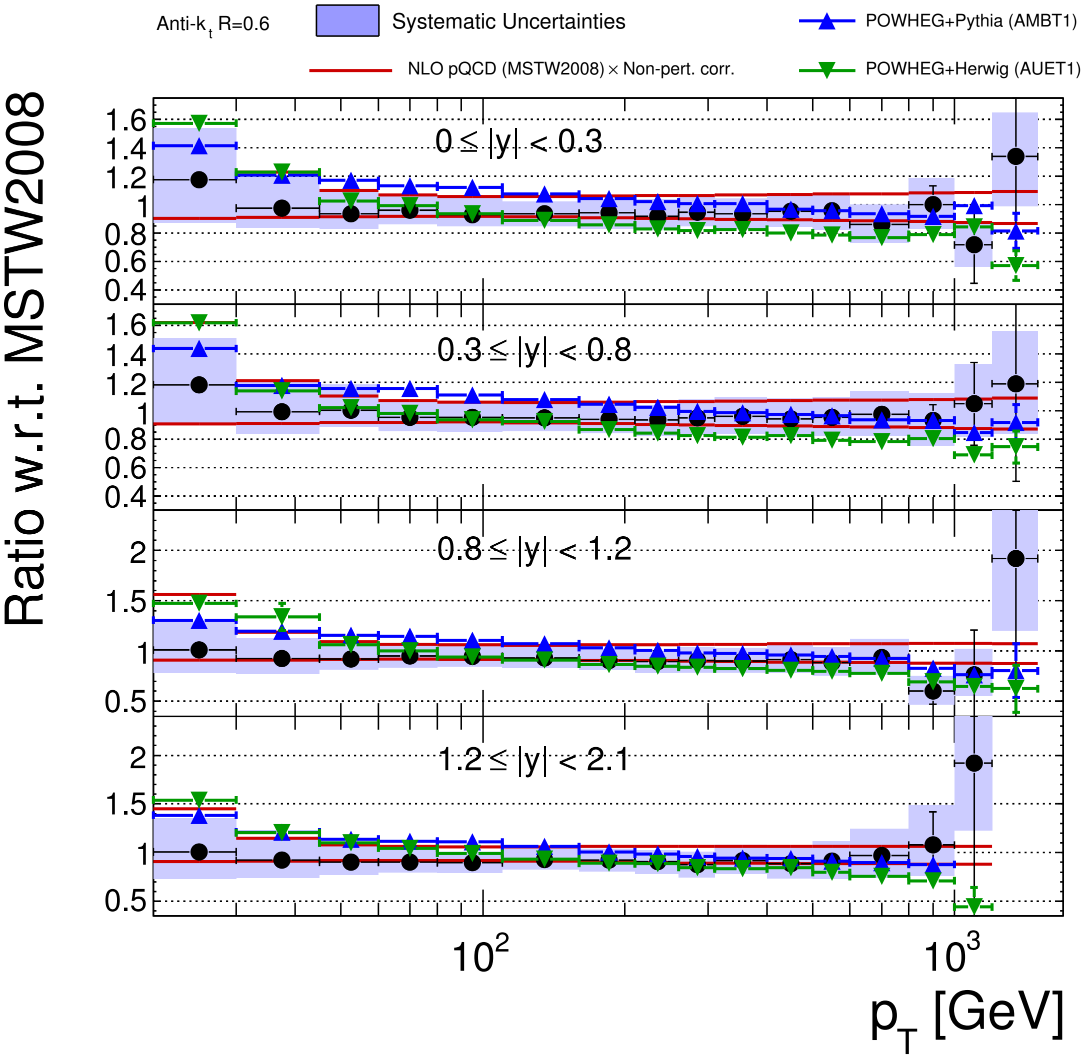

Figure 7.1: Inclusive jet double-differential cross section as a function of jet p_T in different regions of absolute rapidity for jets identified using the anti-k$_t$ algorithm with $R = 0.6$. The ratios of the data and Powheg predictions to the NLO prediction corrected for non-perturbative effects is shown. The NLO prediction and the Powheg prediction use the MSTW2008 PDF set. The total systematic uncertainties on the NLO prediction and measurement are indicated; errors on the POWHEG prediction are purely statistical.

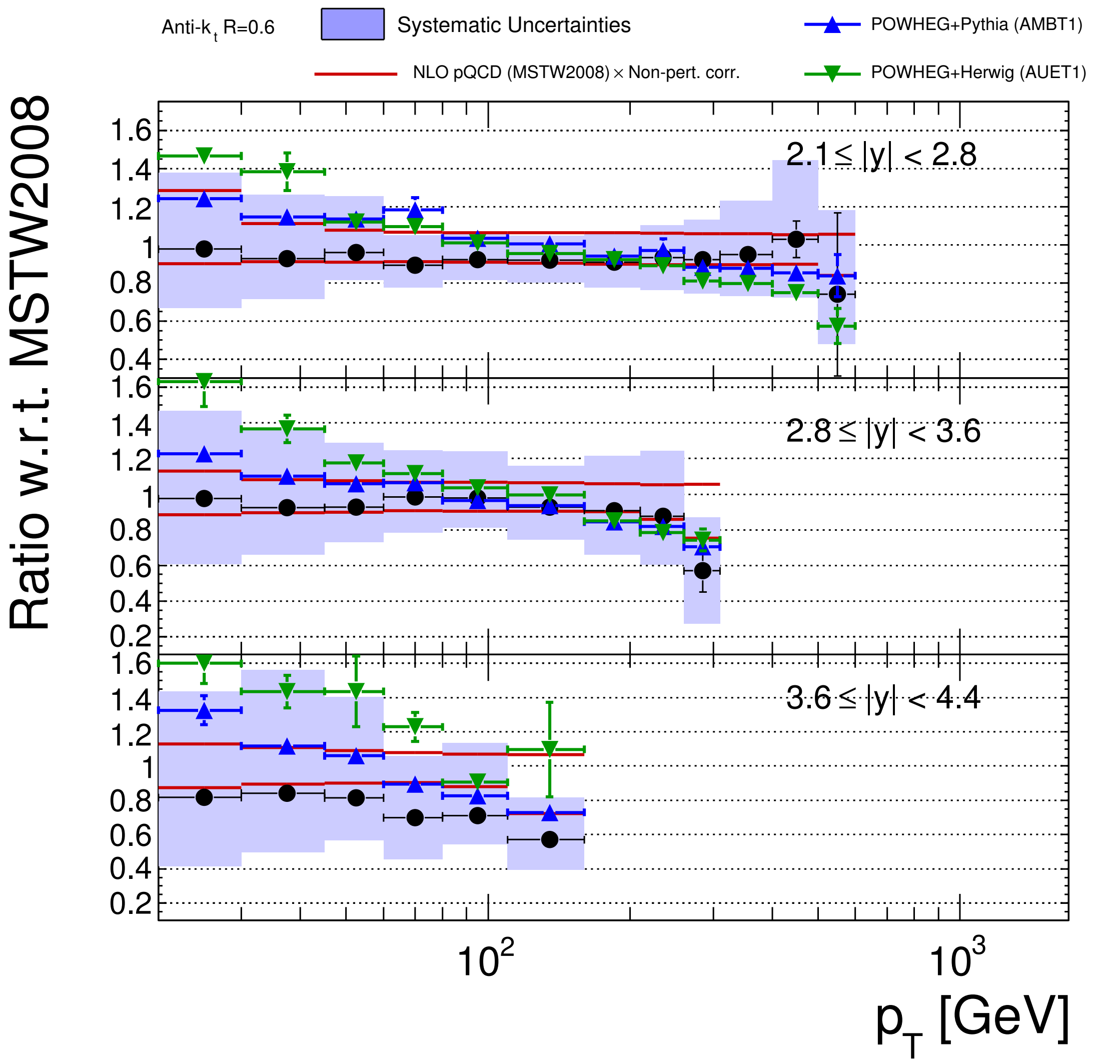

Figure 7.2: Inclusive jet double-differential cross section as a function of jet p_T in different regions of absolute rapidity for jets identified using the anti-k$_t$ algorithm with $R = 0.6$. The ratios of the data and Powheg predictions to the NLO prediction corrected for non-perturbative effects is shown. The NLO prediction and the Powheg prediction use the MSTW2008 PDF set. The total systematic uncertainties on the NLO prediction and measurement are indicated; errors on the POWHEG prediction are purely statistical.

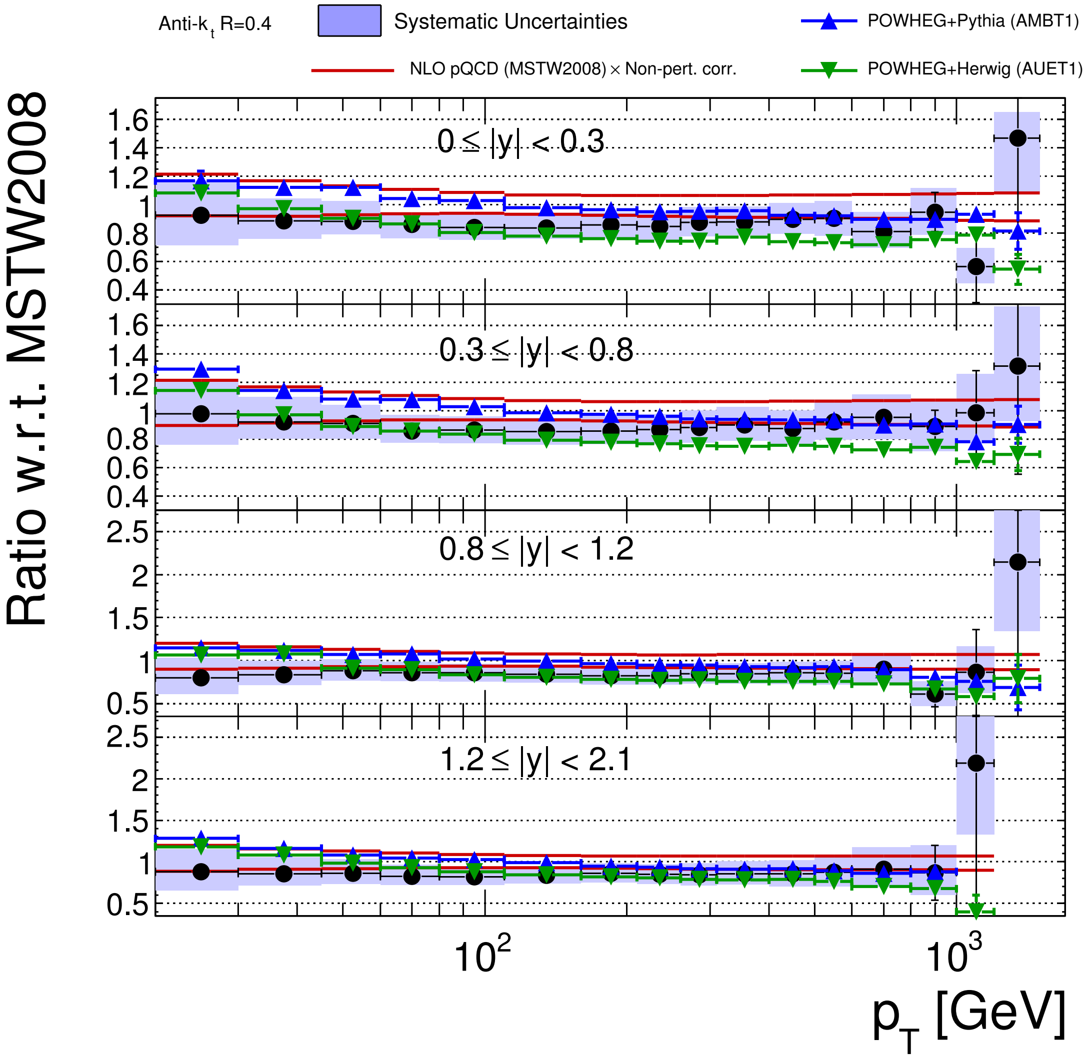

Figure 7.3: Inclusive jet double-differential cross section as a function of jet p_T in different regions of absolute rapidity for jets identified using the anti-k$_t$ algorithm with $R = 0.4$. The ratios of the data and Powheg predictions to the NLO prediction corrected for non-perturbative effects is shown. The NLO prediction and the Powheg prediction use the MSTW2008 PDF set. The total systematic uncertainties on the NLO prediction and measurement are indicated; errors on the POWHEG prediction are purely statistical.

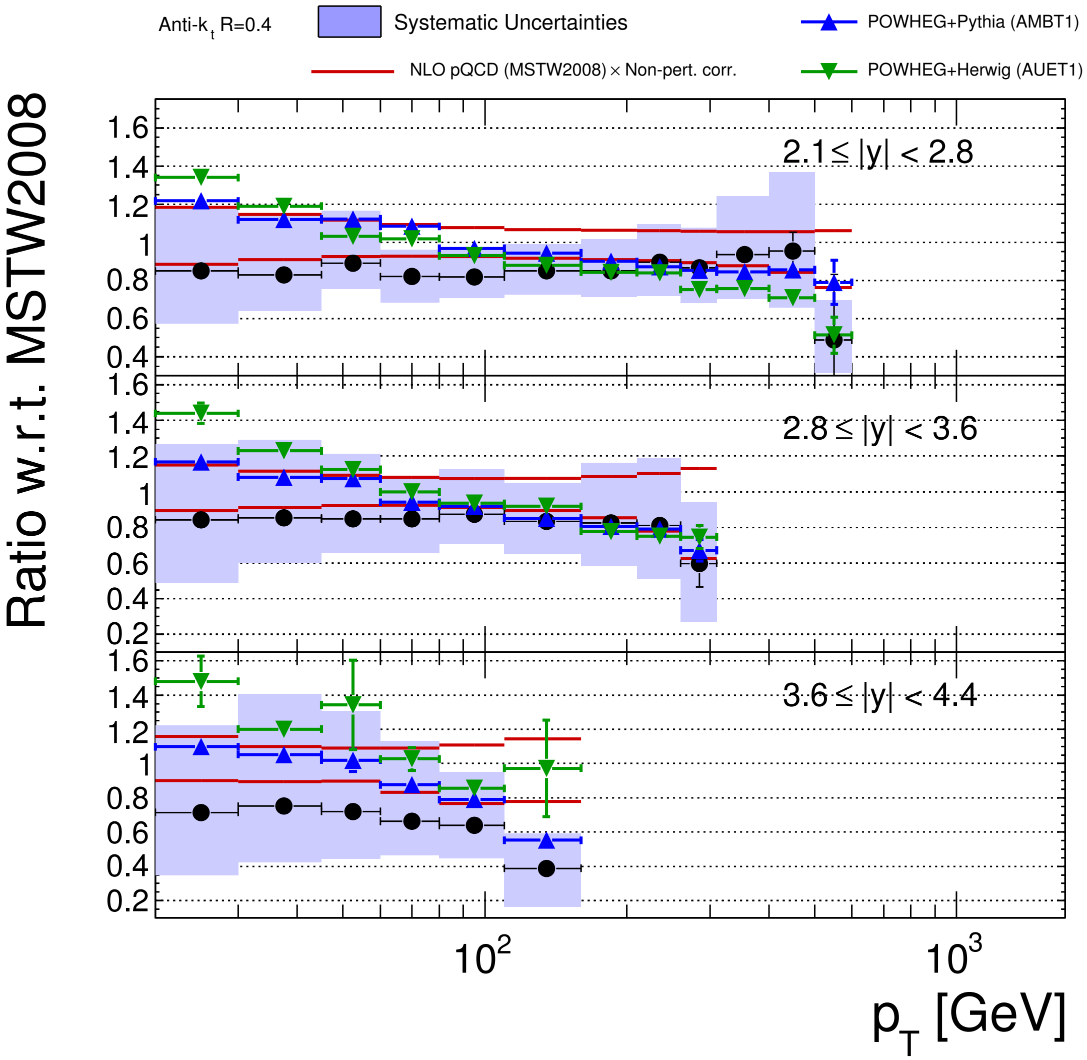

Figure 7.4: Inclusive jet double-differential cross section as a function of jet p_T in different regions of absolute rapidity for jets identified using the anti-k$_t$ algorithm with $R = 0.4$. The ratios of the data and Powheg predictions to the NLO prediction corrected for non-perturbative effects is shown. The NLO prediction and the Powheg prediction use the MSTW2008 PDF set. The total systematic uncertainties on the NLO prediction and measurement are indicated; errors on the POWHEG prediction are purely statistical.

Chapter 8 Conclusions

Inclusive jet double-differential cross sections have been measured for jets reconstructed with the anti-k$_t$ algorithm using the full 2010 ATLAS data set, consisting of 37.3 ± 1.2 pb^{-1} of integrated luminosity. These cross sections are shown as a function of jet transverse momentum in seven ranges of jet rapidity. Results have been shown for two jet sizes, $R = 0.6$ and $R = 0.4$, which each have different sensitivity to the non-perturbative effects coming from underlying event, fragmentation, and hadronization.

Measurements cover the unprecedented range of $20 \leq p_T < 1500$ GeV and $|y| < 4.4$, surpassing the previous measurements of $50 \leq p_T < 700$ GeV and $|y| < 2.4$ at $\sqrt{s} = 1.96$ TeV from the Tevatron experiments [2][3]. The measured cross sections are in good agreement with NLO perturbative QCD predictions over 18 orders of magnitude, constituting one of the most stringent tests of QCD. In addition to validating QCD in this new kinematic territory, the results confirm the precision of jet reconstruction and calibration in ATLAS, an essential component of many physics analyses.

The results are compared with predictions from several different PDF sets. Good agreement is observed in comparisons to all sets, with the HERAPDF set giving the predictions that most closely follow the data. Small differences are seen in the high-p_T and high $|y|$ regions, where previous measurements to constrain the PDFs do not exist. This indicates the utility of including this data in future PDF derivations, in particular to constrain the low-x region probed by forward jets and the high-x gluon component probed by high-p_T jets.

The systematic uncertainties on the lowest p_T bins in the central rapidity regions are small enough to be useful to constrain the large uncertainties on non-perturbative effects as modeled in various Monte Carlo generators. Indeed, the measurements across the full kinematic range are already being used as inputs to tunes for future ATLAS Monte Carlo generation, which will be used for background studies for a variety of new physics searches performed by ATLAS in the coming years.

Appendix A Inclusive Jet Trigger Efficiencies

The combination of data from the various jet trigger streams that were available in 2010 is detailed in Section 4.5. In this appendix, the inclusive jet trigger efficiencies, as measured in data, are shown for both Level-1 and Level-2 jet triggers for $R = 0.6$ and $R = 0.4$ jets.

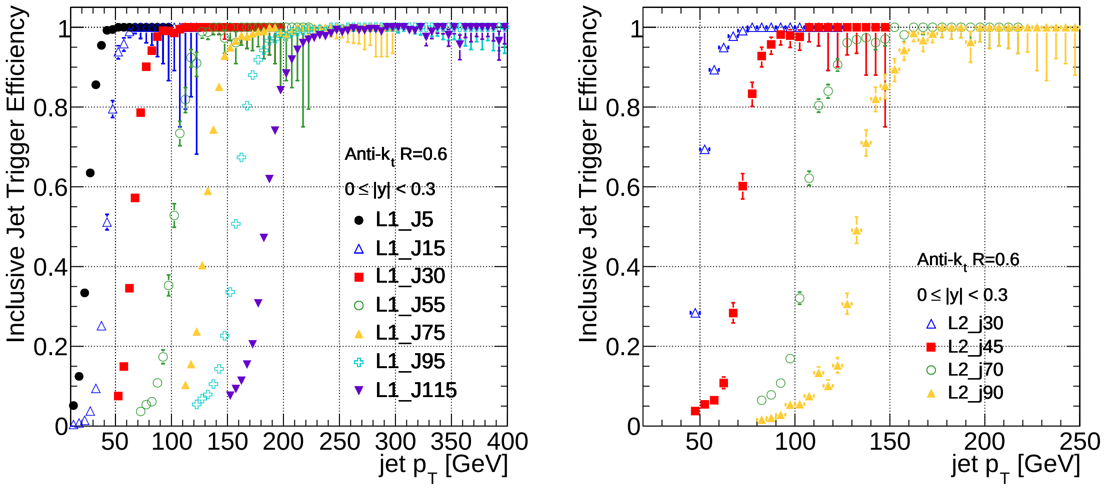

(a)

(b)

Figure A.1: Inclusive jet trigger efficiencies for $R = 0.6$ jets in the region $0 \leq |y| < 0.3$, shown for the Level-1 (a) and Level-2 (b) jet trigger items used for this analysis.

.

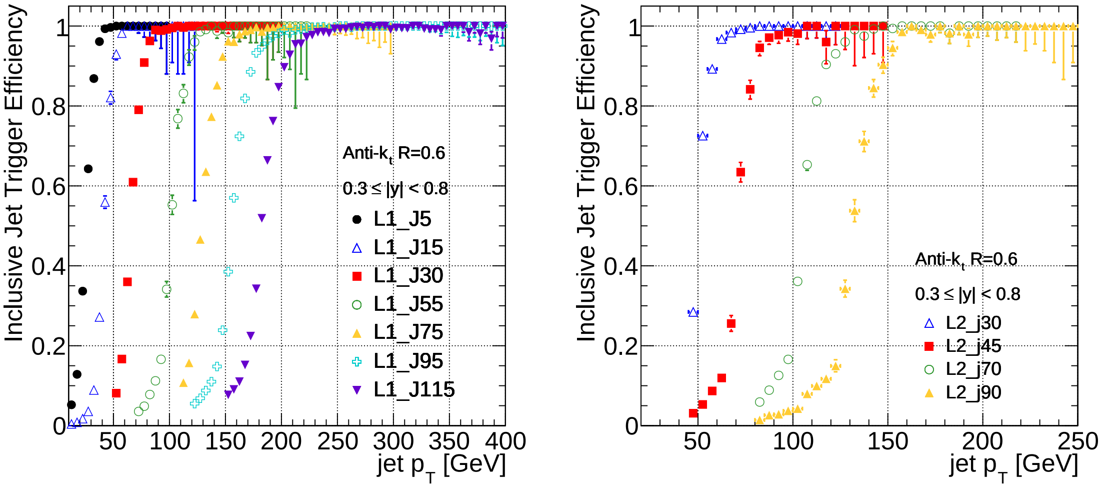

(a) (b)

Figure A.2: Inclusive jet trigger efficiencies for $R = 0.6$ jets in the region $0.3 \leq |y| < 0.8$, shown for the Level-1 (a) and Level-2 (b) jet trigger items used for this analysis.

.

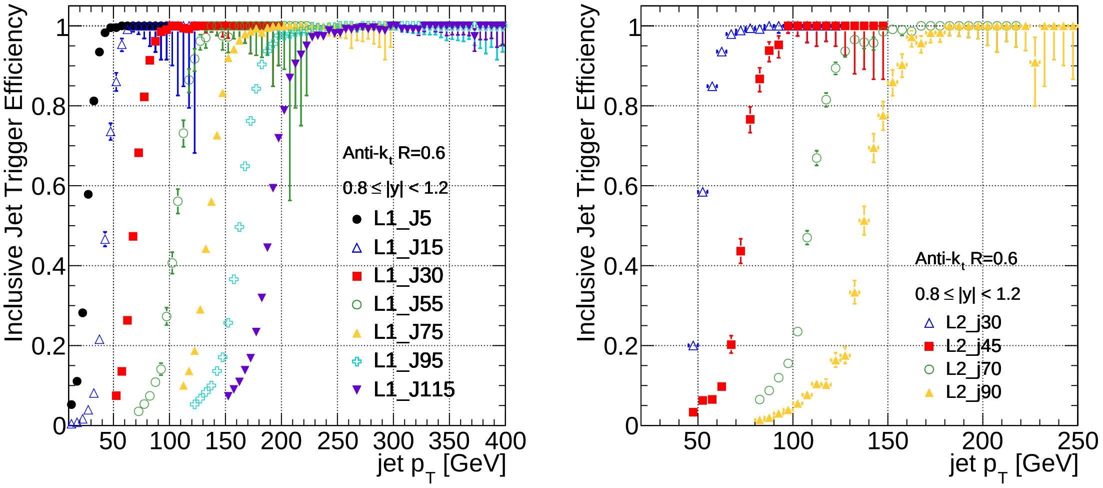

(a) (b)

Figure A.3: Inclusive jet trigger efficiencies for $R = 0.6$ jets in the region $0.8 \leq |y| < 1.2$, shown for the Level-1 (a) and Level-2 (b) jet trigger items used for this analysis.

.

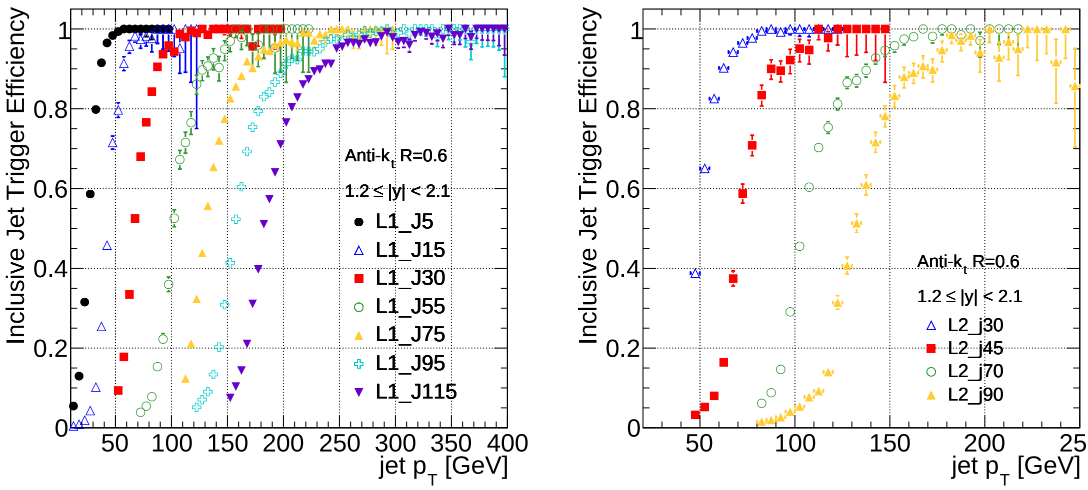

(a) (b)

Figure A.4: Inclusive jet trigger efficiencies for $R = 0.6$ jets in the region $1.2 \le |y| < 2.1$, shown for the Level-1 (a) and Level-2 (b) jet trigger items used for this analysis.

.

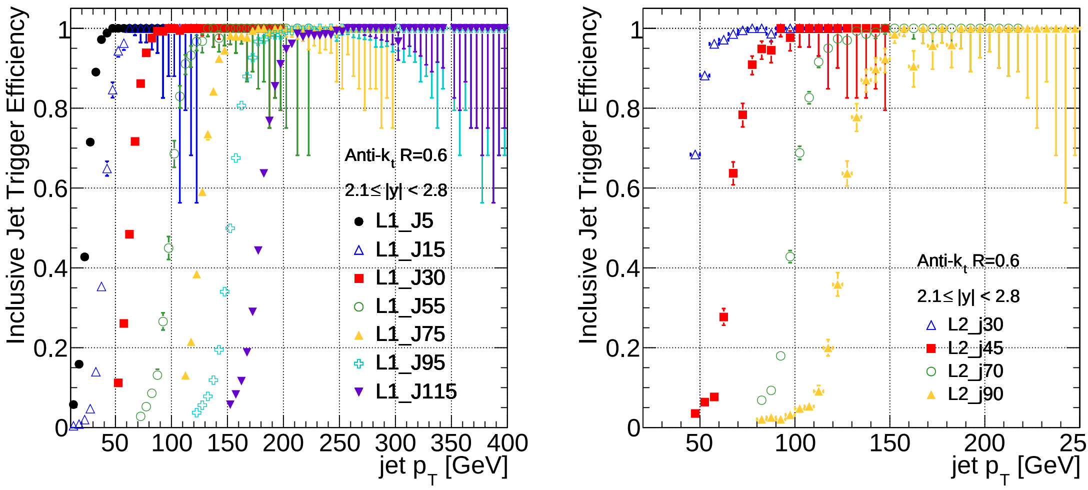

(a) (b)

Figure A.5: Inclusive jet trigger efficiencies for $R = 0.6$ jets in the region $2.1 \le |y| < 2.8$, shown for the Level-1 (a) and Level-2 (b) jet trigger items used for this analysis.

.

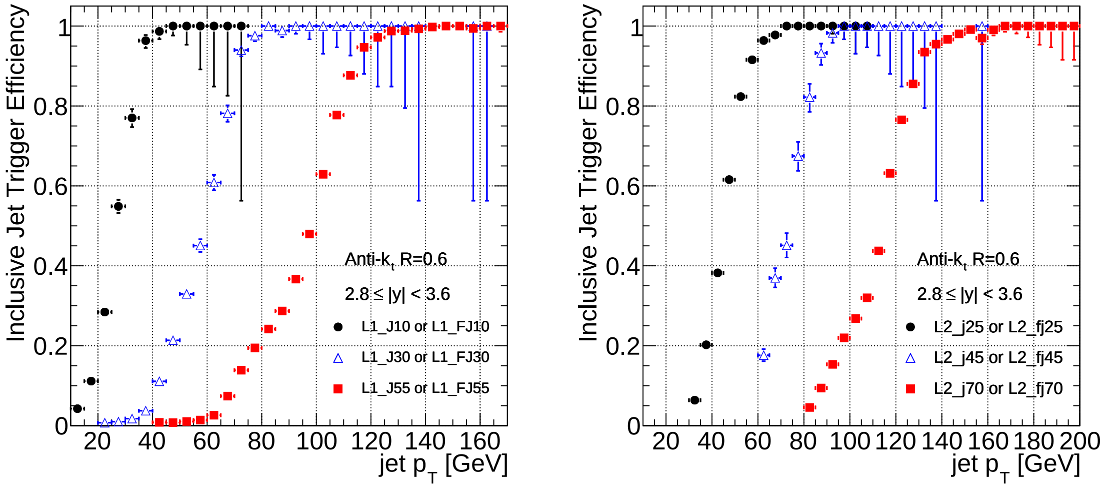

(a) (b)

Figure A.6: Inclusive jet trigger efficiencies for $R = 0.6$ jets in the region $2.8 \leq |y| < 3.6$, shown for the Level-1 (a) and Level-2 (b) jet trigger items used for this analysis.

.

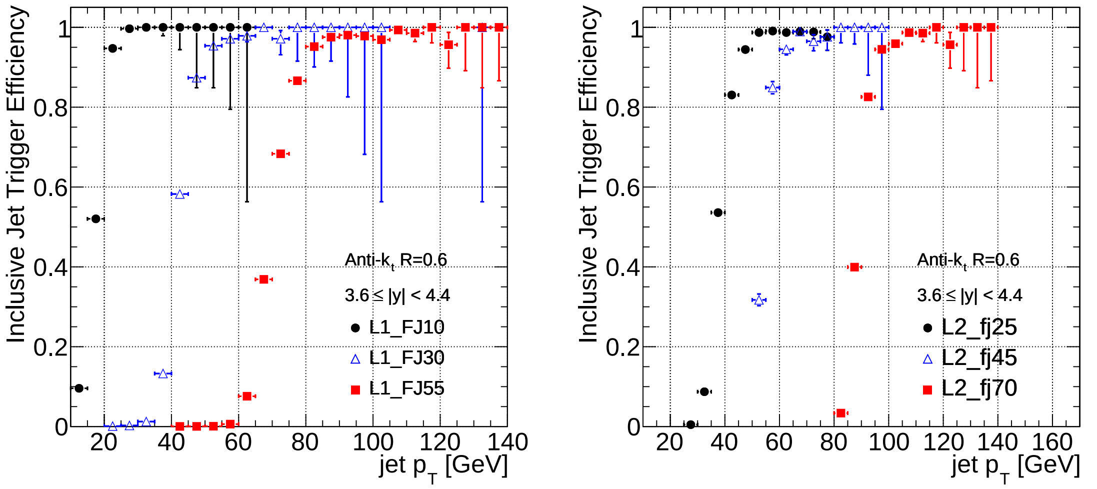

(a) (b)

Figure A.7: Inclusive jet trigger efficiencies for $R = 0.6$ jets in the region $3.6 \leq |y| < 4.4$, shown for the Level-1 (a) and Level-2 (b) jet trigger items used for this analysis.

.

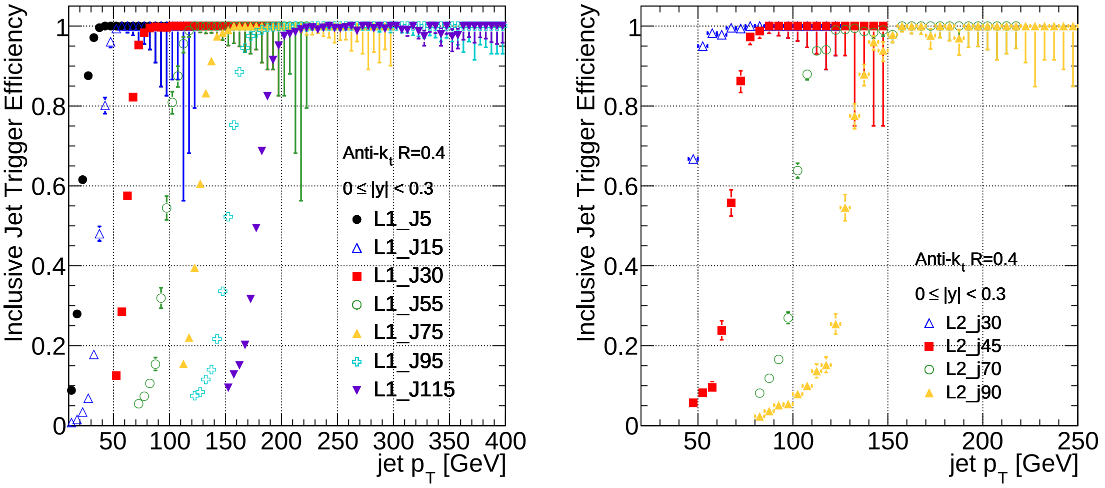

(a) (b)

Figure A.8: Inclusive jet trigger efficiencies for $R = 0.4$ jets in the region $0 \leq |y| < 0.3$, shown for the Level-1 (a) and Level-2 (b) jet trigger items used for this analysis.

.

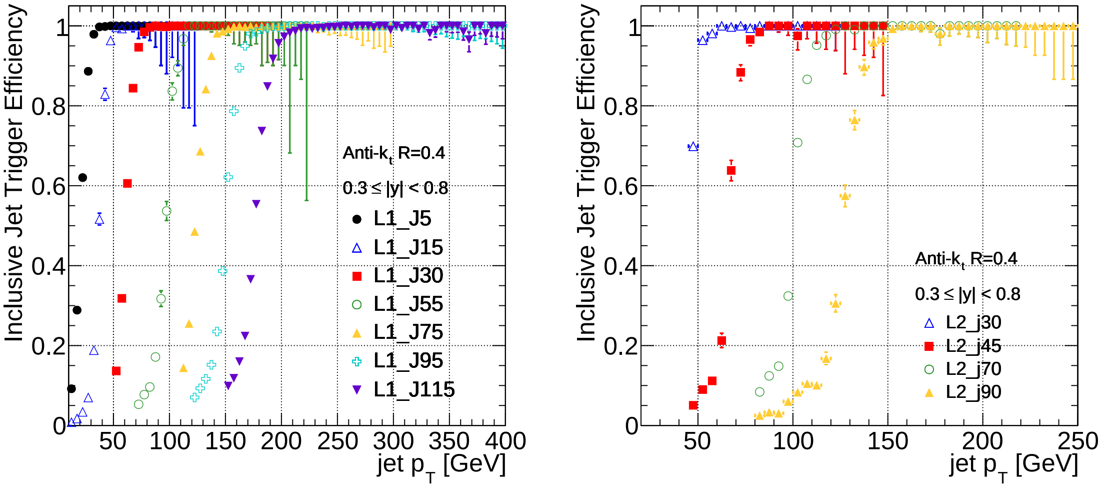

(a) (b)

Figure A.9: Inclusive jet trigger efficiencies for $R = 0.4$ jets in the region $0.3 \leq |y| < 0.8$, shown for the Level-1 (a) and Level-2 (b) jet trigger items used for this analysis.

.

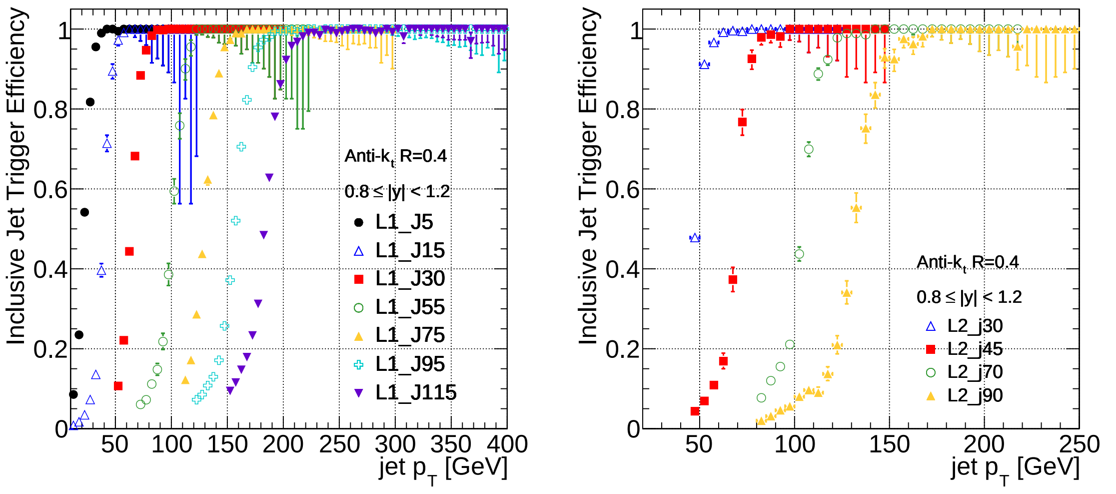

(a) (b)

Figure A.10: Inclusive jet trigger efficiencies for $R = 0.4$ jets in the region $0.8 \leq |y| < 1.2$, shown for the Level-1 (a) and Level-2 (b) jet trigger items used for this analysis.

.

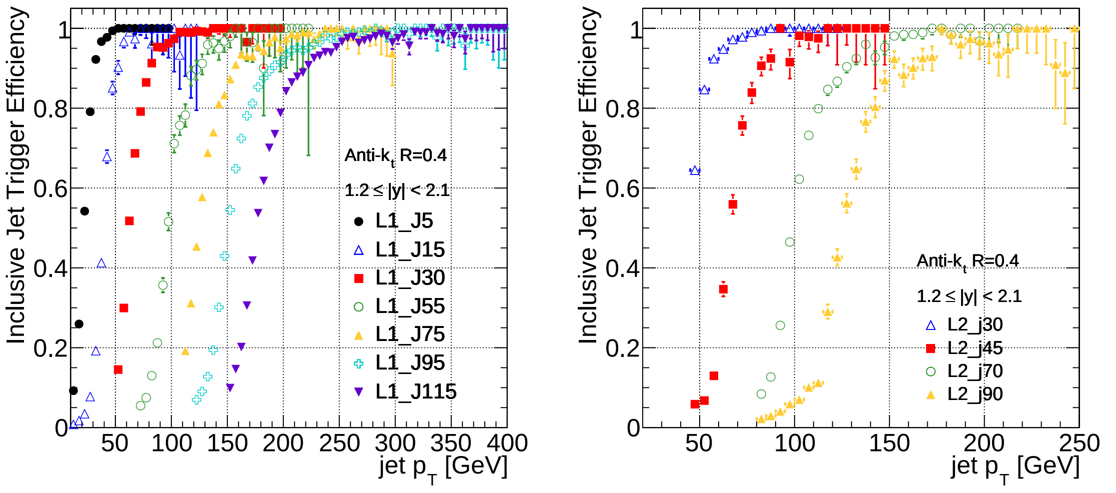

(a) (b)

Figure A.11: Inclusive jet trigger efficiencies for $R = 0.4$ jets in the region $1.2 \leq |y| < 2.1$, shown for the Level-1 (a) and Level-2 (b) jet trigger items used for this analysis.

.

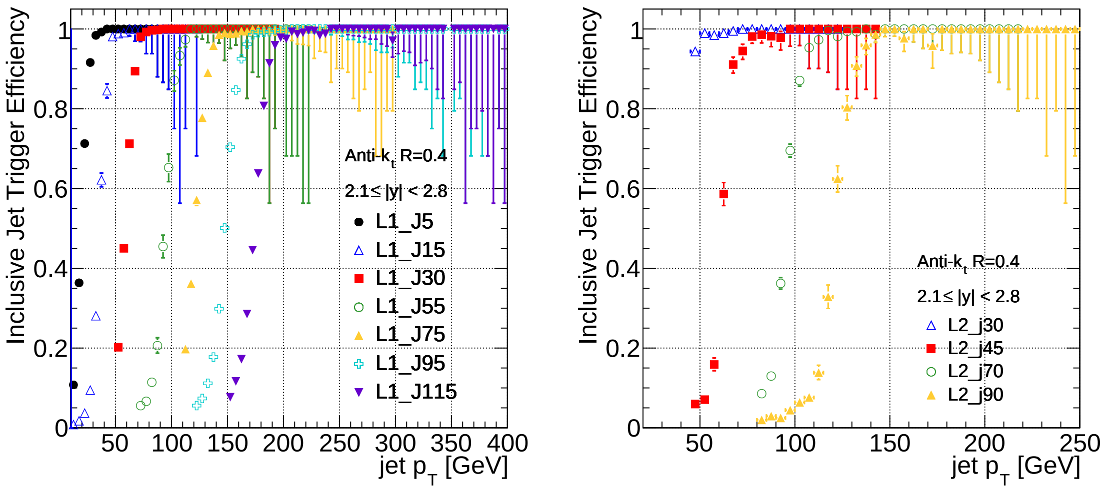

(a)

(b)

Figure A.12: Inclusive jet trigger efficiencies for $R = 0.4$ jets in the region $2.1 \leq |y| < 2.8$, shown for the Level-1 (a) and Level-2 (b) jet trigger items used for this analysis.

.

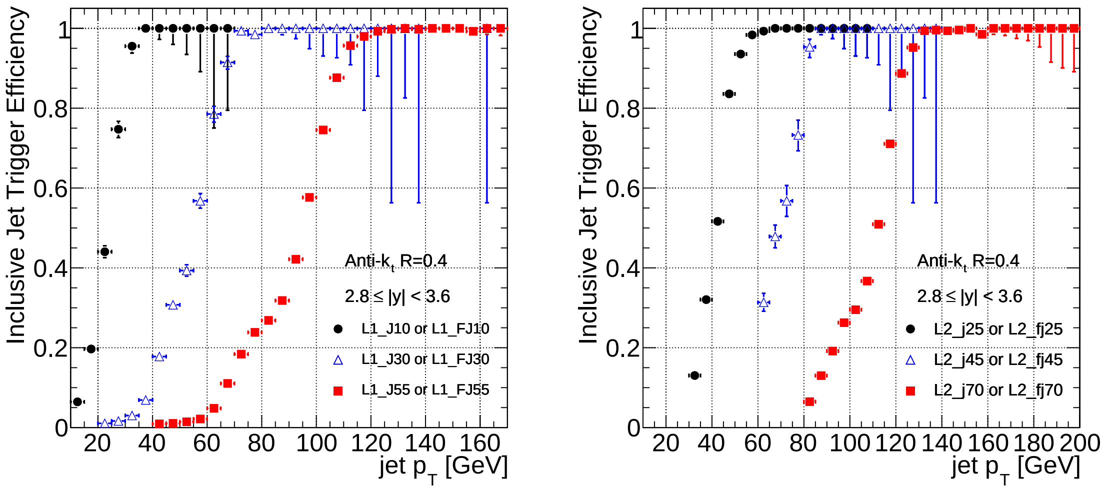

(a)

(b)

Figure A.13: Inclusive jet trigger efficiencies for $R = 0.4$ jets in the region $2.8 \leq |y| < 3.6$, shown for the Level-1 (a) and Level-2 (b) jet trigger items used for this analysis.

.

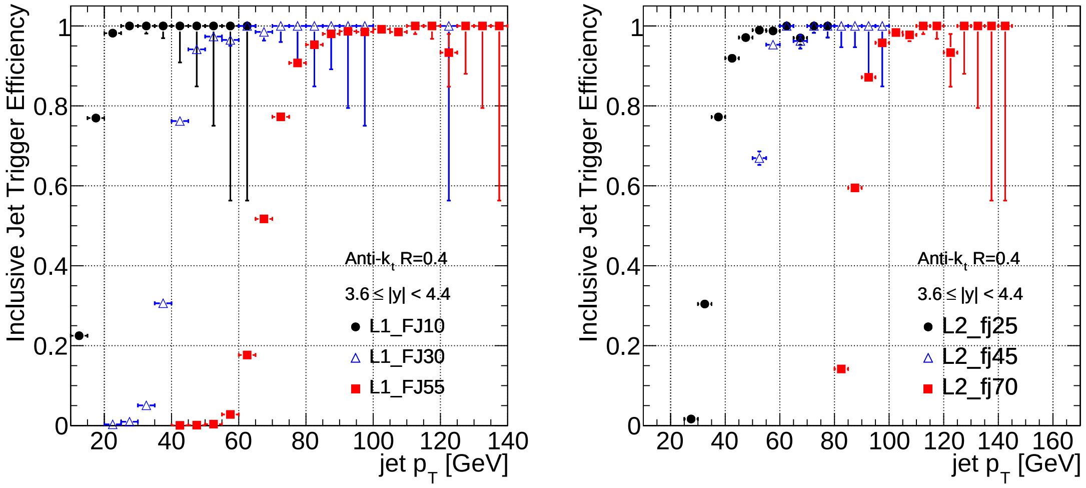

(a)

(b)

Figure A.14: Inclusive jet trigger efficiencies for $R = 0.4$ jets in the region $3.6 \leq |y| < 4.4$, shown for the Level-1 (a) and Level-2 (b) jet trigger items used for this analysis.

.

Appendix B Unfolding Correction Factors

The derivation of the correction factors, and associated uncertainties, used to perform the detector unfolding are detailed in Section 4.7. This appendix contains plots of the unfolding factors and uncertainties for all rapidity bins for $R = 0.6$ and $R = 0.4$ jets.

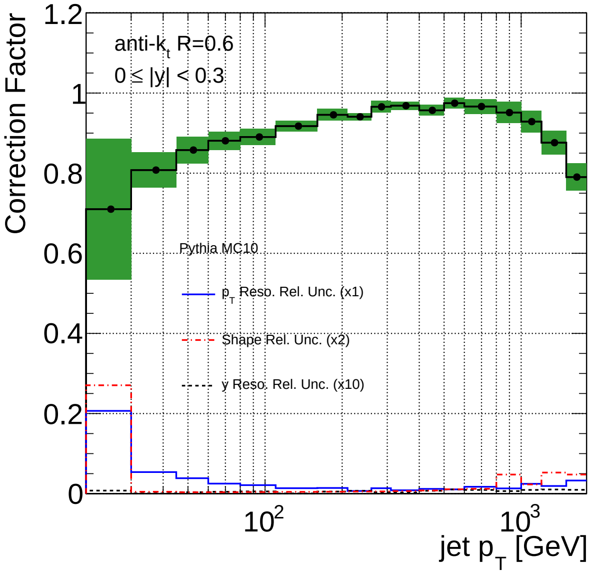

Figure A.1: Unfolding correction factors as a function of jet p_T for $R = 0.6$ jets with $|y| < 0.3$. Relative uncertainties due to jet p_T and angular resolutions and the spectrum shape are shown. Statistical uncertainties are indicated by the black error bars. The shaded region indicates the quadratic sum of the systematic and statistical uncertainties.

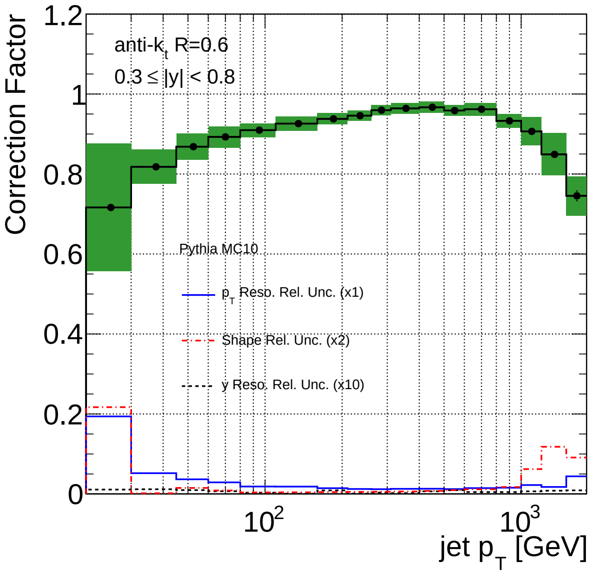

Figure A.2: Unfolding correction factors as a function of jet p_T for $R = 0.6$ jets with $0.3 \leq |y| < 0.8$. Relative uncertainties due to jet p_T and angular resolutions and the spectrum shape are shown. Statistical uncertainties are indicated by the black error bars. The shaded region indicates the quadratic sum of the systematic and statistical uncertainties.

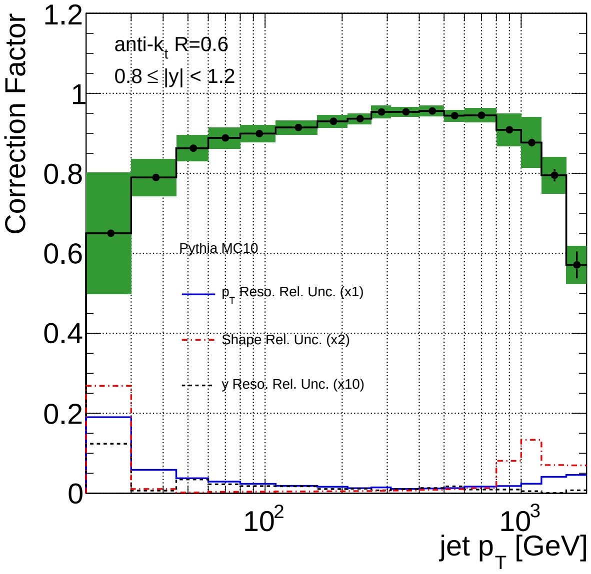

Figure A.3: Unfolding correction factors as a function of jet p_T for $R = 0.6$ jets with $0.8 \leq |y| < 1.2$. Relative uncertainties due to jet p_T and angular resolutions and the spectrum shape are shown. Statistical uncertainties are indicated by the black error bars. The shaded region indicates the quadratic sum of the systematic and statistical uncertainties.

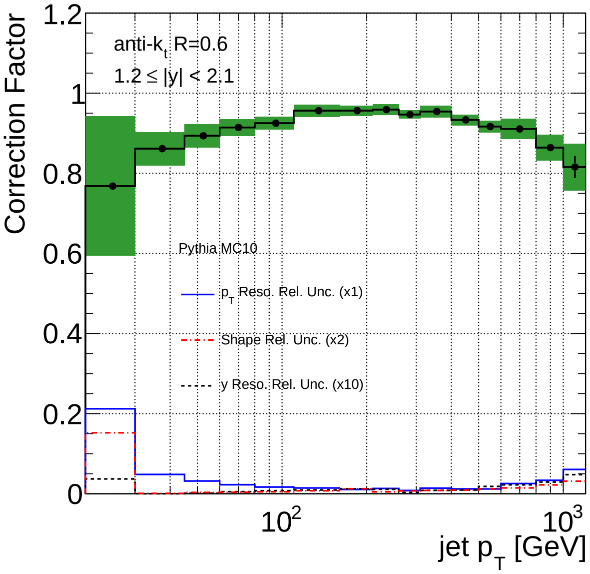

Figure A.4: Unfolding correction factors as a function of jet p_T for $R = 0.6$ jets with $1.2 \leq |y| < 2.1$. Relative uncertainties due to jet p_T and angular resolutions and the spectrum shape are shown. Statistical uncertainties are indicated by the black error bars. The shaded region indicates the quadratic sum of the systematic and statistical uncertainties.

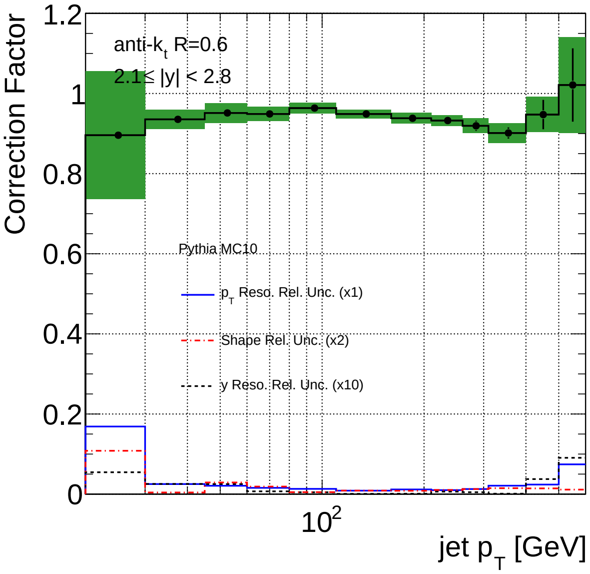

Figure A.5: Unfolding correction factors as a function of jet p_T for $R = 0.6$ jets with $2.1 \leq |y| < 2.8$. Relative uncertainties due to jet p_T and angular resolutions and the spectrum shape are shown. Statistical uncertainties are indicated by the black error bars. The shaded region indicates the quadratic sum of the systematic and statistical uncertainties.

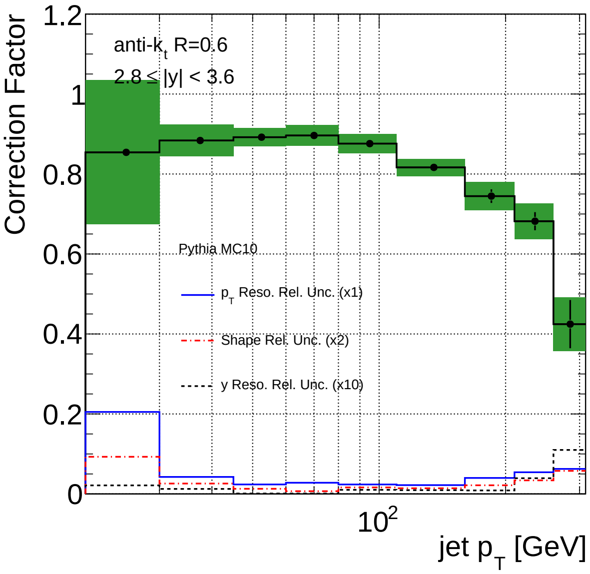

Figure A.6: Unfolding correction factors as a function of jet p_T for $R = 0.6$ jets with $2.8 \leq |y| < 3.6$. Relative uncertainties due to jet p_T and angular resolutions and the spectrum shape are shown. Statistical uncertainties are indicated by the black error bars. The shaded region indicates the quadratic sum of the systematic and statistical uncertainties.

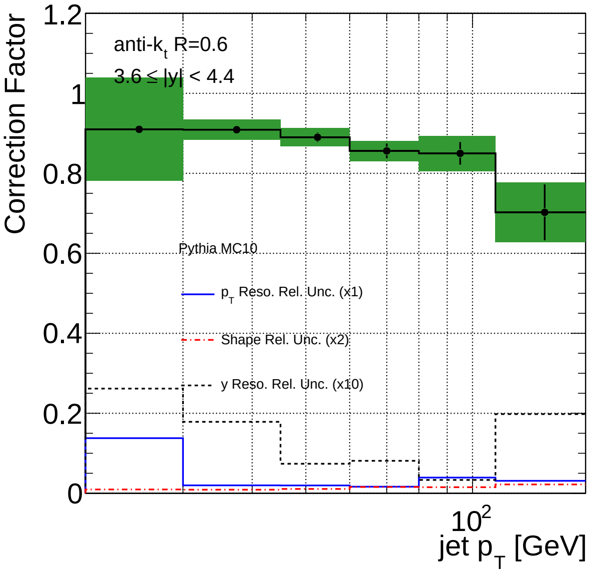

Figure A.7: Unfolding correction factors as a function of jet p_T for $R = 0.6$ jets with $3.6 \leq |y| < 4.4$. Relative uncertainties due to jet p_T and angular resolutions and the spectrum shape are shown. Statistical uncertainties are indicated by the black error bars. The shaded region indicates the quadratic sum of the systematic and statistical uncertainties.

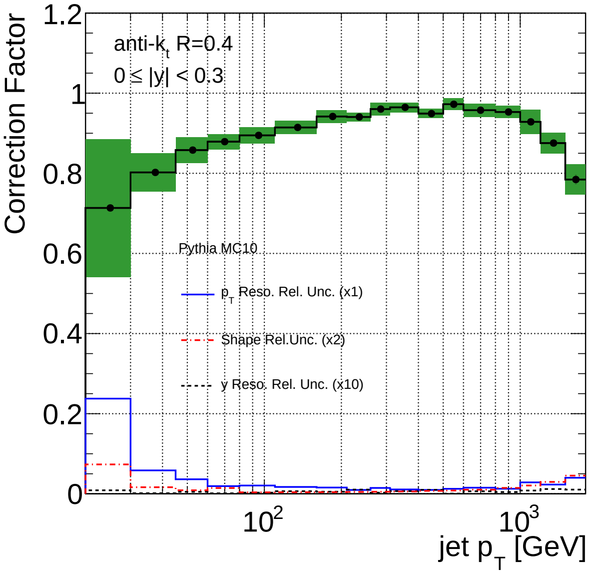

Figure A.8: Unfolding correction factors as a function of jet p_T for $R = 0.4$ jets with $|y| < 0.3$. Relative uncertainties due to jet p_T and angular resolutions and the spectrum shape are shown. Statistical uncertainties are indicated by the black error bars. The shaded region indicates the quadratic sum of the systematic and statistical uncertainties.

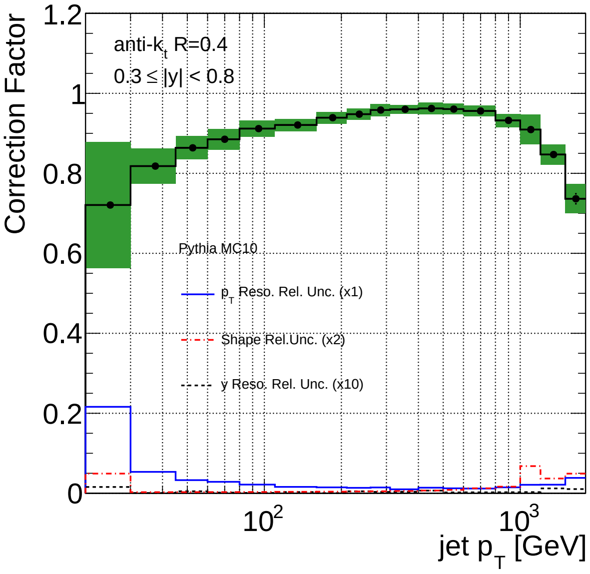

Figure A.9: Unfolding correction factors as a function of jet p_T for $R = 0.4$ jets with $0.3 \leq |y| < 0.8$. Relative uncertainties due to jet p_T and angular resolutions and the spectrum shape are shown. Statistical uncertainties are indicated by the black error bars. The shaded region indicates the quadratic sum of the systematic and statistical uncertainties.

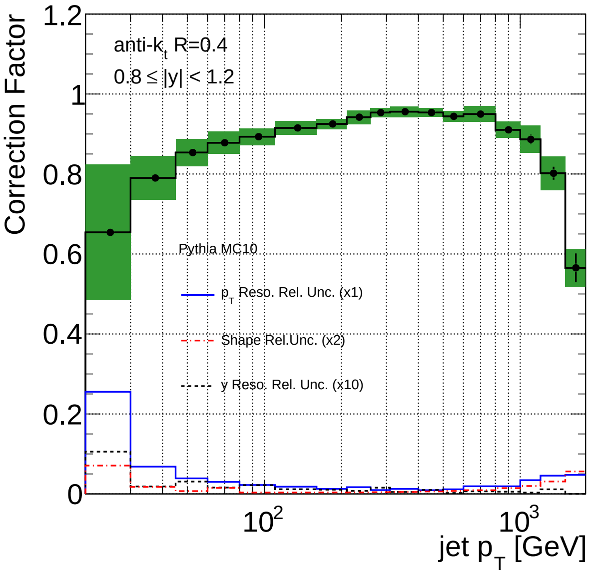

Figure A.10: Unfolding correction factors as a function of jet p_T for $R = 0.4$ jets with $0.8 \leq |y| < 1.2$. Relative uncertainties due to jet p_T and angular resolutions and the spectrum shape are shown. Statistical uncertainties are indicated by the black error bars. The shaded region indicates the quadratic sum of the systematic and statistical uncertainties.

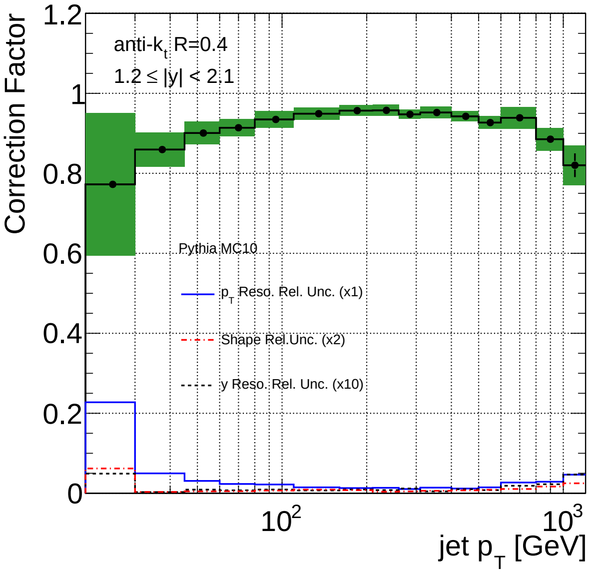

Figure A.11: Unfolding correction factors as a function of jet p_T for $R = 0.4$ jets with $1.2 \leq |y| < 2.1$. Relative uncertainties due to jet p_T and angular resolutions and the spectrum shape are shown. Statistical uncertainties are indicated by the black error bars. The shaded region indicates the quadratic sum of the systematic and statistical uncertainties.

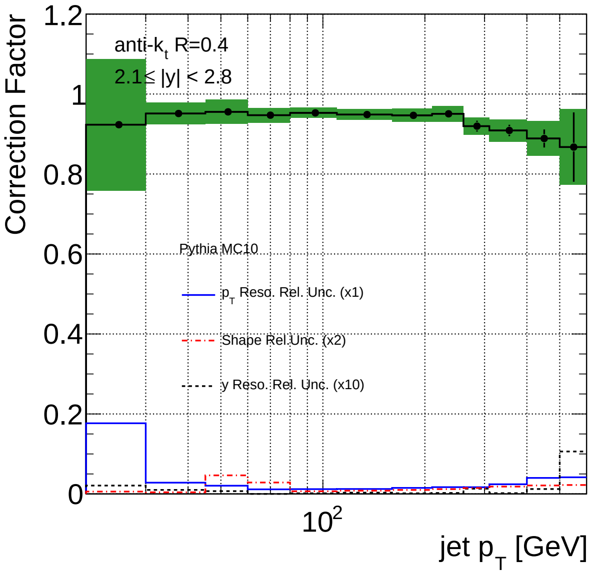

Figure A.12: Unfolding correction factors as a function of jet p_T for $R = 0.4$ jets with $2.1 \leq |y| < 2.8$. Relative uncertainties due to jet p_T and angular resolutions and the spectrum shape are shown. Statistical uncertainties are indicated by the black error bars. The shaded region indicates the quadratic sum of the systematic and statistical uncertainties.

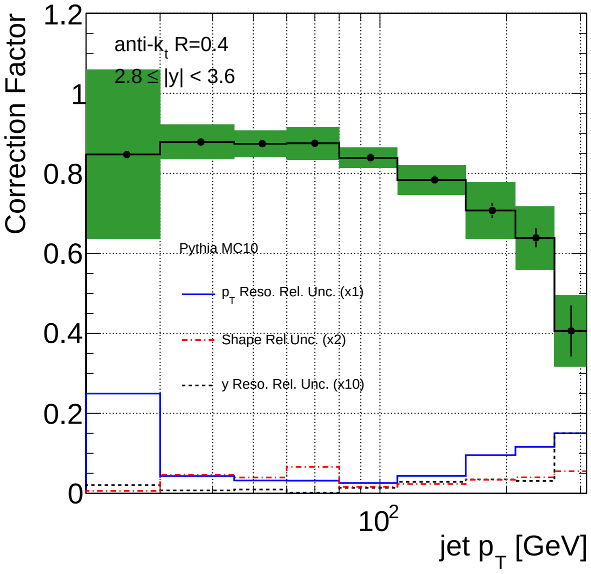

Figure A.13: Unfolding correction factors as a function of jet p_T for $R = 0.4$ jets with $2.8 \leq |y| < 3.6$. Relative uncertainties due to jet p_T and angular resolutions and the spectrum shape are shown. Statistical uncertainties are indicated by the black error bars. The shaded region indicates the quadratic sum of the systematic and statistical uncertainties.

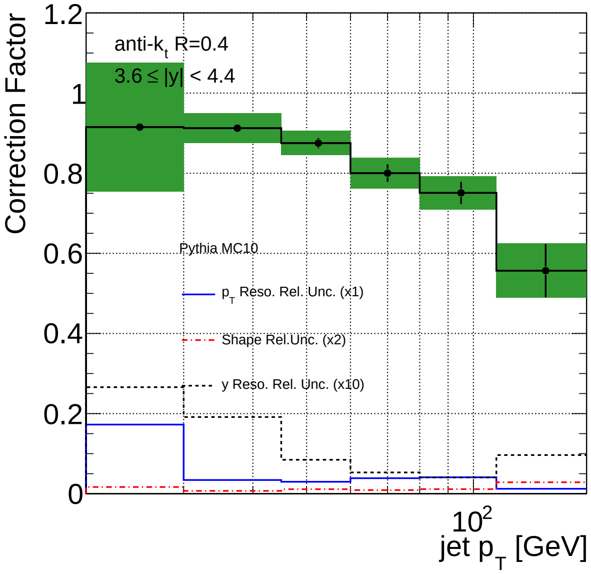

Figure A.14: Unfolding correction factors as a function of jet p_T for $R = 0.4$ jets with $3.4 \leq |y| < 4.4$. Relative uncertainties due to jet p_T and angular resolutions and the spectrum shape are shown. Statistical uncertainties are indicated by the black error bars. The shaded region indicates the quadratic sum of the systematic and statistical uncertainties.

Appendix C Statistical Errors on Unfolding Factors

The unfolding factors for each bin of the cross section measurement are defined in Monte Carlo, as explained in Section 4.7, using the equation

$$C = \frac{N^{MC}_{truth}}{N^{MC}_{reco}}, \tag{A.1}$$

where N^{MC}_{truth} is the number of truth jets falling in a given p_T and $|y|$ bin, and N^{MC}_{reco} is the number of reconstructed jets that fall into the same bin. The statistics available in Monte Carlo affects the uncertainty on the correction factors, especially in the high p_T and high rapidity regions. The statistical uncertainties on N^{MC}_{truth} and N^{MC}_{reco}, however, are not totally independent, and correlations must be taken into account in assigning a statistical uncertainty on the final correction factor, C.

To clarify these correlations, the correction factor for each bin can be written as

$$C = \frac{a+b}{a+c}, \tag{A.2}$$

where a is the number of truth jets in a given bin that correspond to reconstructed jets in the same bin, b is the number of truth jets in a given bin that *do not* correspond to reconstructed jets in the same bin, and c is the number of reconstructed jets in a given bin that *do not* correspond to truth jets in the same bin. The quantities a, b, and c are then uncorrelated, with the statistical errors on each given by

$$\sigma = \sqrt{\sum_{jets} w^2_{jet}}. \tag{A.3}$$

Here, w_{jet} is the product of the weight given a particular jet by the procedure used to modify the p_T spectrum shape and any weight used to combine Monte Carlo samples generated with different cross sections. The errors on the numerator and denominator of Equation A.2 can then be written as

$$\sigma^2_{a+b} = \sigma^2_a + \sigma^2_b \text{ and } \sigma^2_{a+c} = \sigma^2_a + \sigma^2_c, \tag{A.4}$$

where σ_a, σ_b, and σ_c are the statistical errors on the quantities a, b, and c, respectively.

The total error on the correction factor can then be shown to be:

$$\sigma_C = \sqrt{\sigma_b^2(\frac{1}{a+c})^2 + \sigma_c^2(\frac{a+b}{(a+c)^2})^2 + \sigma_a^2(\frac{b-c}{(a+c)^2})^2} \tag{A.5}$$

In the limit of $a \rightarrow 0$, this simplifies to the case of a ratio of two statistically independent quantities, as expected.

Appendix D Systematic Uncertainties on the $R = 0.4$ Jet Cross Sections

The propagation of the experimental uncertainties to the final measured cross section is explained in Section 4.8. In this appendix, the relevant individual uncertainties and the total systematic uncertainty are shown for the $R = 0.4$ jet cross sections. Similar plots for $R = 0.6$ jet cross sections are shown in Section 4.8.

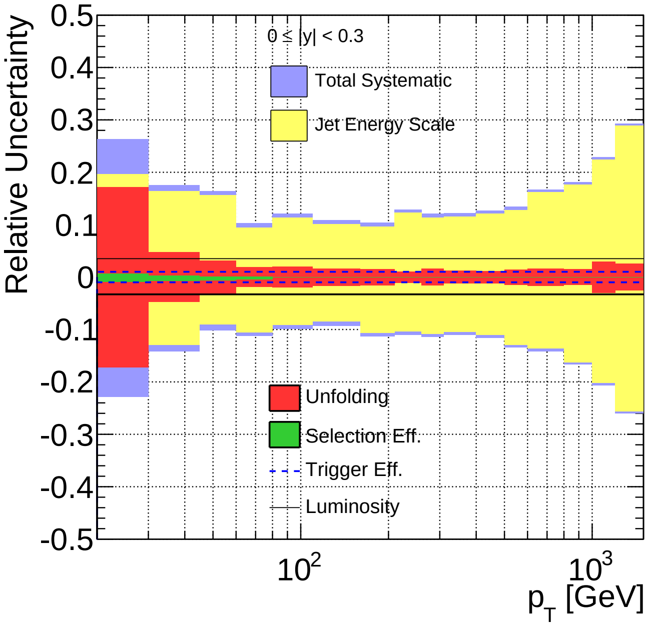

Figure A.1: Total relative uncertainty on the inclusive jet cross section and contribution from each uncertainty source, for $R = 0.4$ jets in the region $0 \leq |y| < 0.3$.

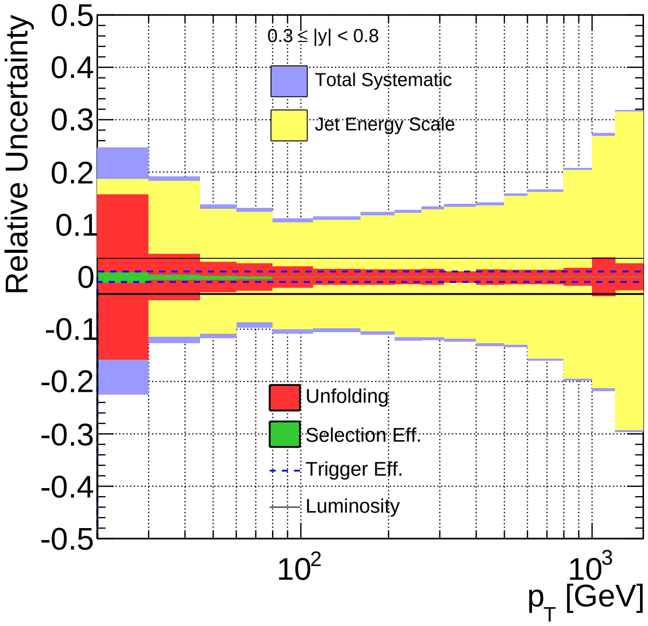

(a)

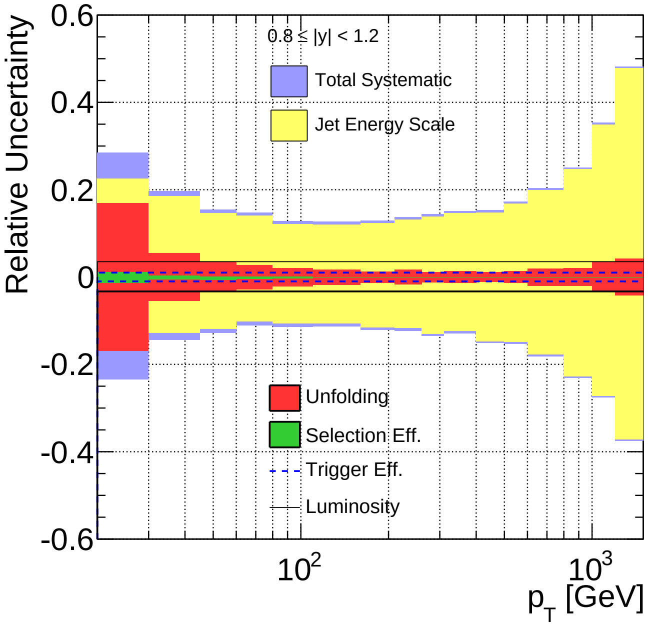

(b)

Figure A.2: Total relative uncertainty on the inclusive jet cross section and contribution from each uncertainty source, for $R = 0.4$ jets in the region $0.3 \leq |y| < 0.8$ (a) and $0.8 \leq |y| < 1.2$ (b).

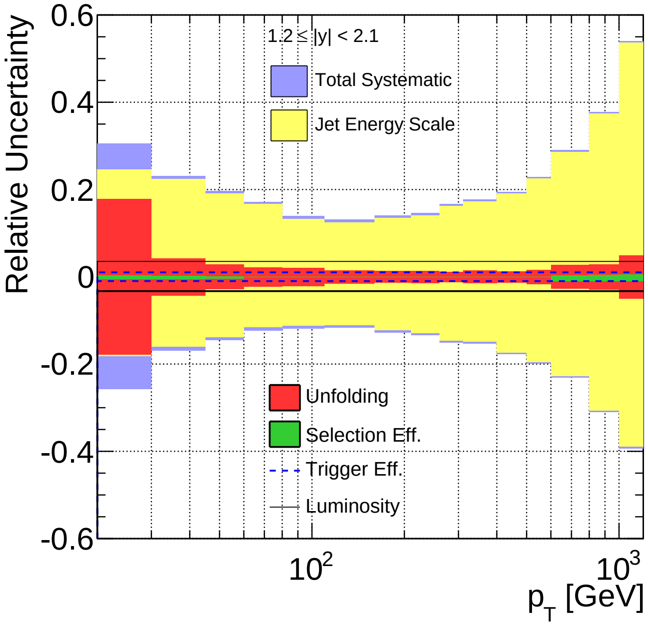

(a)

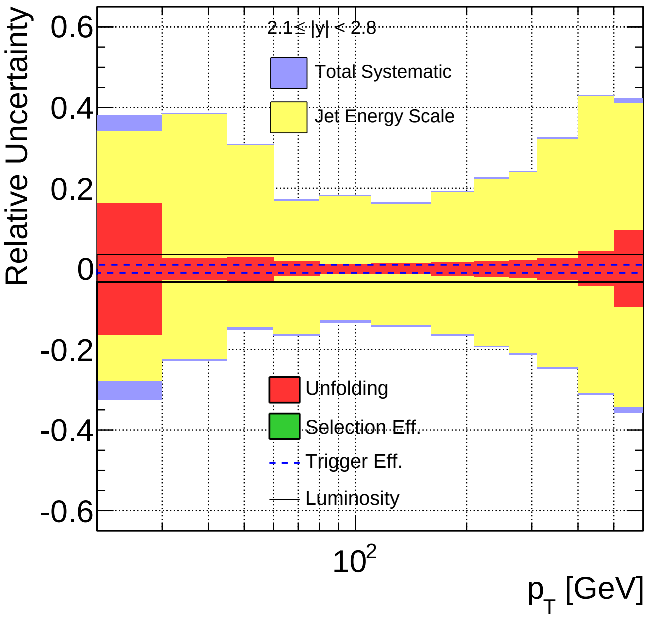

(b)

Figure A.3: Total relative uncertainty on the inclusive jet cross section and contribution from each uncertainty source, for $R = 0.4$ jets in the region $1.2 \leq |y| < 2.1$ (a) and $2.1 \leq |y| < 2.8$ (b).

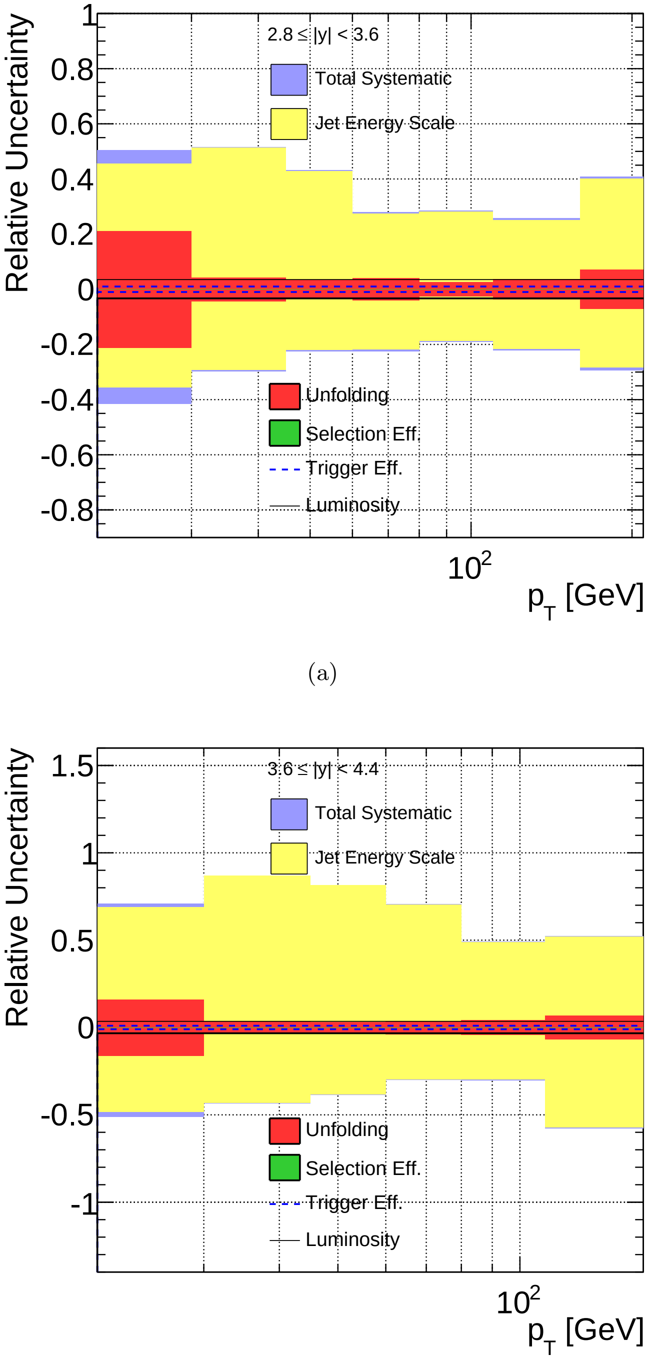

(a)

(b)

Figure A.4: Total relative uncertainty on the inclusive jet cross section and contribution from each uncertainty source, for $R = 0.4$ jets in the region $2.8 \leq |y| < 3.6$ (a) and $3.6 \leq |y| < 4.4$ (b).

Appendix E Theoretical Uncertainties on the $R = 0.4$ Jet Cross Sections

The derivation of the components of the uncertainty on the theoretical cross section prediction, namely the uncertainties due to choice of PDF, renormalization and factorization scales, α_s, and modeling of non-perturbative effects, is detailed in Section 5. This appendix contains plots of the both the total uncertainty on the predicted $R = 0.4$ inclusive jet cross sections and the contributions from individual sources. Similar plots for the $R = 0.6$ cross sections are shown in Section 5.

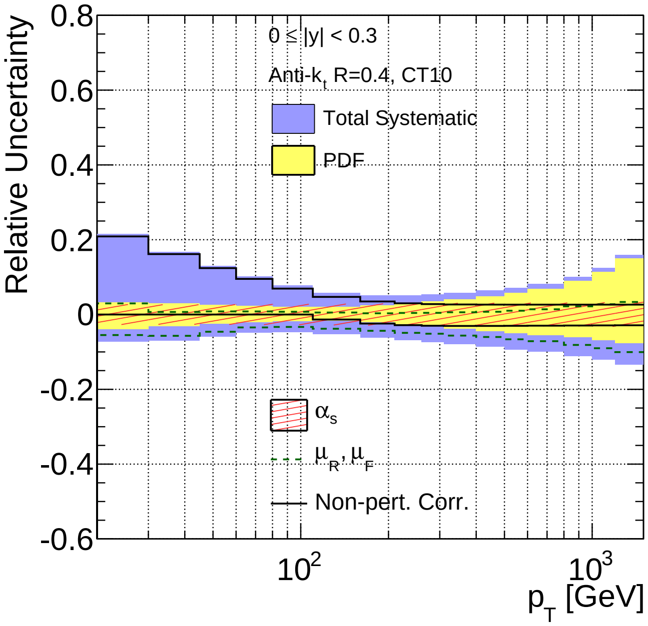

Figure A.1: Total relative uncertainty on the predicted NLO inclusive jet cross section and contribution from each uncertainty source, for $R = 0.4$ jets in the region $0 \leq |y| < 0.3$.

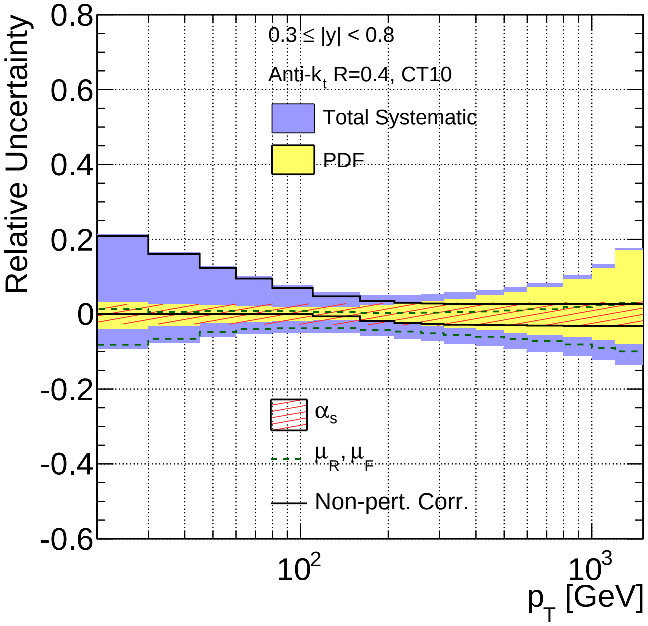

(a)

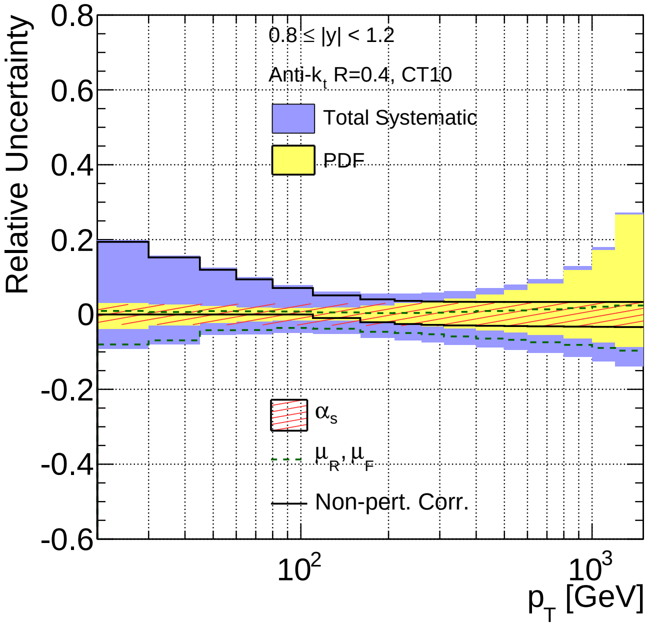

(b)

Figure A.2: Total relative uncertainty on the predicted NLO inclusive jet cross section and contribution from each uncertainty source, for $R = 0.4$ jets in the region $0.3 \leq |y| < 0.8$ (a) and $0.8 \leq |y| < 01.2$ (b).

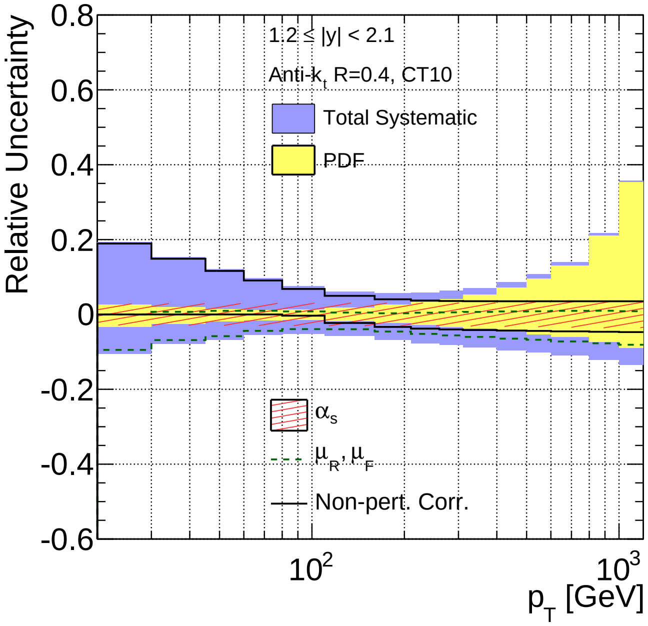

(a)

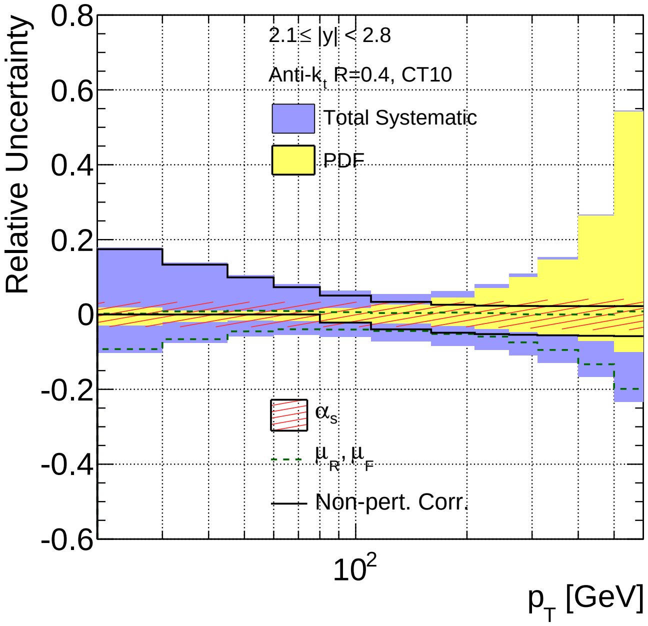

(b)

Figure A.3: Total relative uncertainty on the predicted NLO inclusive jet cross section and contribution from each uncertainty source, for $R = 0.4$ jets in the region $1.2 \leq |y| < 2.1$ (a) and $2.1 \leq |y| < 2.8$ (b).

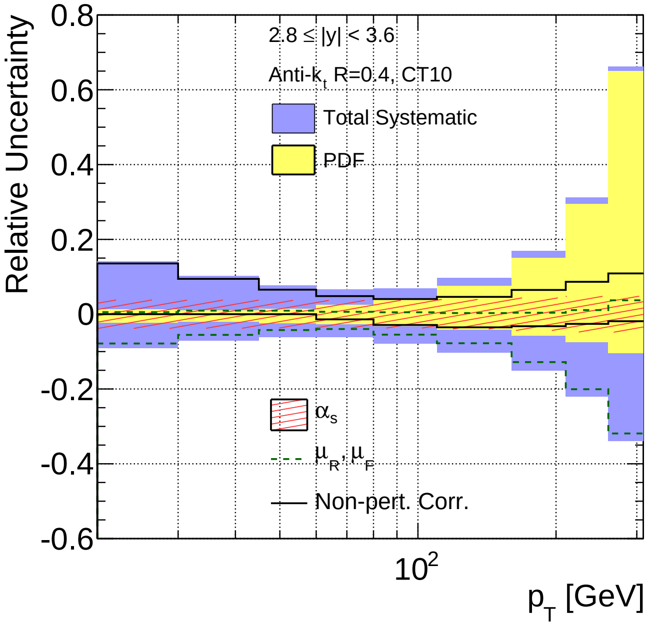

(a)

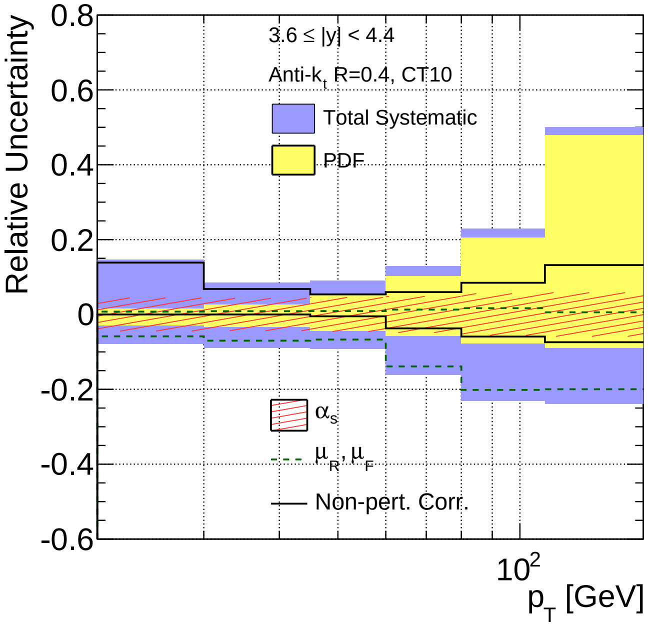

(b)

Figure A.4: Total relative uncertainty on the predicted NLO inclusive jet cross section and contribution from each uncertainty source, for $R = 0.4$ jets in the region $2.8 \leq |y| < 3.6$ (a) and $3.6 \leq |y| < 4.4$ (b).

Appendix F Non-perturbative Corrections

The derivation of the non-perturbative correction factors, used to correct parton-level NLO perturbative QCD calculations for the effects of hadronization and underlying event, is detailed in Section 5.2. This appendix contains the baseline non-perturbative correction factors, as derived from Pythia MC10 Monte Carlo, and the systematic variations obtained from Pythia with the Perugia2010 tune and Herwig++, for both $R = 0.4$ and $R = 0.6$ jets.

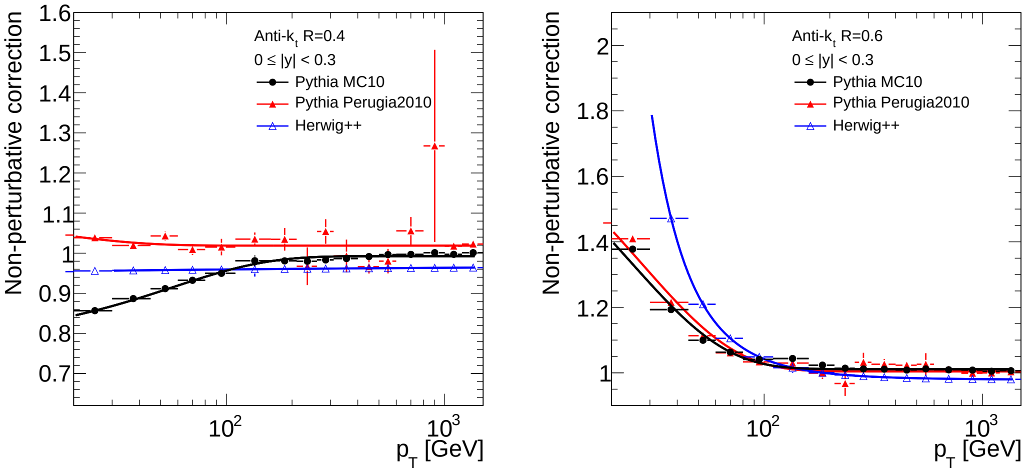

(a) (b)

Figure A.1: Baseline non-perturbative corrections obtained from Pythia MC10 and systematic variations obtained from Pythia with the Perugia2010 tune and Herwig++, for $R = 0.4$ jets (a) and for $R = 0.6$ jets (b) with $0 \leq |y| < 0.3$.

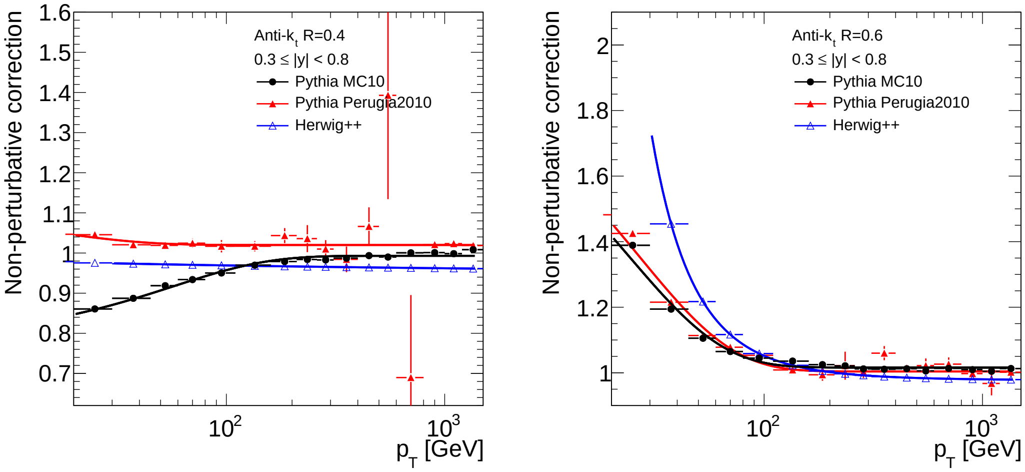

(a) (b)

Figure A.2: Baseline non-perturbative corrections obtained from Pythia MC10 and systematic variations obtained from Pythia with the Perugia2010 tune and Herwig++, for $R = 0.4$ jets (a) and for $R = 0.6$ jets (b) with $0.3 \leq |y| < 0.8$.

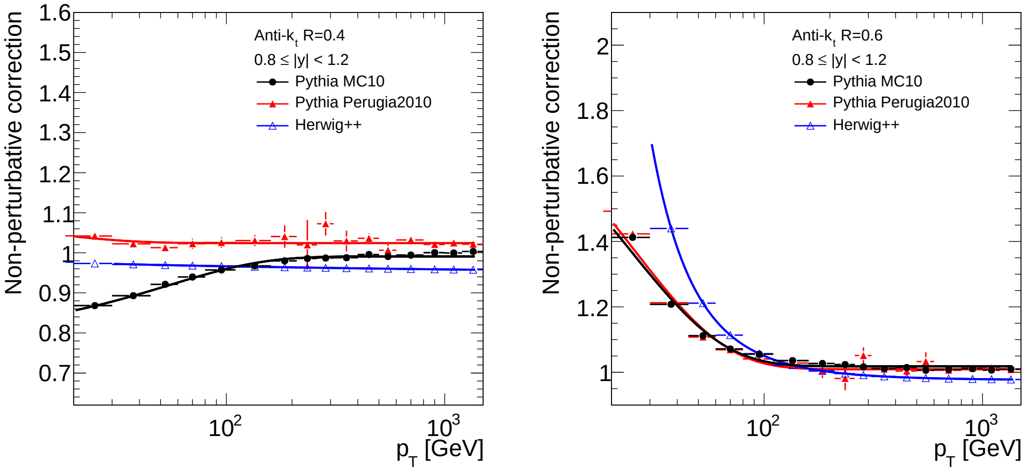

(a) (b)

Figure A.3: Baseline non-perturbative corrections obtained from Pythia MC10 and systematic variations obtained from Pythia with the Perugia2010 tune and Herwig++, for $R = 0.4$ jets (a) and for $R = 0.6$ jets (b) with $0.8 \leq |y| < 1.2$.

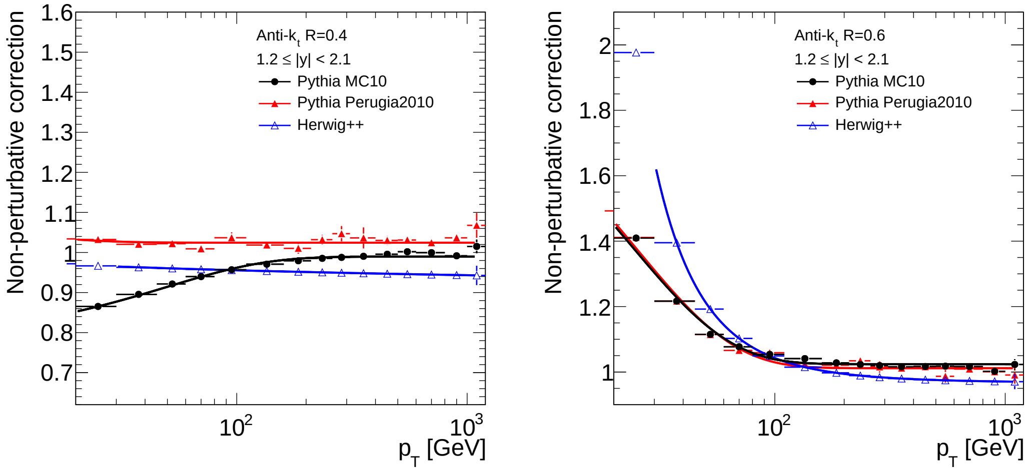

(a) (b)

Figure A.4: Baseline non-perturbative corrections obtained from Pythia MC10 and systematic variations obtained from Pythia with the Perugia2010 tune and Herwig++, for $R = 0.4$ jets (a) and for $R = 0.6$ jets (b) with $1.2 \leq |y| < 2.1$.

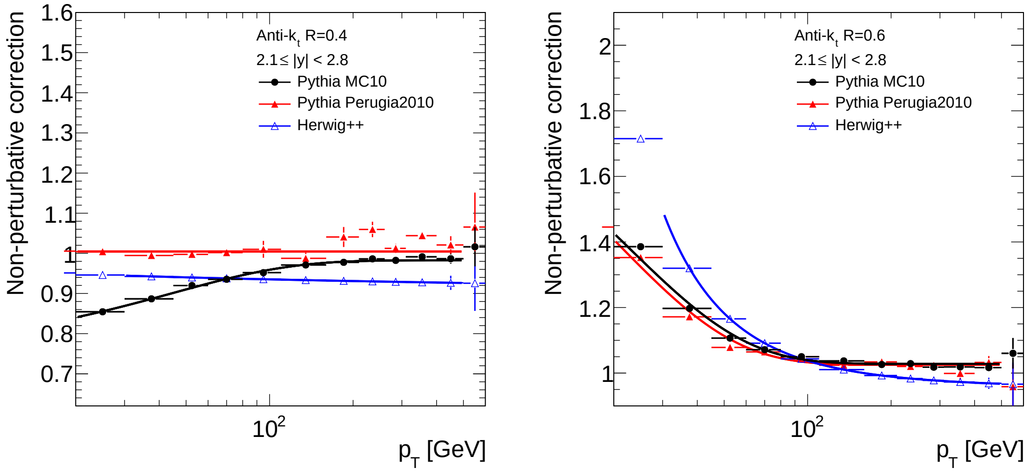

(a) (b)

Figure A.5: Baseline non-perturbative corrections obtained from Pythia MC10 and systematic variations obtained from Pythia with the Perugia2010 tune and Herwig++, for $R = 0.4$ jets (a) and for $R = 0.6$ jets (b) with $2.1 \leq |y| < 2.8$.

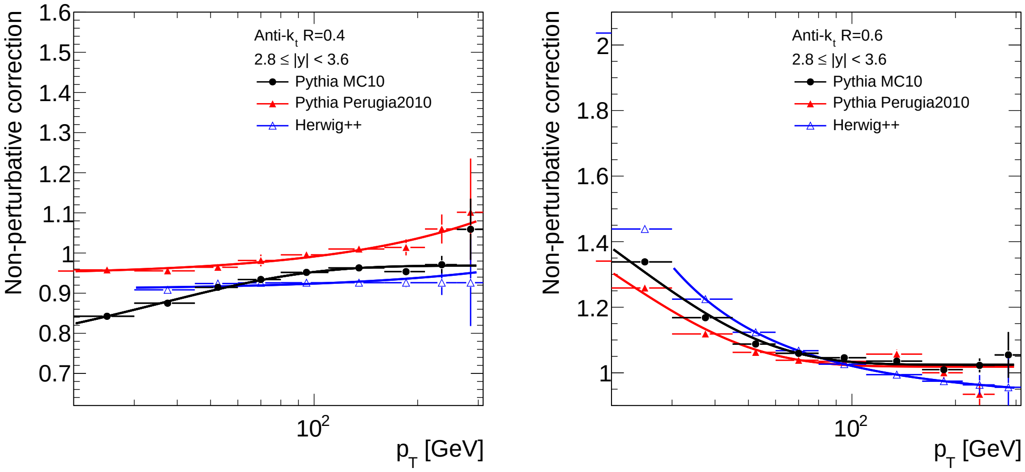

(a) (b)

Figure A.6: Baseline non-perturbative corrections obtained from Pythia MC10 and systematic variations obtained from Pythia with the Perugia2010 tune and Herwig++, for $R = 0.4$ jets (a) and for $R = 0.6$ jets (b) with $2.8 \leq |y| < 3.6$.

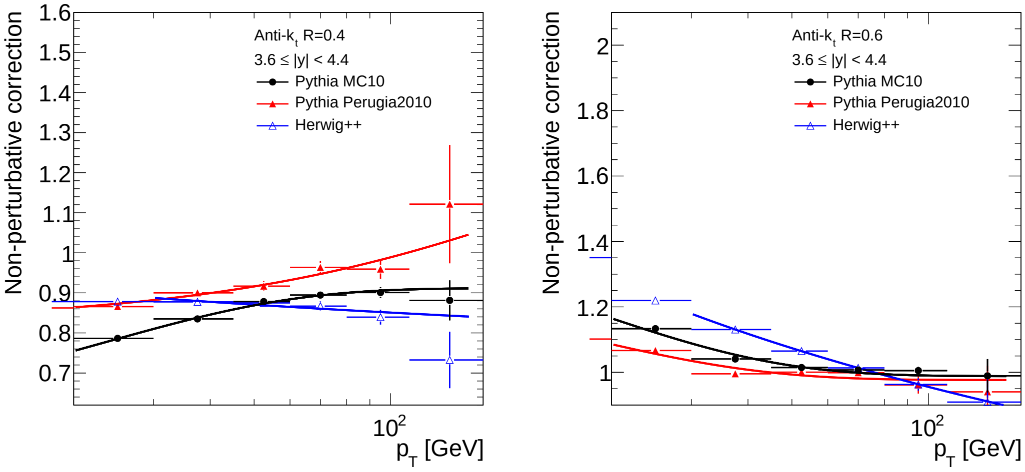

(a) (b)

Figure A.7: Baseline non-perturbative corrections obtained from Pythia MC10 and systematic variations obtained from Pythia with the Perugia2010 tune and Herwig++, for $R = 0.4$ jets (a) and for $R = 0.6$ jets (b) with $3.6 \leq |y| < 4.4$.

Appendix G Cross Section Tables

This appendix contains tables listing, for each bin of p_T and rapidity, the number of measured jets, the measured jet cross section along with relative statistical and systematic errors, the NLO predicted cross section, the NLO predicted cross section with corrections for non-perturbative effects applied, and the total relative error on the theoretical prediction. Results are shown for both $R = 0.6$ and $R = 0.4$ inclusive jet cross sections. All errors are listed as fractional uncertainties.

p_T [GeV]	20-30	30-45	45-60	60-80	80-110	110-160	160-210	210-260
Jets	60910	10228	1658	23785	126400	134594	93292	22060
Cross section	1.1e+07	1.35e+06	2.28e+05	5.49e+04	1.14e+04	1.92e+03	318	77.1
Rel. Stat. Err.	0.0041	0.0099	0.025	0.0065	0.0028	0.0027	0.0033	0.0067
Rel. Syst. Err.	$^{+0.31}_{-0.26}$	$^{+0.22}_{-0.14}$	$^{+0.17}_{-0.11}$	$^{+0.11}_{-0.11}$	$^{+0.12}_{-0.088}$	$^{+0.094}_{-0.096}$	$^{+0.1}_{-0.12}$	$^{+0.13}_{-0.11}$
NLO cross section	6.73e+06	1.09e+06	2.07e+05	5.09e+04	1.13e+04	1.91e+03	316	78.9
NLO + non. pert.	8.96e+06	1.32e+06	2.32e+05	5.41e+04	1.16e+04	1.94e+03	320	79.8
Rel. theory error	$^{+0.76}_{-0.09}$	$^{+0.23}_{-0.081}$	$^{+0.096}_{-0.075}$	$^{+0.058}_{-0.07}$	$^{+0.044}_{-0.068}$	$^{+0.041}_{-0.072}$	$^{+0.045}_{-0.078}$	$^{+0.049}_{-0.04}$

p_T [GeV]	260-310	310-400	400-500	500-600	600-800	800-1000	1000-1200	1200-1500
Jets	29293	14767	3707	939	351	56	7	3
Cross section	25.3	7.1	1.58	0.409	0.0757	0.0119	0.00145	0.00039
Rel. Stat. Err.	0.0058	0.0082	0.016	0.033	0.053	0.13	0.38	0.58
Rel. Syst. Err.	$^{+0.12}_{-0.1}$	$^{+0.11}_{-0.12}$	$^{+0.13}_{-0.11}$	$^{+0.13}_{-0.14}$	$^{+0.16}_{-0.15}$	$^{+0.19}_{-0.17}$	$^{+0.23}_{-0.21}$	$^{+0.29}_{-0.26}$
NLO cross section	25.1	7.16	1.58	0.411	0.0864	0.0121	0.00213	0.000322
NLO + non. pert.	25.4	7.24	1.6	0.416	0.0874	0.0122	0.00215	0.000325
Rel. theory error	$^{+0.054}_{-0.089}$	$^{+0.059}_{-0.096}$	$^{+0.066}_{-0.1}$	$^{+0.075}_{-0.11}$	$^{+0.085}_{-0.11}$	$^{+0.1}_{-0.12}$	$^{+0.13}_{-0.13}$	$^{+0.17}_{-0.15}$

Table A.1: Measured inclusive jet double-differential cross section per GeV and per unit rapidity as a function of p_T for anti-k$_t$ jets with $R = 0.6$ in the region $0 \leq |y| < 0.3$, compared to NLO perturbative QCD calculations corrected for non-perturbative effects. All errors listed are fractional uncertainties.

p_T [GeV]	20-30	30-45	45-60	60-80	80-110	110-160	160-210	210-260
Jets	98789	16924	2786	38091	203651	215908	148226	35133
Cross section	1.09e+07	1.35e+06	2.35e+05	5.27e+04	1.12e+04	1.86e+03	301	74.1
Rel. Stat. Err.	0.0032	0.0077	0.019	0.0051	0.0022	0.0022	0.0026	0.0053
Rel. Syst. Err.	$^{+0.28}_{-0.24}$	$^{+0.21}_{-0.16}$	$^{+0.18}_{-0.11}$	$^{+0.13}_{-0.1}$	$^{+0.11}_{-0.1}$	$^{+0.11}_{-0.099}$	$^{+0.11}_{-0.1}$	$^{+0.11}_{-0.12}$
NLO cross section	6.57e+06	1.07e+06	1.99e+05	4.9e+04	1.08e+04	1.82e+03	299	74
NLO + non. pert.	8.81e+06	1.3e+06	2.23e+05	5.23e+04	1.12e+04	1.85e+03	304	75.2
Rel. theory error	$^{+0.62}_{-0.088}$	$^{+0.21}_{-0.082}$	$^{+0.097}_{-0.072}$	$^{+0.062}_{-0.069}$	$^{+0.045}_{-0.067}$	$^{+0.04}_{-0.072}$	$^{+0.044}_{-0.078}$	$^{+0.049}_{-0.84}$

p_T [GeV]	260-310	310-400	400-500	500-600	600-800	800-1000	1000-1200	1200-1500
Jets	46086	23442	5492	1424	577	72	13	3
Cross section	23.7	6.73	1.42	0.366	0.0743	0.00899	0.00158	0.000227
Rel. Stat. Err.	0.0047	0.0065	0.013	0.026	0.042	0.12	0.28	0.58
Rel. Syst. Err.	$^{+0.13}_{-0.12}$	$^{+0.14}_{-0.13}$	$^{+0.15}_{-0.13}$	$^{+0.15}_{-0.14}$	$^{+0.17}_{-0.15}$	$^{+0.2}_{-0.19}$	$^{+0.26}_{-0.22}$	$^{+0.31}_{-0.29}$
NLO cross section	23.4	6.61	1.44	0.37	0.0751	0.00985	0.0016	0.000213
NLO + non. pert.	23.8	6.71	1.46	0.376	0.0763	0.01	0.00162	0.000216
Rel. theory error	$^{+0.053}_{-0.089}$	$^{+0.059}_{-0.096}$	$^{+0.066}_{-0.1}$	$^{+0.075}_{-0.11}$	$^{+0.086}_{-0.12}$	$^{+0.11}_{-0.13}$	$^{+0.14}_{-0.14}$	$^{+0.18}_{-0.15}$

Table A.2: Measured inclusive jet double-differential cross section per GeV and per unit rapidity as a function of p_T for anti-k$_t$ jets with $R = 0.6$ in the region $0.3 \leq |y| < 0.8$, compared to NLO perturbative QCD calculations corrected for non-perturbative effects. All errors listed are fractional uncertainties.

p_T [GeV]	20-30	30-45	45-60	60-80	80-110	110-160	160-210	210-260
Jets	74915	12565	1957	27704	148804	154035	102434	23433
Cross section	8.91e+06	1.19e+06	2.02e+05	4.87e+04	1.03e+04	1.64e+03	258	61.2
Rel. Stat. Err.	0.0037	0.0089	0.023	0.006	0.0026	0.0025	0.0031	0.0065
Rel. Syst. Err.	$^{+0.28}_{-0.23}$	$^{+0.22}_{-0.17}$	$^{+0.2}_{-0.11}$	$^{+0.12}_{-0.12}$	$^{+0.13}_{-0.11}$	$^{+0.12}_{-0.11}$	$^{+0.12}_{-0.11}$	$^{+0.12}_{-0.13}$
NLO cross section	6.19e+06	9.97e+05	1.85e+05	4.53e+04	9.88e+03	1.63e+03	265	64
NLO + non. pert.	8.45e+06	1.22e+06	2.09e+05	4.86e+04	1.02e+04	1.67e+03	270	65.2
Rel. theory error	$^{+0.56}_{-0.086}$	$^{+0.18}_{-0.079}$	$^{+0.085}_{-0.072}$	$^{+0.056}_{-0.069}$	$^{+0.043}_{-0.068}$	$^{+0.04}_{-0.073}$	$^{+0.046}_{-0.081}$	$^{+0.05}_{-0.06}$

p_T [GeV]	260-310	310-400	400-500	500-600	600-800	800-1000	1000-1200	1200-1500
Jets	30311	14628	3401	786	297	20	3	1
Cross section	19.4	5.19	1.09	0.249	0.047	0.00304	0.00044	8.85e-05
Rel. Stat. Err.	0.0057	0.0083	0.017	0.036	0.058	0.22	0.58	1
Rel. Syst. Err.	$^{+0.15}_{-0.13}$	$^{+0.15}_{-0.13}$	$^{+0.16}_{-0.15}$	$^{+0.17}_{-0.15}$	$^{+0.2}_{-0.18}$	$^{+0.25}_{-0.23}$	$^{+0.33}_{-0.28}$	$^{+0.47}_{-0.37}$
NLO cross section	20.1	5.47	1.15	0.275	0.0506	0.0053	0.000636	5.45e-05
NLO + non. pert.	20.4	5.57	1.17	0.28	0.0515	0.0054	0.000647	5.55e-05
Rel. theory error	$^{+0.055}_{-0.093}$	$^{+0.06}_{-0.097}$	$^{+0.069}_{-0.11}$	$^{+0.08}_{-0.11}$	$^{+0.096}_{-0.12}$	$^{+0.13}_{-0.13}$	$^{+0.18}_{-0.14}$	$^{+0.28}_{-0.15}$

Table A.3: Measured inclusive jet double-differential cross section per GeV and per unit rapidity as a function of p_T for anti-k$_t$ jets with $R = 0.6$ in the region $0.8 \leq |y| < 1.2$, compared to NLO perturbative QCD calculations corrected for non-perturbative effects. All errors listed are fractional uncertainties.

p_T [GeV]	20-30	30-45	45-60	60-80	80-110	110-160	160-210	210-260
Jets	127564	21811	3444	44545	13514	38972	27689	33300
Cross section	7.86e+06	1.01e+06	1.64e+05	3.72e+04	7.6e+03	1.23e+03	184	40.8
Rel. Stat. Err.	0.0028	0.0068	0.017	0.0047	0.0086	0.0051	0.006	0.0055
Rel. Syst. Err.	$^{+0.35}_{-0.27}$	$^{+0.26}_{-0.19}$	$^{+0.24}_{-0.15}$	$^{+0.17}_{-0.12}$	$^{+0.13}_{-0.12}$	$^{+0.13}_{-0.12}$	$^{+0.13}_{-0.12}$	$^{+0.14}_{-0.14}$
NLO cross section	5.45e+06	8.46e+05	1.52e+05	3.63e+04	7.69e+03	1.23e+03	187	42.6
NLO + non. pert.	7.46e+06	1.04e+06	1.72e+05	3.9e+04	8.02e+03	1.26e+03	191	43.6
Rel. theory error	$^{+0.45}_{-0.084}$	$^{+0.14}_{-0.076}$	$^{+0.064}_{-0.069}$	$^{+0.043}_{-0.067}$	$^{+0.038}_{-0.069}$	$^{+0.042}_{-0.075}$	$^{+0.047}_{-0.084}$	$^{+0.052}_{-0092}$

p_T [GeV]	260-310	310-400	400-500	500-600	600-800	800-1000	1000-1200	1200-1500
Jets	9010	17653	3226	608	163	10	1	-
Cross section	11.3	2.83	0.454	0.0841	0.0113	0.000659	6.21e-05	-
Rel. Stat. Err.	0.011	0.0075	0.018	0.041	0.078	0.32	1	-
Rel. Syst. Err.	$^{+0.16}_{-0.15}$	$^{+0.18}_{-0.16}$	$^{+0.2}_{-0.17}$	$^{+0.22}_{-0.2}$	$^{+0.28}_{-0.24}$	$^{+0.38}_{-0.29}$	$^{+0.56}_{-0.36}$	-
NLO cross section	12.3	3	0.509	0.0942	0.0123	0.000683	3.94e-05	-
NLO + non. pert.	12.6	3.07	0.522	0.0964	0.0126	0.000699	4.03e-05	-
Rel. theory error	$^{+0.059}_{-0.099}$	$^{+0.068}_{-0.1}$	$^{+0.085}_{-0.11}$	$^{+0.11}_{-0.12}$	$^{+0.14}_{-0.13}$	$^{+0.22}_{-0.14}$	$^{+0.37}_{-0.15}$	-

Table A.4: Measured inclusive jet double-differential cross section per GeV and per unit rapidity as a function of p_T for anti-k$_t$ jets with $R = 0.6$ in the region $1.2 \leq |y| < 2.1$, compared to NLO perturbative QCD calculations corrected for non-perturbative effects. All errors listed are fractional uncertainties.

p_T [GeV]	20-30	30-45	45-60	60-80	80-110	110-160	160-210	210-260
Jets	65881	11443	1872	22753	112391	100478	49869	8045
Cross section	5.93e+06	7.18e+05	1.2e+05	2.4e+04	4.7e+03	635	72.4	11.9
Rel. Stat. Err.	0.0039	0.0093	0.023	0.0066	0.003	0.0032	0.0045	0.011
Rel. Syst. Err.	$^{+0.41}_{-0.32}$	$^{+0.36}_{-0.23}$	$^{+0.31}_{-0.15}$	$^{+0.18}_{-0.13}$	$^{+0.15}_{-0.12}$	$^{+0.14}_{-0.13}$	$^{+0.17}_{-0.15}$	$^{+0.18}_{-0.18}$
NLO cross section	4.27e+06	6.04e+05	1.06e+05	2.38e+04	4.66e+03	650	77.5	12.8
NLO + non. pert.	5.76e+06	7.31e+05	1.18e+05	2.55e+04	4.86e+03	670	79.7	13.2
Rel. theory error	$^{+0.28}_{-0.09}$	$^{+0.099}_{-0.076}$	$^{+0.057}_{-0.076}$	$^{+0.045}_{-0.073}$	$^{+0.043}_{-0.077}$	$^{+0.049}_{-0.084}$	$^{+0.062}_{-0.095}$	$^{+0.083}_{-01}$

p_T [GeV]	260-310	310-400	400-500	500-600	600-800	800-1000	1000-1200	1200-1500
Jets	6357	1680	114	3	-	-	-	-
Cross section	2.23	0.321	0.0205	0.000584	-	-	-	-
Rel. Stat. Err.	0.013	0.024	0.094	0.58	-	-	-	-
Rel. Syst. Err.	$^{+0.23}_{-0.19}$	$^{+0.3}_{-0.23}$	$^{+0.4}_{-0.3}$	$^{+0.59}_{-0.35}$	-	-	-	-
NLO cross section	2.49	0.359	0.0224	0.001	-	-	-	-
NLO + non. pert.	2.56	0.369	0.0231	0.00103	-	-	-	-
Rel. theory error	$^{+0.11}_{-0.11}$	$^{+0.16}_{-0.12}$	$^{+0.28}_{-0.13}$	$^{+0.57}_{-0.17}$	-	-	-	-

Table A.5: Measured inclusive jet double-differential cross section per GeV and per unit rapidity as a function of p_T for anti-k$_t$ jets with $R = 0.6$ in the region $2.1 \leq |y| < 2.8$, compared to NLO perturbative QCD calculations corrected for non-perturbative effects. All errors listed are fractional uncertainties.

p_T [GeV]	20-30	30-45	45-60	60-80	80-110	110-160	160-210	210-260
Jets	52953	8541	1216	9985	12134	46819	2574	611
Cross section	3.9e+06	4.44e+05	6.4e+04	1.23e+04	1.84e+03	146	7.03	0.376
Rel. Stat. Err.	0.0043	0.011	0.029	0.01	0.0091	0.0046	0.02	0.04
Rel. Syst. Err.	$^{+0.51}_{-0.38}$	$^{+0.48}_{-0.29}$	$^{+0.39}_{-0.21}$	$^{+0.26}_{-0.2}$	$^{+0.27}_{-0.17}$	$^{+0.25}_{-0.2}$	$^{+0.34}_{-0.27}$	$^{+0.42}_{-0.31}$
NLO cross section	2.89e+06	3.83e+05	5.97e+04	1.15e+04	1.81e+03	159	8.27	0.491
NLO + non. pert.	3.78e+06	4.53e+05	6.58e+04	1.21e+04	1.87e+03	163	8.48	0.503
Rel. theory error	$^{+0.12}_{-0.1}$	$^{+0.059}_{-0.09}$	$^{+0.052}_{-0.085}$	$^{+0.048}_{-0.079}$	$^{+0.06}_{-0.086}$	$^{+0.09}_{-0.096}$	$^{+0.16}_{-0.11}$	$^{+0.31}_{-0.15}$

p_T [GeV]	260-310	310-400	400-500	500-600	600-800	800-1000	1000-1200	1200-1500
Jets	23	-	-	-	-	-	-	-
Cross section	0.011	-	-	-	-	-	-	-
Rel. Stat. Err.	0.21	-	-	-	-	-	-	-
Rel. Syst. Err.	$^{+0.53}_{-0.52}$	-	-	-	-	-	-	-
NLO cross section	0.0248	-	-	-	-	-	-	-
NLO + non. pert.	0.0254	-	-	-	-	-	-	-
Rel. theory error	$^{+0.66}_{-0.24}$	-	-	-	-	-	-	-

Table A.6: Measured inclusive jet double-differential cross section per GeV and per unit rapidity as a function of p_T for anti-k$_t$ jets with $R = 0.6$ in the region $2.8 \leq |y| < 3.6$, compared to NLO perturbative QCD calculations corrected for non-perturbative effects. All errors listed are fractional uncertainties.

p_T [GeV]	20-30	30-45	45-60	60-80	80-110	110-160	160-210	210-260
Jets	18835	59867	5610	8214	10073	557	-	-
Cross section	1.51e+06	1.47e+05	1.35e+04	1.26e+03	76.2	0.82	-	-
Rel. Stat. Err.	0.0073	0.0041	0.013	0.011	0.01	0.042	-	-
Rel. Syst. Err.	$^{+0.76}_{-0.49}$	$^{+0.85}_{-0.41}$	$^{+0.72}_{-0.3}$	$^{+0.51}_{-0.35}$	$^{+0.6}_{-0.23}$	$^{+0.44}_{-0.3}$	-	-
NLO cross section	1.56e+06	1.62e+05	1.66e+04	1.91e+03	122	1.84	-	-
NLO + non. pert.	1.75e+06	1.7e+05	1.69e+04	1.91e+03	121	1.82	-	-
Rel. theory error	$^{+0.11}_{-0.11}$	$^{+0.092}_{-0.092}$	$^{+0.091}_{-0.093}$	$^{+0.12}_{-0.1}$	$^{+0.22}_{-0.14}$	$^{+0.58}_{-0.27}$	-	-

Table A.7: Measured inclusive jet double-differential cross section per GeV and per unit rapidity as a function of p_T for anti-k$_t$ jets with $R = 0.6$ in the region $3.6 \leq |y| < 4.4$, compared to NLO perturbative QCD calculations corrected for non-perturbative effects. All errors listed are fractional uncertainties.

p_T [GeV]	20-30	30-45	45-60	60-80	80-110	110-160	160-210	210-260
Jets	27993	5918	1110	16582	93011	103410	74293	17971
Cross section	4.97e+06	7.82e+05	1.53e+05	3.82e+04	8.47e+03	1.47e+03	253	62.9
Rel. Stat. Err.	0.006	0.013	0.03	0.0078	0.0033	0.0031	0.0037	0.0075
Rel. Syst. Err.	$^{+0.26}_{-0.23}$	$^{+0.18}_{-0.14}$	$^{+0.16}_{-0.1}$	$^{+0.1}_{-0.11}$	$^{+0.12}_{-0.099}$	$^{+0.11}_{-0.093}$	$^{+0.1}_{-0.11}$	$^{+0.13}_{-0.11}$
NLO cross section	6.02e+06	9.54e+05	1.82e+05	4.54e+04	1.01e+04	1.71e+03	284	71.3
NLO + non. pert.	5.15e+06	8.43e+05	1.65e+05	4.22e+04	9.58e+03	1.66e+03	279	70.5
Rel. theory error	$^{+0.22}_{-0.073}$	$^{+0.17}_{-0.07}$	$^{+0.13}_{-0.059}$	$^{+0.1}_{-0.048}$	$^{+0.078}_{-0.047}$	$^{+0.059}_{-0.052}$	$^{+0.051}_{-0.061}$	$^{+0.051}_{-0.069}$

p_T [GeV]	260-310	310-400	400-500	500-600	600-800	800-1000	1000-1200	1200-1500
Jets	24061	12333	3122	797	300	48	5	3
Cross section	20.6	5.9	1.32	0.346	0.0641	0.0102	0.00104	0.00039
Rel. Stat. Err.	0.0064	0.009	0.018	0.035	0.058	0.14	0.45	0.58
Rel. Syst. Err.	$^{+0.12}_{-0.11}$	$^{+0.12}_{-0.11}$	$^{+0.13}_{-0.12}$	$^{+0.13}_{-0.13}$	$^{+0.17}_{-0.14}$	$^{+0.18}_{-0.17}$	$^{+0.23}_{-0.21}$	$^{+0.29}_{-0.26}$
NLO cross section	22.6	6.48	1.43	0.377	0.0792	0.0111	0.00197	0.000299
NLO + non. pert.	22.4	6.43	1.42	0.374	0.0786	0.0111	0.00196	0.000296
Rel. theory error	$^{+0.054}_{-0.073}$	$^{+0.058}_{-0.08}$	$^{+0.064}_{-0.086}$	$^{+0.072}_{-0.093}$	$^{+0.081}_{-0.1}$	$^{+0.1}_{-0.11}$	$^{+0.12}_{-0.12}$	$^{+0.16}_{-0.13}$

Table A.8: Measured inclusive jet double-differential cross section per GeV and per unit rapidity as a function of p_T for anti-k$_t$ jets with $R = 0.4$ in the region $0 \leq |y| < 0.3$, compared to N O perturbative QCD calculations corrected for non-perturbative effects. All errors listed are fractional uncertainties.

p_T [GeV]	20-30	30-45	45-60	60-80	80-110	110-160	160-210	210-260
Jets	45019	9753	1840	26728	150170	166246	117461	28412
Cross section	4.99e+06	7.85e+05	1.53e+05	3.66e+04	8.3e+03	1.43e+03	239	60.1
Rel. Stat. Err.	0.0047	0.01	0.023	0.0061	0.0026	0.0025	0.0029	0.0059
Rel. Syst. Err.	$^{+0.25}_{-0.23}$	$^{+0.19}_{-0.13}$	$^{+0.14}_{-0.12}$	$^{+0.13}_{-0.097}$	$^{+0.11}_{-0.11}$	$^{+0.12}_{-0.11}$	$^{+0.12}_{-0.11}$	$^{+0.13}_{-0.12}$
NLO cross section	5.69e+06	9.2e+05	1.76e+05	4.35e+04	9.56e+03	1.63e+03	268	66.5
NLO + non. pert.	4.89e+06	8.15e+05	1.6e+05	4.06e+04	9.12e+03	1.59e+03	264	65.8
Rel. theory error	$^{+0.21}_{-0.094}$	$^{+0.17}_{-0.077}$	$^{+0.13}_{-0.06}$	$^{+0.1}_{-0.052}$	$^{+0.078}_{-0.05}$	$^{+0.059}_{-0.05}$	$^{+0.052}_{-0.058}$	$^{+0.052}_{-0.065}$

p_T [GeV]	260-310	310-400	400-500	500-600	600-800	800-1000	1000-1200	1200-1500
Jets	37810	19575	4565	1220	510	62	11	3
Cross section	19.4	5.6	1.18	0.314	0.0653	0.00774	0.00134	0.000226
Rel. Stat. Err.	0.0051	0.0071	0.015	0.029	0.044	0.13	0.3	0.58
Rel. Syst. Err.	$^{+0.13}_{-0.12}$	$^{+0.14}_{-0.12}$	$^{+0.14}_{-0.13}$	$^{+0.16}_{-0.13}$	$^{+0.17}_{-0.16}$	$^{+0.21}_{-0.2}$	$^{+0.27}_{-0.22}$	$^{+0.32}_{-0.3}$
NLO cross section	21.2	6	1.31	0.338	0.0691	0.00909	0.00148	0.000197
NLO + non. pert.	21	5.96	1.3	0.335	0.0686	0.00903	0.00147	0.000196
Rel. theory error	$^{+0.054}_{-0.072}$	$^{+0.058}_{-0.078}$	$^{+0.065}_{-0.085}$	$^{+0.072}_{-0.093}$	$^{+0.083}_{-0.1}$	$^{+0.11}_{-0.11}$	$^{+0.13}_{-0.12}$	$^{+0.18}_{-0.14}$

Table A.9: Measured inclusive jet double-differential cross section per GeV and per unit rapidity as a function of p_T for anti-k$_t$ jets with $R = 0.4$ in the region $0.3 \leq |y| < 0.8$, compared to NLO perturbative QCD calculations corrected for non-perturbative effects. All errors listed are fractional uncertainties.

p_T [GeV]	20-30	30-45	45-60	60-80	80-110	110-160	160-210	210-260
Jets	33473	7206	1365	19462	110429	118561	81312	18926
Cross section	3.93e+06	6.71e+05	1.41e+05	3.38e+04	7.56e+03	1.26e+03	204	49.7
Rel. Stat. Err.	0.0055	0.012	0.027	0.0072	0.003	0.0029	0.0035	0.0073
Rel. Syst. Err.	$^{+0.29}_{-0.23}$	$^{+0.2}_{-0.14}$	$^{+0.15}_{-0.13}$	$^{+0.15}_{-0.11}$	$^{+0.13}_{-0.11}$	$^{+0.13}_{-0.11}$	$^{+0.13}_{-0.12}$	$^{+0.14}_{-0.12}$
NLO cross section	5.44e+06	8.61e+05	1.65e+05	3.99e+04	8.76e+03	1.46e+03	239	58.1
NLO + non. pert.	4.72e+06	7.69e+05	1.52e+05	3.73e+04	8.38e+03	1.42e+03	235	57.4
Rel. theory error	$^{+0.2}_{-0.093}$	$^{+0.16}_{-0.08}$	$^{+0.12}_{-0.055}$	$^{+0.1}_{-0.053}$	$^{+0.078}_{-0.049}$	$^{+0.062}_{-0.051}$	$^{+0.056}_{-0.063}$	$^{+0.056}_{-0.069}$

p_T [GeV]	260-310	310-400	400-500	500-600	600-800	800-1000	1000-1200	1200-1500
Jets	24743	12194	2852	670	255	18	3	1
Cross section	15.8	4.34	0.911	0.212	0.0405	0.00274	0.000445	8.92e-05
Rel. Stat. Err.	0.0064	0.0091	0.019	0.039	0.063	0.24	0.58	1
Rel. Syst. Err.	$^{+0.14}_{-0.13}$	$^{+0.15}_{-0.13}$	$^{+0.15}_{-0.15}$	$^{+0.17}_{-0.15}$	$^{+0.2}_{-0.18}$	$^{+0.25}_{-0.23}$	$^{+0.35}_{-0.28}$	$^{+0.48}_{-0.38}$
NLO cross section	18.1	5.02	1.05	0.252	0.0467	0.00488	0.000587	5.06e-05
NLO + non. pert.	17.9	4.97	1.04	0.25	0.0462	0.00484	0.000582	5.01e-05
Rel. theory error	$^{+0.058}_{-0.074}$	$^{+0.063}_{-0.081}$	$^{+0.07}_{-0.089}$	$^{+0.08}_{-0.094}$	$^{+0.095}_{-0.1}$	$^{+0.13}_{-0.11}$	$^{+0.18}_{-0.13}$	$^{+0.27}_{-0.14}$

Table A.10: Measured inclusive jet double-differential cross section per GeV and per unit rapidity as a function of p_T for anti-k$_t$ jets with $R = 0.4$ in the region $0.8 \leq |y| < 1.2$, compared to NLO perturbative QCD calculations corrected for non-perturbative effects. All errors listed are fractional uncertainties.

p_T [GeV]	20-30	30-45	45-60	60-80	80-110	110-160	160-210	210-260
Jets	60603	12839	2323	31501	10066	30178	22421	27350
Cross section	3.75e+06	5.96e+05	1.11e+05	2.62e+04	5.71e+03	948	149	33.5
Rel. Stat. Err.	0.0041	0.0088	0.021	0.0056	0.01	0.0058	0.0067	0.006
Rel. Syst. Err.	$^{+0.31}_{-0.26}$	$^{+0.23}_{-0.17}$	$^{+0.2}_{-0.15}$	$^{+0.17}_{-0.12}$	$^{+0.14}_{-0.12}$	$^{+0.13}_{-0.12}$	$^{+0.14}_{-0.13}$	$^{+0.15}_{-0.13}$
NLO cross section	4.71e+06	7.41e+05	1.34e+05	3.21e+04	6.88e+03	1.1e+03	168	38.7
NLO + non. pert.	4.07e+06	6.62e+05	1.23e+05	3.02e+04	6.6e+03	1.07e+03	166	38.3
Rel. theory error	$^{+0.19}_{-0.1}$	$^{+0.15}_{-0.079}$	$^{+0.12}_{-0.068}$	$^{+0.097}_{-0.055}$	$^{+0.076}_{-0.052}$	$^{+0.061}_{-0.058}$	$^{+0.057}_{-0.068}$	$^{+0.059}_{-0.07}$

p_T [GeV]	260-310	310-400	400-500	500-600	600-800	800-1000	1000-1200	1200-1500
Jets	7596	14614	2721	511	132	7	1	-
Cross section	9.5	2.33	0.387	0.0715	0.00945	0.000473	6.25e-05	-
Rel. Stat. Err.	0.011	0.0083	0.019	0.044	0.087	0.38	1	-
Rel. Syst. Err.	$^{+0.17}_{-0.15}$	$^{+0.18}_{-0.15}$	$^{+0.19}_{-0.18}$	$^{+0.23}_{-0.2}$	$^{+0.29}_{-0.23}$	$^{+0.38}_{-0.31}$	$^{+0.54}_{-0.39}$	-
NLO cross section	11.2	2.74	0.467	0.0863	0.0113	0.000629	3.6e-05	-
NLO + non. pert.	11.1	2.71	0.462	0.0854	0.0112	0.000622	3.56e-05	-
Rel. theory error	$^{+0.063}_{-0.082}$	$^{+0.071}_{-0.088}$	$^{+0.087}_{-0.095}$	$^{+0.11}_{-0.1}$	$^{+0.14}_{-0.11}$	$^{+0.22}_{-0.12}$	$^{+0.36}_{-0.13}$	-

Table A.11: Measured inclusive jet double-differential cross section per GeV and per unit rapidity as a function of p_T for anti-k_t jets with $R = 0.4$ in the region $1.2 \leq |y| < 2.1$, compared to NLO perturbative QCD calculations corrected for non-perturbative effects. All errors listed are fractional uncertainties.

p_T [GeV]	20-30	30-45	45-60	60-80	80-110	110-160	160-210	210-260
Jets	29839	6539	1242	16075	83061	78106	39983	6545
Cross section	2.76e+06	4.17e+05	8.02e+04	1.69e+04	3.43e+03	493	58.5	9.9
Rel. Stat. Err.	0.0058	0.012	0.028	0.0079	0.0035	0.0036	0.005	0.012
Rel. Syst. Err.	$^{+0.38}_{-0.33}$	$^{+0.39}_{-0.23}$	$^{+0.31}_{-0.15}$	$^{+0.17}_{-0.17}$	$^{+0.18}_{-0.13}$	$^{+0.16}_{-0.15}$	$^{+0.19}_{-0.16}$	$^{+0.23}_{-0.19}$
NLO cross section	3.62e+06	5.38e+05	9.32e+04	2.09e+04	4.2e+03	582	70.5	11.6
NLO + non. pert.	3.09e+06	4.77e+05	8.52e+04	1.96e+04	4.01e+03	566	69	11.4
Rel. theory error	$^{+0.18}_{-0.1}$	$^{+0.14}_{-0.076}$	$^{+0.11}_{-0.058}$	$^{+0.081}_{-0.054}$	$^{+0.063}_{-0.06}$	$^{+0.054}_{-0.072}$	$^{+0.063}_{-0.084}$	$^{+0.082}_{-0.095}$

p_T [GeV]	260-310	310-400	400-500	500-600	600-800	800-1000	1000-1200	1200-1500
Jets	5201	1415	96	2	-	-	-	-
Cross section	1.83	0.273	0.0163	0.000331	-	-	-	-
Rel. Stat. Err.	0.014	0.027	0.1	0.71	-	-	-	-
Rel. Syst. Err.	$^{+0.24}_{-0.21}$	$^{+0.33}_{-0.25}$	$^{+0.43}_{-0.31}$	$^{+0.42}_{-0.36}$	-	-	-	-
NLO cross section	2.27	0.324	0.0201	0.000901	-	-	-	-
NLO + non. pert.	2.23	0.318	0.0198	0.000885	-	-	-	-
Rel. theory error	$^{+0.11}_{-0.11}$	$^{+0.15}_{-0.13}$	$^{+0.27}_{-0.17}$	$^{+0.54}_{-0.23}$	-	-	-	-

Table A.12: Measured inclusive jet double-differential cross section per GeV and per unit rapidity as a function of p_T for anti-k$_t$ jets with $R = 0.4$ in the region $2.1 \leq |y| < 2.8$, compared to NLO perturbative QCD calculations corrected for non-perturbative effects. All errors listed are fractional uncertainties.

p_T [GeV]	20-30	30-45	45-60	60-80	80-110	110-160	160-210	210-260
Jets	25328	5254	816	7094	9312	37101	2067	514
Cross section	1.87e+06	2.7e+05	4.22e+04	8.54e+03	1.34e+03	112	5.39	0.29
Rel. Stat. Err.	0.0063	0.014	0.035	0.012	0.01	0.0052	0.022	0.044
Rel. Syst. Err.	$^{+0.5}_{-0.42}$	$^{+0.52}_{-0.3}$	$^{+0.43}_{-0.23}$	$^{+0.28}_{-0.22}$	$^{+0.29}_{-0.19}$	$^{+0.26}_{-0.22}$	$^{+0.41}_{-0.29}$	$^{+0.47}_{-0.37}$
NLO cross section	2.5e+06	3.41e+05	5.25e+04	1.05e+04	1.62e+03	145	7.41	0.433
NLO + non. pert.	2.1e+06	3e+05	4.77e+04	9.81e+03	1.54e+03	139	7.17	0.419
Rel. theory error	$^{+0.14}_{-0.09}$	$^{+0.1}_{-0.07}$	$^{+0.077}_{-0.061}$	$^{+0.066}_{-0.062}$	$^{+0.069}_{-0.079}$	$^{+0.097}_{-0.1}$	$^{+0.17}_{-0.15}$	$^{+0.31}_{-0.22}$

p_T [GeV]	260-310	310-400	400-500	500-600	600-800	800-1000	1000-1200	1200-1500
Jets	21	-	-	-	-	-	-	-
Cross section	0.00937	-	-	-	-	-	-	-
Rel. Stat. Err.	0.22	-	-	-	-	-	-	-
Rel. Syst. Err.	$^{+0.57}_{-0.54}$	-	-	-	-	-	-	-
NLO cross section	0.0216	-	-	-	-	-	-	-
NLO + non. pert.	0.0209	-	-	-	-	-	-	-
Rel. theory error	$^{+0.66}_{-0.34}$	-	-	-	-	-	-	-

Table A.13: Measured inclusive jet double-differential cross section per GeV and per unit rapidity as a function of p_T for anti-k$_t$ jets with $R = 0.4$ in the region $2.8 \leq |y| < 3.6$, compared to NLO perturbative QCD calculations corrected for non-perturbative effects. All errors listed are fractional uncertainties.

p_T [GeV]	20-30	30-45	45-60	60-80	80-110	110-160	160-210	210-260
Jets	10053	36985	3894	6326	8009	472	-	-
Cross section	8.08e+05	9.2e+04	9.21e+03	908	53.5	0.547	-	-
Rel. Stat. Err.	0.01	0.0052	0.016	0.013	0.011	0.046	-	-
Rel. Syst. Err.	$^{+0.71}_{-0.51}$	$^{+0.87}_{-0.44}$	$^{+0.82}_{-0.39}$	$^{+0.71}_{-0.3}$	$^{+0.49}_{-0.3}$	$^{+0.52}_{-0.58}$	-	-
NLO cross section	1.37e+06	1.43e+05	1.49e+04	1.63e+03	104	1.9	-	-
NLO + non. pert.	1.07e+06	1.2e+05	1.3e+04	1.46e+03	94.5	1.73	-	-
Rel. theory error	$^{+0.15}_{-0.079}$	$^{+0.086}_{-0.089}$	$^{+0.09}_{-0.092}$	$^{+0.13}_{-0.16}$	$^{+0.23}_{-0.23}$	$^{+0.5}_{-0.24}$	-	-

Table A.14: Measured inclusive jet double-differential cross section per GeV and per unit rapidity as a function of p_T for anti-k$_t$ jets with $R = 0.4$ in the region $3.6 \leq |y| < 4.4$, compared to NLO perturbative QCD calculations corrected for non-perturbative effects. All errors listed are fractional uncertainties.

Bibliography

[1] Gerald C. Blazey and Brenna L. Flaugher, *Inclusive jet and dijet production at the Tevatron.* Ann. Rev. Nucl. Part. Sci. **49**, (1999) 633–685, [`doi: 10.1146/annurev.nucl.49.1.633`], [`hep-ex/9903058`].

[2] V.M. Abazov et al., the **DZero** Collaboration, *Measurement of the inclusive jet cross section in $p\bar{p}$ collisions at $\sqrt{s}$=1.96 TeV.* Phys. Rev. Lett. **101**, (2008) 062001, [`doi: 10.1103/PhysRevLett.101.062001`], [`arXiv:0802.2400`].

[3] T. Aaltonen et al., the **CDF** Collaboration, *Measurement of the inclusive jet cross section at the Fermilab Tevatron $p\bar{p}$ collider using a cone-based jet algorithm.* Phys. Rev. D. **78**, (2008) 052006, [`doi: 10.1103/PhysRevD.78.052006`], [`arXiv:0807.2204`].

[4] F. D. Aaron et al., the **H1 and ZEUS** Collaboration, *Combined Measurement and QCD Analysis of the Inclusive ep Scattering Cross Sections at HERA.* JHEP **01**, (2010) 109, [`doi: 10.1007/JHEP01(2010)109`], [`arXiv:0911.0884`].

[5] F. Abe et al., the **CDF** Collaboration, *Inclusive Jet Cross Section in $\bar{p}p$ Collisions at $\sqrt{s}$ = 1.8 TeV.* Phys. Rev. Lett. **77**(3), (1996) 438–443, [`doi: 10.1103/PhysRevLett.77.438`].

[6] C. Amsler et al., the **Particle Data Group** Collaboration, *Review of particle physics.* Phys. Lett. **B667**, (2008) 1–1340, [`doi: 10.1016/j.physletb.2008.07.018`].

[7] P.A.M. Dirac, *The Quantum Theory of the Electron.* Proc. R. Soc. Lond. **A 117**, (1928) 610–624, [`doi: 10.1098/rspa.1928.0023`].

[8] F. Dyson, *The Radiation Theories of Tomonaga, Schwinger, and Feynman.* Physical Review **75**, (1949) 486–502, [`doi: 10.1103/PhysRev.75.486`].

[9] A. Arbuzov et al., *The present theoretical error on the Bhabha scattering cross section in the luminometry region at LEP.* Physics Letters B **383**, (1996) 238–242, [`doi: 10.1016/0370-2693(96)00733-2`].

[10] S.L. Glashow, *Partial Symmetries of Weak Interactions*. Nucl. Phys. **22**, (1961) 579–588, [`doi: 10.1016/0029-5582(61)90469-2`].

[11] A. Salam and J.C. Ward, *Electromagnetic and weak interactions*. Phys. Lett. **13**, (1964) 168–171, [`doi: 10.1016/0031-9163(64)90711-5`].

[12] S. Weinberg, *A Model of Leptons*. Phys. Rev. Lett. **19**(21), (1967) 1264–1266, [`doi: 10.1103/PhysRevLett.19.1264`].

[13] F.J. Hasert et al., *Observation of neutrino-like interactions without muon or electron in the Gargamelle neutrino experiment*. Phys. Lett **B46**, (1973) 138–140.

[14] Charles Y. Prescott, *Parity violation in electron scattering* Published in the International School on Electron and Pion Interactions with Nuclei at Intermediate Energies Electron and Pion Interactions with Nuclei at Intermediate Energies, Rome, Italy, 18-29 Jun 1979.

[15] G. Banner et al., the **The UA2 Collaboration** Collaboration, *Observation of single isolated electrons of high transverse momentum in events with missing transverse energy at the CERN $\bar{p}p$ collider*. Phys. Lett **B122**, (1983) 476–485.

[16] G. Arnison et al., the **The UA1 Collaboration** Collaboration, *Experimental Observation of Lepton Pairs of Invariant Mass Around 95 GeV at the CERN SPS Collider*. Phys. Lett **B126**, (1983) 398.

[17] G.D. Rochester and C.C. Butler, *Evidence for the Existence of New Unstable Elementary Particles*. Nature **160**, (1947) 855, [`doi: 10.1038/160855a0`].

[18] M. Gell-Mann, *A schematic model of baryons and mesons*. Phys. Lett. **8**, (1964) 214–215, [`doi: 10.1016/S0031-9163(64)92001-3`].

[19] G. Zweig, *An SU(3) model for strong interaction symmetry and its breaking*. CERN-TH 401 (1964).

[20] G. Zweig, *An SU(3) model for strong interaction symmetry and its breaking 2*. CERN-TH 412 (1964).

[21] E.D. Bloom et al., *High-Energy Inelastic e-p Scattering at 6° and 10°*. Phys. Rev. Lett. **23**, (1969) 930–934, [`doi: 10.1103/PhysRevLett.23.930`].

[22] M. Breidenbach et al., *Observed Behavior of Highly Inelastic Electron-Proton Scattering.* Phys. Rev. Lett. **23**, (1969) 935–939, [`doi: 10.1103/PhysRevLett.23.935`].

[23] R.P. Feynman, *Behavior of Hadron Collisions at Extreme Energies.* In *Proceedings of the 3rd Topical Conference on High Energy Collision of Hadrons, Stony Brook, N.Y.* (1969).

[24] M. Gell-Mann H. Fritzsch and H. Leutwyler, *Advantages of the color octet gluon picture.* Phys. Lett. **B26**, (1973) 365–368, [`doi: 10.1016/0370-2693(73)90625-4`].

[25] H. Fritzsch and M. Gell-Mann, *Current Algebra: Quarks and What Else?* In *Proceedings of the XVI International Conference on High Energy Physics, University of Chicago and the National Accelerator Laborator, Sept. 1972* (1972).

[26] K. Nakamura et al., the **Particle Data Group** Collaboration. J. Phys. **G37**.

[27] F. Abe et al., the **CDF** Collaboration, *Observation of Top Quark production in* $p\bar{p}$ *Collisions with the Collider Detector at Fermilab.* Phys. Rev. Lett. **74**, (1995) 2626–2631, [`doi: 10.1103/PhysRevLett.74.2626`], [`hep-ex/9503002`].

[28] S. Abachi et al., the **DZero** Collaboration, *Search for High Mass Top Quark Production in* $p\bar{p}$ *Collisions at* $\sqrt{s}$*=1.8 TeV.* Phys. Rev. Lett. **74**, (1995) 2422–2426, [`doi: 10.1103/PhysRevLett.74.2422`], [`hep-ex/9411001`].

[29] P.W. Higgs, *Broken Symmetries, Massless Particles and Gauge Fields.* Phys. Lett. **12**, (1964) 132–133.

[30] H.D. Politzer, *Reliable perturbative results for strong interactions.* Phys. Rev. Lett. **30**, (1973) 1346–1349, [`doi: 10.1103/PhysRevLett.30.1346`].

[31] D.J. Gross and F. Wilczek, *Ultraviolet behavior of non-Abelian gauge theories.* Phys. Rev. Lett. **30**, (1973) 1343–1346, [`doi: 10.1103/PhysRevLett.30.1343`].

[32] W. Bietenholz et al., *Exploring the Nucleon Structure from First Principles of QCD.* In *Proceedings of the XXXIII Symposium on Nuclear Physics, Cocoyoc (Morelos, Mexico), January 5-8, 2010*, edited by Libertad Barrón-Palos, Roelof Bijker, Ruben Fossion, and David Lizcano, 012011 (IOP Journal of Physics: Conference Series) (2010), [`doi: 10.1088/1742-6596/239/1/012011`], [`arXiv:1004.2100`].

[33] J. Collins, D. Soper and G. Sterman, *Factorization of Hard Processes in QCD*. Adv. Ser. Direct. High Energy Phys. **5**, (1988) 1–91, [`hep-ph/0409313`].

[34] A.D. Martin, W.J. Stirling, R.S. Thorne, and G. Watt, *Parton distributions for the LHC*. Eur. Phys. J. **C63**, (2009) 189–285, [`doi: 10.1140/epjc/s10052-009-1072-5`], [`arXiv:0901.0002`], figures from the MSTW Website.

[35] Yu.L. Dokshitzer, *Calculation of the Structure Functions for Deep Inelastic Scattering and e+ e- Annihilation by Perturbation Theory in Quantum Chromodynamics*. Sov. Phys. JETP **46**, (1977) 641–653.

[36] V.N. Gribov and L.N. Lipatov, *Deep inelastic e p scattering in perturbation theory*. Sov. J. Nucl. Phys. **15**, (1972) 438–450.

[37] G. Altarelli and G. Parisi, *Asymptotic freedom in parton language*. Nucl. Phys. **B126**, (1977) 298, [`doi: 10.1016/0550-3213(77)90384-4`].

[38] W.K. Tung et al., *Global QCD Analysis and Collider Phenomenology–CTEQ*. In *Proceedings of the 15th International Workshop on Deep-Inelastic Scattering and Related Subjects, Munich, April 2007*, edited by G. Grindhammer and K. Sachs (Atlantis Press, Amsterdam) (2007), [`ISBN: 9783935702232`], [`doi: 10.3360/dis.2007.28`], [`arXiv:0707.0275`].

[39] H.L. Lai et al., *New parton distributions for collider physics*. Phys. Rev. **D82**, (2010) 074024, [`doi: 10.1103/PhysRevD.82.074024`].

[40] P.M. Nadolsky et al., *Implications of CTEQ global analysis for collider observables*. Phys. Rev. **D78**, (2008) 013004, [`doi: 10.1103/PhysRevD.78.013004`], [`arXiv:0802.0007`].

[41] Richard D. Ball et al., the **NNPDF** Collaboration, *A determination of parton distributions with faithful uncertainty estimation*. Nucl. Phys. **B809**, (2009) 1–63, [`doi: 10.1016/j.nuclphysb.2008.09.037`], [`arXiv:0808.1231`].

[42] M. Ubiali et al., *Combined PDF and strong coupling uncertainties at the LHC with NNPDF2.0*. In *Proceedings of the conference "Rencontres de Moriond, QCD and High Energy Interactions", 2010* (2010).

[43] A. Cooper-Sarkar, *HERAPDF fits including F_2(charm) data* (2010).

[44] T. Sjöstrand, S. Mrenna, and P. Skands, *PYTHIA 6.4 physics and manual.* JHEP **05**, (2006) 026, [`doi: 10.1088/1126-6708/2006/05/026`], [`hep-ph/0603175`].

[45] T. Gleisberg et al., *SHERPA 1.α, a proof-of-concept version.* JHEP **02**, (2004) 056, [`doi: 10.1088/1126-6708/2004/02/056`], [`hep-ph/0311263`].

[46] G. Marchesini et al., *HERWIG: A Monte Carlo event generator for simulating hadron emission reactions with interfering gluons. Version 5.1 - April 1991.* Comput. Phys. Commun. **67**, (1992) 465, [`doi: 10.1016/0010-4655(92)90055-4`].

[47] M. Bahr et al., *Herwig++ Physics and Manual.* Eur. Phys. J. **C58**, (2008) 639–707, [`doi: 10.1140/epjc/s10052-008-0798-9`], [`arXiv:0803.0883`].

[48] T. Sjöstrand, *Monte Carlo Tools.* In *Proceedings of the 65th Scottish Universities Summer School in Physics: LHC Physics, St. Andrews, 16-29 August 2009*, edited by T. Binoth, C. Buttar, and P.J. Clark (Taylor and Francis) (2011), [`ISBN: 978-1-4398377-0-2`], to be published, [`arXiv:0911.5286`].

[49] S. Agostinelli et al., *Geant4 - a simulation toolkit.* Nucl. Inst. Meth. **A506**, (2003) 250–303, [`doi: 10.1016/S0168-9002(03)01368-8`].

[50] A. Sherstnev and R.S. Thorne, *Parton Distributions for LO Generators.* Eur. Phys. J. **C55**, (2008) 553–575, [`doi: 10.1140/epjc/s10052-008-0610-x`], [`arXiv:0711.2473`].

[51] B. Andersson, G. Gustafson, G. Ingelman, and T. Sjöstrand, *Parton fragmentation and string dynamics.* Phys. Rep. **97**, (1983) 31, [`doi: 10.1016/0370-1573(83)90080-7`].

[52] G. Aad et al., the **ATLAS** Collaboration, *Charged particle multiplicities in pp interactions at $\sqrt{s}$=0.9 and 7 TeV in diffractive limited phase space measured with the ATLAS detector at the LHC and a new* PYTHIA*6 tune.* ATLAS-CONF 2010-031 (2010).

[53] P.Z. Skands, *The Perugia Tunes.* In *Proceedings of the First International Workshop on Multiple Partonic Interactions at the LHC (MPI@LHC08), Perugia, Italy, October*

27-31, 2008, edited by P. Bartalini and L. Fanò, 284–297 (DESY-PROC-2009-06, DESY, Germany) (2010), [`arXiv:1003.4220`].

[54] G. Aad et al., the **ATLAS** Collaboration, *Study of Jet Shapes in Inclusive Jet Production in pp Collisions at* $\sqrt{s} = 7$ *TeV using the ATLAS Detector* [`arXiv:1101.0070`], submitted to Phys. Rev. D.

[55] B.R. Webber, *A QCD Model for Jet Fragmentation Including Soft Gluon Interference.* Nucl. Phys. **B238**, (1984) 492–528, [`doi: 10.1016/0550-3213(84)90333-X`].

[56] G. Aad et al., the **ATLAS** Collaboration, *Track-based underlying event measurements in pp collisions at sqrt{s}=900 GeV and 7 TeV with the ATLAS Detector at the LHC* (2010-081).

[57] S.D. Ellis et al., *Jets in Hadron-Hadron Collisions.* Prog. Part. Nucl. Phys. **60**, (2008) 484–551, [`doi: 10.1016/j.ppnp.2007.12.002`], [`arXiv:0712.2447`].

[58] J.E. Huth et al., *Toward a Standardization of Jet Definitions.* In *Proceedings of the 5th DPF Summer Study on High-energy Physics, Snowmass, CO, USA, 25 June - 23 July 1990*, edited by E.L. Berger (World Scientific, River Edge, NJ) (1992), [`ISBN: 9789810209315`].

[59] G.C. Blazey et al., *Run II Jet Physics: Proceedings of the Run II QCD and Weak Boson Physics Workshop.* FERMILAB-Conf 00/092-E (2000), [`hep-ex/0005012v2`].

[60] M. Cacciari, G.P. Salam, and G. Soyez, *The anti-*k_t *jet clustering algorithm.* JHEP **0804**, (2008) 063, [`doi: 10.1088/1126-6708/2008/04/063`], [`arXiv:0802.1189`].

[61] A. Breskin and R. Voss (eds.) *The CERN Large Hadron Collider: Accelerator and Experiments*, volume Volume 1: LHC Machine, ALICE, and ATLAS (CERN, Geneva) (2009), [`ISBN: 9789290833376`].

[62] The LEP Injector Study Group, *LEP design report, Vol. 2, The LEP main ring.* CERN-LEP 84-01, Geneva (1984).

[63] S. van der Meer, *Calibration of the effective beam height in the ISR.* CERN-ISR-PO 68-31 (1968).

[64] G. Anders et al., *LHC Bunch Current Normalisation for the April-May 2010 Luminosity Calibration Measurements.* CERN-ATS-Note 2011-004 (2011).

[65] G. Aad et al., the **ATLAS** Collaboration, *Expected Performance of the ATLAS Experiment, Detector, Trigger and Physics.* CERN-OPEN 2008-020, Geneva (2008), [`ISBN: 9789290833215`].

[66] G. Aad et al., the **ATLAS** Collaboration, *The ATLAS Experiment at the CERN Large Hadron Collider.* JINST **3**, (2008) S08003, [`doi: 10.1088/1748-0221/3/08/S08003`].

[67] G. Aad et al., the **ATLAS** Collaboration, *Performance of primary vertex reconstruction in proton-proton collisions at sqrt7 TeV in the ATLAS experiment.* ATLAS-CONF 2010-069 (2010).

[68] G. Aad et al., the **ATLAS** Collaboration, *Readiness of the ATLAS Liquid Argon Calorimeter for LHC Collisions.* ATLAS-LAR 2009-01-004 (2009), accepted for publication in Eur. Phys. J. C, [`arXiv:0912.2642`].

[69] M. Aharrouche et al., *Energy linearity and resolution of the ATLAS electromagnetic barrel calorimeter in an electron test-beam.* Nucl. Inst. Meth. **A568**, (2006) 601–623, [`doi: 10.1016/j.nima.2006.07.053`].

[70] W. E. Cleland and E. G. Stern, *Signal processing considered for liquid ionization calorimeter in a high rate environment.* Nucl. Instrum. and Methods **A338**, (1994) 467.

[71] G. Aad et al., the **ATLAS** Collaboration, *ATLAS Computing Technical Design Report.* CERN-LHCC 2005-022 (2005), see also the Athena Online Manual.

[72] I. Bird et al., *LHC computing Grid. Technical design report.* CERN-LHCC 2005-024 (2005), [`ISBN: 9789290832539`].

[73] J. Adelman et al., *ATLAS Offline Data Quality Monitoring.* In *Proceedings of the 17th International Conference on Computing in High Energy and Nuclear Physics, Prague, Czech Republic, 21-27 March 2009*, 042018 (IOP Journal of Physics: Conference Series) (2010), [`doi: 10.1088/1742-6596/219/4/042018`].

[74] R. Fruhwirth, W. Waltenberger, and P. Vanlaer, *Adaptive vertex fitting.* J. Phys. **G34**.

[75] M. Cacciari and G.P. Salam, *Dispelling the N**3 myth for the k(t) jet-finder*. Phys. Lett. **B641**, (2006) 57–61, [`doi: 10.1016/j.physletb.2006.08.037`], [`hep-ph/0512210`].

[76] Z. Marshall, *A Measurement of Jet Shapes in Proton-Proton Collissions at 7.0 TeV Center-of-Masss Energy with the ATLAS Detector at the Large Hadron Collider*. CERN-THESIS 2010-142 (2010).

[77] G. Aad et al., the **ATLAS** Collaboration, *Jet energy resolution and reconstruction efficiencies from in-situ techniques with the ATLAS Detector Using Proton-Proton Collisions at a Center of Mass Energy* $\sqrt{s}$*=7 TeV*. ATLAS-CONF 2010-054 (2010).

[78] G. Aad et al., the **ATLAS** Collaboration, *Properties of Jets and Inputs to Jet Reconstruction and Calibration with the ATLAS Detector Using Proton-Proton Collisions at* $\sqrt{s}$*=7 TeV*. ATLAS-CONF 2010-053 (2010).

[79] M. Plamandon M. Cooke, P.S. Mangeard et al., the **ATLAS** Collaboration, *In situ commissioning of the ATLAS electromagnetic calorimeter with cosmic muons*. ATLAS-LARG-PUB 2007-013 (2007).

[80] G. Aad et al., the **ATLAS** Collaboration, *Jet energy scale and its systematic uncertainty in proton-proton collisions at* $\sqrt{s} = 7$ *TeV in ATLAS 2010 data*. ATLAS-CONF 2010-032 (2011).

[81] G. Aad et al., the **ATLAS** Collaboration, *In-situ jet energy scale and jet shape corrections for multiple interactions in the first ATLAS data at the LHC*. ATLAS-CONF 2011-030 (2011).

[82] D. Lopez, E. W. Hughes, and A. Schwartzman, *A Simple* p_T*- and* η*-Dependent Monte Carlo-Based Jet Calibration*. ATL-PHYS-INT 2009-077 (2009).

[83] G. Aad et al., the **ATLAS** Collaboration, *ATLAS Calorimeter Response to Single Isolated Hadrons and Estimation of the Calorimeter Jet Scale Uncertainty*. ATLAS-CONF 2011-028 (2011).

[84] M.L. Mangano et al., *ALPGEN, a generator for hard multiparton processes in hadronic collisions*. JHEP **07**, (2003) 001, [`doi: 10.1088/1126-6708/2003/07/001`], [`hep-ph/0206293`].

[85] G. Corcella et al., *HERWIG 6: An event generator for hadron emission reactions with interfering gluons (including supersymmetric processes)*. JHEP **01**, (2001) 010, [`doi:10.1088/1126-6708/2001/01/010`], [`hep-ph/0011363`].

[86] J.M. Butterworth, J.R. Forshaw, and M.H. Seymour, *Multiparton interactions in photoproduction at HERA*. Zeit. f. Phys. **C72**, (1996) 637–646, [`doi:10.1007/s002880050286`], [`hep-ph/9601371`].

[87] G. Aad et al., the **ATLAS** Collaboration, *In-situ pseudorapidity intercalibration for evaluation of jet energy scale uncertainty using dijet events in proton-proton collisions at* $\sqrt{s} = 7$ *TeV*. ATLAS-CONF 2011-014 (2011).

[88] G. Aad et al., the **ATLAS** Collaboration, *Determination of the ATLAS jet energy measurement uncertainty using photon-jet events in proton-proton collisions at* $\sqrt{s} = 7$ *TeV*. ATLAS-CONF 2011-031 (2011).

[89] G. Aad et al., the **ATLAS** Collaboration, *Measurement of the inclusive isolated prompt photon cross section in pp collisions at* $\sqrt{s} = 7$ *TeV with the ATLAS detector* [`arXiv:1012.4389`], accepted by Phys. Rev. D.

[90] G. Aad et al., the **ATLAS** Collaboration, *Probing the jet energy measurement at the TeV-scale using the multi-jet balance technique in proton-proton collisions at* $\sqrt{s} = 7$ *TeV*. ATLAS-CONF 2011-029 (2011).

[91] G. Aad et al., the **ATLAS** Collaboration, *Data-Quality Requirements and Event Cleaning for Jets and Missing Transverse Energy Reconstruction with the ATLAS Detector in Proton-Proton Collisions at a Center-of-Mass Energy of sqrt(s)=7 TeV*. ATLAS-CONF 2010-038 (2010).

[92] G. Aad et al., the **ATLAS** Collaboration, *Charged-particle multiplicities in pp interactions at* $\sqrt{s} = 900$ *GeV measured with the ATLAS detector at the LHC*. Phys. Lett. **B688**, (2010) 21–42, [`arXiv:1003.3124`].

[93] G. Aad et al., the **ATLAS** Collaboration, *Luminosity Determination Using the ATLAS Detector*. ATLAS-CONF 2010-060 (2010).

[94] G. Aad et al., the **ATLAS** Collaboration, *Updated Luminosity Determination in pp Collisions at* $\sqrt{s} = 7$ *TeV using the ATLAS Detector*. ATLAS-CONF 2011-034 (2011).

[95] G. Aad et al., the **ATLAS** Collaboration .

[96] Z. Nagy, *Next-to-leading order calculation of three-jet observables in hadron-hadron collisions.* Phys. Rev. **D68**, (2003) 094002, [`doi: 10.1103/PhysRevD.68.094002`].

[97] T. Carli et al., *A posteriori inclusion of parton density functions in NLO QCD final-state calculations at hadron colliders: The APPLGRID Project.* Eur. Phys. J. **C66**, (2010) 503–524, [`doi: 10.1140/epjc/s10052-010-1255-0`].

[98] H.-L. Lai et al., *Uncertainty induced by QCD coupling in the CTEQ global analysis of parton distributions.* [`arXiv:1004.4624`].

[99] A. Buckley et al., *Rivet user manual.* [`arXiv:1003.0694`].

[100] S. Alioli, K. Hamilton, P. Nason, C. Oleari, and E. Re, *Jet pair production in POWHEG.* Technical report (2010), [`hep-ex/1012.3380`].

[101] G. Aad et al., the **ATLAS** Collaboration, *First tuning of HERWIG/JIMMY to ATLAS data.* ATL-PHYS-PUB 2010-014 (2010).

[102] G. D'Agostini, *A multidimensional unfolding method based on Bayes' theorem.* Nucl. Instrum. and Methods **A362**, (1995) 487–498, [`doi: 10.1016/0168-9002(95)00274-X`].

[103] A. Höcker and V. Kartvelishvili, *SVD approach to data unfolding.* Nucl. Instrum. and Methods **A372**, (1996) 469–481, [`doi: 10.1016/0168-9002(95)01478-0`].

[104] Estia J. Eichten, Kenneth D. Lane, and Michael E. Peskin, *New Tests for Quark and Lepton Substructure.* Phys. Rev. Lett. **50**(11), (1983) 811–814, [`doi: 10.1103/PhysRevLett.50.811`].

[105] G. Aad et al., the **ATLAS** Collaboration, *Search for quark contact interactions in dijet angular distributions in pp collisions at measured with the ATLAS detector.* Physics Letters B **694**(4-5), (2011) 327 – 345.